Next Generation Structural Technologies: Implementing High Force-To-Volume Energy Absorbers

Geoffrey W. Rodgers

A thesis
presented for the Degree

of

Doctor of Philosophy

in

Mechanical Engineering
at the
University of Canterbury
Christchurch, New Zealand

University of Canterbury
2009

This thesis is dedicated in memory of my Grandfather,

Hugh McLennan Calder – 1926-2009

Abstract

This thesis explores the design development, experimental testing, and structural implementation of high force-to-volume (HF2V) damping devices. The development of damage-free structural design methods requires an alternate means of dissipating energy, as eliminating structural damage eliminates the primary energy dissipation mechanism. The HF2V devices developed within this thesis provide a damage-free energy dissipation mechanism and can be used in structures subjected to earthquake excitation. The devices developed are much smaller, more compact versions of lead extrusion dampers previously utilised for structural applications such as base-isolation. The devices provide the same force levels in a significantly smaller package, greatly extending the possible applications. Therefore, the development of these devices is a significant step towards developing damage-free structural design methods and reducing the impact of seismic events on a society.

The results indicate that the HF2V devices provide repeatable, consistent energy dissipation on repeated cycles, without any stiffness or strength degradation, and without any requirements for repair or replacement following an earthquake. This outcome is unique to these devices, and these characteristics are not available with the alternatives typically used within this field, such as yielding steel fuse-bars or proprietary viscous dampers. These devices therefore provide a unique opportunity to provide large energy dissipation in a very compact package that can easily be incorporated into a structural connection. At $100-300 each the devices cost several orders of magnitude less than proprietary viscous dampers and are much smaller physically, but provide equivalent or greater force capacity, making them an economically and technologically feasible option.

The devices are implemented into three structural systems, with numerous configurations tested for each structural system to provide alternate methodologies and delineate the contributions to response. The structural implementations show significant promise and highlight several key design recommendations to optimise their use. Finally, analytical models of varying complexity of the device and connection response are developed. The simple models are intended as an initial design tool, with the more detailed models developed as evaluation tools for initial designs. These models provide the tools to incorporate these devices into design practices and create a bridge to the profession.

Overall, this thesis develops high force-to-volume damping devices from an initial concept, through prototype development, to structural implementation and associated modelling. The key design issues are identified and significant progress is made towards this design approach receiving uptake by the profession.

Acknowledgements

I would like to express my appreciation to everyone who helped my through the time I have worked on this thesis. Obviously, my thanks go to my supervisors, Professor Geoff Chase, Professor John Mander, Assoc. Prof. Rajesh Dhakal, and Assoc. Prof. Greg MacRae who gave me invaluable support and advice throughout the whole journey. Your strong supervision and mentoring has made this project, and the research outcomes, possible. I also wish to give special thanks to my family and friends who helped give me perspective during the very busy times, when work sometimes seemed to dominate my life.

I would like to thank the technicians and students that I have worked with on this research. There have been many postgrads and technicians that have helped me and been a pleasure to work with. Particular thanks go to Kevin Solberg for his support as we collaborated on the experimental aspects of this research. I'd like to thank technicians Rodney Elliott, John Maley, and in particular Tim Perigo, whose great sense of humour always lightened the mood in the lab, and made golf trips all that much more enjoyable. My appreciation also goes to Lance Cleeve and Doug Heaton of C&M Technologies for construction of the dampers used in this research.

I would like to thank my fellow postgrads and officemates who provided great friendship and support, and were always able to see the lighter side of research. Your companionship and combined sense of humour always made the tough times more manageable.

My thanks also go to those who funded this research, in particular the Tertiary Education Commission through the Bright Futures Scheme, and Fulbright New Zealand and the Earthquake Commission for the Fulbright-EQC Graduate Award that saw me travel to

Texas A&M for part of my thesis. I would like to thank all my friends and colleagues at Texas A&M for making that experience so special and so very memorable. I will remember Texas, and my experiences and people I met there, very warmly.

All of the support that I have received from my supervisors, family and friends, both in New Zealand and in Texas, is greatly appreciated. In particular, I would like to give special thanks to my parents, who have always given me love, support and guidance and been there for me at every stage of my life. Without your ongoing support and dedication, I would not be where I am today. Thank you.

Table of Contents

List of Figures

List of Tables

Chapter 1: Introduction

History has shown the devastating impact that large earthquakes can have in terms of immediate damage and loss of life, as well as in terms of long-term effects on an economy. The damage to important infrastructure during an earthquake can lead to further damage and loss to a community. Following the San Francisco Earthquake of 1906, the subsequent fires burned out of control for three days, destroyed 490 city blocks, and caused more damage than the direct effect of the earthquake itself. In the days, weeks and months following an earthquake, critical infrastructure such as fire stations and hospitals can be either out-of-service or operating at severely reduced capacity, during the time at which they are needed the most. In some ways more significantly, structural damage puts workers out of homes and/or eliminates jobs as workers cannot get into damaged premises to work, with a flow-on effect that can damage economies for decades. Therefore the need to develop communities that are more resilient to this significant natural hazard is of great importance, but often overlooked for more immediate priorities as large, damaging earthquakes occur relatively rarely.

One of the earliest and strongest earthquakes recorded was the Lisbon earthquake of 1755. Estimates vary, but the earthquake claimed between 10,000 and 100,000 lives, and had a total cost estimated between 32 and 40% of the Portuguese GDP (Pereira 2006). More recent earthquakes have also highlighted the major effects earthquakes can have on a society. The 1989 Loma Prieta Earthquake (Magnitude 6.9) killed 63 people, and caused an estimated US$6-10 billion in property loss alone (United States Geological Survey (USGS) 1999b). The 1995 Kobe earthquake (Magnitude 6.9) killed more than 6,000 people, caused US$100 billion in damage and left over 300,000 people homeless (Horwich 2000; United States

Geological Survey (USGS) 1999a). Moreover, the 1994 Northridge Earthquake (Magnitude 6.7) killed 57 people and caused more than US$20 billion in damage.

Earthquakes are a constant risk to societies located in seismically active areas, where the next big event is simply a question of probability. Following the large events of Loma Prieta in 1989 and Northridge in 1994, California is subjected to an ever-present risk of another large seismic event. The United States Geological Survey estimated in 1999 that there was a 70% probability of a magnitude 6.7 or greater quake, capable of causing widespread damage, striking the San Francisco Bay region before 2030 (United States Geological Survey (USGS) 1999a). This study was superseded in a 2008 report which placed the probability of having one or more magnitude 6.7 or larger earthquake in the California area over the next 30 years at greater than 99% (United States Geological Survey (USGS) 2008). Although these statistics are specific to the seismic region of California, they reflect the ongoing risk to any society located within a seismically active region.

In the more recent earthquakes in the Unites States that occurred in Northridge and Loma Prieta, relatively few lives were lost, but significant cost was associated with both structural damage and the associated down-time and interruption to business activities. The cost associated with down-time from structural damage can often exceed the direct cost from the damage alone, and have ongoing effects on an society (Comerio 2006). Therefore, although modern structural design has made significant progress in reducing the threat to human life during an earthquake, the associated cost still presents a major risk to a region's economy.

Earthquake ground motions impart a significant amount of energy into a structure. To protect life-safety and prevent collapse this energy must be absorbed to prevent excessive displacement response. Modern structural design seeks to absorb this energy through

sacrificial damage to specifically designed locations within the structure, much like crumple-zones in automobiles. The design of structures seeks to form localised inelastic deformation at the end of the beams, referred to as plastic hinge zones, to protect life-safety by maintaining column integrity and preventing structural collapse. The damage associated with this inelastic deformation absorbs a significant amount of energy and reduces the magnitude of the structural response to the ground acceleration.

Figure 1.1: Severe damage to the Olive View Hospital from the 1971 San Fernando earthquake (M = 6.7)

Figure 1.1 shows the damage to the Olive View Hospital from the 1971 San Fernando earthquake. In the aftermath of a large earthquake, when there are many people injured and there is an increased need for medical treatment, hospital services may be severely interrupted. The damage seen in Figure 1.1 has absorbed large amounts of response energy from the structure and collapse was prevented saving many lives and preventing many injuries. However, the major damage will result in significant cost and downtime during the rebuilding phase, which will have long term effects on the society and the local, or even national, economy. In particular, as a result of this damage and downtime, many people will lose jobs, and many of the local residents may move to unaffected areas further affecting the long-term prospect of the local economy.

As a result of the economic cost from these and other recent earthquakes, the development of damage-free structures has gained significant research momentum in recent years. In particular, research has been undertaken for both concrete and steel structures that provide a controlled rocking response at the beam-column interface. The connections are designed so that they can deform without damage to the connection or the beam-end where localised damage in the form of a plastic hinge would traditionally be located. However, eliminating the structural damage also eliminates one of the key means of absorbing response energy. Therefore, if the damage is eliminated, the energy needs to be absorbed through an alternative means, to maintain life safety. This research thus provides a mean to extend structural engineering to both preserve life safety, while at the same time preserving the social and economic outcomes.

Research over the past decade has also investigated the use of jointed precast concrete connections. These connections use pre-cast beams and columns that are not connected to one another in the traditional sense, but are instead separate entities. These structural elements can then be held together by steel tendons that run through the beams and columns and are then post-tensioned to hold the structure together.

Research and development of precast concrete jointed and rocking structures has gained considerable momentum over the past two decades. In particular, there has been significant research on so-called PRESSS systems (Priestley et al. 1999), and on damage-avoidance design (DAD) (Ajrab et al. 2004; Bradley et al. 2008; Holden et al. 2003; Mander and Cheng 1997). These systems, designed to accommodate inelastic behaviour by rocking at specially detailed joints, have proven to provide a level of seismic resistance comparable to current standards while remaining almost (in the case of PRESSS) or essentially (in the case of DAD) damage-free. Furthermore, such systems do not suffer excessive residual

displacement, a common occurrence in conventional sacrificially designed systems that can result in the complete loss of the structure due to excessive yielding and/or damage to beams or connections.

Precast jointed and rocking systems exhibit non-linear response by connection opening instead of the conventional sacrificial, energy dissipating, formation of a plastic hinge. As a result, they have markedly less inherent energy dissipation than ductile monolithic systems (Cheok and Lew 1991; Priestley and Tao 1993). Therefore, it is essentially mandatory to provide supplemental energy dissipation devices to these connections to reduce displacement response from earthquakes and provide energy dissipation equivalent to the connections they are replacing.

Similarly to concrete structures, occupant safety and use of steel frame buildings following major earthquakes is often limited by damage to the structural frame system. Most of this damage is restricted to the plastic hinge zones at beam ends or the panel zone within steel beam-column joints. As evidenced by the extensive damage to steel structures following the 1994 Northridge earthquake, repair costs and downtime can be substantial to owners and users of such structures, creating a significant, long-term social and economic impact. Existing welded steel moment frames are designed to tolerate substantial yielding and plastic rotation under earthquake loads. This sacrificial design approach can lead to permanent, and often irreparable, damage when inter-story drifts (rotations) exceed the 2% design level.

Presently, steel connections are designed using sacrificial yielding at beam ends (plastic hinge formation) to dissipate dynamic response energy (Standards New Zealand. 1997). Plastic hinges form at the ends of beams, causing permanent damage and the possibility of failure under extreme inter-story drifts due to flange buckling or weld fracture. The

associated damage can be difficult, time consuming and expensive to repair. It is thus desirable to have damage-free connections, eliminating expensive repairs and enabling businesses to continue without causing further financial loss to the owner or tenants. One approach for providing this mechanism is a sliding hinge joint (Clifton 2005; MacRae et al. 2007). This design approach utilises a controlled rocking interface with specifically designed friction interfaces that dissipate energy during a response cycle. This method is effective at providing non-linear structural response in an essentially damage-free manner. However, partial loss of bolt pre-tension on successive cycles can lead to some stiffness and/or strength degradation.

For both concrete and steel connections, the development of damage-free structures requires the development of a reliable and economically feasible alternate energy dissipation mechanism that can be placed into structures in potentially large numbers. An early application presented by Stanton et al. (1997), utilised mild steel rods running across a concrete connection and grouted in ducts. These rods were designed to yield in tension and compression to dissipate energy. However, test results showed that the bond between the grout and steel deteriorated, and undesirable stiffness and strength degradation was observed. In addition, repeated cycles led to bar fracture in some tests due to low-cycle fatigue, showing an inherent weakness in any sacrificial yielding-steel energy dissipation approach, be it a device or by sacrificial design.

Subsequent research has highlighted alternative mild steel energy dissipation devices, bolted externally across the joint region. Bradley et al. (2008) demonstrated externally mounted steel yielding devices with substantially reduced, but not eliminated, stiffness or strength degradation. However, due to low-cycle fatigue and residual stresses these devices would still have to be replaced following an earthquake. In addition, they only offer repeated peak

dissipation when yielded further than a previous cycle. Subsequent smaller cycles, the vast majority of any given earthquake input, thus receive minimal or no dissipation.

The work of Bradley et al. (2008) also demonstrated that their steel yielding devices were prone to buckle. This buckling reduced the axial load and energy dissipation capacities (Dhakal and Maekawa 2002). Amaris et al. (2006) demonstrated that with externally mounted buckling-restrained mild steel bars, slightly improved performance may be obtained. However, their system retained the same fatigue-prone and residual force deficiencies of Bradley et al. (2008). Hence, none of these concepts offers the consistency, over any size cycle, to repeatably dissipate energy.

Overall, it can be seen that all of this previous work essentially moves the damage mechanism to a sacrificial component fitted to the connection. Although this approach provides a more easily repaired connection, repair or replacement is still likely to be necessary following a seismic event. In addition, the stiffness and strength degradation displayed by most of the sacrificial elements results in less energy being dissipated during subsequent cycles. More succinctly, these approaches are all non-optimal.

The ability to dissipate earthquake response energy in a damage-free manner requires the development of devices that can provide large resistive forces. The devices also need to provide a means of repeatedly and consistently dissipating energy, regardless of response cycle size or history, so that following an earthquake no repair or replacement is needed, to minimise down-time and the associate cost to an economy. Finally, they need to be compact so that they do not infringe on the architectural aesthetics or function of the structure.

The specific aim of this research is to further develop lead damping devices (Robinson and Greenbank 1975; Robinson and Greenbank 1976) to absorb structural energy during an earthquake in a controlled manner, with repeatable behaviour. In contrast to the very large dampers previously deployed in New Zealand and elsewhere, the device must be sufficiently compact to allow placement in situations with tight volume constraints, while still providing the same high levels of force seen in previous, much larger devices. Ideally, the dampers should also be inexpensive and thus, commercially viable in regular wide-scale use. This research uses lead as the working material due to its unique rheological properties and low re-crystallisation temperature. The high yield forces provided by lead dampers give the ability to modify and reduce seismic response through hysteretic energy dissipation within the device alone. Thus, they would have the potential to markedly reduce damage in the structural elements. This research modifies the basic designs and principles of these larger dampers to create significantly smaller 120-400kN devices. Obtaining equivalent force levels in significantly smaller devices dramatically expands possible applications if they can be made for relatively low cost.

The cost of the devices in this research was approximately $300-400 per device for the small numbers produced. Bigger production runs of these devices could yield an estimated cost within the $100-300 range, representing a very low cost for the large structural applications presented within this thesis. The cost of commercial viscous dampers for these types of applications are typically $10,000-30,000 each (Marriott et al. 2009), representing a substantial increase in cost of a connection that is not economically viable. Therefore, the devices developed within this thesis, costing 1-2 orders of magnitude less, are a far more economical alternative, if they can provide the desired behaviour in the proof-of-concept analytical and experimental research presented.

1.1. Objective and Scope

The main objective of this study is to investigate the feasibility of developing high force-to-volume (HF2V) damping devices to provide structural energy dissipation. Analytical and experimental studies are undertaken to develop the devices, investigate their structural implementation, and identify design issues and considerations. The study focuses on several main areas:

- The development and experimental testing of high force-to-volume damping devices to achieve large resistive forces in a very compact package able to fit within structural connections.
- Analytical modelling of structural response to relate the device performance to known and accepted design guidelines as a bridge to the profession
- Experimental investigation of the implementation of these devices into both concrete and steel connections.
- Develop models to describe the observed experimental behavior for use in design analyses and finite element codes.

The overall approach of this thesis is to develop a new means of energy dissipation, taking the results from initial prototype development, through laboratory testing and structural implementation, to final designs and associated models that can be used by the profession.

1.2. Chapter Overview

Chapter 2 presents the development and testing of a range of experimental prototype lead-extrusion devices to develop the concept, characterize the response, and provide design equations that relate the device parameters to the expected force levels.

Chapter 3 presents an initial analytical investigation into the possible response reductions that can be achieved with the addition of the HF2V devices to a single degree-of-freedom structure. The response reductions are also extended to standard design equations to create a bridge to the profession and increase the likelihood of uptake.

Chapter 4 presents an experimental structural implementation where the HF2V devices are externally connected to a jointed, pre-cast concrete connection utilizing damage avoidance principles. Several key outcomes are noted and in particular the influence of flexibility in the elements that connect the HF2V devices into the structural system.

Chapter 5 and 6 present an experimental investigation where the HF2V devices are implemented into a second jointed, pre-cast, concrete connection. In these chapters the HF2V devices are cast internally into the beams ends, and the dampers contribute larger damping forces to the connection.

Chapter 7 presents the design and experimental testing of a damage-free steel connection using HF2V devices. Multiple configurations are tested and key design issues are identified.

Chapter 8 presents the development of a model to describe the behavior of pre-cast concrete connections with HF2V devices, such as those in Chapters 4-6. The model is relatively simple, but has associated limitations.

Chapter 9 presents the development of a velocity-dependent device model that incorporates the effects of flexibility from the damper shaft and connecting elements. The model is also extended to include member flexibilities and a connection level model is developed that describes the behavior of the steel connection in Chapter 7.

Chapter 10 presents an advanced model for precast concrete connections with HF2V devices, and includes the effects of yielding in the tendons, loss of post-tensioning, friction and asymmetry from non-centrally located tendons.

Chapters 11 and 12 present the overall conclusions to the research and discusses possible extensions and future work.

1.3. Summary

This chapter has presented the motivation for this research and an introduction to the devices developed and tested within this thesis. Overall, earthquakes pose a significant risk in seismically active regions. The development of damage-free design methodologies is crucial is developing resilient communities that can more easily withstand seismic events. The key issue with damage-free design is the ability to provide an alternate means of energy dissipation. The development of a cost-effective, high force, yet small volume version of previous lead extrusion dampers would enable this energy dissipation, and make a significant

step towards damage-free structures becoming a realistic design alternative. Structural implementation, experimental testing and model development will provide proof-of-concept validation, as well as indentify key design issues and provide the path for uptake by the profession.

Chapter 2: Device Design And Development

High performance, but relatively very small size, lead dampers are designed and tested in this chapter to characterise their force-displacement behaviour. The result is trade-off curves relating device geometry to force capacity. This approach parameterises the design space and enables further devices to be designed for a range of potential structural applications. Peak forces of 120-350kN were obtained experimentally for devices that had dimensions small enough that they could fit within standard structural connections.

2.1. Introduction:

Earthquakes and other large environmental hazards can cause significant movement in a structure and cause major cracking and degradation in structural integrity. The associated damage can be difficult and expensive to repair even though modern structural design methods seek to localise damage to specific areas such as plastic hinge zones. Although this damage provides significant energy dissipation during a seismic event, it is preferable to dissipate energy without permanent structural damage to reduce the economic impact of an earthquake from damage and downtime.

The specific aim of the research in this chapter is to develop lead damping devices (Robinson and Greenbank 1975; Robinson and Greenbank 1976) to absorb energy during an earthquake in a controlled manner, with repeatable behaviour, in a compact package. Thus, they would have the potential to markedly reduce damage in the structural elements. Lead extrusion dampers have been used for energy dissipation in structural applications including base isolation (Cousins and Porritt 1993). Historically, these devices have been volumetrically

very large. Figure 2.1 presents a photograph from Cousins and Porritt (1993), which shows devices with force capacities of 100 and 700kN, and a person to indicate scale. These devices are seen to be quite large, but are suitable for the applications previously considered, as the space available has not typically been tightly restricted.

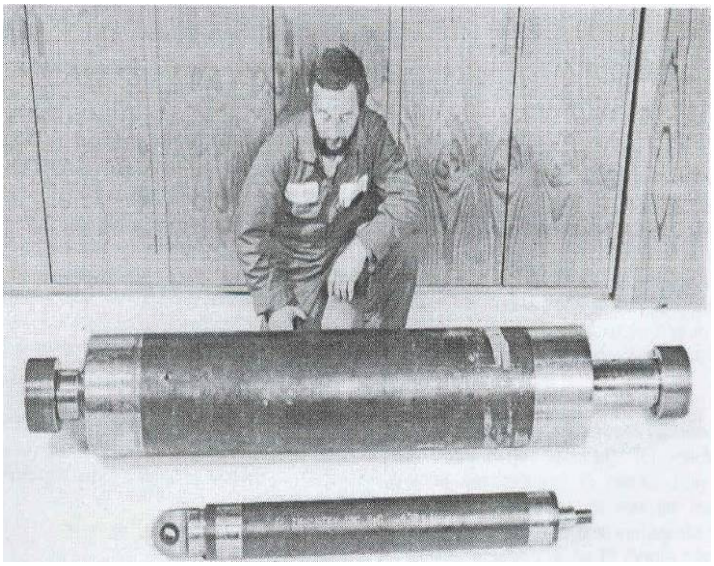

Figure 2.1: Previous lead extrusion devices with significantly larger dimensions. The devices shown have 100 and 700 kN force capacities. (Source: (Cousins and Porritt 1993))

The large size of these previous devices has been an impediment that has prevented their placement into new applications with tight volume constraints, such as those in Figure 2.2. The large volume of the previous devices also makes them relatively expensive to produce, further limiting the number of possible applications. This research modifies the basic designs and principles of these larger dampers to create significantly smaller 120-400kN devices. Obtaining equivalent force levels in significantly smaller devices dramatically expands possible applications if they can be made for relatively low cost.

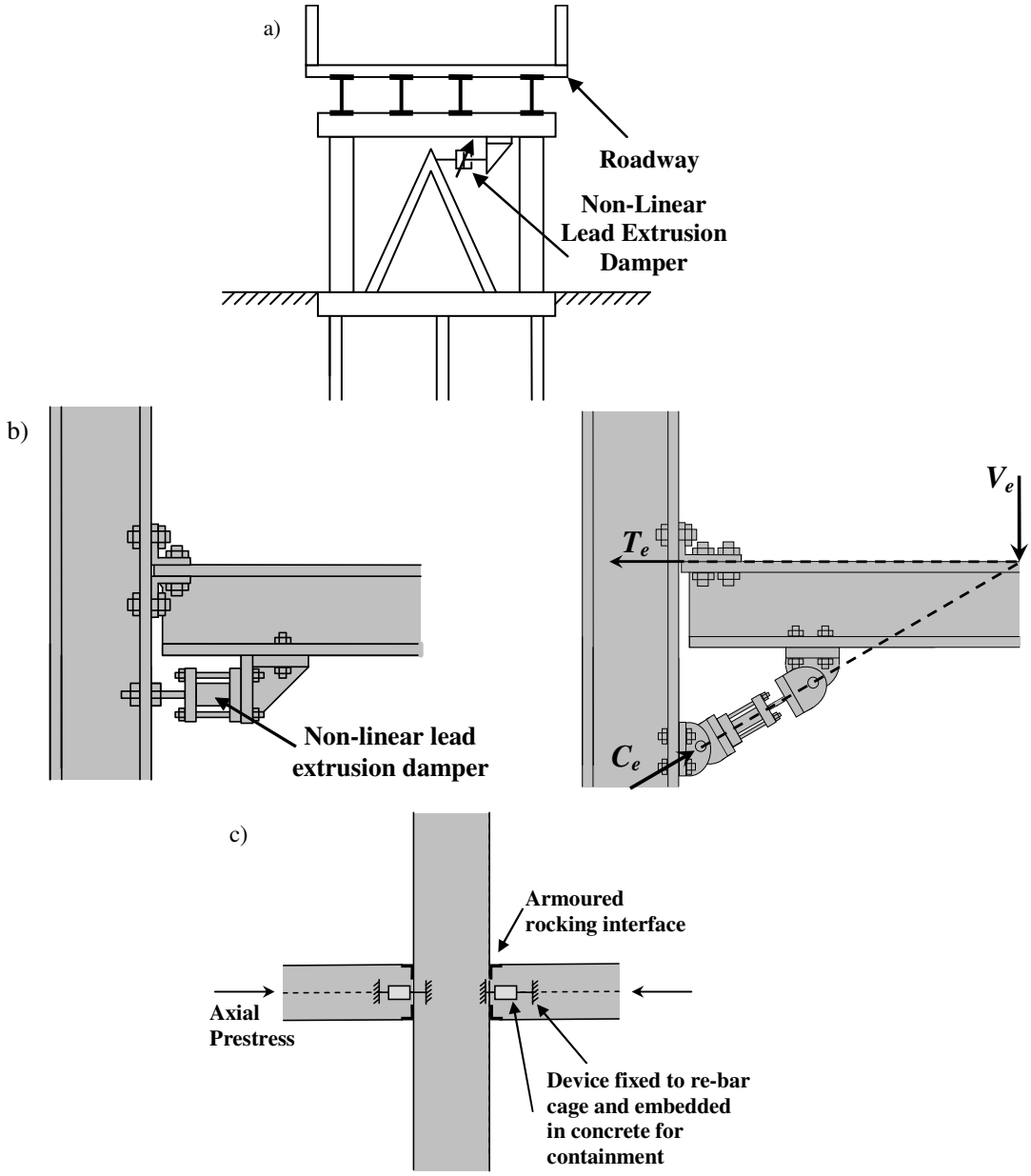

Figure 2.2: Possible applications for lead extrusions dampers; a) in a bridge pier, b) a seismic moment-frame steel beam-column connection, and a seismic load-balancing frame system, and c) in a reinforced concrete joint utilising Damage Avoidance Design (DAD)

One possible application for compact high force-to-volume extrusion dampers is in bridge piers, as shown schematically in Figure 2.2a. In this application, the load taken by the extrusion damper reduces the lateral demand on the columns. This method of using high force-to-volume (HF2V) extrusion dampers to provide supplemental damping is also very amenable to bridge piers that use a Damage Avoidance Design (DAD) approach. These type of DAD connections utilise a rocking interface and eliminate structural damage by

eliminating the damage mechanism. Thus, they also eliminate one of the primary methods of energy dissipation. Therefore, these piers typically have low inherent structural damping and must therefore be augmented by the use of supplemental damping systems. A pier utilising these principles and HF2V devices can provide hysteretic energy absorption similar to that of a ductile concrete system, but in a damage-free manner. They can thus eliminate the need for costly repair following an earthquake while maintaining full structural function.

Another possible application enabled by the highly reduced size of the device is presented in Figure 2.2b, where an extrusion damper is fitted directly into a steel beam-column connection. The relatively small extrusion damper provides a resistive force against joint rotation and consequently provides hysteretic energy absorption, preventing yielding of the elements of the main structural steel frame. The placement of the damper below the bottom flange of the beam results in larger displacements in the damper for a given design drift, and consequently larger energy dissipation. Figure 2.2b also shows both the seismic moment-frame steel beam-column connection, as well as a seismic load-balancing frame concept, where the vertical component of the damper force provides a reaction to the shear force, V_e. Again, small relative device size (volume) enables placement within or nearly within a standard structural connection.

Figure 2.2c shows a schematic representation of how such a HF2V device can be incorporated directly into a reinforced concrete beam-column connection that utilises Damage Avoidance Design (DAD) principles. The schematic of Figure 2.2c shows the extrusion damper cast directly into the end of the beam and connected to the column. In this application, joint opening at the armoured rocking interface caused by joint rotation will displace the shaft of the damper, providing hysteretic energy absorption. The key advantage

of a system such as this is the ability to provide energy absorption in a damage-free and repeatable manner within the existing structural connection.

An important consideration for the applications presented in Figures 2.2b and 2.2c is a reliable mechanism for shear transfer. For the concrete connection, a set of shear keys that interface between the beam end and column face can be utilised. For the steel connection, and shear plate could be provided between the column and the beam web. This plate can be slotted in the horizontal direction so that it can carry vertical shear but not prevent joint rotation.

Extrusion dampers can be characterised into two groups based upon fundamental design differences. These types are the bulged-shaft and constricted tube type extrusion dampers (Cousins and Porritt 1993). The relative merits of each type are well documented (Cousins and Porritt 1993) and focus upon ease of manufacture and ability to produce a repeatable and consistent hysteresis loop. Both types of extrusion damper provide a resistive force by plastically extruding the working material through an orifice created by an annular restriction. Bulged-shaft extrusion dampers utilise a streamlined bulge on the central shaft to create the orifice, whereas the constricted tube type utilise a constriction on the bore of the outer cylinder. The bulged-shaft design was chosen in this research for ease of manufacture and consequently low-cost. Low-cost is an important consideration for widespread adoption or use of extrusion damping technology across a given structure, where the ability to use them within a structural connection as in Figure 2.2 implies using a relatively large number of them. A cross-sectional schematic of the bulged-shaft design is presented in Figure 2.3a.

The damper is designed to fit into confined spaces within and around structural connections, such as the applications presented in Figure 2.2. For example, Figure 2.2b shows a steel

connection application with tight space constraints, where the damper must fit between the flanges of universal column sections nominally 350mm deep (W14 in American steel design codes) to broaden possible application into steel high rise structures. Thus, in this case, the shaft has been limited to approximately 30mm in diameter, in-line with maximum fitting sizes commonly used in structural applications. Shaft material is limited to high strength steel, such as 4140 to eliminate manufacturing difficulties and cost increases associated with less accessible materials.

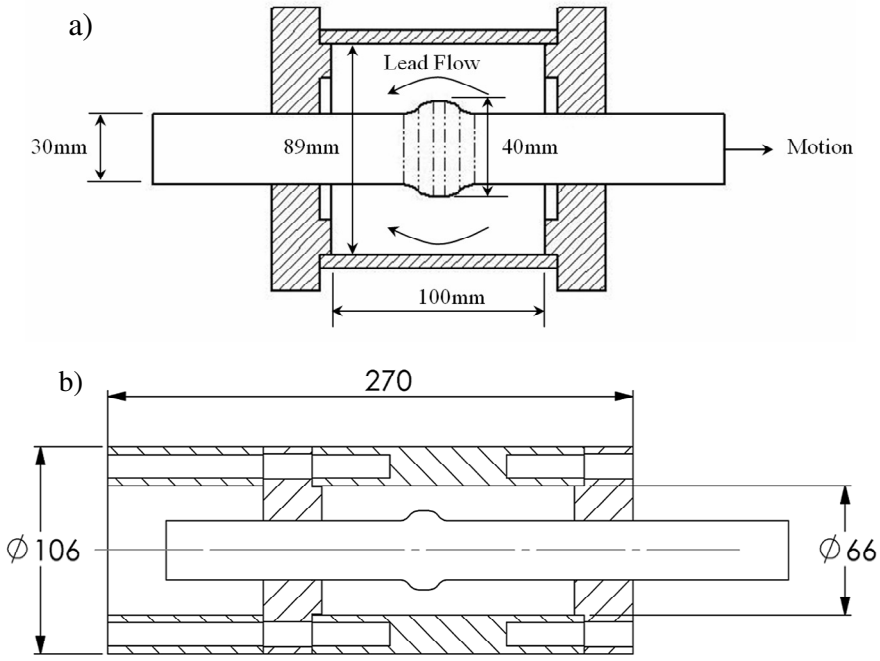

Figure 2.3: Cross-Sectional view of different lead extrusion damper configurations.

Figure 2.3b shows the final prototype device design and dimensions with a 40mm bulge on a 30mm shaft. After a review of existing designs a tear-shaped bulge was chosen. The limiting factor in the design is the 30mm, high strength steel shaft with a yield force of approximately 500kN, which is greater than the desired 250-400kN peak force levels for most structural applications.

This chapter reports on the testing and analysis of these damping devices to obtain and characterise the desired behaviour and device design space. The primary goal is a device with a high force to volume ratio that enables widespread placement directly into structural connections. The majority of the tests undertaken were quasi-static square-waves at approximately 0.1 mm/s. Some higher velocity tests were also undertaken to characterise velocity dependence.

2.2. Methods:

2.2.1. Basic Physics:

In a bulged-shaft lead extrusion damper, the lead is confined in a cylinder with the bulged-shaft through the centre, as shown in Figure 2.3. As the shaft is forced through the cylinder, the lead is forced to flow through the annular restriction. This plastic flow adsorbs a large amount of energy due to the shearing and deformation that occurs, providing high resistive forces. These high resistive forces enable an extrusion damper to be much stiffer, and capable of absorbing far more energy than an equivalent sized fluid viscous damper. Two major factors limit the amount of energy that can be dissipated. First, the shaft yield load restricts force levels, and is defined by practical limits on shaft diameter and manufacturing and cost limitations on shaft material. Second, the heat produced by the damper on repeated cycles can soften the immediately surrounding lead and reduce the resistance. Both factors can be reasonably managed by the device design.

One major potential issue with this method of damping is the formation of voids within the working material during extrusion (Rodgers et al. 2007b). For a lead extrusion damper, this

void formation can be attributed to the compression of the lead, expansion of the confining cylinder wall, and casting imperfections. These imperfections include air gaps or micro-sized voids that can be compressed. Hence, as the bulge moves through the material it is compressed into a smaller volume, leaving a trailing void behind the bulge on the shaft. Thus, as the bulge passes through this void on subsequent cycles when the direction reverses, the damper experiences less resistance (at least initially) and dissipates much less energy depending on the size of the void.

To minimize void formation in this research the lead is prestressed. This pre-stressing helps reduce casting porosity and air gaps before the damper is used. Thus the size of the void, as a percentage of the total lead volume, is reduced and the device maintains its peak design force.

2.2.2. Existing Models:

It appears that limited attempts have been made to fit a model to the experimental characteristics of similar dampers (Skinner et al. 1993). However, Pearson and Parkins (1960) give a relationship between the force and associated cylinder and orifice areas during a similar extrusion process. As the lead in the damper is essentially being extruded between the bulge and cylinder of the damper this model was applied in an initial attempt to characterize the damper forces, and is defined:

$$F = \left\langle \left[Y \ln\left(\frac{A}{a}\right) + Y \right] \exp(M) - Y \right\rangle (A - a) \qquad (2\text{-}1)$$

where F = the extrusion force; Y = yield strength for the working material; A = annular area around the shaft, as shown in Figure 2.4, corresponding to the cross-sectional area of the

extruding bar in Pearson and Parkins; a = annular area of orifice again shown in Figure 2.4, corresponding to the cross-section area of extruded rod in Pearsons and Parkins.; *(A-a)* represents the projected face area of the bulge over which direct stress is applied to the shaft; and M = a constant specific to the extrusion process, defined:

$$M = \frac{4\mu L}{D} \tag{2-2}$$

where μ = the co-efficient of friction between the working material and steel shaft; L = the length of the shaft in sliding contact with the working material and device end caps, relating to the billet length in Pearson et al.; and D = Effective diameter corresponding to annular lead area A, as shown in Figure 2.4, corresponding to the billet diameter used in the work of Pearson and Parkins.

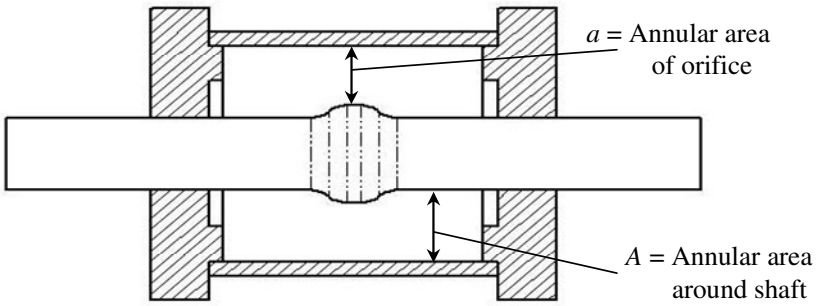

Figure 2.4: Schematic representation of the first device, showing area used in Equation (2-1).

Note that as the bulge diameter approaches the cylinder wall Equation (2-1) results in $F \rightarrow \infty$ as might be expected. The value of infinity implies plastic yielding of the shaft or bulge. It should be noted that the model presented in Pearson et al. is for a classic extrusion process and the model parameters do not translate directly to the parameters of the lead extrusion dampers studied here, and thus close analogies are utilised to define the model.

2.2.3. Experimental Methods:

Quasi-static compression tests were undertaken on an initial design, which is shown in Figure 2.3a, to characterise the force-displacement behaviour. Further testing was undertaken at a range of shaft velocities to experimentally determine the velocity exponent, which defines the increase in resistive force seen with increased shaft velocity as energy is dissipated more rapidly via faster extrusion. The velocity exponent can thus be utilised to relate the force from quasi-static test results to the force levels in full speed testing with velocities representing realistic values for the applications presented in Figure 2.2. This force-velocity relationship is defined (Pekcan et al. 1999):

$$F = C_{\alpha}\dot{x}^{\alpha} \tag{2-3}$$

where F = the extrusion damper force; $\dot{x}$ = velocity of the shaft; α = velocity coefficient (constant); and C_{α} = damper constant determined by physical prototype testing.

Testing and design was carried out using an iterative approach, with the results of each experimental test being used to calibrate empirical models and provide insight into the dominant factors of the extrusion process. The initial design utilised a conservative bulge diameter of 40mm on a 30mm shaft. This result, along with an estimate of force using Equation (2-1), led to the design and manufacture of a 50mm diameter bulge on a 30mm shaft. These results and their linear relationship were used to produce and test a 58mm diameter bulge on a 30 mm diameter shaft, to provide more data and better characterise the empirical models being developed within this study.

Using these three results an accurate estimate of the forces that might be produced was obtained through interpolation between experimental results. Further testing with the 40 and 50mm bulges on a device with a 66mm internal cylinder diameter, which is shown in Figure 2.3b, added more data with respect to the design variables of cylinder size and volume. The overall test results were compared to Equation (2-1) to create empirical device design trade-off curves. The effect of prestressing the cast lead was also investigated.

The devices tested comprise:

- 1a) Device of Figure 2.3a with 40mm and 50mm bulges without prestress
- 1b) Device of Figure 2.3a with 40mm, 50mm and 58mm bulges and prestress
- 2) Device of Figure 2.3b with 40mm and 50mm bulges and prestress

Devices 1a and 1b are used to examine the effect of prestressing the lead and the corresponding effect on the peak force achieved, as well as the shape of the hysteresis loop, and ability to achieve repeatable device behaviour. Devices 1b and 2 provide a variety of results with prestress, with the design parameters of cylinder diameter and bulge size being independently varied.

2.3. Results and Discussion:

2.3.1. Results without Prestress:

Initial manufacturing methods for these experimental devices used as-cast lead as the working material. When the lead solidified, shrinkage of the working material occurred along with the development of small micro-voids due to trapped air. These effects are typical and to

be expected. Hence, the lead did not completely fill the volume inside the damper, and these extra volumes can be compressed and contribute to creating a trailing void behind the bulge. The presence of trapped air was amplified by the rapid solidification of the lead as it contacted the cylinder walls and endcap and underwent non-uniform cooling through the volume. To mitigate this problem, the device cylinders were preheated to reduce the cooling rate and enable more of the trapped air to escape before the lead solidified.

The hysteresis loop for a 40mm diameter bulge and no prestress is presented in Figure 2.5a and shows that the first stroke produced a peak force of 90kN that was reasonably constant throughout the stroke. During the return stroke the force was significantly lower at around 50kN until “new” material was enetered at the device midpoint. After the initial return stoke the peak force was effectively constant at around 50kN throughout all subsequent strokes. Therefore, the area enclosed within the hysteresis loop was reduced after the first passage of the bulge which thus reduced the energy absorbed by the damper. An important observation is that the 90kN force produced on the first stroke was much nearer the predicted value of approximately 80 kN using Equation (2-1).

The cause of this drop in force is the coring out of the lead as the bulge travels through the cylinder. This coring effect is facilitated by the lead compressing and closing up micro-voids and casting porosity, rather than flowing around the bulge as desired. The cylindrical trailing void produced was measured by opening the device and removing the lead intact. It had a measured diameter of 38mm, indicating that the lead was only flowing back about 1mm around each side. This cylindrical coring effect results in much less resistance on the bulge as it is forced through the cylinder because it faces only about 2mm of lead for a 40mm bulge compared to the full 10mm annular bulge face height, thus reducing the resistive force produced.

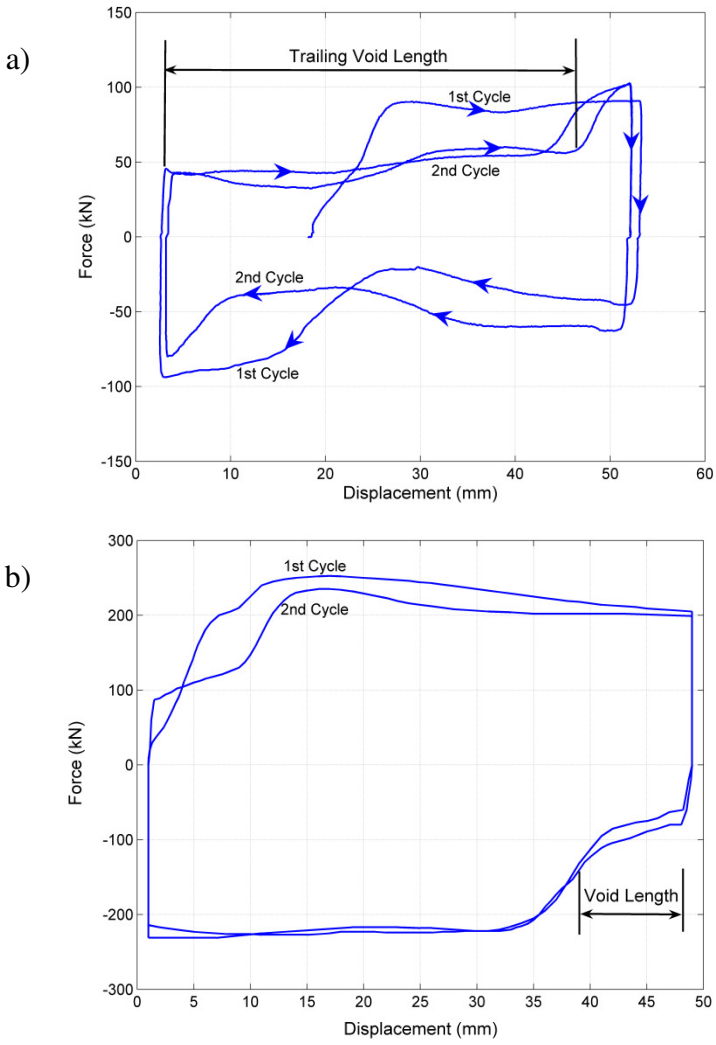

Figure 2.5: Hysteresis loop for Device 1a with a) 40mm diameter and b) 50mm diameter bulge

Effectively, the lead compressed enough so that approximately 8-10% of the total cylinder volume was lost. This reduction in volume, coupled with the relatively small 40mm diameter bulge on a 30mm diameter shaft made a relatively constant void of 38mm diameter along the entire shaft length. This void is, as noted, very apparent in the results of Figure 2.5. Figure 2.6a presents a photo of the disassembled device showing the different regions including the trailing void and Figure 2.6b presents a corresponding cross-sectional schematic.

a)

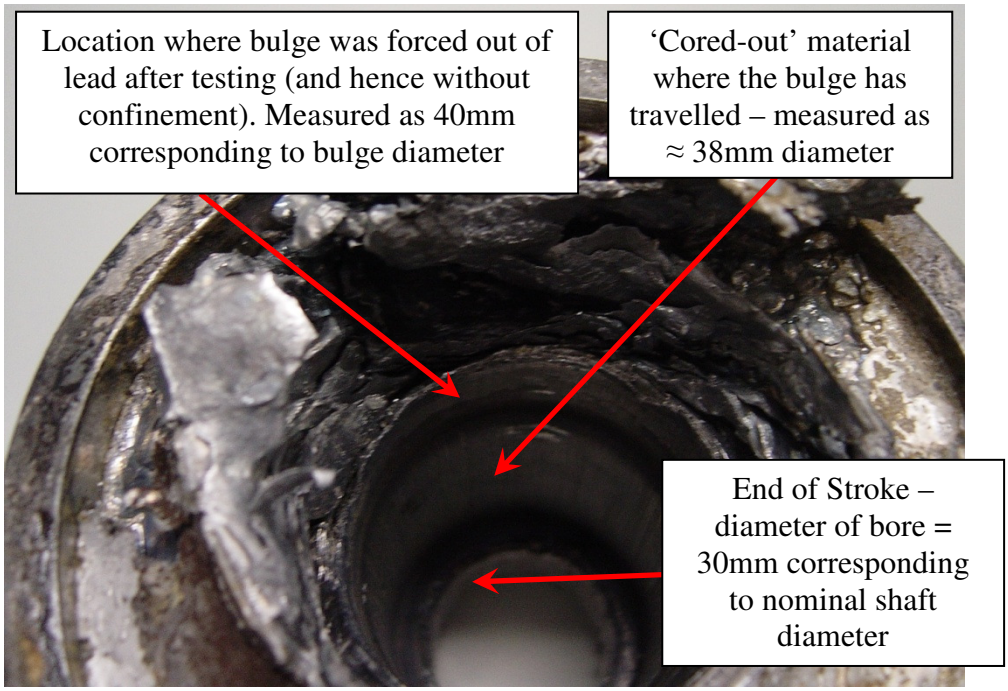

b)

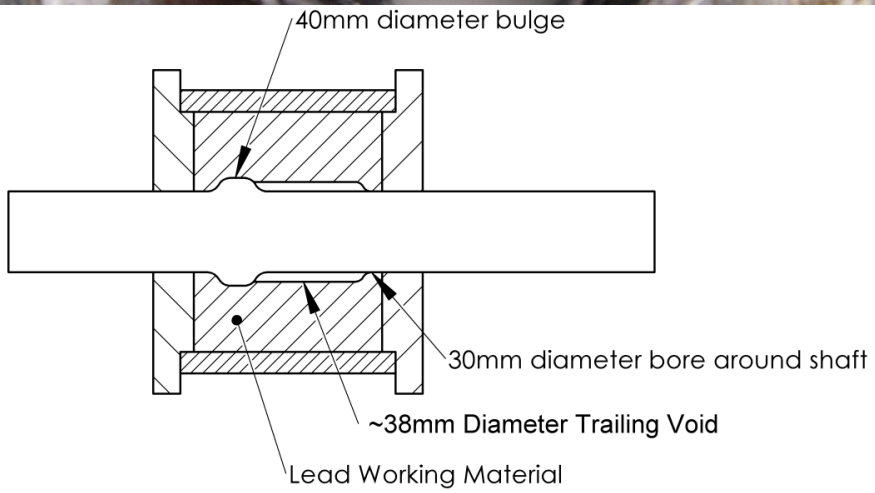

Figure 2.6: Disassembled device showing the trailing void a) a photograph looking in the end of the device and b) a corresponding cross-sectional schematic.

The hysteresis loop for the 50mm bulge without prestress is presented in Figure 2.5b, and shows similar characteristics to the 40mm case in Figure 2.5a. However, it has reduced coring effects or voids. Because of the increase in diameter of the bulge relative to the shaft, the same volume of air void, as a percentage of total volume, has a much reduced length. This result is seen in Figure 2.5b where the trailing void is now only approximately 10mm long compared to approximately 42mm in Figure 2.5a. These results thus show a more optimal 'square' loop than the 40mm case, with relatively smaller "cut-outs" from the corners of the

hysteresis loop being the only effects of the trailing void. After this initial cut-out, the peak force from the original stroke is reached, enabling the damper to absorber nearly as much energy as on the initial stroke. The shape of the loop shows the trailing void created behind the bulge to be only approximately 10mm, indicating a much improved result. The peak force produced was between 220-230kN, closer to expected values from Equation 2-1 of 200kN.

Importantly, these voids or coring effects may be amplified if insufficient confining force is provided by the outer cylinder. Strain gauges mounted on the 6.5mm thick cylinder wall of Device 1 revealed plastic deformation of up to 2% as the bulge passed inside the lead. This deformation will also contribute to the trailing void formation as perfect confinement of the working material was not maintained. Large factors of safety are recommended for cylinder walls, as yielding will reduce the confinement, and have a detrimental effect on response. Reducing the void is important to maximize energy dissipation and time at peak force. To minimise the amount of compression of the lead during cyclic testing and hence reduce trailing void formation, the same devices were tested after pre-stressing the as-cast lead.

2.3.2. Results with Prestress:

Following solidification of the as-cast lead within the cylinder, a 400kN force was applied to compress any air voids present in the casting and put a residual compressive stress on the lead working material. Figures 2.7a-c show the hysteresis loops of the results from Device 1(b) with 40, 50 and 58mm bulges respectively. Figures 2.8a-b shows the hysteresis loops of the results from the thicker walled and narrower diameter Device 2, with 40 and 50mm bulges.

Due to slight variability of the peak force during any single stroke of the device, no single value can accurately represent these peak force levels. Therefore, both the peak force, and an

estimated average force level across the post-yield portion of the loop are included to indicate hysteretic performance of the devices. Table 2.1 summarises these peak and average forces for all five sets of results in Figures 2.7 and 2.8, where the average force is the effective mean value across the top, peak force portion of the hysteresis loop.

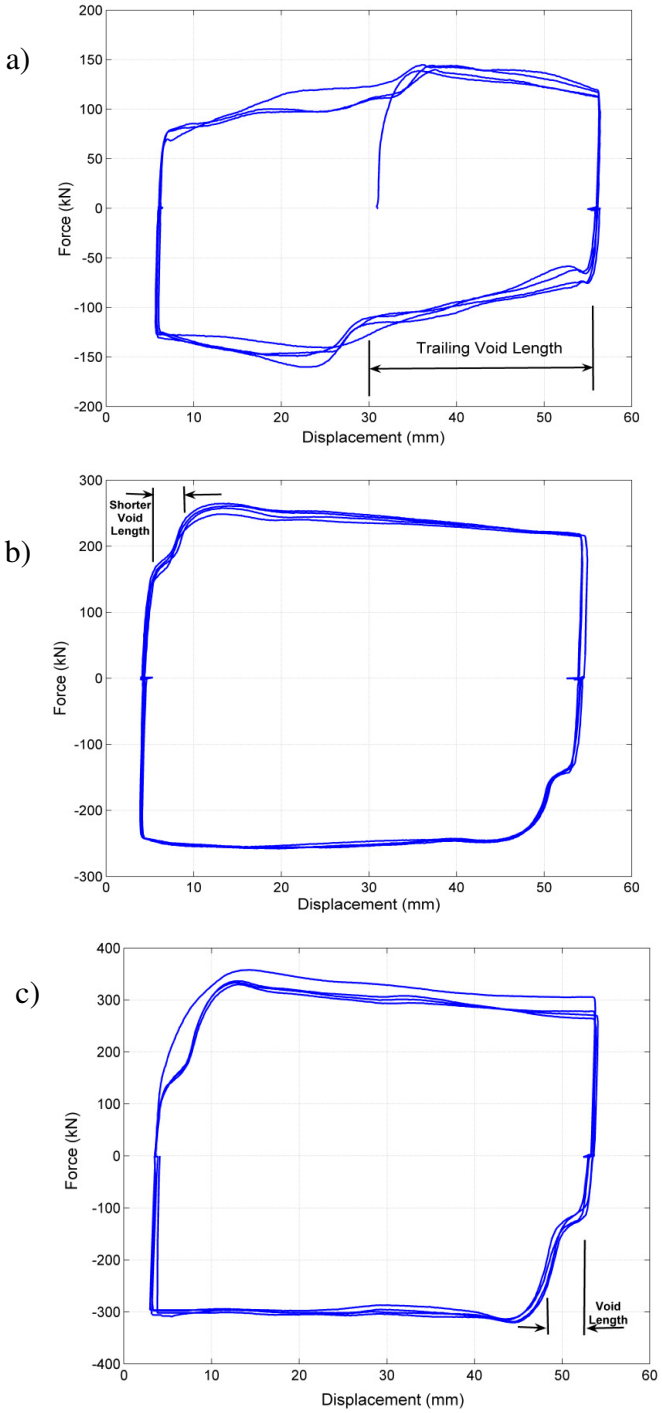

Figure 2.7: Results for prestressed lead using Device 1b and a) 40mm, and b) 50mm and c) 58mm diameter bulge.

Table 2.1: Summary of prestressed device results

Bulge Size (mm)	Max Force (kN)	Average Force (kN)
Device 1b:		
40	170	125
50	255	230
58	360	305
Device 2:		
40	205	160
50	350	300

a)

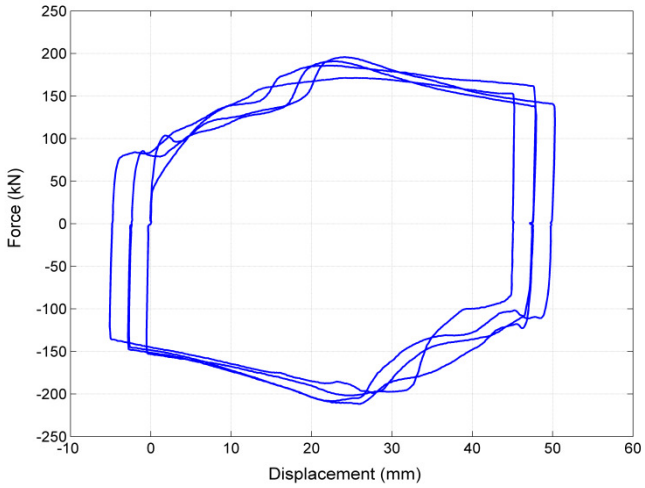

b)

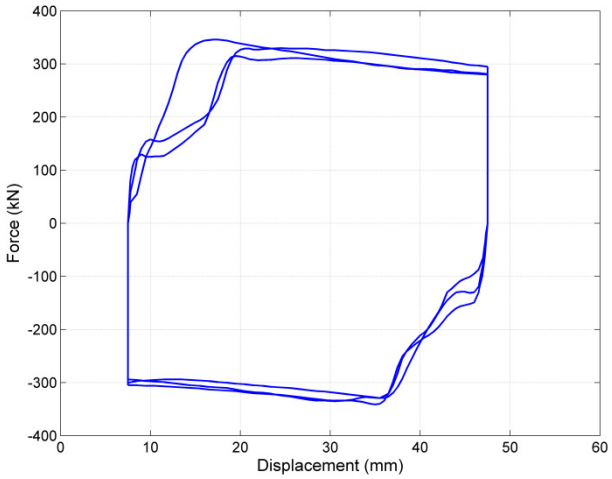

Figure 2.8: Hysteresis loop for device 2 with prestressed lead, and a) 40mm, and b) 50mm diameter bulges.

The hysteresis loops presented in Figures 2.7 are much ‘squarer’, more optimal loops that dissipate more energy than the equivalent loops in Figure 2.5. They also show far less influence due to void formation. The trailing void remains, but has been reduced dramatically by the application of prestress. The results presented in Figure 2.7b show that trailing voids are only approximately 2-3mm long for the larger 50mm bulge compared with 20mm for the 40mm bulge as presented in Figure 2.7a.

Again, a fixed void volume, as a percentage of total lead volume, represents a shorter trailing void for the larger diameter bulges. However, these voids are at least three times (3x) smaller in volume than those for the same devices without prestress. Hence, around the hysteresis loop, there are much smaller drops in force, more time at peak force, and consequently more energy absorption and dissipation through the cycle.

Another important aspect of the prestress is the rise in force produced by the dampers. More specifically. Table 2.1 shows an increase of 80kN for the 40mm bulge (from an initial peak force of 90kN without prestress) and 35kN for the 50mm bulge (from an initial peak force of 220kN without prestress) from the non-prestressed results of Device 1a. This result can be attributed to the reduction in casting porosity by the compression of the lead in the prestressing process, and greater constriction of the lead due to the residual compressive stress. However, the larger bulge size also provides a greater constriction by forcing the lead working material through a smaller annular gap. Thus, as the bulge size increases this difference in force due to adding prestress decreases.

Prestressing decreases the trailing void volume by 3-5 times when compared to non-prestressed tests over Devices 1a and b. This reduction was determined by post-testing disassembly and measurement of the internal voids within the devices as shown in Figure 2.6,

and can also be seen in the hysteresis loops of Figures 2.5 and 2.7. A force reduction still remains over part of the stroke when the smaller 40mm bulge is used with prestress, and this effect appears unavoidable unless an extremely large prestress force is applied. In this case, the force reduction is also partly due to the relatively low height of the 40mm bulge over the 30mm shaft. Since the 40mm bulge has a relatively small face area, a given trailing void volume will produce a noticeable reduction in force over a longer part of the stroke than it would with a larger bulge and face area. This effect is thus minimised using the larger bulge sizes of 50 and 58mm.

The results of Device 1b with the larger 50 and 58mm diameter bulges, presented in Figures 2.7b-c, show almost no reduction in force due to void formation. The only influence of any coring effects is a small 'cut out' in the hysteresis loop corners for the first 2-4mm of every stroke. However, this small reduction is not large enough to have significant effects. This cut out may be reduced further by applying greater pre-stress load to the lead. That said, the almost perfectly square shape of these results means the device is absorbing almost the maximum amount of energy per cycle within the given force and displacement constraints at these relatively low prestress levels relative to the prestress that could have been applied.

Similar results are presented in Figure 2.8 for Device 2, with 40 and 50mm diameter bulges, although these loops show slightly greater coring effects. It is important to note that the design of Device 2 permitted only a relative very limited prestress of approximately 100kN. Device 2 still achieved average forces of 160-300kN and relatively square hysteresis loops. Most of the force increase compared to Device 1b with the same bulge and shaft diameters is attributed to the smaller internal cylinder diameter of 66mm compared to 89mm for Device 1b. It should also be noted that Device 2 also had a significantly larger cylinder wall thickness than that of Device 1, providing better containment of the working material and

thus requiring (comparatively) lower prestress compared to the thinner walled design of Device 1.

2.3.3. Experimental Design Relationships:

The average peak forces from the test results presented in Table 2.1 were used to relate device design parameters to force produced. Figure 2.9a shows the relationship of bulge diameter to force for the experimental results and includes the estimated 40kN friction force. The upper force limit is defined by the shaft axial compression yield strength at maximum bulge diameter for Device 1b. Also plotted in Figure 2.9a is the relationship between force and bulge diameter, as predicted by the extrusion model of Equation (2-1). Note that the fitted line is almost exactly linear and thus quite different from the exponential extrusion-based behaviour defined in Equation (2-1).

Figure 2.9b shows the relationship between force and the device area ratio. This area ratio is defined as the net projected face area of the bulge divided by the net annular lead area. The net projected face area of the bulge is defined as the cross-sectional area of the bulge with the cross-sectional area of the shaft subtracted and is thus the annular area. The net lead area is the total internal cylinder area with the shaft cross-sectional area subtracted to give the net annular cross-sectional area of lead present around the shaft. The overall area ratio, as plotted on the horizontal axis of Figure 2.9b is thus a measure of the area reduction required for extrusion. Its value ranges from [0, 1] covering the no bulge case (0) to the limiting case where the bulge diameter is equal to the internal cylinder diameter (1).

When plotting results for both devices that have included prestress (Device 1b and Device 2) in Figure 2.9b, the force is seen to be a linear relationship to the area ratio for each device.

However, each device exhibits a different linear relationship. Finally, these linear trends in Figure 2.9b clearly show an increasing level of force as the internal cylinder diameter is increased, clearly indicating that, as expected, the scale of the device affects the force level.

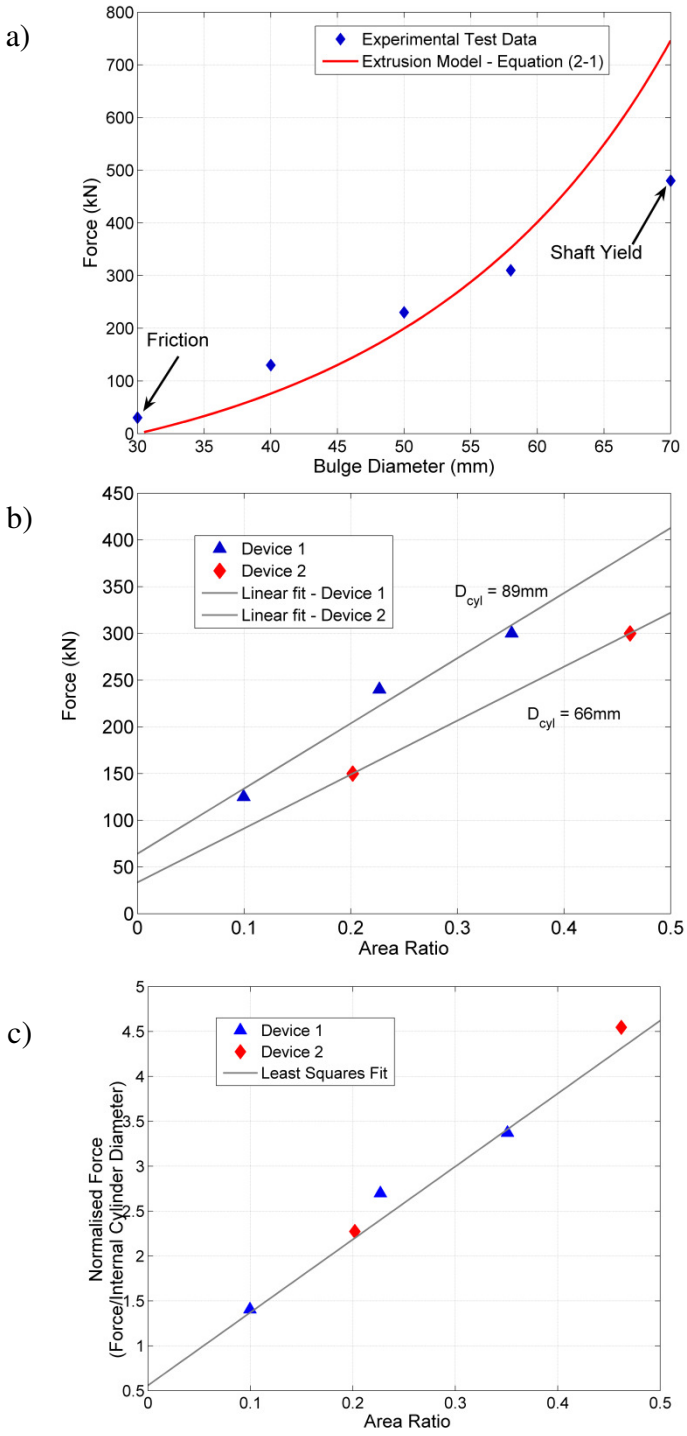

Figure 2.9: a) Relationship of force to bulge diameter for Device 1b experimental versus Equation (2-1); b) Force vs Area Ratio for both devices; and c) Normalised Force vs Area Ratio for both Devices 1b and 2. Note that a bulge diameter of 70mm in a) indicates a bulge diameter equal to the internal cylinder diameter.

In the interests of enabling future designs to incorporate devices of different scales, it is desirable to determine experimental relationships that are independent of the device scale. Therefore, a normalisation procedure is required to remove the scale factor, and for convenience the internal cylinder diameter is chosen as this scale parameter. After this normalisation procedure, the normalised force level for each device is obtained, and represents the average experimental force level divided by the internal cylinder diameter. Figure 2.9c presents the normalised force level plotted against the area ratio, and shows a relatively strong linear relationship for all experimental results independent of device scale, unifying the five experimental results. The development of an overall estimate of device force independent of device scale enables future devices of varying scale to be designed quickly and accurately and is an important step to provide a basis for eventual uptake by the profession.

As an alternative to the extrusion theory presented, a more straight forward stress-based model was considered. Considering equilibrium of the shaft, and using an approach similar to the Mohr-Coulomb failure criteria (Ugural 1991) for a quasi-brittle material, the resistive force for the device, F_D, is defined:

$$F_D = \tau_D A_{shaft} + \sigma_o A_{bulge} \tag{2-4}$$

where τ_D = shear stress due to the load between the shaft and the lead; σ_o = direct stress imposed on the bulge face area, A_{shaft} = surface area of the shaft; and A_{bulge} = annular area of the bulge.

Fitting the values of τ_D and σ_o to the experimental data of Device 1b at bulge diameters of 40, 50, and 58mm, and using a least squares fit yielded τ_D = 6.0MPa and σ_o = 140MPa.

These results can be found from examining Mohr's circle of stress for lead in the unconfined condition. First, the maximum shear stress is $\tau_D = \sigma_y/2$ where σ_y = unconfined yield stress of lead, equal to 11-18MPa (Boss 1968; Boss 1992). Second, σ_o is well above the unconfined compression strength. However, further insight can be obtained by accounting for the confining stress applied to the lead by the cylinder. Due to the relatively thin wall thickness (6.5mm) of the cylinder in Device 1b, the maximum confining stress can be defined as a value corresponding to the yield stress of the cylinder wall. Basic thin-walled pressure vessel theory (Shigley et al. 2004) gives a value of the confining stress applied to the lead, σ_C, equal to 36MPa at an induced stress of 250MPa in the mild steel cylinder used here. This result implies a confined lead strength relationship defined:

$$\sigma_{PbC} = \sigma_y + 3.6\sigma_C \qquad (2\text{-}5)$$

where σ_{PbC} is the confined yield stress of the lead.

The shear stress calculated, leads to a force for an un-bulged shaft of 37.7kN, which is very close to experimental estimates of the friction force of 40kN from un-prestressed experiments obtained using a 40mm bulge. However, only limited experimental results are available from these initial prototype design tests. More results would enable one to fully verify this new model. However, the match between the experiment and model in Figure 2.9c covers the experiments presented here and provides a great deal of further insight into the true

mechanical behaviour of these devices. It is clearly not the exponential extrusion behaviour considered in previous works.

2.3.4. Velocity Dependence

Low velocity experiments were performed using Device 1b with the 50mm diameter bulge to investigate its velocity dependence. Results are presented in Figure 2.10. Figure 2.10 also shows a velocity dependent device model conforming to Equation (2-3), where the value of α is set to 0.12 as presented in Cousins and Porritt (1993). The value of the device constant, C_α was then calculated based on a least squares fit to the data, and had a value of approximately 650,000 based on velocity in m/s and force in Newton. If the value of α is included in the least-squares fit, then it is calculated as 0.118, with only a minimal change in C_α. This result and Figure 2.10 indicates that the velocity dependence of the prototype device can be well modelled by Equation (2-3) at the velocities considered. It should be noted that the maximum test velocity in Figure 2.10 is 1.3 mm/s, which is considerably lower than the value of 1 m/s which is sometimes used as a convenient reference velocity for viscous dampers (Pekcan et al. 1999).

Limitations in testing equipment prevented higher speed tests on these specific prototypes. It should be noted that in the work of Robinson and Greenback (1976) and Cousins and Porritt (1993), testing of similar devices is undertaken at velocities up to approximately 5 m/s, yielding a similar $\alpha = 0.12$ value. In the earlier work (Robinson and Greenbank 1976) it was initially determined that the behaviour did change at higher velocities, with a transition at approximately 1 x 10^{-4} m/s, where at the lower velocities $\alpha = 0.12$, and at higher velocities the velocity exponent changed to $\alpha = 0.03$. However, the different velocity exponent

observed was also for different device designs of bulged shaft and constricted tube dampers. The later work (Cousins and Porritt 1993) determined that the different device design was the cause of the different velocity exponents, and that for bulged shaft designs, such as those used in this thesis, the value of $\alpha = 0.12$ was constant across the range of test velocities from 1 x 10^{-10} m/s up to approximately 5 m/s.

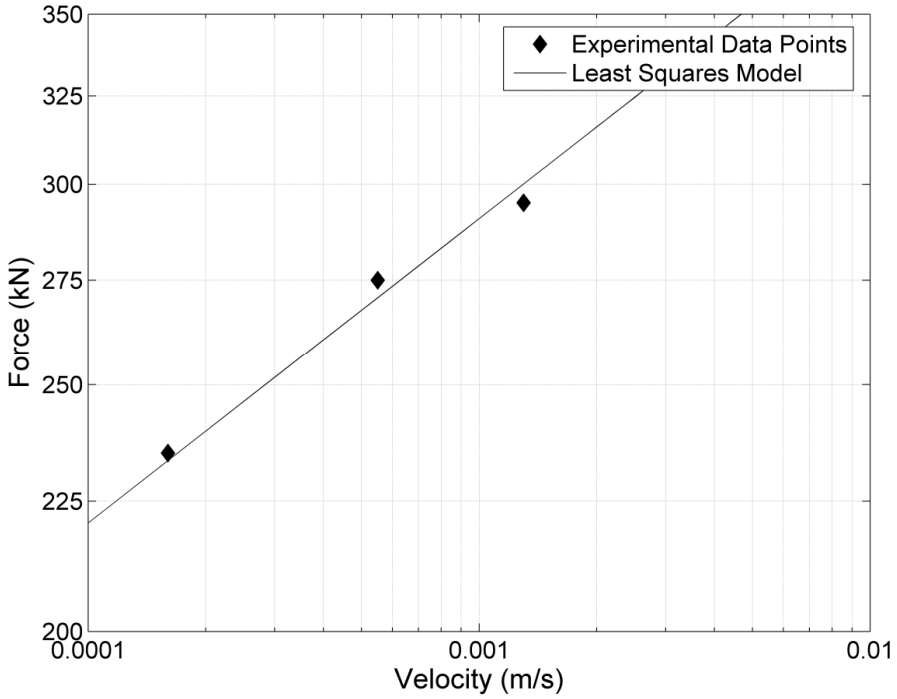

Figure 2.10: Experimental results for a full-scale prototype tested at a range of velocities, and velocity dependent model from Equation (2-3), with α set to 0.12, and C_α fitted in a least-squares sense

2.4. Summary:

Dampers with force levels ranging from 100-400 kN have been experimentally designed and implemented. These devices are also sufficiently compact to fit into structural connections creating a true high force-to-volume (HF2V) device. Prestressing the lead working material is critical as it removes casting porosity, prevents the formation of a trailing void, and provides a beneficial compressive residual stress. The result is that the hysteresis loop is more

optimally ‘square’ and the resistive forces generated and energy dissipated increase. To obtain the optimal, perfectly square hysteresis loop, a combination of careful device design and the application of prestress are important. The reasons for the higher force-to-volume ratio, compared to the earlier devices can be attributed to several key factors. The extrusion area ratio, an indication of the reduction required for extrusion, has a large influence on the force capacity of the device. The presence of prestress within the lead also has an influence on the force capacity of the device, contributing to this increased force-to-volume ratio.

Detailed trade-off analysis is used to develop simple design curves relating peak force levels to the fundamental device design parameters. These trade-off curves allow force levels to be predicted for similar devices, and allow further devices to be easily designed for any structural application. The predictive capability of these curves in designing new devices is validated in Chapters 4 and 5. An important trend seen in the experimental results is that the relationships between force and device parameters do not follow the extrusion models presented in prior research. From this result, a new model of the device process is also briefly proposed and presented. Overall, the compact HF2V dampers presented are an important initial step towards a wide variety of novel applications and improved structural resilience.

Thus, this chapter presents and validates the idea that such devices can be made and perform to a design curve specification. No prior devices offer this combination of repeatable energy dissipation and compact device size. Subsequent chapters will explore their use in design and experimental validation.

Chapter 3: Simplified Spectral Analysis of Device Implementation

The results presented in Chapter 2 have identified that the novel high force-to-volume damping devices presented offer the opportunity to practically emplace significant energy dissipation directly into structural connections. As a result, significant reduction in seismic response could be obtained. The results of Chapter 2 have shown that prototypes with force levels of 250-300 kN are realistic and practical to design. This result validates the use of such realistic force levels for response simulations to develop initial design equations and methods.

Therefore, response spectra analysis is performed in this chapter to provide a preliminary investigation into the feasibility of these devices to mitigate seismic response. Response spectral analysis across multiple, probabilistically scaled, earthquake suites from the SAC project (Somerville et al. 1997) are used to investigate the response reductions that can be achieved by the addition of this type of damping. Representative statistics and damping reduction factors are utilised to characterise the modification of response in a form suitable for current performance based design methods.

3.1. Introduction:

Chapter 2 presents the experimental development of novel HF2V dampers that can provide large resistive force, while maintaining compact outer dimensions. The velocity dependent elastic-plastic behaviour demonstrated by these dampers is shown to provide an almost ideal square hysteresis loop. As a result, it encloses the maximum possible area within the force-displacement plane, providing the maximum energy dissipation achievable per cycle in a consistent and repeatable manner.

The primary goal of the research within this chapter is to investigate the potential impact of these HF2V devices on structural seismic response. The analytical investigation is performed using response spectra for a seismically excited, linear elastic, equivalent single degree of freedom structure, similar to that previously presented schematically in Figure 2-2a. Seismic response simulations are performed using the three suites of probabilistically scaled earthquake records from the SAC project (Somerville et al. 1997). Performance is measured by the use of appropriate log-normal statistics (Chase et al. 2004; Limpert et al. 2001), focusing on spectral acceleration and the corresponding reduction factors. Spectral acceleration reduction is used as an indication of the reduction in damage to non-structural components. For the linear structure utilised here, the displacements and accelerations are closely related and therefore either metric provides an indication of response reduction. Multiple equation regression analysis is then utilised to develop expressions to estimate the damping reduction factors for structural design purposes. Finally, the systematic bias introduced by incorporating these approximate equations for the damping reduction factors into design analyses is also characterised.

3.2. Device Modelling And Analysis:

3.2.1. Theoretical Device Characterisation for Design Applications

A lead extrusion damper can be modelled as a non-linear velocity dependent damper, where the damper force, F, is defined:

$$F = C_\alpha \dot{x}^\alpha \tag{3-1}$$

where C_α = a constant dependent on device geometry and working material; $\dot{x}$ = the velocity of the damper shaft; and α = the velocity exponent.

Pekcan et al (1999) investigated the seismic performance of a class of dampers conforming broadly to Equation (3-1). Across a broad spectrum of response, they showed that the impact or affect of such non-linear dampers can be characterised in terms of equivalent viscous damping, ξ_d.

$$\xi_d = \frac{\varepsilon}{1+\alpha}\left(\frac{2\pi}{0.75}\right)^{0.15(\alpha-1)} g^{0.5(0.85\alpha+0.15)} S_d^{0.5(1.15\alpha-0.15)} C_d^{0.5(0.85\alpha-1.85)} \qquad (3\text{-}2)$$

where S_d = the spectral displacement (m), $C_d = V_b/W$ = the normalised base-shear demand (dimensionless), V_b = the total base shear force (N), W = the total seismic weight (N), g = the acceleration due to gravity (m/s^2), and ε = the non-dimensional damper capacity defined:

$$\varepsilon = \frac{C_\alpha \dot{x}_{ref}^{\alpha}}{W} \qquad (3\text{-}3)$$

where $\dot{x}_{ref}$ = a reference velocity used as a standard when testing velocity sensitive dampers. By convention, and for convenience, several manufacturers take this value as $\dot{x}_{ref}$ = 1 m/s. It should be noted that Equation (3-2) is empirical (Pekcan et al. 1999), but it has been derived based upon a broad spectrum of earthquake records and uses a power absorption equivalence instead of an energy equivalence.

For bulged shaft lead dampers a value of α in the range of α = 0.11 to 0.15 is appropriate based upon previous research (Cousins and Porritt 1993) and the experimental results presented in Chapter 2. Thus, for convenience, by substituting α = 0.13, and g = 9.81 m/s^2 into Equation (3-2), equivalent damping can be estimated independent of the spectral displacement amplitude, S_d:

$$\xi_{d_{\alpha=0.13}} = \frac{0.90}{C_d^{0.87}} \varepsilon \qquad (3\text{-}4)$$

where ε can be thought of as the normalised damper capacity, defined as the peak damper force for a full speed test. Note that the value of α = 0.13 is used for convenience, to make Equation (3-4) independent of the spectral displacement amplitude, S_d. If the value determined in Chapter 2 of α = 0.12 was used instead, then Equation (3-4) would not be independent of, but rather very weakly dependent on, the value of S_d.

Typically, ε in Equation (3-4) is defined with respect to the structural weight as a convenient reference, and as defined in Equation (3-3). This result shows that the equivalent viscous damping for a bulged shaft type of lead extrusion damper is invariant to the displacement magnitude. Given the velocity dependence of the device and relatively constant force capacity at a given velocity, this result should be expected.

3.3. Spectral Analysis of Seismic Response Reduction for Design

3.3.1. Structure and modelling

The structure modelled for spectral analysis and statistical quantization of the effectiveness of HF2V damping devices is based on an equivalent single-degree of freedom (SDOF) system similar to that presented in Figure 2.2a. Internal, structural viscous damping equal to 5% of critical is assumed, which is typical for creating structural design spectra (Chopra 1995).

Additional damping over the baseline structure in this analytical investigation is provided by a non-linear bulge-shaft type HF2V damper, with a velocity exponent of α = 0.12, which is selected based on previously published research (Cousins and Porritt 1993), and the velocity dependence study in Chapter 2. The non-dimensional damper capacity, or force ratio, ε, from Equation (3-3), for the extrusion dampers is parametrically set at 1, 2, 5 and 10 % of total structural weight. The value of the device constant C_α in Equation (3-1) is calibrated to give the prescribed force level corresponding to a percentage of structure weight, and at a reference velocity of 1 m/s.

The structure model is utilised to create response spectra for all earthquake records in the three suites from the SAC project (Somerville et al. 1997). Each suite includes ten different time histories, with two orthogonal directions for each history. The low, medium and high suites represent ground motions having probabilities of exceedance of 50% in 50 years, 10% in 50 years, and 2% in 50 years respectively. The acceleration histories have been scaled to approximately conform to the 1997 NEHRP design spectrum for firm soil at the specified return periods. The time histories for both the low and medium suite are all derived from actual recordings of crustal earthquakes on stiff soils. For the high suite, five of the time histories are from recorded near-fault events, and the other five are synthetically generated.

3.3.2. Statistical Analysis of Results

Representative statistics were evaluated from the individual structural responses for the 20 earthquake records within each suite. Statistical analysis showed the response quantities conform to a log-normal distribution (Limpert et al. 2001). The two parameters that characterise the log-normal distribution are the median, $\hat{x}$, and log-normal multiplicative standard deviation, $\hat{\sigma}$, were thus determined for each suite.

$$\hat{x} = \exp\left(\frac{1}{n}\sum_{i=1}^{n}\ln(x_i)\right) \tag{3-5}$$

where x_i are the response metric for ground motion i, and n = 20 for a given suite.

$$\hat{\sigma} = \exp\sqrt{\frac{1}{n-1}\sum_{i=1}^{n}(\ln(x_i/\hat{x}))^2} \tag{3-6}$$

To illustrate the change in response variables across the entire response spectrum both the median and dispersion factors are plotted against structural natural period.

3.3.3. Analysis Methodology

The acceleration spectral response is measured and gives an indication of the performance of the HF2V damper at preventing damage to the non-structural components of the building. For each seismic input the maximum response acceleration magnitude is obtained from each analysis. The geometric mean, or median, peak acceleration response of the earthquake records within each suite is plotted for non-dimensional damper capacities of ε = 0, 1, 2, 5,

and 10% of total seismic weight, to indicate the reductions achieved with the addition of the HF2V dampers of different capacities. The analysis is repeated for each structural period T_n = 0.1 - 5 seconds to create the response spectra.

The log-normal multiplicative standard deviation, $\hat{\sigma}$, is presented to give an indication of the spread of the results within each suite. Reduction factors from the $\varepsilon = 0$ case (no device, unaltered structure) are calculated for the geometric mean spectral acceleration response within each suite to more clearly represent the response reductions achieved with different levels of added non-dimensional damper capacity, ε. A maximum value of ε = 10% of total seismic weight is selected to ensure realistic damper forces for the applications considered.

To relate the results of the spectral analysis to design guidelines, regression analysis is used to develop equations to approximate the damping reduction factors. Multiplicative error factors are then calculated to indicate the error introduced by using these equations to approximate the reduction factors calculated from the spectral analyses. Finally, the seismic demand spectrum is calculated for all levels of damper capacity, ε, and the error factors between these spectra and the overall geometric mean spectra from the medium suite are calculated. These error factors indicate whether the seismic demand spectrum design approach is conservative.

3.4. Spectral Analysis Results

3.4.1. Spectral Response Simulation Results

The individual spectral response for each of the earthquakes in all 3 suites was simulated with the addition of lead extrusion dampers utilising characteristic force levels, ε = 0, 1, 2, 5, 10% of total structural weight. Note that the ε = 0 case is done to show the response without any added devices. The geometric mean, or median, response spectra for each suite is presented in the left column of Figure 3.1 and clearly shows the response reductions achieved by the addition of extrusion damping. The peak response values decrease notably across all suites as the non-dimensional damper capacity, ε, increases from 0% to a maximum of 10% of total structural weight. The median response spectrum for each suite is presented for ε = 0, 1, 2, 5, and 10% of structural weight. To indicate the effect that the added damping has on the spread of the results, the multiplicative standard deviation, $\hat{\sigma}$, is plotted against structural natural period for the same cases, and presented in the right column of Figure 3.1.

The reductions achieved across a suite of earthquakes by the addition of this type of damping can also be represented by the use of damping reduction factors. These factors are a clear way of presenting the reductions that can be achieved across a response spectrum. The damping reduction factors for the geometric mean responses are presented in Figure 3.2, where the reduction factor is a divisive factor, and represents the factor by which division of the uncontrolled response yields the response with the added damper.

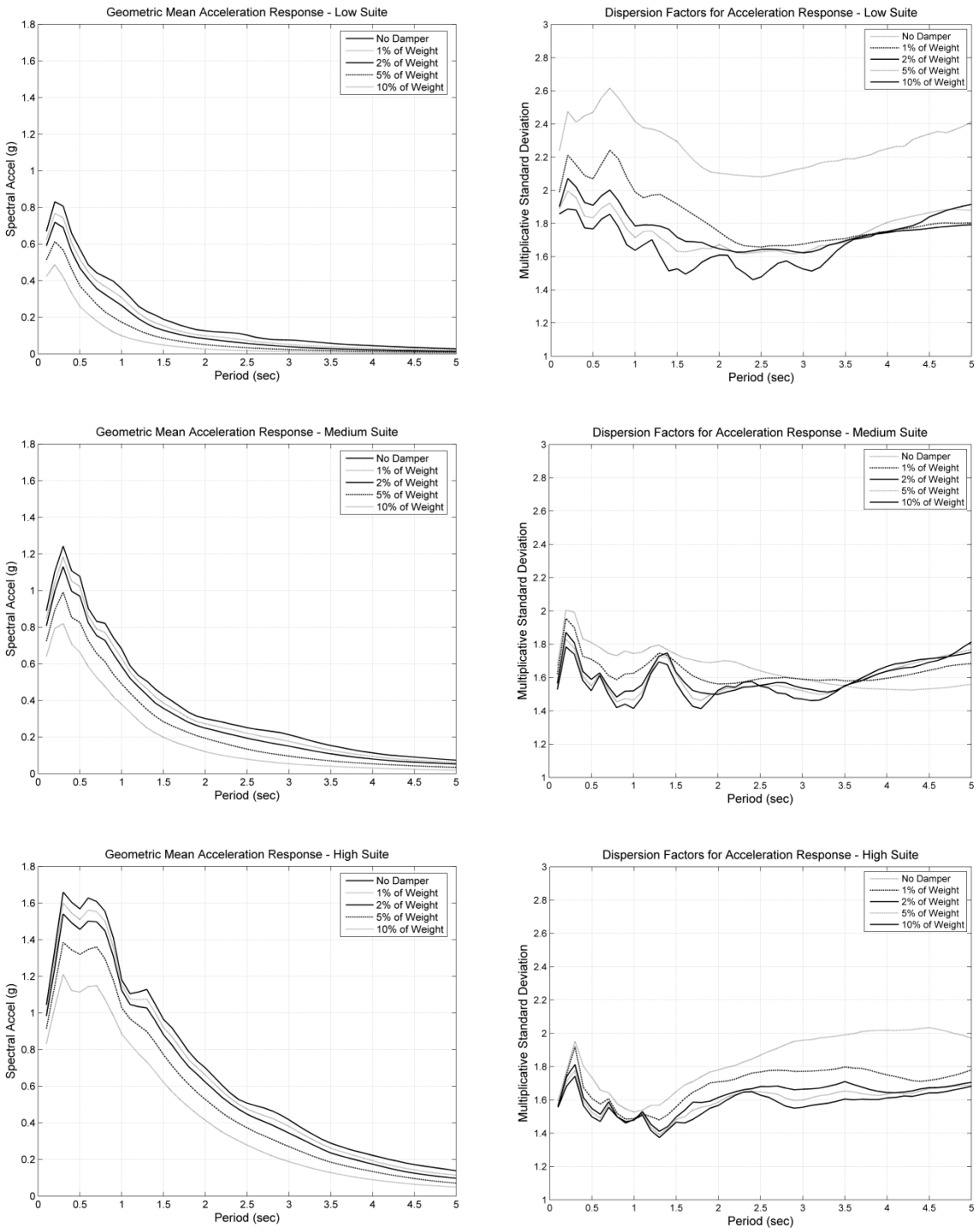

Figure 3.1: Geometric mean acceleration response spectra and log-normal multiplicative standard deviation, $\hat{\sigma}$, for each suite

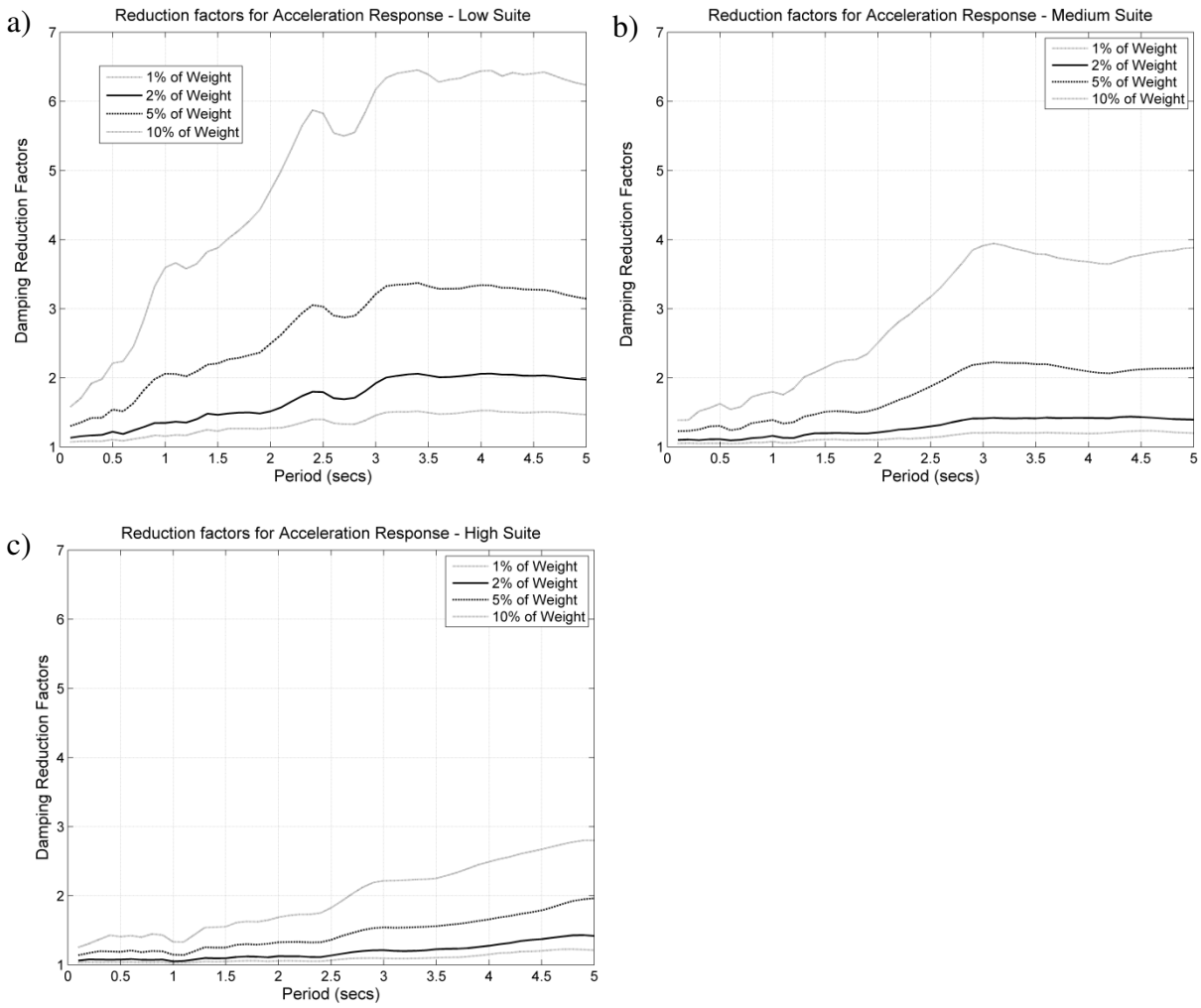

Figure 3.2: Damping reduction factors for the geometric mean responses for a) the low suite, b) the medium suite, and c) the high suite.

The damping reduction factors are characterised into three regions based upon existing bifurcation points. These three regions are the constant displacement, constant velocity, and constant acceleration regions. They are defined graphically in Figures 3.3. For low periods the reductions are low and approximately linear with added damping as a fraction of seismic weight. At high periods the reductions are again relatively constant and exhibit a different linear trend with added damper force capacity. The intermediate region is defined using interpolation between these linear regions and provides good agreement with the experimental results. This approach of segregating the spectra into the different regions is broadly similar to the approach used in some loading codes (ATC-40 1996).

The largest damping reduction factors in Figure 3.2 are seen in the constant displacement region of the spectra for the low suite, with an average reduction factor of approximately 6.4 for a $\varepsilon = 10\%$ of structural weight extrusion damper. This value compares with average reduction factors for the same force capacity of approximately 3.75 and 2.5 for the same region in the medium and high suite spectra, respectively. Overall, these reduction factors represent substantial decreases in the spectral acceleration response with the use of realistically sized extrusion dampers.

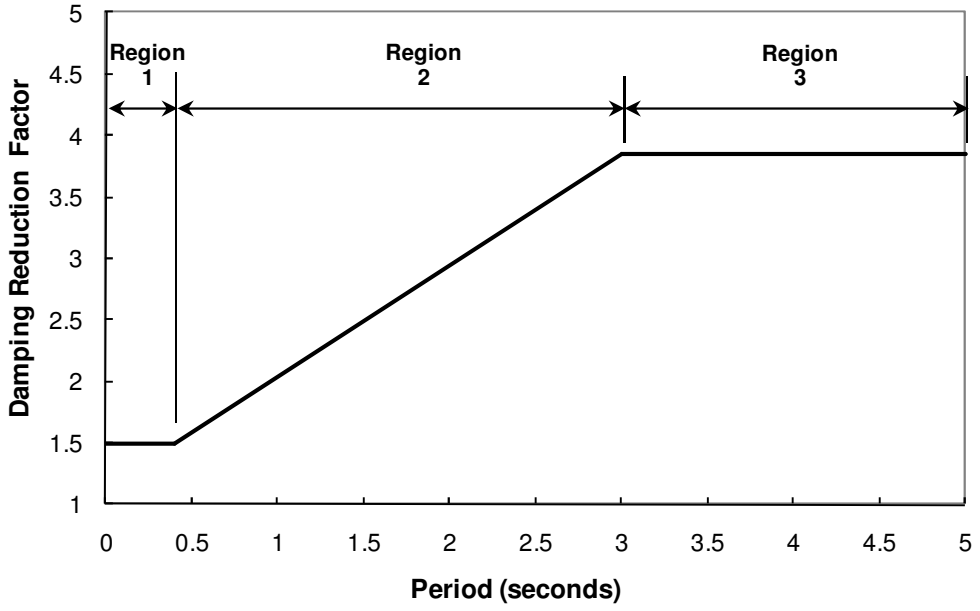

Figure 3.3: Typical reduction factor plot showing the constant acceleration (Region 1), constant velocity (Region 2), and constant displacement region (Region 3)

The reduction factors in the range of $T \approx 1$sec, a period typical for a medium rise structure, are approximately 3.6, 1.8, and 1.4 for the low, medium, and high suites respectively, using an $\varepsilon = 10\%$ of structural weight damper, as seen in Figures 3.2a-c. These reduction factors are smaller than those seen in the constant displacement region, but are at a more common period for widespread structural design.

The reduction factors increase approximately linearly with increasing damper capacity. The average reduction factors for the medium suite in the constant displacement region of the spectrum are approximately 1.2, 1.4, 2.15, and 3.8 for non-dimensional damper capacities, ε, equal to 1, 2, 5, and 10% of total structural weight respectively. The overall average reduction factors at a structural period of T = 1sec are approximately 1.08, 1.16, 1.39, and 1.80 for the same range of damper capacities, ε. Both regions show a strong linear relationship between the reduction factors and the added damper capacity, as might be expected as they linearly increase equivalent damping in Equations (3-2) and (3-4)

The results in Figure 3.2 indicate that the dampers produce the biggest reductions in spectral acceleration for the more vibratory ground motions of the low suite. The reduction factors for the low suite are greater than the average reduction factors from the medium suite across the entire spectrum. The lower damping reduction factors for the high suite indicate that the extrusion dampers may not be as well suited to the large pulses of the high suite near field ground motions, as they are to more vibratory ground motions of the low suite.

3.4.2. Empirical Modelling of Results for Design

To enable the future applications of such HF2V dampers to be incorporated into structural design procedures, it is desirable to develop equations that estimate the damping reduction factors of Figure 3.2. Previous research has utilised non-linear regression analysis to develop a single equation model that approximates the reduction factors across the entire spectrum (Lin and Chang 2004). This research utilises a new method of segregating the spectrum into three regions based upon the existing bifurcation points shown in Figure 3.3, and developing equations for each of these regions.

The damping reduction factor graphs in Figure 3.2 show that there are reasonable variations across the three suites, especially for high additional damping. However, seismic design procedures are normally based upon a 10% in 50 year probability, which corresponds to earthquake design spectra that have characteristics similar to the medium suite (Standards New Zealand - Technical Committee Bd-006-04). Thus, equations are fit to Figure 3.2b based on the median damping reduction factors from the medium suite.

The three regions defined are the constant acceleration, constant velocity, and constant displacement portions of the spectra, with the bifurcation points occurring at natural periods of 0.4 and 3.0 seconds, as shown in Figure 3.3. Linear regression analysis is employed to develop equations for the constant acceleration and constant displacement regions, and linear interpolation between the values at T = 0.4sec and T = 3.0sec is utilised to define the constant velocity region. Regression analysis gives the equation for the constant acceleration region of the medium suite geometric mean reduction factor spectra in Figure 3.2 as:

$$B_a = 1 + 4.43\varepsilon \qquad (T < 0.4 \text{ sec}) \qquad (3\text{-}7)$$

where ε is the damper reference force as a fraction of total structural weight.

Similarly, the equation for the constant displacement region of the reduction factors for the medium suite geometric mean response in Figure 3.2 is defined:

$$B_d = 1 + 26.7\varepsilon \qquad (T \geq 3 \text{ sec}) \qquad (3\text{-}8)$$

Linear interpolation between the natural period values at 0.4 and 3.0 seconds, given by Equations (3-7) and (3-8) respectively, yields the equation for the constant velocity region of Figure 3.2:

$$B_v = 1 + (8.56T + 1.0)\varepsilon \qquad (0.4 \leq T < 3 \text{ sec}) \qquad (3\text{-}9)$$

where T is the structural natural period, and ε is , as before, the damper reference force as a fraction of total structural weight.

For clarity, the reduction factors for the medium suite geometric mean response from Figure 3.2b are reproduced with the corresponding plot of the multiple equation model in Figures 3.4a and 3.4b respectively. The plots are essentially the same with the equations fitting the basic shape well. It is also worth noting for comparison, that for a structure with a natural period of 1s, non-dimensional damping capacities of ε = 1, 2, 5 and 10% of structural weight correspond to total equivalent viscous damping of 7, 9.2, 16.8, and 33.2%, where these equivalent damping values include the 5% inherent structural damping assumed in the analysis (Rodgers et al. 2008a).

The medium suite geometric mean design spectra for 1, 2, 5, and 10% added extrusion damping are reconstructed from the exact spectra with 5% internal damping to verify the multiple equation model of the damping reduction factors. To investigate whether Equations (3-7) to (3-9) derived for the damping reduction factors are suitably accurate for design purposes, it is important to look at the systematic bias that may be introduced by the linearised definition used and shown in Figure 3.4b.

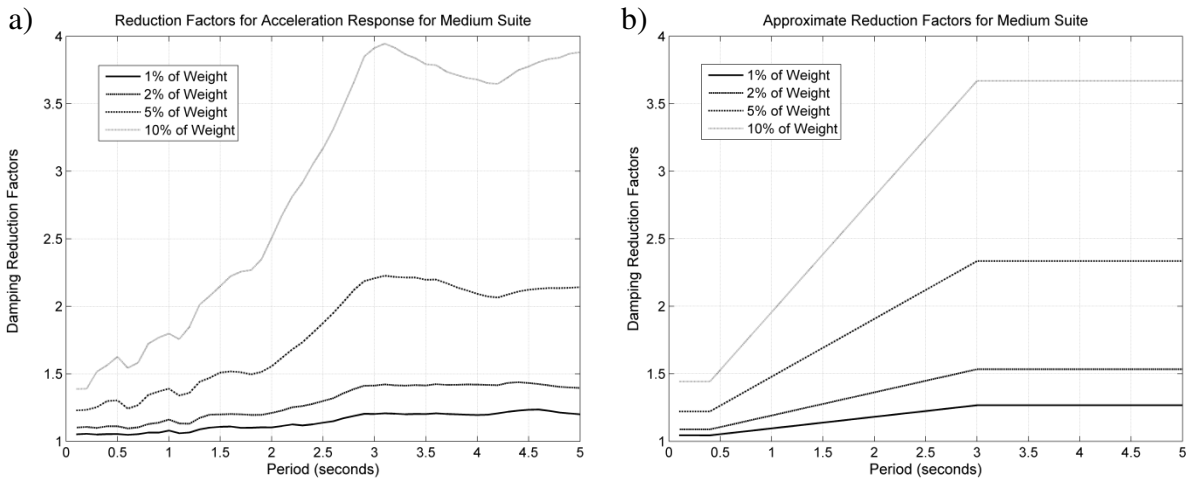

Figure 3.4: a) Reduction factors for the geometric mean response from the medium suite, and b) Approximate reduction factors defined by the multiple equation model.

To represent the systematic bias introduced by the use of equations to approximate the damping reduction factors, the multiplicative error factors are calculated. These error values are determined by dividing the approximate reduction factors of Figure 3.4b by the corresponding exact reduction factors of Figure 3.4a. This calculation gives an indication of the relative error that is introduced by this design approximation. The multiplicative error factors are plotted in Figure 3.5. Results from this analysis indicate that the maximum systematic bias introduced is within the range of +10% and -20%.

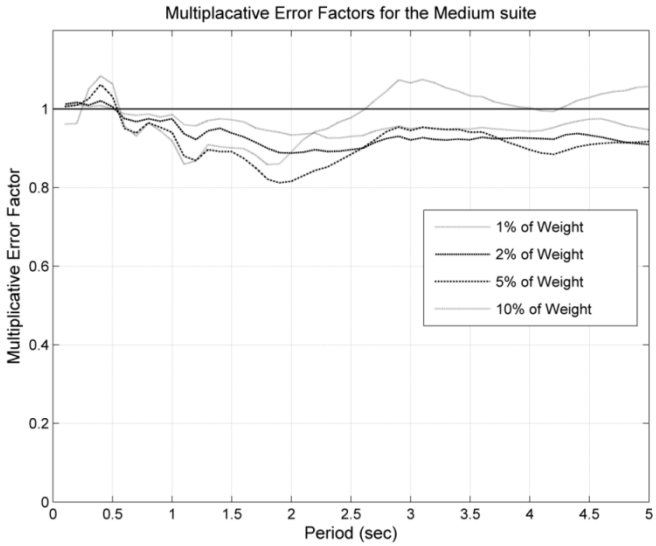

Figure 3.5: Multiplicative error factors for the approximate damping reduction factors of Figure 3.4b divided by the exact reduction factors of Figure 3.4a.

3.4.3. Design Implementation

The seismic demand spectrum is useful where a realistic evaluation of the earthquake hazard can be analysed based on the statistical analysis of past earthquake records (Solberg et al. 2008b). The seismic demand spectrum is defined:

$$C_d = \min\left(\frac{F_a S_s}{B_a}, \frac{F_v S_1}{T B_v}, \frac{F_v S_1 T_d}{T^2 B_d}\right) \quad (3\text{-}10)$$

where F_a and F_v are adjustments on spectral acceleration for short and long periods at different soil classes; S_s and S_1 are spectral acceleration at short periods and the one-second period; B_a, B_v, and B_d are the approximate damping reduction factors defined in Equations (3-7)-(3-9); T = the period of the structure; and T_d = the period at the junction of the constant spectral velocity and displacement portions of the spectra.

Using Equation (3-10), acceleration-period seismic demand spectra for normal soil (where PGA = $F_v S_1$ and $F_a S_s$ = $2.5 F_v S_1$) are presented in Figure 3.6. This analysis essentially recreates Figure 3.1 using Figure 3.4b and Equations (3-7) to (3-10). This approach can thus be used to estimate whether these design equations provide a good estimate, for design, of the likely acceleration response spectra.

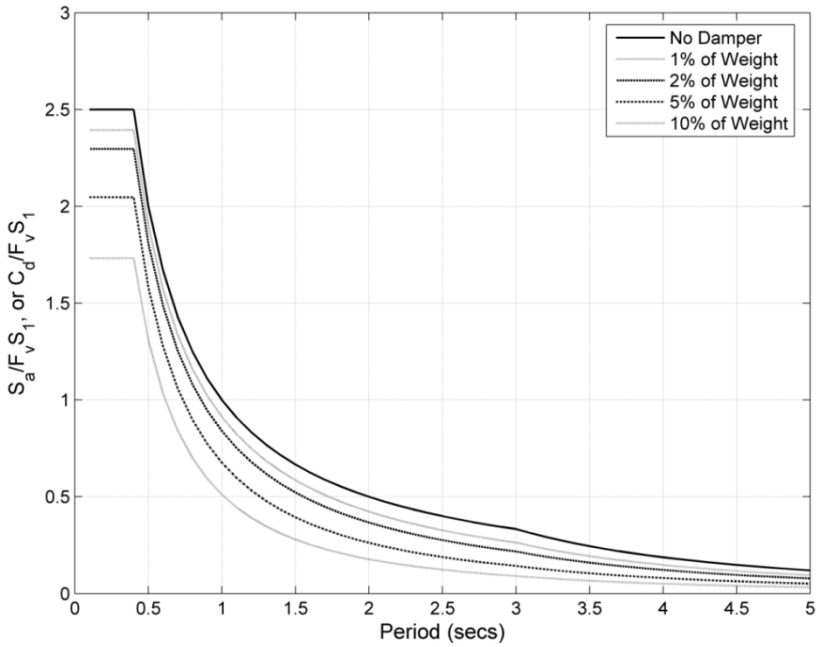

Figure 3.6: Normalised Design Spectra for extrusion dampers where the lateral damping force is given by ε = percentage of seismic weight.

To investigate the systematic bias introduced by the use of this approximated seismic demand spectrum, the divisive error factors are calculated. These factors represent the 'exact' median spectra from the medium suite in Figure 3.1 divided by the seismic demand spectra derived and shown in Figure 3.6. The divisive error factors are presented in Figure 3.7. These factors indicate that across most of the spectrum the seismic demand spectrum is conservative as the divisive factors are less than unity. The exception is for large added damping in the range of approximately 0.8-3.5 second period, where the demand is slightly underestimated, up to a maximum of approximately 10%. Overall, these results in Figure 3.7 indicate that the design approach is generally conservative and reasonably accurate for structural design purposes.

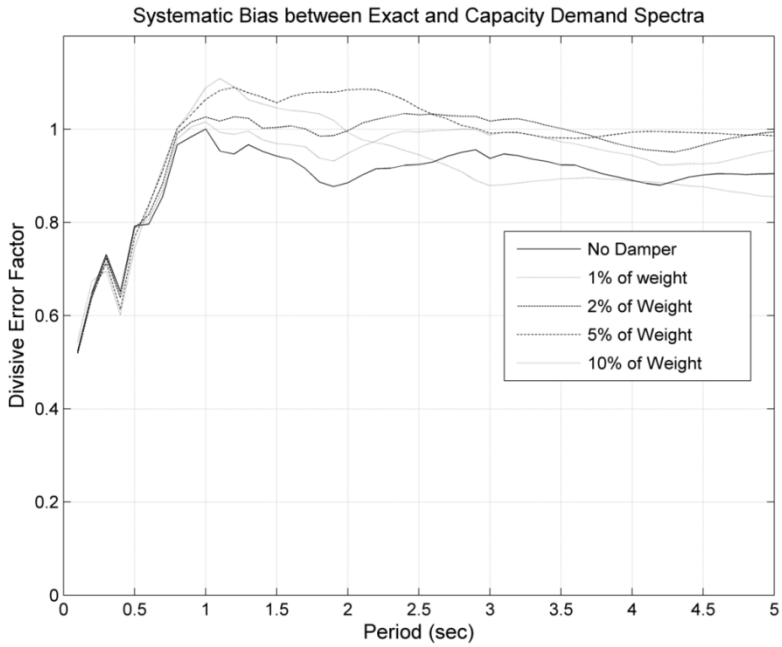

Figure 3.7: Systematic bias between the exact spectra and the capacity-demand spectra (shown in Figure 3.6) with $F_v S_1 = 0.68$. Note that values less than 1.0 imply conservatism.

3.5. Summary

The HF2V concept presented provides force capacity, and hence energy dissipation capacity, on the same order of magnitude of significantly larger devices. Their small size enables placement into structural connections and other areas heretofore unavailable, enabling new potential structural applications at full scale. Comprehensive simulation of structural response across a range of earthquake suites has shown that significant reductions in acceleration response and thus damage can be achieved with realistically sized dampers. Based on the experimental and analytical investigation described, the following conclusions can be drawn:

- Analysis of response spectra shows that the addition of extrusion damping with force levels up to 10% of structural weight can have significant impact on the seismic response, with response reduction factors of up to approximately 6.5. This result represents a significant reduction in the spectral acceleration response with realistic damper sizes, as proved by the construction and testing of a full scale prototype.

- Average reduction factors in the constant displacement region of the spectra, with the addition of extrusion damping equal to 10% of building weight, were approximately 6.4, 3.75, and 2.5 for the low, medium and high suites respectively.
- Reduction factors in the range of T = 1sec, are 3.6, 1.8, and 1.4 for the low, medium, and high suite respectively, for a 10% structural weight damper. These reduction factors are smaller than those in the constant displacement region, but are at a more common period for widespread structural design.
- Multiple equation regression analysis enables development of empirical expressions to model the effect of response reduction through the lead dampers. Multiplicative error factors indicate that the maximum systematic bias introduced by using the reduction factor equations in design analyses is within the range of +10% and -20%.
- The divisive error factors, representing the exact spectra divided by the seismic demand spectra show that this design approach is conservative and overestimates the demand across the spectrum, except for large added damping between 0.8 and 3.5 second periods, where it slightly underestimates the demand up to a maximum of approximately 10%.

This research provides a preliminary investigation that demonstrates that high force to volume extrusion dampers can be incorporated into previously unviable areas of structural design. The results generated in this chapter provide a simplified analysis that indicates that such devices can be accurately incorporated into standard design procedures using acceleration design spectra and metrics.

Chapter 4: Jointed Precast Concrete Connection with External HF2V Devices

The development of the high force-to-volume energy dissipation devices in Chapter 2 and the analytical study validating their potential impact on structural response presented in Chapter 3 have indicated that structural implementation of these devices is feasible and likely to result in notable response reductions. In addition, the results of Chapter 3 show that the capability of these devices can also be readily incorporated into standard design procedures and analysis, enabling more immediate access by the profession. Thus, in this chapter, the devices are experimentally validated. In particular, HF2V devices are applied to a jointed precast concrete connection in collaboration with a civil engineering postgraduate studying other methods of material yielding based energy dissipation.

Tests are performed on a near full-scale beam-column joint subassembly utilizing externally mounted compact HF2V devices. Two configurations are considered: an exterior joint with two seismic beams and one gravity beam framing into a central column, and a corner joint with only one seismic beam and one gravity beam framing into a column. Quasi-static tests are performed to column drifts up to 4%. The experiments are used to validate the efficacy of the HF2V device concept in dissipating energy, and to examine issues around connection and device re-centering.

4.1. Introduction

Research and development of precast concrete jointed and rocking structures has gained considerable momentum over the past two decades. In particular, there has been significant research on so-called PRESSS systems (Priestley et al. 1999), and on damage-avoidance design (DAD) (Ajrab et al. 2004; Bradley et al. 2008; Holden et al. 2003; Mander 2004;

Mander and Cheng 1997; Solberg et al. 2009). These systems, designed to accommodate inelastic behaviour by rocking at specially detailed joints, have proven to provide a level of seismic resistance comparable to current standards while remaining almost (in the case of PRESSS) or essentially (in the case of DAD) damage-free. Furthermore, such systems do not suffer excessive residual displacement, a common occurrence in conventional sacrificially designed systems that can result in the complete loss of the structure due to excessive yielding and/or damage to beams or connections.

Precast jointed and rocking systems exhibit non-linear response by connection opening instead of the conventional sacrificial energy dissipating formation of a plastic hinge. As a result, they have markedly less inherent energy dissipation than ductile monolithic systems (Cheok and Lew 1991; Priestley and Tao 1993). Therefore, it is desirable to provide supplemental energy dissipation devices to these connections to reduce displacement response from earthquakes.

An early application presented by Stanton et al. (1997), utilised mild steel rods running across the connection and grouted in ducts. These rods were designed to yield in tension and compression to dissipate energy. Although test results revealed satisfactory hysteretic energy dissipation, because the bond between the grout and steel deteriorated, undesirable stiffness and strength degradation was also observed. In addition, repeated cycles led to bar fracture in some tests due to low-cycle fatigue, showing an inherent weakness in any sacrificial yielding-steel energy dissipation approach, be it a device or by sacrificial design. More specifically, such yielding based energy dissipation systems, as in the case of Stanton et al (1997), cannot provide consistent energy dissipation for every cycle of any (relative) size (Rodgers et al. 2008b).

Subsequent research has highlighted alternative mild steel energy dissipation devices, bolted externally across the joint region. Bradley et al. (2008) demonstrated externally mounted steel yielding devices with substantially reduced, but not eliminated, stiffness or strength degradation. However, these devices were prone to buckling, which will reduce the axial load and energy dissipation capacities (Dhakal and Maekawa 2002). Due to low-cycle fatigue and residual stresses, these devices would have to be replaced following an earthquake. In addition, they only offer repeated peak dissipation when yielded further than a previous cycle. Subsequent smaller cycles, the bulk of an earthquake input, thus receive minimal or no dissipation. These alternatives essentially move the damage mechanism to a sacrificial component. While this approach provides a more easily repaired connection, damage is still present and repair or replacement is still likely to be necessary. More succinctly, these approaches are all non-optimal, and the devices developed within this research offer a unique ability to consistency dissipate energy, over any size cycle.

It then becomes apparent that a more robust form of energy dissipation is needed that satisfies several objectives:

- energy dissipators should have zero (0) risk of low-cycle fatigue or bar fracture;
- energy dissipators should be ideally located within the beam-column joint region to minimize architectural disruption;
- residual forces in the energy dissipator should either re-centre or creep back towards zero over time to ensure the structure re-centres;
- the cost of devices should be economical compared to conventional (ductile) design solutions.

In response to these objectives, the HF2V devices presented in Chapter 2 were developed. For the application in this chapter a nominal design force of 120 kN was used in place of the yielding steel fuse bars used in Solberg (2007) and Li (2006). Implementing these HF2V devices should provide a DAD structural subassembly that exhibits little to no stiffness or strength degradation over any combination of input cycles.

4.2. Device Details

A set of two dampers were designed according to the design and trade-off relationships described in Chapter 2 and presented in Figure 2.9. The devices had a design force of 120 kN, and were to be externally mounted to the DAD joint, through a steel plate cast into the beam used to hold yielding fuse-bars in Li (2006) and Solberg (2007). To achieve the desired design force of 120 kN, a different scale of device to that previously constructed was required.

All previous devices constructed and discussed in Chapter 2 had utilised a 30mm nominal shaft diameter. The requirement for an even smaller device and the lower design force lead to a design using a 20 mm nominal shaft diameter, 32mm bulge diameter, and internal cylinder diameter of 50mm. The hysteresis loops for one of these devices subjected to cyclic quasi-static testing is presented in Figure 4.1, along with a photograph of the device with a standard 355 ml soft drink can to indicate scale. It should be noted that the different, smaller scale of this device made design difficult due to the limited range over which the models presented in Figure 2.9 were calibrated. However, the design force of a nominal, quasi-static 120kN force was achieved and provided additional data to verify the design models derived in Chapter 2.

The experimental testing presented in this chapter is intended to confirm the benefits of such devices when incorporated into ductile or DAD jointed connections.

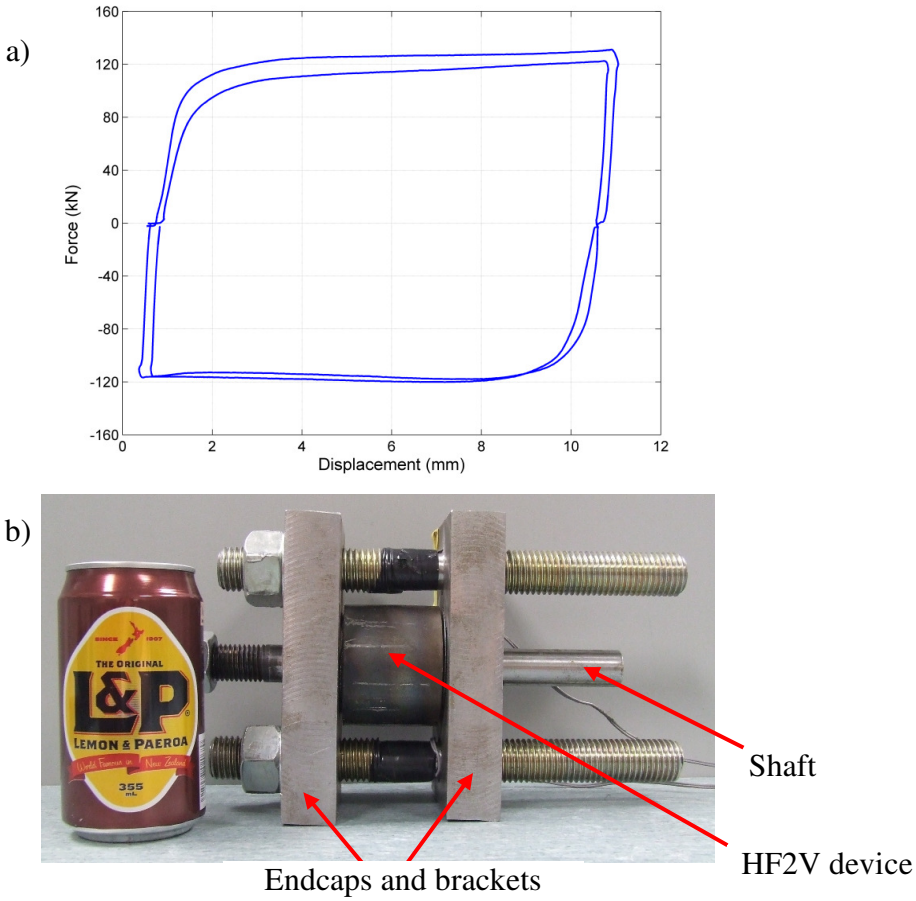

Figure 4.1: High force-to-volume (HF2V) device for concrete joint, a) hysteresis loop of damper, and b) damper photograph with soft drink can for scale including mounting brackets.

4.3. Design Details

4.3.1. Subassembly Development

The structural subassembly development was primarily done by a fellow postgraduate student, Kevin Solberg (Solberg 2007), with the HF2V devices being incorporated into this DAD connection design. This thesis presents a detail of the structural connection design for completeness, but focuses on the performance of the subassembly with the HF2V devices. Contrast is made to the performance using yielding steel fuse bars (Li 2006; Solberg 2007),

and the inherent energy dissipation provided by friction within the prestressing system utilized in this design. Moreover, additional experiments were done to delineate the effects of the HF2V devices and experimentally investigate the static re-centering limit of the connection, which are also unique to this research.

A 3D subassembly representing an exterior joint on a lower floor of a ten storey prototype building was developed as shown in Figure 4.2. The subassembly consisted of two beams cut at their midpoints and an orthogonal beam cut at its midpoint, the approximate location of the point of contraflexure. All of these members frame into a central column. The orthogonal beam, referred to as the gravity beam, was designed for supporting one-way precast flooring panels. The other two beams, referred to as the seismic beams, were designed for predominantly seismic forces. The dimensions of the prototype members were taken from previous similar research (Li et al. 2008). Specific dimensions include: 850mm square columns, 700mm deep by 500mm wide beams, and a 3.6m storey height. The prototype joint was assumed to have a moment capacity of 500kNm.

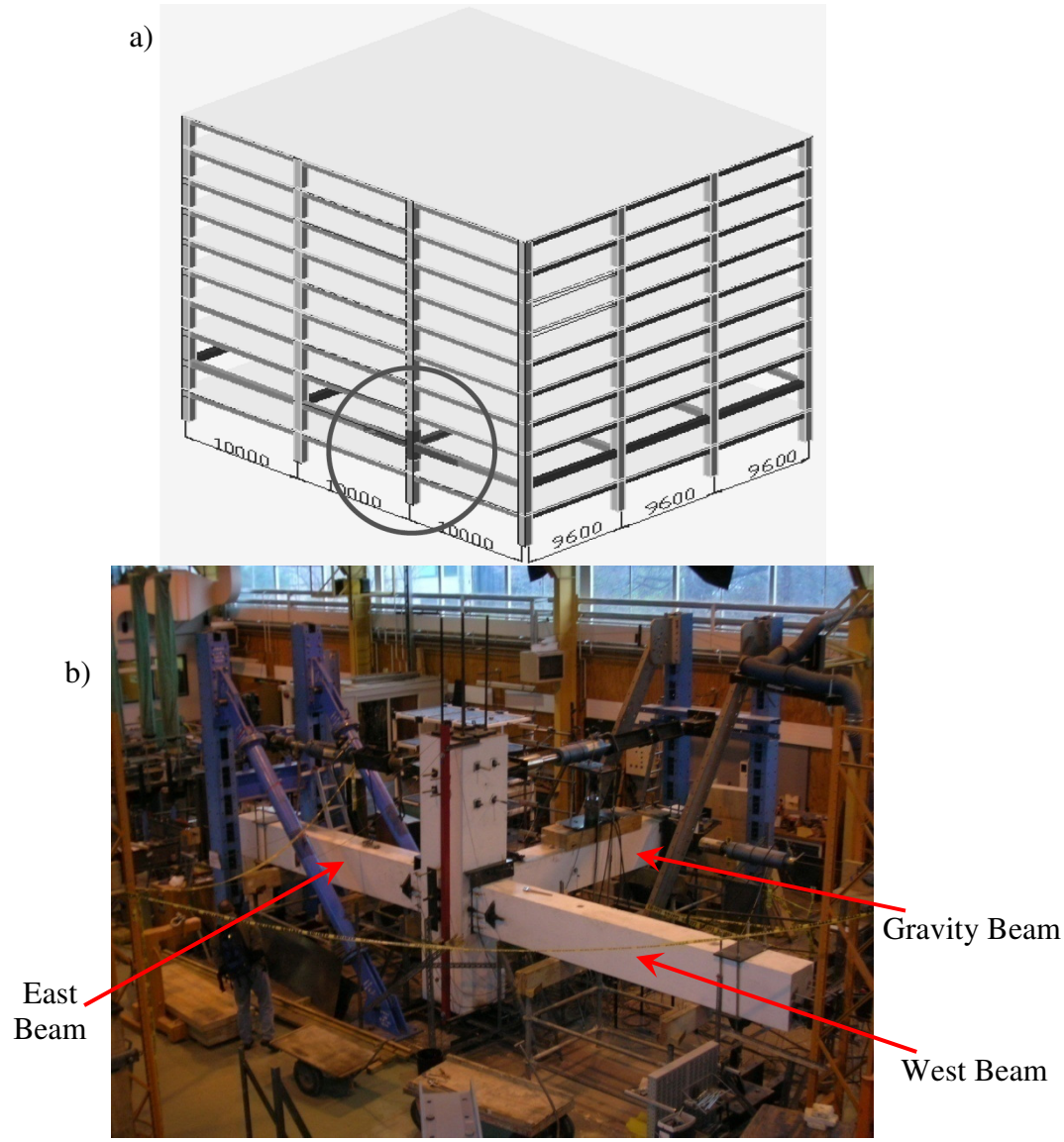

Figure 4.2: a) Prototype structure showing location of subassembly (Li et al. 2008); b) photograph of experimental setup

Given these constraints, the subassembly was scaled to 80 percent of the prototype building. The column was scaled to 750mm square and the beams scaled to 560mm deep by 400 mm wide. Figure 4.3a shows the seismic beams, column and basic dimensions (Solberg 2007). Minimal longitudinal reinforcement (ratio of 0.01) was provided for the column and the beams. Figure 4.3b illustrates the basic reinforcing layout for the beams and column (Solberg 2007).

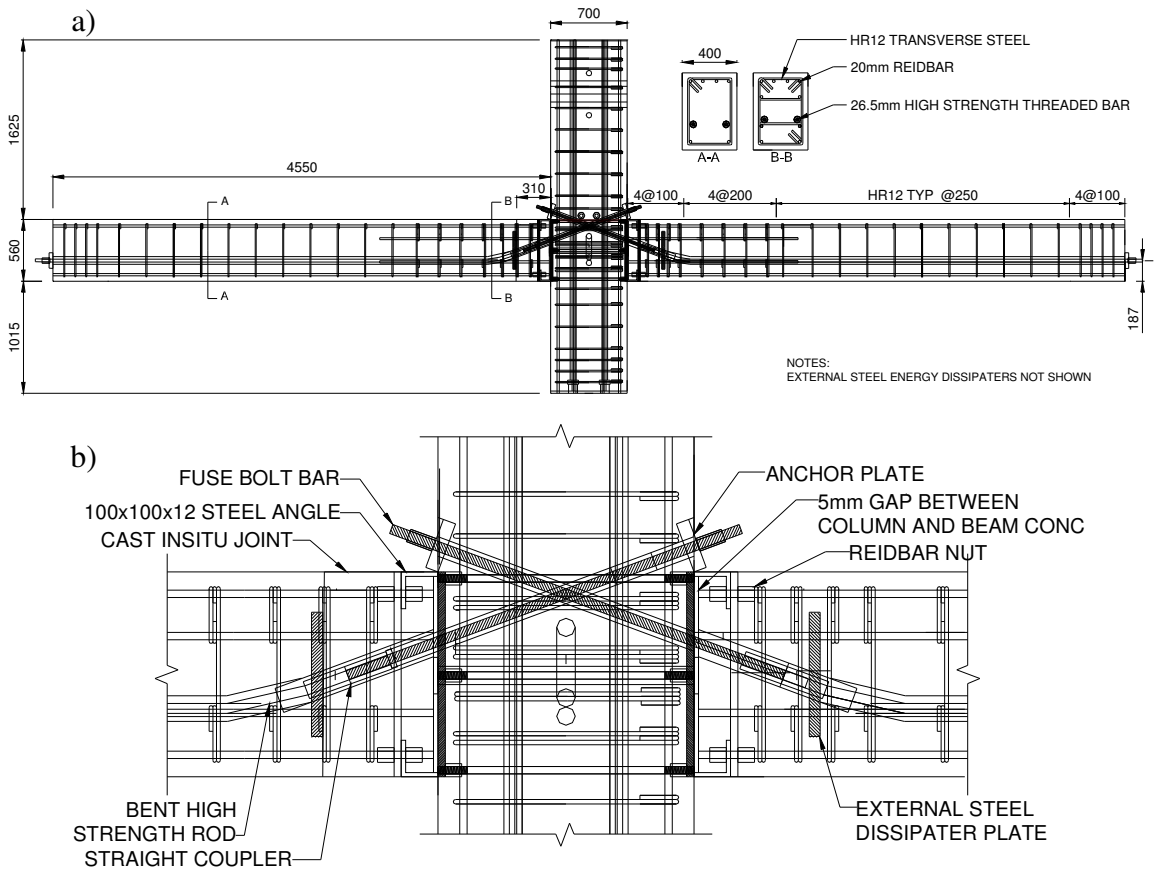

Figure 4.3: a) Elevation of the seismic beams and column, and b) Detail of the seismic beam-column experimental subassembly (Rodgers et al. 2008b; Solberg 2007).

The reinforcement arrangements were designed for the expected strength of the rocking joint from the dissipation devices and prestressing, and were intended to remain elastic. Four D20 longitudinal threaded rebars (Reidbar^{TM}, $f_y = 500$MPa) were provided top and bottom, providing the required moment capacity of $\phi M_n = 260$kNm. Due to the presence of axial load from prestress, minimal transverse steel requirements governed the design, thus 12mm diameter (HR12, $f_y = 500$MPa) stirrups were provided in the beam at a spacing of $d/2$ and a closer spacing at the ends. Additional transverse reinforcement was provided in the top and bottom 1.2m from the beam ends to confine the concrete in these high compression zones.

Unbonded post-tensioned prestressing was provided by two 26.5mm diameter high-strength thread-bars placed in 50mm PVC ducts, each post-tensioned to 200kN, giving 400kN of total prestress to each seismic beam, as illustrated in Figure 4.3b. A detailed diagram of the seismic beam-column joint is given in Figure 4.3b. The "seismic" beams utilized a straight coupler system where the tendons were pre-bent at the joint end to a radius of approximately 1.8m, allowing proper alignment with the angled rod running through the column. The fuse bolt-bar was machined to 75 percent of its effective area to ensure any yielding in the prestress system would be limited to the replaceable through-column bolt-bar. The tendon detailing resulted in an eccentricity of 190mm from the top rocking edge, and 370mm from the bottom rocking edge. At the beam end, a 100x100x12 inverted steel angle was used at top and bottom of the joint and the face of concrete was recessed 5mm. This design ensured that contact with the column was limited to the steel and allowed the angle's buried flange to mechanically develop stress in the beam's longitudinal rebars using Reidbar^{TM} nuts.

By the nature of precast concrete and rocking connections, it is critical that the face of the beam be aligned flush with the column. Therefore, offsite erection of a full length beam section may lead to on-site misalignment issues, which could affect rocking behaviour. To mitigate potential misalignment and to also allow for construction tolerances similar to current standards, a 310mm cast insitu closure pour was provided on the west seismic beam. Such a closure pour is expected to be cast on-site after the armouring angles have been adjusted to ensure a flush face at both ends and the post tensioning rods are coupled together.

High strength, fibre-reinforced concrete using 2 percent Dramix^{TM} steel fibres by weight was used in the insitu end to compare its behaviour to the regular strength concrete of the east beam. The mix was designed for high strength and good workability. The measured

compressive cylinder strength of the high strength concrete was f'_c= 70MPa, while the east beam and the remainder of the west beam concrete was measured as f'_c= 37MPa.

At each joint, four 30mm diameter shear keys were installed, tapered 5° inward to ensure they do not jam when the specimen rocks at the beam-column joint. These were designed to be screwed into the face of the column via a cast in double nut. The shear keys were designed to resist gravity and seismic shear forces. One shear key was located in each corner, providing torsional resistance.

4.3.2. High Force-to-Volume (HF2V) Devices

HF2V devices were designed, as noted in Section 4.2, to be mounted externally on purpose-built plates in the beams. An exploded assembly of the HF2V dampers designed for the connection is given in Figure 4.4 along with the beam mounting plate that they were connected to. Rectangular end caps were bolted together via two attachment rods, which also anchored the device to the beam's anchor plate. One end of the central shaft was threaded, allowing it to be coupled to a threaded rod anchored to the column. The threaded rod running through the column was anchored on each end of the column face using a nut and steel plate washer. A photograph of the actual experimental device and mounting configuration is given in Figure 4.5, as well as the picture showing scale in Figure 4.1.

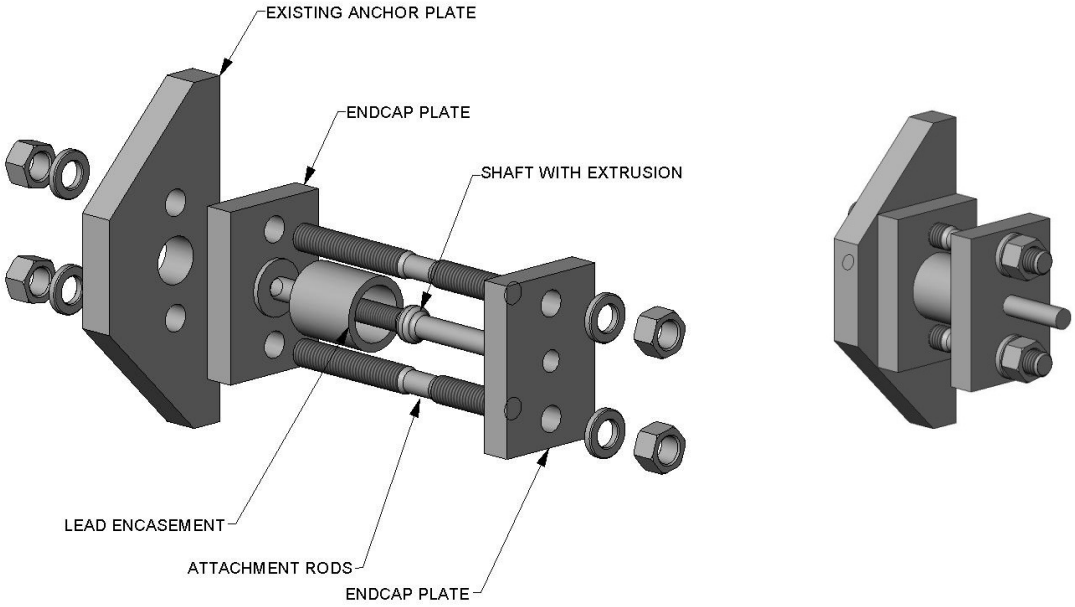

Figure 4.4: The HF2V device externally mounted to the beam's anchor plate. See also Figures 4.1 and 4.5 for images of the actual device and scale.

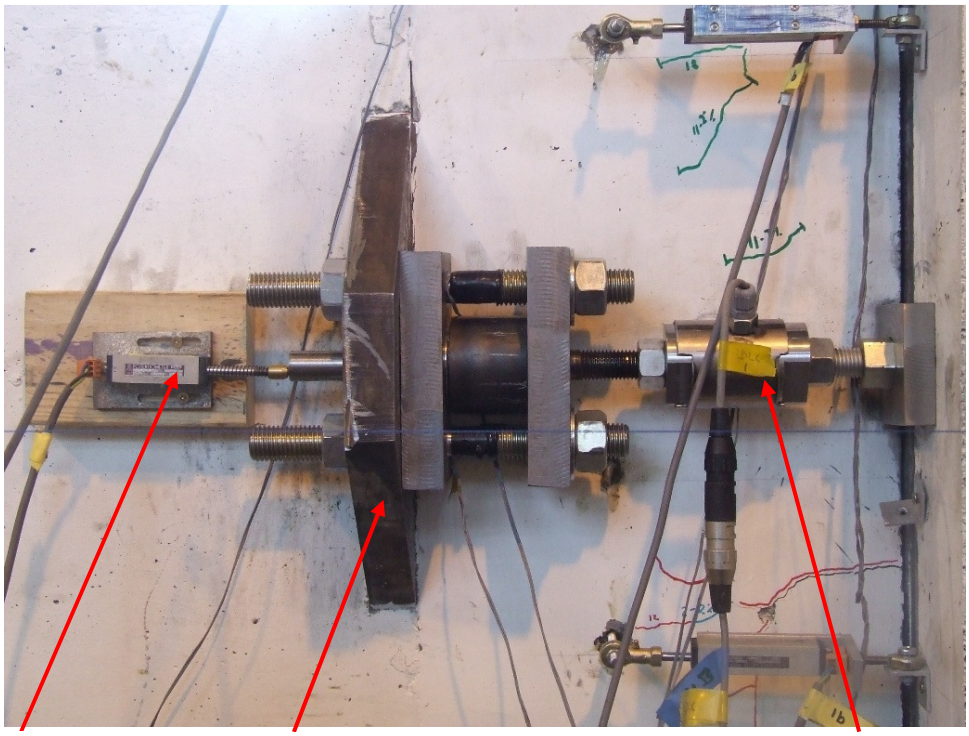

Figure 4.5: Photograph of the HF2V device mounted to the beam anchor plate with connecting rod anchored to column.

Device force capacity affects the mechanics and behaviour of the joint. More specifically, to ensure the connection is capable of closing, the moment contribution from the initial prestress force provided through the longitudinal tendon in Figure 4.3 must exceed the contribution from the dampers. This criterion can be written:

$$\phi M_{PS,i} \geq \Omega_{diss} M_{diss} \tag{4-1}$$

where $M_{PS,i}$ = moment contribution at the joint from the initial prestress force; M_{diss} = moment contribution at the joint from the energy dissipation devices in compression; Ω_{diss} = overstrength factor of the dissipation devices (taken as 1.5); ϕ = undercapacity factor for the prestress (taken as 0.85). Dividing the contribution from prestress by the contribution from the dissipation devices gives a ratio of their expected contribution:

$$\lambda = \frac{\phi M_{PS,i}}{\Omega_{diss} M_{diss}} \tag{4-2}$$

To ensure the system re-centres, $\lambda \geq 1$ must hold true indicating that the moment $M_{PS,i}$ must be $1/\phi$ times larger than the device force times 1.5. The dampers were therefore specifically designed to provide the same level of energy dissipation as the mild steel devices adopted in Li et al. (2008), corresponding to the designed 120kN HF2V device yield force. Note that this design force corresponds to λ = 1.3 and 2.5 in the East-West direction of Figure 4.2 for positive and negative moment, respectively, which reflects the eccentricity of the tendons at the joint. As two seismic beams meet at the one column, the overall joint is symmetric, as the eccentricity of the tendon profile is counteracted when the opposing beam is opening in the opposite direction, giving an overall ratio of λ = 1.9 in the East-West direction.

4.4. Experimental Set-up and Methods

Figure 4.6 shows the overall experimental test setup including a) a plan view, and b) a South elevation view. As shown in Figure 4.6, loads were applied to the specimen by three hydraulic actuators: Actuators A and B were installed to the reaction frame and top of the east and south face of the column, respectively, and actuator C was installed in the east-west direction at the end of the gravity beam. Actuator C was intended to stabilize the specimen, with its movement synchronised to one-half the displacement of Actuator A. Load cells were installed in-series with each actuator. Additional load cells were attached at the strut of each beam, the jacking point of each post-tensioned rod, and on the connecting rods to the HF2V devices.

To measure rotation at the joint, 3 linear potentiometers were installed on both faces of each joint, totalling 18 potentiometers. Two additional linear potentiometers were installed against the bottom face of each beam to measure vertical movement. At several locations around the specimen rotary potentiometers were installed to measure local displacement. Two 5mm strain gauges were installed on each bolt bar to measure any potential yielding that may occur during testing. To measure the response of the HF2V dampers a load cell and strain gauges were attached to the anchor rod of each device. A spring potentiometer was mounted on the back of each device to measure the displacement of the device shaft.

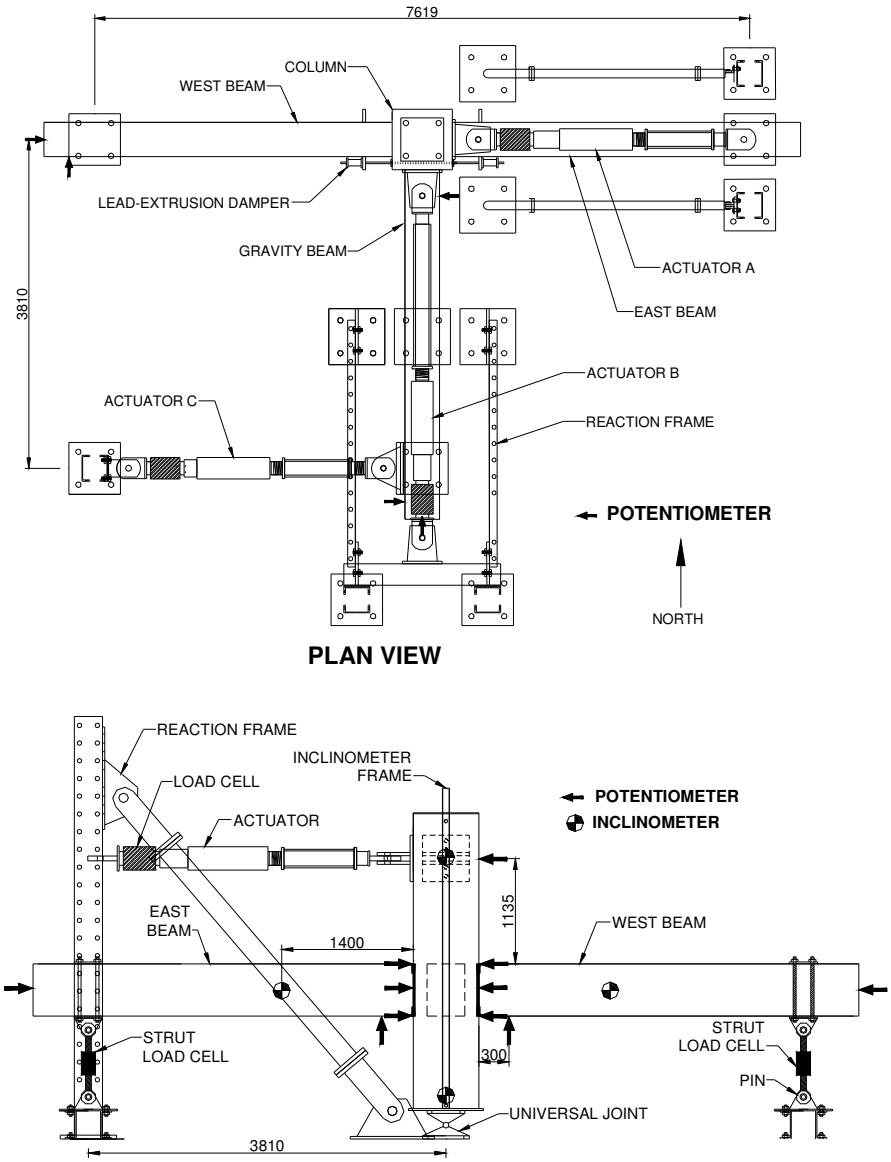

Figure 4.6: a) Plan view, and b) North Elevation view of the experimental set-up (Rodgers et al. 2008b; Solberg 2007).

The instrumentation was installed and calibrated to use 70-85% of the total sensor range during testing to 4% column drift. Using data acquisition with ±2048 counts, this approach gave approximately 3000-3500 counts for 4% drift, giving resolution of approximately ±0.1 kN on the actuator loadcells, ±0.05 kN on the device loadcells, ±0.15 mm on the large rotary potentiometers, and a theoretical resolution of approximately 10μm on the smaller linear potentiometers. The control system operated with a typical deadband of 1 count, equating to ±0.15 mm on the lateral column displacement.

The testing regime was relatively straightforward, and focuses entirely on the performance of the HF2V dampers for different design levels of story drift. Cyclic quasi-static (QS) tests were performed at varying levels of story drift. These tests were uni-directional in the East-West direction. The North-South direction is largely disregarded in this investigation, since its performance has already been reported in previous studies (Bradley et al. 2008; Solberg et al. 2008a).

The testing was conducted in two phases. The first phase used a single damper attached to the south side of each seismic beam. The second phase involved removing the east beam and both dampers were placed on the west beam, thus doubling its damping capacity, (giving re-centering ratios λ^{+}=0.65; λ^{-}=1.25). The second configuration thus represents a corner joint of the prototype building, which is also asymmetric in its opening and hysteretic behavior without the (removed) East beam.

4.5. Experimental Results

4.5.1. Exterior Joint Assembly

Experimental results from this section focus on the global performance of the specimen and the local performance of the HF2V dampers. The local behaviour of the specimen (i.e. cracking, crushing, prestress, etc.) was not the focus of the work in this thesis and has been reported previously by research collaborators for analysis with yielding fuse-bars (Bradley et al. 2008; Solberg et al. 2008a). Therefore, these aspects of the results are outside the scope of this thesis and are not reported here, where the focus is on the impact and validation of the HF2V devices.

For purposes of comparison, Figure 4.7 presents results of Quasi-Static testing in the East-West direction to a maximum column drift of 2 percent for three cases: (i) prestress only; (ii) mild steel energy dissipators; (iii) and the HF2V devices.

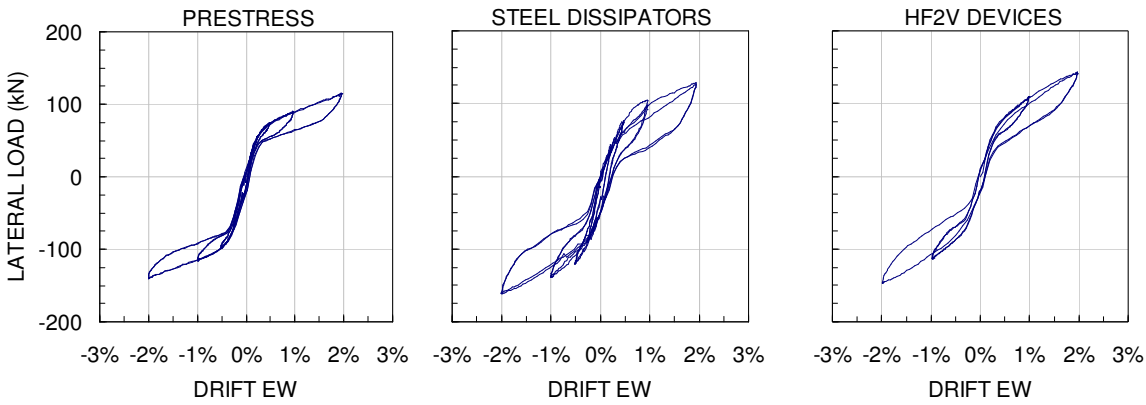

Figure 4.7: Comparison of the performance considering (a) prestress only; (b) steel dissipators; and (c) HF2V devices for 2 fully reversed cycles at 1% and 2% drift amplitudes

With prestress only it is apparent the system still provides some level of energy dissipation, largely due to the friction effects under movement reversal arising from the draped and bent tendons and thread-bars within the ducts at or across the column connection. The steel devices provide the most hysteretic energy dissipation for these small drift cycles, and the HF2V devices also provide additional, nearly equal, energy dissipation. The specimen with steel devices exhibits some strength degradation for just these four (total) cycles. This loss can be traced to the fact that the steel dissipators will undergo plastic deformation in tension, and will not recover that deformation in compression in part due to buckling. The HF2V devices are consistent across all cycles.

Partial buckling of the dissipators also means that less dissipation occurs on subsequent loading cycles, potentially leading to larger earthquake induced displacements later in the record or event. More explicitly, only peak cycles receive full dissipation with the mild steel dampers, rather than every cycle regardless of size. The HF2V devices do not exhibit this

effect. The hysteresis loops of the specimen that utilises the HF2V devices are completely stable, showing no apparent strength degradation on the second cycle of loading for a given drift amplitude, even if it is smaller than prior loading cycles.

On larger displacement cycles to 3% drift, the HF2V dampers provided a significantly greater amount of hysteretic energy dissipation. This result can be seen in Figure 4.8, where an additional two cycles to 3% drift reveals a markedly large change in response. The overall specimen exhibited some drop in strength during reloading to the previous peak, but no overall capacity was lost.

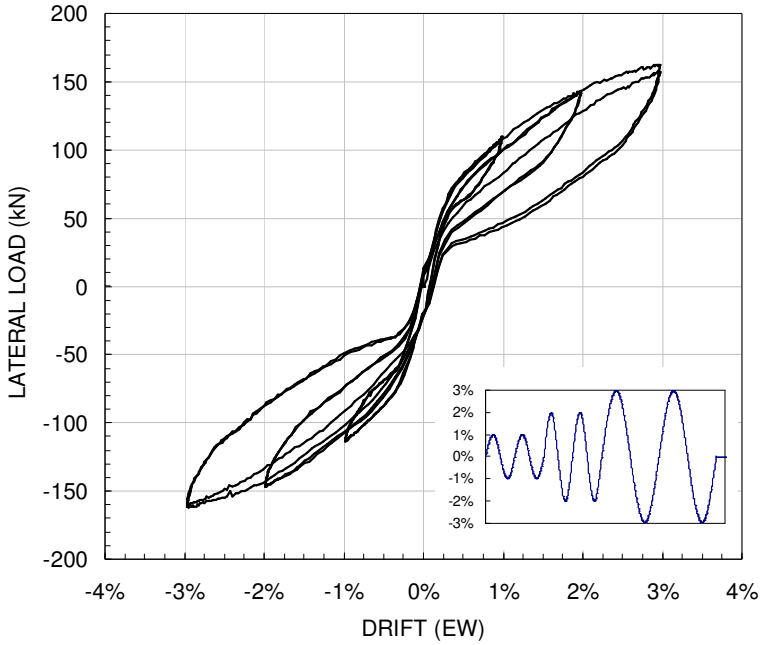

Figure 4.8: Response of the specimen with HF2V dampers to 3 percent drift. (inset: quasi-static loading regime)

The cause of the increase in energy dissipation at 3% drift can be seen more clearly in the 'in-service' force-displacement response of the two HF2V devices, which are shown in Figure 4.9. Before the specimen reached a drift of 3 percent, the devices behaved essentially in an elastic manner. At 3% drift, the devices were fully engaged and were able to dissipate large amounts of energy, with the shaft moving approximately 3.5mm.

Upon subsequent loading and unloading, the device exhibits an "elasto-plastic" type of response, with slight "pinching" at zero force. This pinching can be attributed to take-up within the connecting threaded elements of the device. The shaft does not entirely return to its initial position, but upon completion of the test remains about 1.5mm from its initial position, due to take-up and device mount flexibility. The difference between the device behavior during quasi-static compression testing and the in-service behavior can be attributed to the flexibility of the connecting elements. However, at a given drift level, the HF2V devices were very consistent and thus the small strength degradation noted in Figure 4.8 is due to the low-level yielding of the prestresing tendons, and internal flexibilities and take-up within the device mounts and connecting elements, and not the devices themselves.

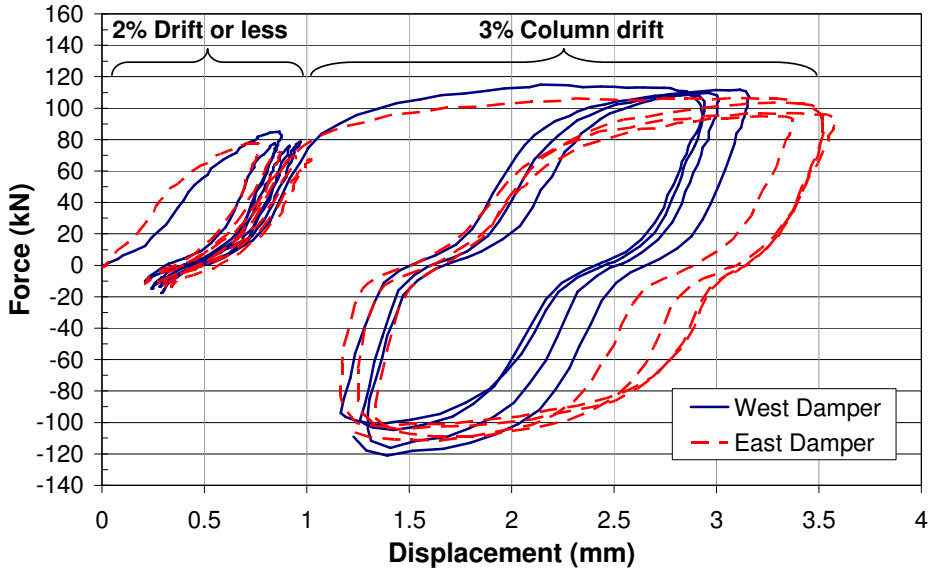

Figure 4.9: In-service force-displacement response of the HF2V devices

After testing, the residual compression force in the HF2V damper and anchor shaft was approximately 90kN. A logarithmic decrement of force towards zero residual force occurred over time, as shown in Figure 4.10. Within the first 5 hours the force in the devices had dropped by approximately 50kN or almost 45% of the peak residual compression force. This behavior is a clear advantage of the lead extrusion dampers over the steel fuse bars or similar

yielding, sacrificial approaches. More specifically, as well as remaining completely damage-free and operating efficiently for every cycle, the residual compressive force creeps out of the devices, leading to complete self-centering of the joint. Note also that the low residual forces in Figure 4.10 are well within the ($\lambda > 1.0$) re-centering capability of the joint defined in Equation (4-2).

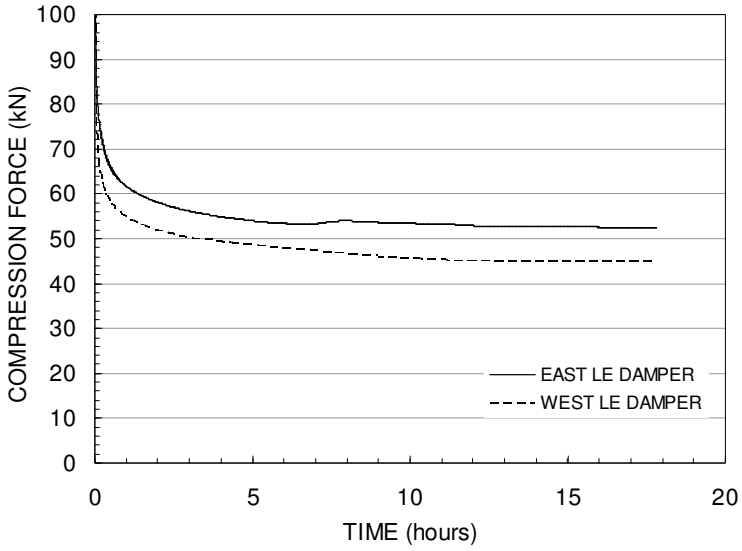

Figure 4.10: HF2V device force over time.

4.5.2. Corner Joint Assembly

As noted in the previous section, after the initial testing, the east beam was removed and its damper was relocated to the West beam, doubling the beam's energy dissipation capacity. Figure 4-11 presents a photograph of the experimental specimen with the East beam removed and both HF2V devices mounted on the West beam.

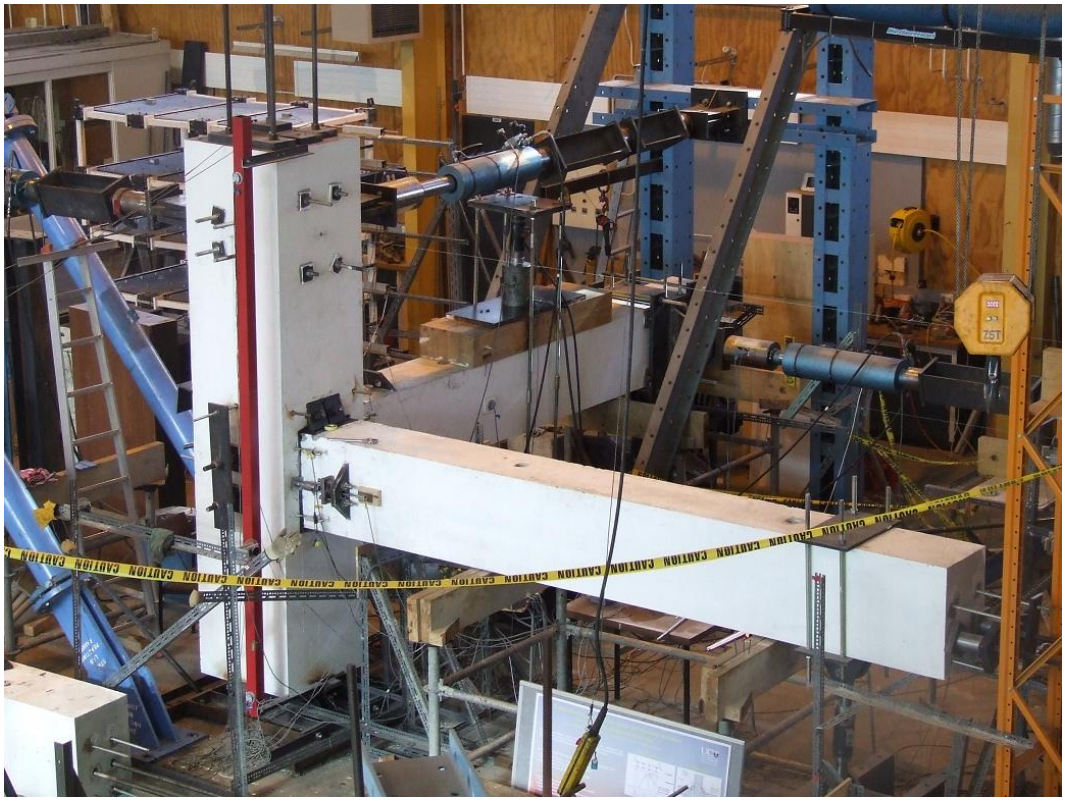

Figure 4.11: Photograph of the corner joint with the East beam removed.

Figure 4.12 presents the response of the corner joint specimen with and without the HF2V devices, subjected to fully reversed loading cycle from 0.5 to 4% story drift. The asymmetry of the force-drift response is due to the eccentricity of the tendon with respect to the beam mid-depth. Although this asymmetry has always been present, the hysteresis loops presented in Figures 4.7 and 4.8 do not show this asymmetry, as the presence of both the East and West beam balance out this effect. More specifically, although the forces at each interface were asymmetrical, the west interface was undergoing the opposite joint rotation to the east interface, resulting in overall symmetry of the hysteresis loops. The removal of the East beam removed this affect, resulting in the clear asymmetry seen in Figure 4.12.

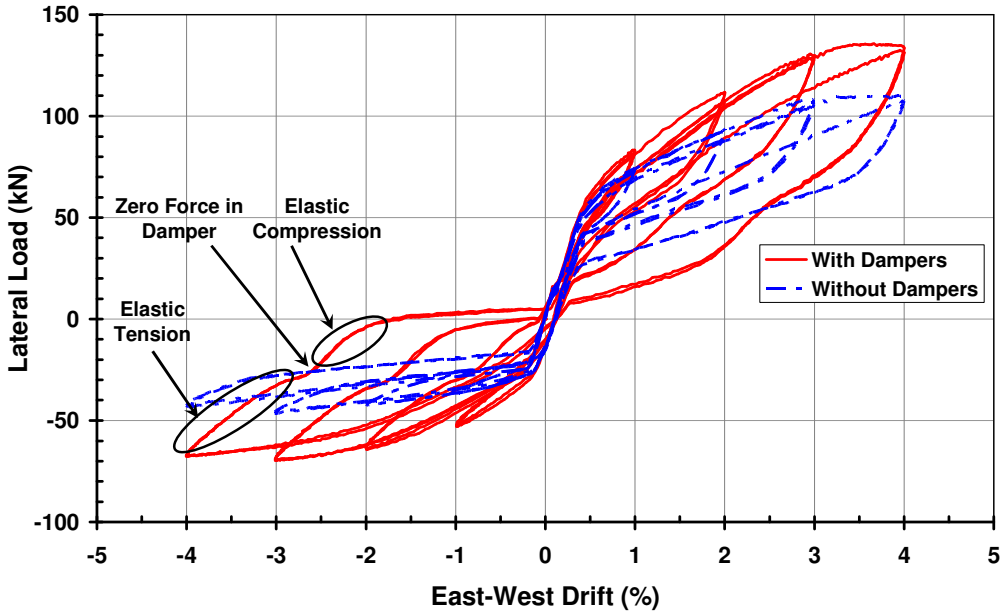

Figure 4.12: Response of corner joint specimen QS testing to 4% drift.

It is apparent that the specimen exhibits significantly more energy dissipation when compared to previous tests in Figures 4.7 and 4.8. This result is expected due to the increased damping forces created by using both devices on one beam. However, re-centering was still apparent despite $\lambda < 1.0$ for negative direction loading, with smaller tendon eccentricity. Finally, the residual displacements were still negligible.

Some pinching, indicated as localised 'flattening' in the hysteresis loop, was observed during the unloading phase. This phenomenon is attributed to take-up within the threaded anchor rods that occurs when the net rod forces change from tension to compression. This phenomenon was confirmed by the load cell readings indicating that this behaviour coincided with zero-load in the devices, at which point the connecting rods also carry zero load, indicating the load reversal point

Interestingly, the area enclosed within the hysteresis loops for the joint without the dampers (dashed line in Figure 4.12) shows a large disparity between the two directions. Again, this phenomenon can be traced back to the tendon profile. The inherent hysteresis for the joint

without dampers is primarily related to the well-known friction effects that exist in draped tendons. In this case, it is friction between the prestressing tendons and the PVC ducts in which they are contained. The bent tendon profile results in notable friction between the tendon and PVC ducts, as the tendon undergoes deformation during gap opening and rubs against the curved ducts. It is expected that the larger forces for positive joint drifts will lead to larger frictional forces, and therefore an even greater amount of inherent energy dissipation due to friction.

Under positive loading, when the drifts exceeded 3%, some minor strength degradation was observed as a result of yielding of the reduced-section thread-bars. This behavior is not considered to be a bad feature, rather it was intended by the design. If substantial yielding occurs when story drift exceeds a very large value, such as 5 percent, then the connecting reduced section thread-bars can be replaced. Thus, yielding at extreme motions beyond the 2-3% maximum design drift is taken up by easily replaced components.

Finally, to quantify the relative amounts of damping provided by the jointed connection the areas enclosed within the hysteresis loops was numerically integrated. This calculation was done for all major cases including: without any supplemental damping devices, with yielding steel fuse bars, and with the HF2V dampers. These areas represent the total energy dissipated. The results of these calculations are presented in Table 4.1, where the values represent the average enclosed area across 4 peaks to each drift level, resulting from two fully reversed sinusoidal loading patterns.

Table 4.1: Energy dissipated for different joint configurations (J). Note the steel fuse bars are not tested in the corner joint configuration, and the HF2V dampers are at a minimum capacity for the size of the connection for the external joint setup.

		Drift Level (%)					
		0.25	**0.5**	**1**	**2**	**3**	**4**
External Joint Configuration	**Post-Tensioning Only**	67	141	420	1208	2372	-
	Steel Fuse Bars	114	331	819	2200	-	-
	HF2V Dampers	-	-	440	1601	3419	-
Corner Joint Configuration	**Post-Tensioning Only**	-	-	223	666	1297	2007
	HF2V Dampers	-	-	247	946	2380	4230

It should be noted that since the results are an average over 4 cycles, the values do not necessarily represent a stable and repeatable amount of energy dissipation. Thus, large dissipation on the first cycle to a given drift with yielding fuse bars may not be matched on subsequent cycles. In particular, at 2% drift levels, an overall average of 2200J is dissipated by the joint with steel fuses, compared with 1600J for the joint with HF2V dampers. However, the much larger dissipation for the steel is only due to the large dissipation on the initial cycles, with the 3rd and 4th cycles having dissipation of approximately 1800J or less, bringing it much closer to the energy dissipated by the joint with the HF2V dampers. Moreover, the steel fuses were not tested in uni-directional testing up to 3 or 4% drift, so comparisons could not be made at larger drifts where the HF2V further improved energy dissipation. Finally, it is worth noting that the HF2V devices suffered no damage or failure.

The larger dissipation from the HF2V dampers at higher drifts can be attributed to the take-up or slackness and flexibility in the connecting elements. The corner joint results show that at 1% column drift, the HF2V dampers increase the inherent hysteretic damping of the joint by approximately 11%, whereas the increase over the undamped joint becomes 42, 84, and 110% at column drifts of 2, 3, and 4% respectively. The lack of contribution at the lower drift levels could be mitigated by more careful design and construction of the connecting elements to eliminate flexibility and take-up/slack.

Overall, the energy dissipation provided by the HF2V dampers is thus somewhat under represented due to both the conservative size (relatively small force capacity) of the dampers chosen, and sources of flexibility. Much larger dampers could be readily provided in the external joint configuration while maintaining static joint re-centering ability, as demonstrated by the corner joint configuration. Hence, the highly repeatable (cycle-to-cycle) HF2V device results could be readily improved by increasing the device force capacity, thus matching or exceeding the sacrificial steel fuse bar results seen in Table 4.1.

4.6. Discussion

The performance of the specimen met the two primary performance objectives: (i) the dissipation of considerable energy by the supplemental HF2V devices; and (ii) with no structural damage. This proof-of-concept experiment has validated the efficacy of incorporating HF2V devices into a beam-column joint to reliably dissipate seismic energy. Although the devices were slow to 'engage' and take full effect at small drifts due to mount flexibility and connection details, at higher drifts it was found that the specimen exhibited much larger hysteresis loops and therefore absorbed considerably more energy than sacrificial mild steel devices, which buckled in compression offering no absorption in that direction. The flexibility issue could be easily mitigated in design by selecting a larger shaft diameter and/or connecting rods with lower levels of stress during operation. The ability of the HF2V devices to dissipate the residual compressive force over time through creep effects means that essentially zero moment exists at zero drift ensuring full re-centering capability of the structure. Moreover, no maintenance of the damping system following an earthquake is expected to be needed. Covering the device to protect them from any effects of fire may also be desirable.

As noted previously, the devices were slow to 'engage', as evidenced by the stark difference in hysteretic energy dissipation shown in Figure 4.7 and Figure 4.8, between 2% and 3% column drift. This lag was traced (in part) to the anchoring system utilized. Given the properties of the anchor rod, its elongation at the yield force of the damper (120kN) would be approximately 2.5mm. Given a column drift of 2%, which corresponds to a connection rotation of about 0.015 radians, the maximum expected gap-opening at the location of the extrusion dampers is 4.5mm. The elongation of the rod would account for more than half this amount, thus seriously reducing the effectiveness of the device. This effect is magnified by the fact that each connecting element (the coupler, nuts, anchor plates) exhibit some degree of take-up, which must also be accommodated before the full yield force of the dissipator can be reached. Given the elastic stiffness of the damper (200kN/mm), such effects can be notably detrimental to the full effectiveness of the dampers' contribution to the joint. This effect can be further explained looking at the system based on strain energy. For maximum energy dissipation, it is desirable to have the minimum amount of elastic strain energy in the connecting elements, so that the largest displacement is applied directly to the dampers, which will in turn lead to the greatest effectiveness of the HF2V devices in absorbing energy.

The lag effect of damper mount and connecting rod flexibility is also part of the reason the specimen exhibited minor strength degradation on secondary cycles. At the completion of a cycle, the damper and its connecting elements would be in compression. At the onset of a reversed cycle, the anchor rods need to first transition from a fully elastic compression state to an elongation in tension, thus requiring even greater displacements of the joint for engaging of the dissipation device to occur. This effect may be considerably reduced if the damper and its anchorage elements are prestressed, thus eliminating any sources of flexibility and take-up in the system. Other solutions include lower stresses in all elements connecting

to the HF2V devices, if warranted, or embedded devices within the concrete members. In future efforts, care should be taken when designing the dissipator anchorage, with specific attention given to eliminating any slack or take-up within the system.

During the initial development of these devices, as presented in Chapter 2, and from previous published work (Cousins and Porritt 1993) it was found that the peak yield force of the devices was weakly velocity dependent, with a velocity exponent in the range of 0.11-0.15. This effect may be beneficial, as under very rapid displacements, such as would be expected in a large earthquake, the device would provide significant additional damping to the structure not seen in these Quasi-static tests. This velocity-dependent increase in force allows the dampers to provide a dissipative peak force capacity higher than the restoring force from prestress, while still allowing the connection to re-center upon unloading at near zero velocity. These results are in direct contrast to sacrificial steel-yielding bars/devices.

However, if the increase is significant, it is possible that the increased force could be detrimental to the weak beam-strong column, capacity design principles utilised in this sample structure design. Therefore, the damper velocity characteristics should be utilised to predict peak force levels for the dampers under full dynamic loading, and these forces incorporated into the capacity design procedures. In particular, careful design can account for, and eliminate, any detrimental effects relating to this velocity dependence. More specifically, careful damper design, based on the design equations presented in Chapter 2, along with careful connection design to minimize the flexibility and take-up of connecting elements will readily provide an optimal outcome.

4.7. Summary

This study has presented a proof-of-concept experimental investigation. Compact high force-to-volume (HF2V) devices capable of being fitted directly into a structural connection, an alternative to mild-steel energy dissipation devices, were mounted externally across a beam-column joint. Based on the results of this study, the following conclusions can be drawn:

1. It was demonstrated through quasi-static testing that the HF2V dampers could provide a level of energy dissipation comparable to, or in excess of, mild steel devices designed for the same yield force at low drifts. Larger drifts saw significantly increased energy dissipation from the extrusion dampers. Subsequent smaller motions received full dissipation, which would not occur with yielding dissipators.
2. High force-to-volume extrusion dampers offer an attractive alternative to mild steel energy dissipation devices. These devices do not suffer from low-cycle fatigue and the force in the devices creeps back towards zero upon unloading. Therefore, they do not need any maintenance following an earthquake and could be mounted internally. The ability of the device force to creep out over time ensures self-centering of the structure is maintained following an earthquake.

The stiffness of device mounts and connecting elements is an important consideration. Since gap-opening is generally 5-10mm, stiffness plays an important role in the effectiveness of supplemental energy dissipation. Care should be taken when designing the anchorage for these devices. Prestressing the devices will help to eliminate take-up in the system and ensure a more optimal solution.

Chapter 5: Jointed Precast Concrete Connections with Internal HF2V Devices

Based on the results presented in Chapter 4, several major outcomes were observed. The bent tendon profile and associated asymmetry at the beam-column interface resulted in tendon yield occurring at approximately 3% drift for the corner joint configuration. Large asymmetry was seen in the hysteretic response of the corner joint configuration which was also due to the bent tendon profile. Take-up and flexibility within the structural elements connecting the HF2V devices to the subassembly had a significant impact on the overall results. These results led to the conclusion that internally mounting the HF2V device would likely result in less take-up and a better overall subassembly response, and thus an improved DAD connection.

Therefore, a connection similar to that described in Chapter 4 was designed and constructed that utilizes a straight tendon profile in the East-West (seismic) direction and was designed with internally mounted HF2V devices. The HF2V devices had a nominal quasi-static design force of 250 kN doubling that of the prior tests in Chapter 4. The experimental study consisted of a similar 80 percent scale precast concrete 3D beam-column joint subassembly designed with damage-protected rocking connections. An important differentiation from the previous connection presented in Chapter 4 is that HF2V devices were installed in all three beams including the gravity beam, compared to only on the seismic beams for the previous connection. Therefore, unlike in Chapter 4, this chapter presents results for both East-West (seismic) and North-South (gravity) input motions, as both sets of results are pertinent to the HF2V device contributions to the overall subassembly response.

5.1. Introduction

A connection similar to that described in Chapter 4 was designed and constructed in collaboration with a fellow postgraduate (Solberg 2007) that utilizes a straight tendon profile and was designed with internally mounted HF2V devices. The experimental study consisted of an 80 percent scale precast concrete 3D beam-column joint subassembly designed with HF2V devices and damage-protected rocking connections. A prestress system is implemented using post-tensioned high-alloy high-strength unbonded thread-bars through the beams and columns. The HF2V devices were installed in all three beams including the gravity beam, as opposed to only on the seismic beams in Chapter 4. Therefore, this chapter presents results for both East-West (seismic) and North-South (gravity) input motions as both sets of results relate to damper contributions to overall subassembly response.

The relatively conservative size of the HF2V devices (120kN nominal design force) used in the connection of Chapter 4 resulted in far less than optimal energy dissipation. Therefore, the HF2V devices for use in this experimental investigation were designed and constructed with a nominal design force of 250kN. The initial prestress applied to the system was increased to 250kN per tendon (500kN total) compared with a total of 400kN used in the previous connection. This change affects the relative size of the damping system with regard to the overall joint forces and also influences the reserve capacity on re-centering.

The experimental study in this chapter incorporates the findings from the previous chapter, as well as related studies on the same or similar connections (Bradley et al. 2008; Li et al. 2008). It thus focuses on the development and impact of cost effective, reliable energy dissipation and detailing schemes, particularly in comparison to the results in Chapter 4. Detailing of the beam-ends that frame into the column is also modified from Chapter 4 to accommodate the

devices. Otherwise, the connections and experiments are, structurally, quite similar to enhance comparisons.

5.2. Subassembly Development

The subassembly development was intended to follow a similar approach to the previous connection to minimize modifications to the reaction frame and experimental test set-up. The details of the structural design were determined by Kevin Solberg (Solberg 2007) and was designed in collaboration to develop a simple means of internally mounting the HF2V devices. Only limited details are presented on the experimental set-up, with further details being available in Solberg (2007) and Rodgers et al. (2009b). The beams were developed to include a cast in-situ 'closure pour' at the beam ends to incorporate construction tolerances, as well as allow the placement of the HF2V devices. Within the beam end zone, the HF2V damper in each beam can be coupled to a threaded rod anchored in the column, the prestress thread-bars would be coupled to one another, and the channels would be tightened against the face of the column. A detailed overview of the construction sequence is given in Solberg (2007), which focuses on these aspects.

5.2.1. Specimen Design

A 3D subassembly representing an interior joint on a lower floor of a ten storey building was developed, closely similar to the previous subassembly. The subassembly consisted of two beams cut at their midpoints and an orthogonal beam cut at its midpoint. These beams were all connected to a central column. The orthogonal beam, referred to as the gravity beam, was designed to support one-way precast flooring. The other two seismic beams were designed for

predominantly seismic forces. The dimensions of the prototype members were 875 mm square columns, 700 x 500 mm beams, and a 3.6m storey height. The prototype moment capacity of the beam end at the column face was 500 kNm. The subassembly was scaled to 80 percent of the prototype framed structure. The column was scaled to 700 mm square and the beams scaled to 560 mm by 400 mm. The experimental setup was very similar to that presented in Chapter 4, and further details may be found in Solberg (2007). Figure 5.1 illustrates the reinforcing layout for the structural members, where the target longitudinal reinforcement ratio is 0.01. These members were designed to remain elastic under the expected rocking connection strength from the HF2V device and prestress forces.

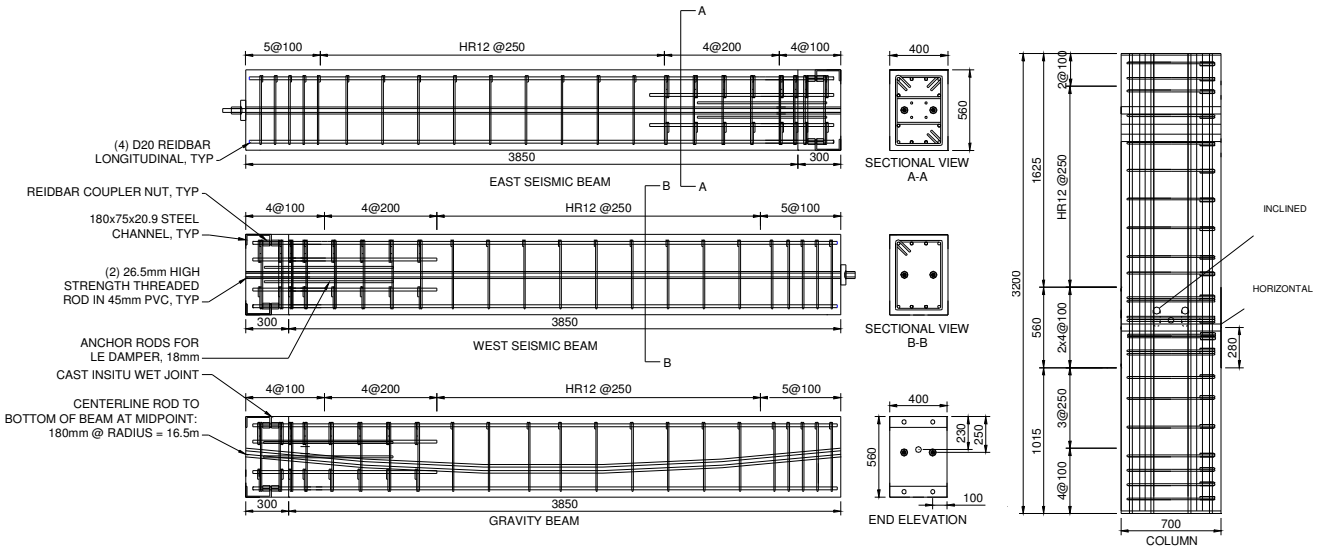

Figure 5.1: Reinforcing detail for the beams and columns (Solberg 2007)

Two 45 mm longitudinal PVC ducts spaced 200 mm apart were provided for the prestress system at the seismic beam vertical centrelines. Two 26.5 mm (MacAlloy^{TM}, f_y = 1100 MPa) thread-bars provided prestress in the seismic direction utilising a straight profile to ease congestion in the column and provide a more constructible solution. The thread-bars in the gravity beam were draped to provide "load-balancing" for the gravity loading from the one-way floor panels. Hence, this thread-bar crosses the joint's centreline at a 30 mm eccentricity.

The main difference to the previous connection is the use of 250kN post-tensioning per tendon, and the straight tendon profile in the East-West direction.

A 300 mm cast in-situ 'wet' joint was provided at the column connection end of each beam. The detailing strategy in the seismic direction is shown in Figure 5.2. The joint was designed to accommodate 150 x 150mm HF2V devices in the centreline of the seismic beams, and at a 50 mm vertical offset from the centreline in the gravity beam. Threaded rods were incorporated into the beams to provide a location mechanism for the HF2V devices.

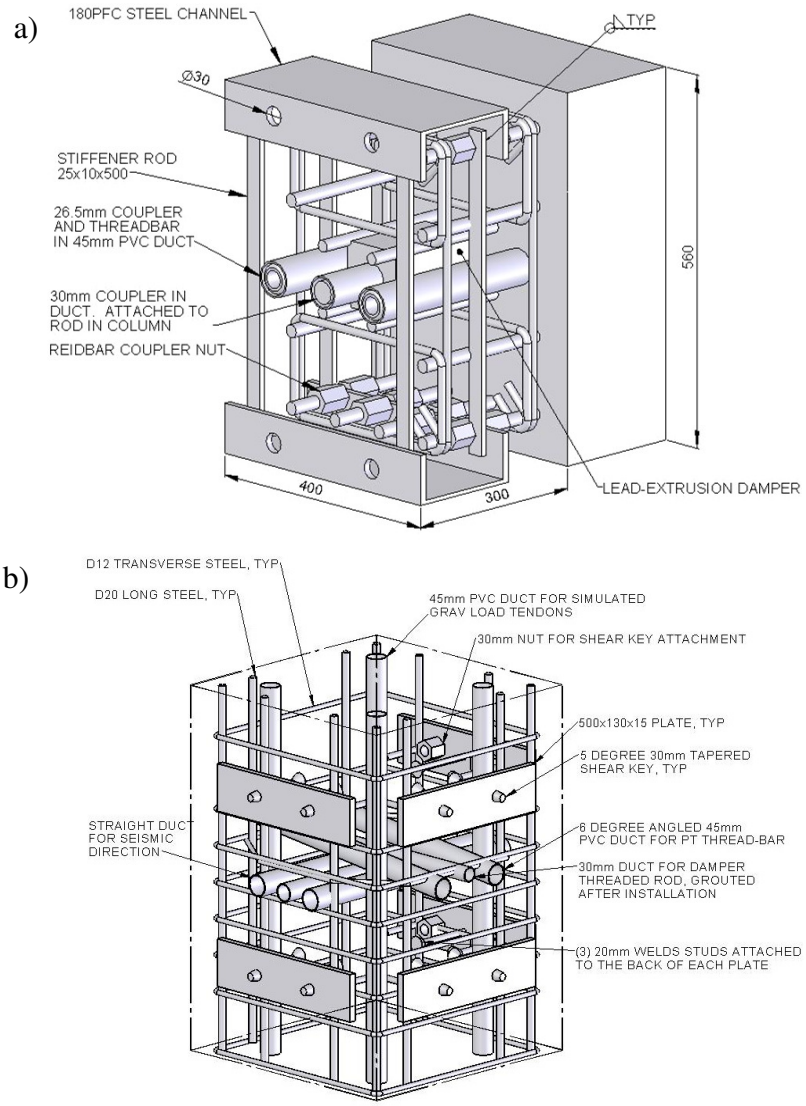

Figure 5.2: Joint region detailing – a) Closure pour region at beam end zone, and b) Column detailing at the joint region (Solberg 2007)

Specific attention was given to the assembly order of the connection so that the subassembly could be constructed onsite and the HF2V devices could be anchored in place. Within the closure pour, the HF2V devices were attached to threaded rods in the beam. The damper shaft was coupled to a threaded rod in the column, which was anchored against a steel washer in a recess on the column face. The dampers were prestressed in place by hand tightening the bolts anchoring the damper to the beam. The damper shaft, coupler, and column threaded rod were all encased in a duct and waterproofed from the concrete. Photographs of the beams with the reinforcing steel for the cast-in-situ section exposed are presented in Figure 5.3. The four central threaded rods are provided for location of the HF2V devices. Also presented in Figure 5.3 is a photograph of one of the beams in place before the final closure pour, with the HF2V device connected. More specific details of the assembly procedure and closure pour are provided in Solberg (2007).

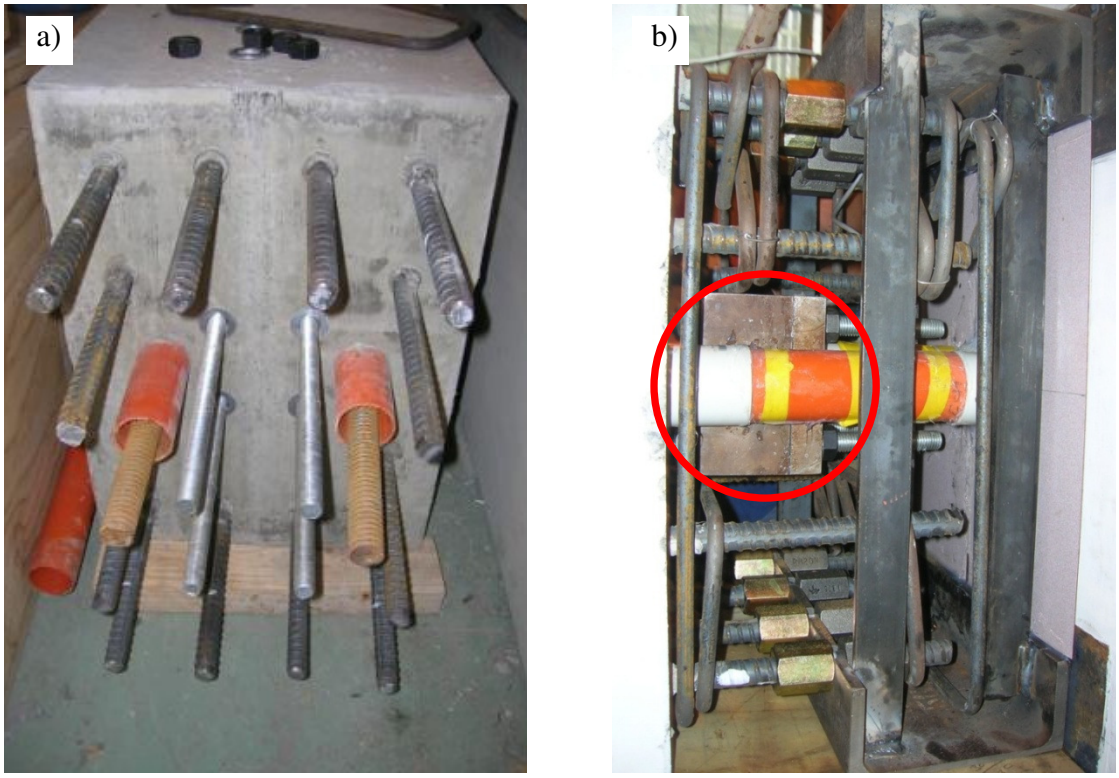

Figure 5.3: Photographs of the cast in-situ joint showing (a) the east beam with the reinforcing, damper location rods, and thread-bars exposed; (b) east beam with the thread-bar enclosed in PVC and HF2V device connected. The HF2V device is circled in red.

5.2.2. The HF2V Devices

The HF2V damper details are shown in Figure 5.4. The devices were designed using the design relationships developed in Chapter 2, to have a quasi-static design force of 250kN. A single HF2V damper is placed within each beam end, as seen in Figure 5.2a. The damper shaft was designed to be coupled to a threaded rod in the column of the same size. Four 18mm (f_y = 300MPa) threaded rods at 100mm centres were cast into the precast beam to anchor the device within the closure pour, via oversize attachment holes on the devices that allow adjustment when coupled to the threaded rod. Figure 5.4a presents the exploded isometric view of a device, while Figure 5.4b presents a photograph of the three devices, and Figure 5.4c shows the hysteresis loops for the three devices subjected to uni-axial testing to validate their force capacity. Note that the devices are all repeatable and very similar in their force capacity generally within ±20-25kN or ±10%, further validating the design relationships of Chapter 2.

The devices designed for these experiments were on a similar scale to those originally constructed as prototypes in Chapter 2, as they have 30mm nominal shaft diameter. The diameter of the chamber for the lead is 70 mm, also placing it within the range constructed for the initial prototypes. The construction of these devices also provides additional data to validate the design relationships of Chapter 2.

To this end, the design models previously presented in Figures 2.9b and 2.9c are presented again in Figure 5.5, but have the additional points added that correspond to the devices constructed for the structural applications in Chapter 4 and 5. These additional points support and further validate the model previously developed. However, the number of data points is still relatively low and the full validation of this model will require more additional points.

Preferably, such additional data points will arise across a broader range of device scales to fully validate the model. For reference, the devices described in Chapter 4 are labeled Device 3, and the devices described within this chapter are labeled Device 4.

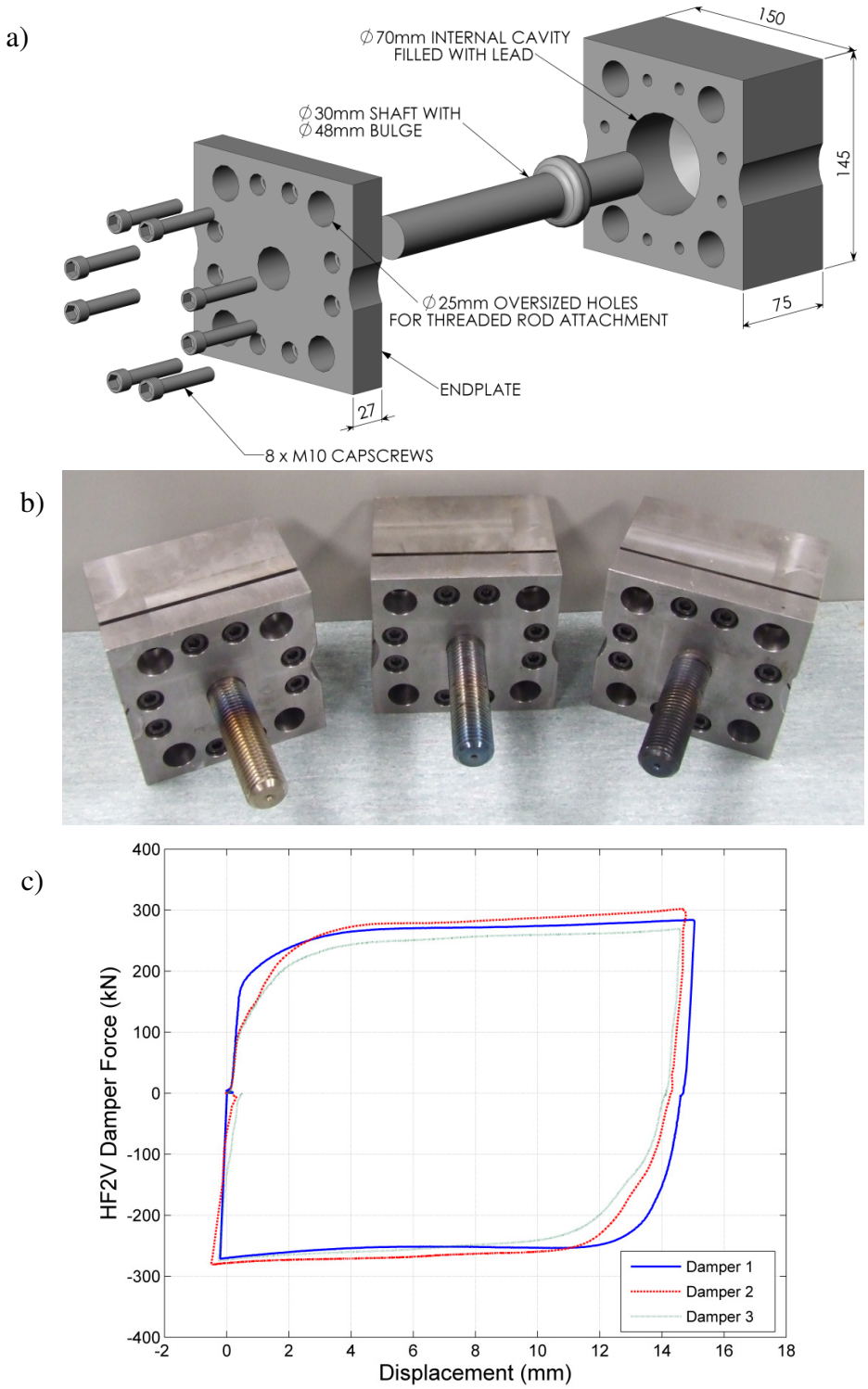

Figure 5.4: HF2V device details a) exploded isometric view, b) photograph of the three dampers, and c) hysteresis loops for the three devices.

a)

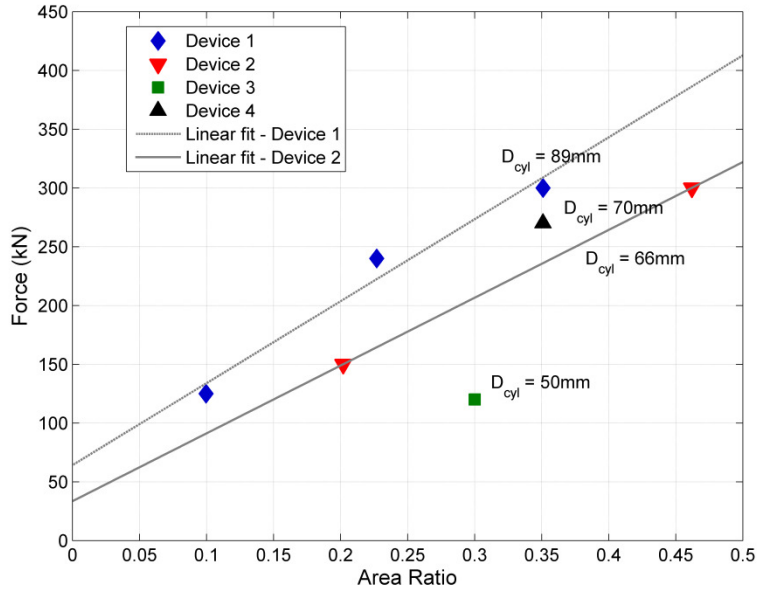

b)

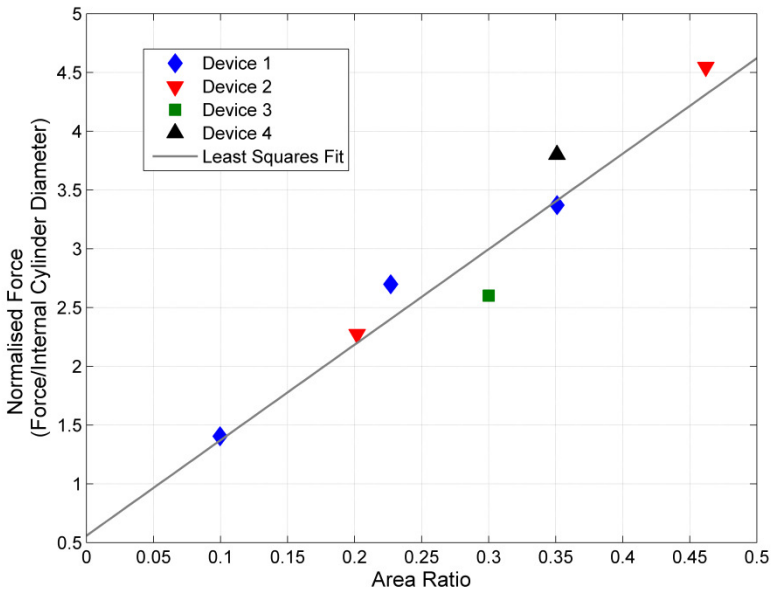

Figure 5.5: a) Force vs Area Ratio for all devices; and b) Normalised Force vs Area Ratio for all devices

An important distinction between the new design and previous designs is the manufacturing process. All previous devices have utilized end-caps and a length of tubing to create the lead filled chamber. These devices were constructed by machining from a solid billet of mild steel. This device manufacturing approach was adopted for several reasons. First, this approach provides a very thick cylinder wall which will provide very good confinement for the lead.

Second, by machining the devices from a solid billet, the manufacturing can be done almost entirely by boring or milling the steel, reducing the amount of turning that is required. This approach may lead to a reduction in machining costs. However, this design concept was a point of much discussion with the company contracted to construct the devices (C&M Technologies, Christchurch, New Zealand), and there was much debate about the lowest cost option of machining. The outcome of the devices constructed for proof-of-concept prototypes in Chapter 2, as well as the devices constructed for structural applications, has shown that the devices can be manufactured in several ways. If large scale production of these devices is warranted, then the design can be easily customized to support whatever machining method is deemed to provide the lowest overall cost.

To ensure the system re-centres, the expected negative moment contribution from the HF2V device in compression should not exceed the expected positive moment contribution from the prestress. Hence, the moment contribution ratio, λ, must be greater than 1.

$$\lambda = \frac{\phi M_{PS,i}}{\Omega_{diss} M_{diss}} > 1 \tag{5-1}$$

where $M_{PS,i}$ = moment contribution from the initial prestress force; M_{diss} = moment contribution from the dissipation devices in compression; Ω_{diss} = overstrength factor of the dissipation devices (taken as 1.5); ϕ = understrength factor for the prestress (taken as 0.85). Rearranging terms gives a ratio of moment contribution from prestress and HF2V devices. Initial post-tensioning of 250kN per thread-bar gives a total of 500 kN at the interface. The dampers were designed for a 250kN yield force, corresponding to λ = 1.23 and 1.06 in the NS direction for positive and negative moment, respectively, and λ = 1.13 in the EW direction.

Figure 5.4c presents experimental force-displacement responses of the HF2V devices in a universal (Avery^{TM}) testing machine. The devices labeled dampers 1, 2 and 3 in Figure 5.4c were installed in the west, east and south joints of the specimen, respectively. The devices provide similar response, with an average yield force of approximately 270kN. Differences in initial stiffness and yield force can likely be attributed to the presence of a small void forming in the lead due to incomplete pre-stressing to remove micro-voids. This behavior relates to the trends seen in Chapter 2, where a small trailing void was sometimes present within the devices even with prestressing.

5.3. Experimental Methods

The experimental test setup is very similar to that presented in Chapter 4. The column was pinned to the floor using a universal joint. Additional pins were on stiff struts near the end of each beam. Actuators A and B were located at the top of the east and south face of the column, respectively. Actuator C was orthogonal to the west face of the gravity beam, in line with the gravity beam support strut, and was used primarily to stabilize the specimen. Rotary potentiometers were installed against the opposite face of each actuator. An additional actuator at mid height of the gravity beam simulates the precast one-way floor panels, with a constant 120kN load spread over a 1.5m timber block.

At one end of each prestress thread-bar anchor, load cells measure the forces in the thread-bars. Four 32 mm high strength thread-bars along the longitudinal column axis were stressed to 500kN for a 2000kN total axial load ($0.1f'_cA_g$), simulating gravity forces. A total of 24 potentiometers measured localized displacements. Within the joint, each coupler connecting the HF2V shaft to the threaded rod in the column was converted to a load cell, consisting of

eight strain gauges compensating for bending and temperature effects. Four strain gauges were placed on the top and bottom web of the beam armouring channels to detect any potential yielding upon gap-opening. It is desirable to have some mechanism to measure the actual HF2V device displacement. However, the internal mounting of the device made it impossible to include any potentiometer onto the device. Therefore, only inferred displacements could be obtained from potentiometers on the external vertical beam faces.

5.3.1. Test Methods

Displacement controlled loading was performed in both the East-West (seismic) and North-South (gravity) directions. As the primary focus of this investigation is to determine damper and member contributions, uni-directional tests in both directions are undertaken to a maximum of 3% drift. All load patterns were fully reversed sine-wave profiles where a positive peak is followed by a negative peak of the same magnitude at each drift increment.

5.4. Experimental Results

An analytical investigation was undertaken by collaborating researchers that generated input records that correspond to earthquake ground motions. That investigation focused on structural validation to prove the absence of any significant member damage during input displacement motions that represent earthquakes of different probability of occurrence (Bradley et al. 2008). The results presented in this chapter focus on the contributions of the dampers in both the seismic and gravity directions, and, in particular, the ability to generate consistent behavior without stiffness or strength degradation.

5.4.1. Quasi-Static Test Results

The response of the subassembly in the seismic and gravity direction are given in Figure 5.6. The specimen was subjected to two fully-reversed displacement cycles, at column drift amplitudes of 0.5, 0.75, 1.5, 2.25, and 3.0 percent. In the EW direction, highly dissipative hysteretic behaviour is apparent. The specimen did not suffer any noticeable stiffness or strength degradation, and stable hysteretic energy dissipation is evident. The maximum recorded residual drift was approximately 0.08%, (2.6% of the maximum drift), and is attributed to friction arising within the prestressing system. Note that two fully-reversed cycles are undertaken at each drift level. The stability and consistency of the subassembly response with HF2V devices is such that it is not immediately apparent from the force-drift response that two cycles are present. The absence of cycle-to-cycle degradation results in the lines being almost perfectly on top of the previous cycle. These results were not the case for the yielding sacrificial steel dissipaters used in a closely similar connection, as shown in Chapter 4.

The East-West direction shows symmetric response due to the centrally located tendons and dampers. The North-South direction shows notable asymmetry in both force levels and enclosed area (energy dissipation) due to both the tendons and dampers being located eccentrically with regard to the beam vertical centerline. These results are thus as expected.

In the NS direction, the results also exhibit relatively stable energy dissipation. The maximum residual drift was 0.12%, (4% of the maximum 3% drift). This value is slightly larger than the EW direction, and is attributed to the increase in prestress friction from the draped tendon profile. Differential friction forces due to reversed cyclic loading contribute to this effect.

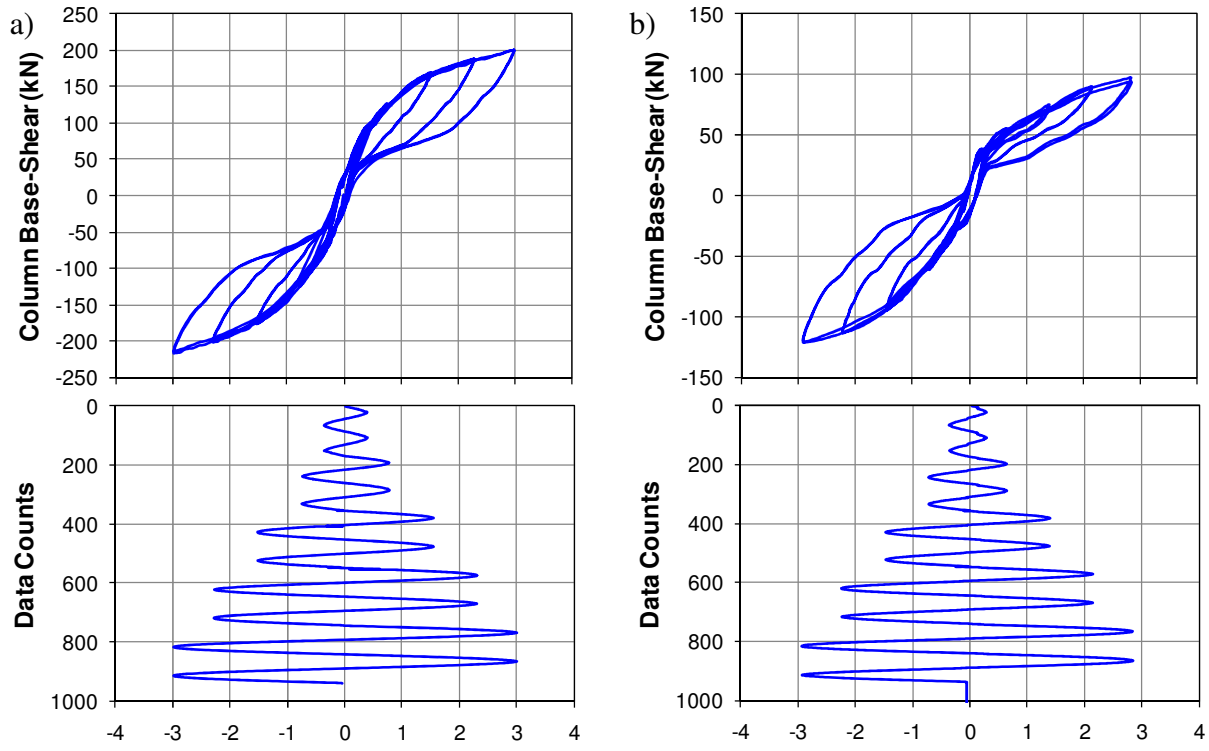

Figure 5.6: Uni-directional experimental testing to 3 percent drift - force-displacement response for: (a) EW seismic direction and (b) NS gravity direction.

These frictional effects can be clearly seen in Figure 5.7a, which shows the change in prestress force for a given column displacement. It is evident that friction between the duct and prestress thread-bars leads to some energy dissipation not considered in the original design. This effect is minimized in the EW direction, where the straight ducts result in less tendon-duct friction. The effects of friction for straight and bent tendon profiles is discussed in more detail in Chapter 10.

Figure 5.7b shows the 'in-service' response of the HF2V damper in the east beam. The apparent in-service stiffness of the damper was reduced compared to the damper tests alone. However, it is very important to note that the displacement in Figure 5.7b is not directly measured, but rather an inferred displacement measured across the joint at the beam mid height by a potentiometer attached to the external column face. It therefore records the mid-

height gap-opening displacement and includes all sources of flexibility from axial stretching of the connecting elements to take-up in the threaded coupler nuts. Due to the embedded device design, direct in-service device displacements were unavailable.

The additional sources of flexibility and slack reduced the contribution of the damper to the overall hysteretic performance on smaller cycles. For example, the HF2V device bulge should start to move at approximately 1 mm of elongation, but was not observed until approximately 2.5mm of inferred displacement. The revised stiffness of the HF2V devices considering the added freedom in the connecting elements is approximately 80kN/mm and approximately 50kN/mm for the gravity and EW joints, respectively. Further improved detailing of device connections would reduce this behaviour. It is reasonable to conclude that although this flexibility can be reduced, it will always be present to some extent and thus have some affect overall performance. This flexibility aspect is discussed in Chapters 9 and 10 where flexibility is modelled with the device response to enable better design and prediction of overall system behavior.

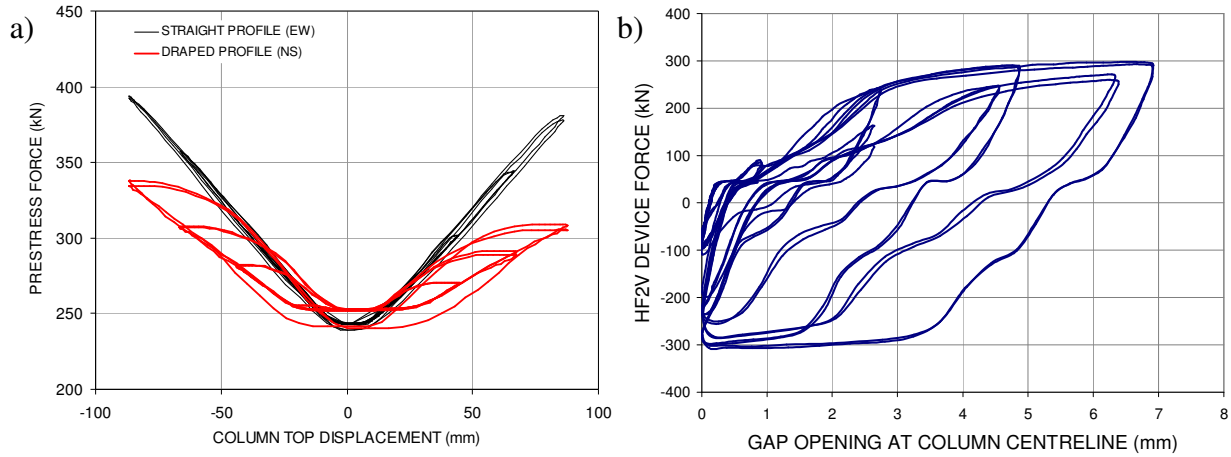

Figure 5.7: Response of (a) the prestress and (b) the 'in-service' performance of the HF2V dampers in the east beam.

Observed damage to the specimen was minimal. Flexural cracks were detected in the beams, spaced at approximately 250 mm, but closed after testing. No flexural cracks were observed in the column. Up to 2% drift, virtually no cracking was observed in the joint region. Some small cracks, approximately 50 mm in length, were observed in the beam corners from the end of the armoring channel's flange. They formed when this region was in compression from connection opening. Beyond 2% drift, some additional cracks were observed, but were minor. No cracks were observed around the armouring in the column, nor were any diagonal shear cracks observed across the joint. No crushing was observed around the steel armouring the column. Upon the completion of testing, there was a prestress loss of 4% per thread-bar in the EW and NS direction.

Figure 5.8 shows the compression force in two of the dampers over time, recorded after QS testing to 3% drift. In the first 8 hours, the initial 200 kN compression force dropped to approximately 100 kN. After 40 hours, it reduced to ~85kN, following the logarithmic decay in Figure 5.8. This decay in damper force with time is one important aspect of the HF2V devices in comparison to any other current dissipator of similar force capacity and size. Note that if yielding steel fuse-bars were used, the residual force following testing will remain and will not creep out following the response cycles.

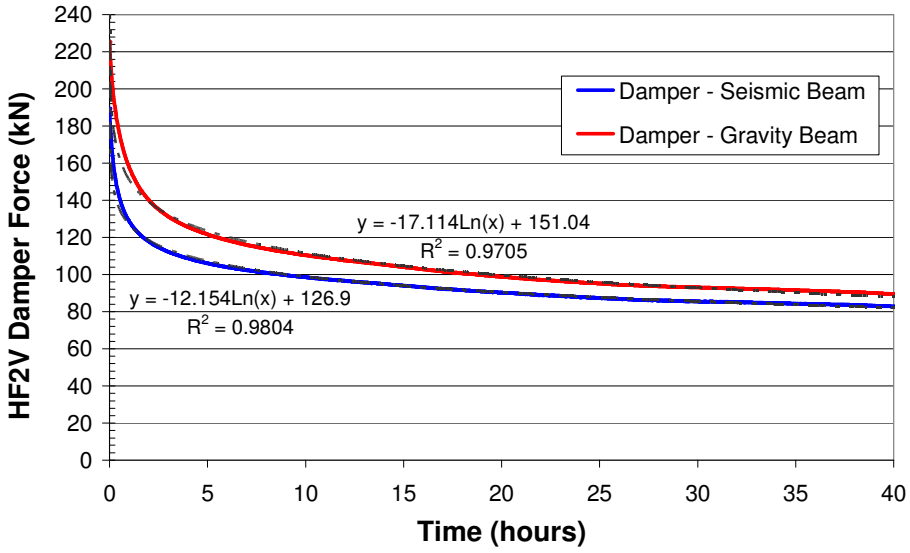

Figure 5.8: Damper force decay over time. Results are plotted for the east and gravity beam damper. The data is fitted to a logarithmic function.

5.5. Discussion

Overall, the specimen performed as expected, exhibiting very stable hysteresis loops with no stiffness or strength degradation and negligible residual drift. This behavior is unique to connections that have a form of repeatable, damage-free energy dissipation as enabled here by the HF2V devices. Minor cracks were observed in the joint region of the beam, ranging in length from 25 to 150 mm. These cracks were confined primarily to the armoured end regions and tended to close after testing. No damage (cracking or crushing) was observed in the column. This was likely attributed to the average axial stress (~0.1f'_c) in the column that suppressed cracking.

A particular focus of this research was an examination of the efficacy of the internal HF2V dampers. Results show that the HF2V dampers successfully achieved their design objectives. The HF2V dampers provided stable energy dissipation, and were shown to effectively 'reset' after testing, as the residual force in the devices decayed logarithmically. This effect is very

desirable, particularly considering that the devices would not have to be serviced or replaced following an earthquake.

Due to the very small connection opening (~5-10 mm), the effectiveness of the HF2V damper is very sensitive to its stiffness and connection to the structural system. To limit stiffness losses from connecting elements the HF2V dampers were tightened against the connecting rods and the threaded rods grouted in the column. However, some minor slack in the connecting elements led to a reduction in stiffness of approximately 60 percent. This result indicates that flexibility of the connecting elements is a key consideration for both design and analysis.

The experimental investigation presented within this chapter considers only the behavior of the structural connection and damping elements. In practice, floor slab effects must also be considered. The fact that this experimental subassembly represents a dilating frame design is an important consideration, as it can lead to damage to the floor slab. Investigation of these effects is outside the scope of this project, but is the focus of ongoing research by other researchers.

Another important consideration is the rate of loading of the subassembly presented in this chapter and in Chapter 4. The testing undertaken was of a quasi-static nature, due to the limitations in the test equipment and control system. While higher speed tests with irregular loading regimes, representative of true earthquake displacement profiles, would be desirable, they could not be done due to the equipment limitations. Irregular loading patterns derived from earthquake simulations, with small reversals in the displacement input, were investigated in the Solberg (2007), but were again only done at quasi-static velocities. Experimental testing at higher velocities is discussed further in the Future Work section.

5.6. Conclusions

The following conclusions can be drawn from this study:

1. The jointed precast concrete specimen with internal HF2V dampers in the beam-end regions satisfied the performance objectives. The specimen remained essentially damage-free, fulfilling the Damage Avoidance Design objective, after being subjected to a range of displacement profiles.

2. The HF2V dampers mounted internally at each beam end provide reliable energy dissipation on every test cycle with basically no stiffness or strength degradation. Residual device compression forces were shown to logarithmically decay through creep towards zero force over time. The devices do not need to be serviced or replaced following an earthquake.

3. The detailing strategy provided an excellent level of protection from damage, while retaining a degree of simplicity and constructability. Throughout quasi-static testing the specimen suffered negligible damage; only some small cracks were observed near the steel armouring and these generally closed after testing.

It should be noted that these conclusion points relate to the structural connection only, and do not take into consideration the important influence of floor slab effects. Testing at higher input velocities would be a desirable addition to this investigation, but was limited due to the test equipment.

Chapter 6: Parametric Study Of Prestress And Damper Contributions To Jointed Precast Concrete Connection Behaviour

A parametric experimental study is performed on the structural subassembly presented in Chapter 5. Multiple displacement input histories or patterns are applied. The goal is to investigate the contribution of the dampers to overall joint hysteresis and stability of the joint hysteretic performance. In particular, the tests are performed both with and without the dampers connected, as well as over a range of different post-tensioning forces. Hence, this study seeks to delineate the specific effects of the different structural elements.

6.1. Introduction

Chapter 5 presents results from basic testing of an experimental subassembly of a jointed precast connection with internally mounted HF2V devices. This initial 80% full-scale experimental study showed that the DAD connection utilized performs in a reliable manner. In particular there is no cycle-to-cycle degradation, and the system exhibits stable energy dissipation, even across repeated large response cycles, as well as subsequent smaller cycles. The study was undertaken partly in conjunction with a fellow postgraduate (Solberg 2007) who performed unrelated tests that investigated the behavior of the specific reinforced concrete structural members, and in particular their resistance to cracking and damage.

After all of this initial testing in Chapter 5 was undertaken, it was of interest to perform a set of additional experiments to investigate and define the specific relative contributions that arise individually from the HF2V devices and the post-tensioned prestress force. These experiments were not intended to be a test of the structure, but rather a parametric study to investigate and delineate the relative contributions to the joint hysteretic response of these

two primary components in the structural mechanics. In Chapter 4, the corner joint configuration was tested with both HF2V devices as a means of increasing the damping force relative to the amount of post-tensioned prestress. In this case, the internal location of the HF2V devices restricted any changes to the damping system. Therefore, to perform this investigation, the initial post-tensioning force was successively reduced to obtain the joint hysteresis under these differing conditions. The subassembly was thus tested with total initial prestress forces of 500, 400, 300, and 200kN.

This parametric study was only undertaken in the East-West seismic direction to limit the total number of tests to 12, as each test took 2-3 hours. More specifically, the subassembly was subjected to fully reversed quasi-static, uni-directional tests at increasing drift amplitudes up to 4% (1, 2, 3, and 4%). For one representative experiment, the subassembly was tested using input displacement profiles with both increasing and decreasing drift amplitudes to investigate the effects of large initial cycles.

Finally, once the whole range of tests was performed with the dampers in place, the connection was opened, and the connecting rods to the dampers were cut. The subassembly was then re-tested at all four different levels of initial post-tensioning. The tests were used to characterize the prestressed connection behavior alone, without the added damper contributions.

6.2. Test Results and Discussion

The post-tensioning system initially provided a total force to the joint of 500 kN. The experimental results for the prototype specimen at this prestress level for input cycles of 1, 2, 3, and 4% drift are presented in Figure 6.1a. Following the application of each loading

protocol, the prestress level was reduced to give total prestress forces of 400, 300, and 200kN. The results for each of these tests at different prestress levels are presented in Figure 6.1b-d. Results are also presented for comparative purposes for the subassembly without the supplemental damping system in Figure 6.1e-h, respectively. Note that all of Figures 6.1 are shown on the same scale for clarity and comparison.

The reduction in initial force in the post-tensioning system was implemented to investigate the contribution of elastic member deflection to the overall hysteresis. This procedure also provides a means of experimentally investigating the reserve capacity on the connection's ability to statically re-centre after an input. By reducing the level of prestress for a set level of added damping, the reserve capacity of re-centering is reduced. It is evident across the results presented in Figures 6.1a-b that only a minimal reduction in column base-shear force level is seen due to the 100kN reduction in total initial prestress force.

It can be seen in Figures 6.1e-h that the overall joint hysteresis without the supplemental damping system exhibits extremely limited hysteretic energy dissipation. Previous research into jointed pre-cast concrete connections using bent tendon profiles, as presented in Chapter 4, show much larger inherent hysteretic energy dissipation. This difference is due to the friction of the bent tendons within the ducts for these latter systems, as in Chapter 4. The straight tendon profile of the prototype specimen tested in Chapter 5 and in this chapter results in much lower friction of the tendons. Hence there is much lower inherent damping provided by hysteretic energy absorption for this particular design approach. Therefore, joints of this type are particularly suitable choices for using supplemental damping systems to provide a means of absorbing energy.

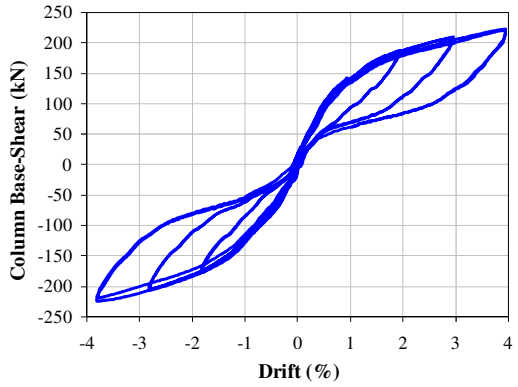

a) 500kN total prestress, with dampers

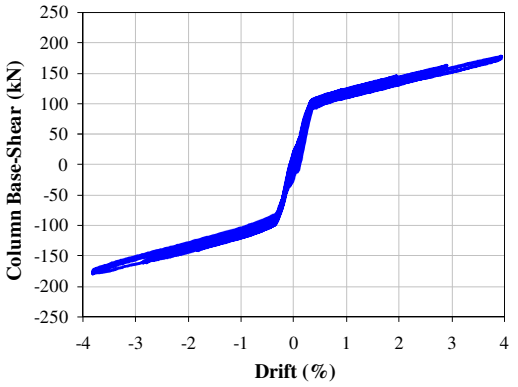

e) 500kN total prestress, without dampers

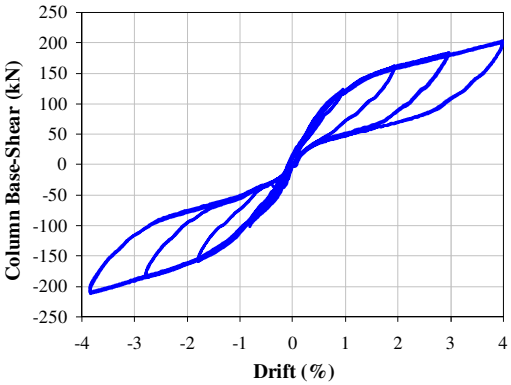

b) 400kN total prestress, with dampers

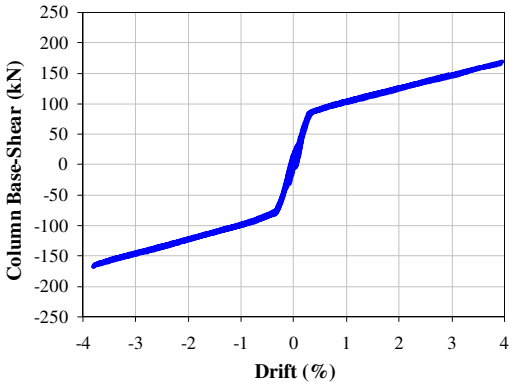

f) 400kN total prestress, without dampers

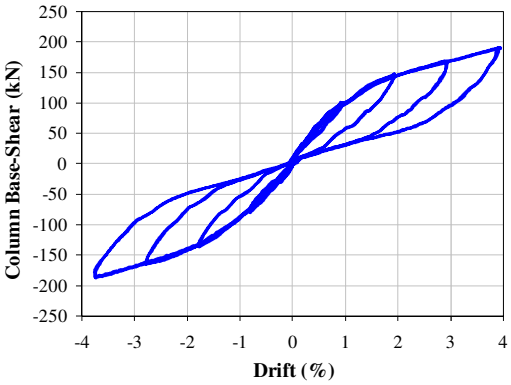

c) 300kN total prestress, with dampers

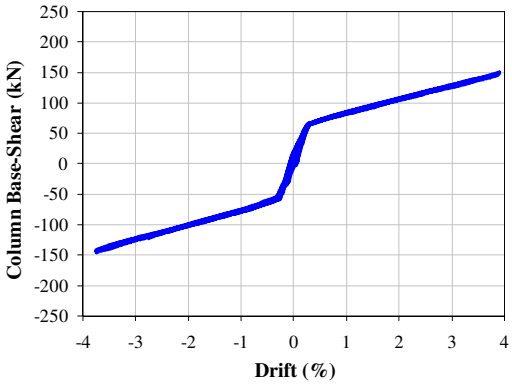

g) 300kN total prestress, without dampers

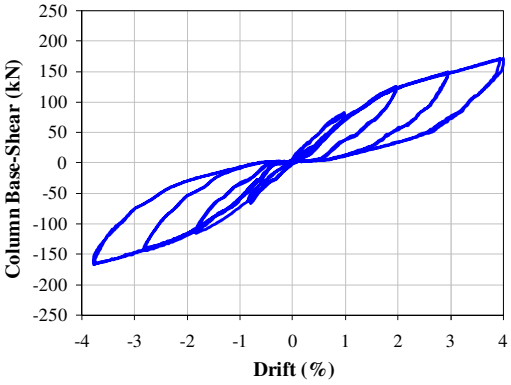

d) 200kN total prestress, with dampers

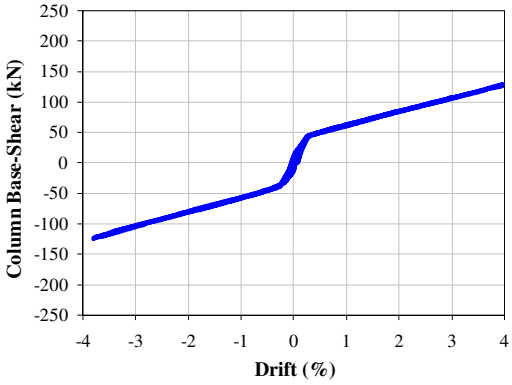

h) 200kN total prestress, without dampers

Figure 6.1: Experimental results matrix at different levels of prestress, with (a-d) and without (e-h) HF2V dampers

It is of interest to experimentally determine the extent of prestress force reduction before the ability of the joint to statically re-centre is lost. The prestress force was successively reduced until the joint reached the static re-centering limit, at a total post-tensioning force of 200kN. The experimental results for uni-directional displacement tests out to 4% drift and with a total prestress force of 200kN are presented in Figures 6.1d and 6.1h. At this lower (200kN) level of post-tensioned prestress and for column drifts larger than 3%, re-centering was only beginning to be lost, as seen by the non-zero displacement for the 3% drift cycle at zero force. Note that re-centering was only lost when the supplemental dampers were connected and not in the corresponding Figure 6.1h. It is also important to note that a total prestress force of 200kN represents a 60% reduction in initial prestress, which is practically unlikely.

The post-tensioned tendons did not yield until well beyond 5% drift and are unlikely to ever experience this level of displacement given design criteria specifying 2% peak drift for a maximum credible event as a median response level. Therefore, this combination of results highlights the ability for designers to incorporate even larger damping forces into such a connection for a given level of prestress. Alternatively, a designer may choose to reduce the level of initial prestress to reduce the total force being transmitted through the joint and structural elements. Overall, it is evident that there is significant flexibility in the design and that it is thus robust to different post-tensioning forces with the HF2V devices.

Figure 6.2 presents an overlay of the experimental results with and without the HF2V devices at 500kN total initial prestress. These results are previously presented separately in Figures 6.1a and 6.1e. It is evident in Figure 6.2 that the response of the subassembly is different only by the addition of the HF2V device forces. The response with the HF2V devices is centered on the response of the connection without added damping. One observation to note is that the response with the HF2V devices has a slight undercut at the

gap-opening point, at around ±0.5% drift. This observation is attributed to the residual compression force in the device which is present due to connection element flexibility. This compression force initially counteracts the post-tensioning forces, until the HF2V device goes into compression, resulting in the undercut seen in Figure 6.2.

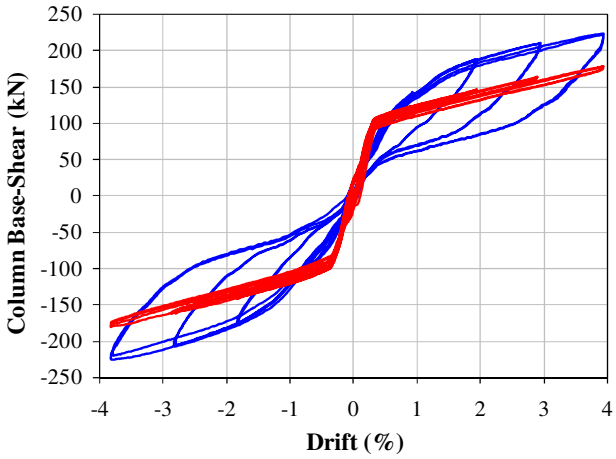

Figure 6.2: Comparison of experimental results at 500kN total prestress, with and without dampers

A particular feature of the DAD connections with HF2V devices is the ability for repeated cycles to operate without stiffness of strength degradation. Figure 6.3 presents reversed sinusoidal loading at the 400kN total prestress level for both increasing and decreasing drift amplitudes. Figure 6.3a presents the same hysteretic results previously presented in Figure 6.1b, along with the associated displacement history. Figure 6.3b presents results for the same joint and same level of total initial prestress force (400kN), put through reversed displacement loading, whereby the large amplitude cycles occur first. It is evident in Figure 6.3 that the overall hysteretic performance was almost identical for both increasing and decreasing displacement input loading regimes, with almost no perceivable difference in the two results. This result clearly demonstrates that DAD connections with HF2V devices can undergo repeated large drift cycles without stiffness or strength degradation or loss of the significant added energy dissipation. Moreover, their performance is thus load-path independent, which is not true for any comparable sacrificial approach.

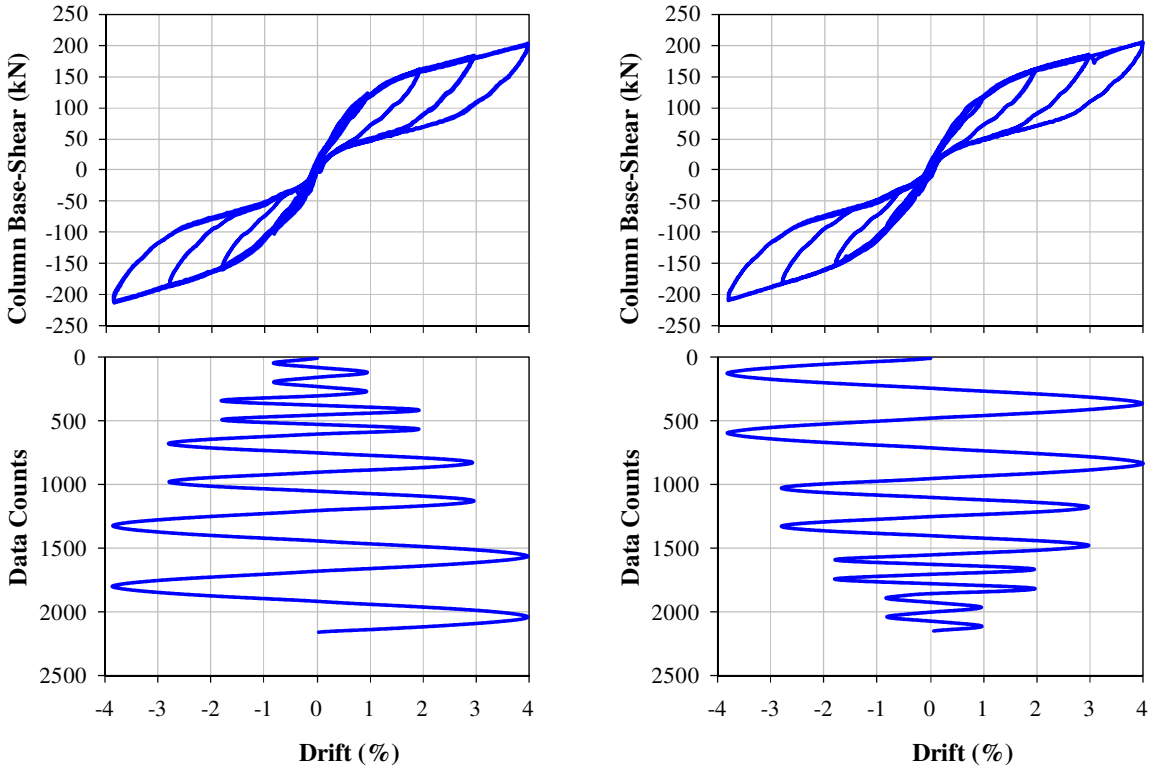

a) increasing drift amplitude *b) decreasing drift amplitude*

Figure 6.3: Comparison of the experimental response with dampers using increasing and decreasing drift amplitudes at 400kN total prestress

The ability to parametrically study a connection in this way is unique to the Damage Avoidance Design principles used in designing and creating this (type of) connection. In particular, the steel armouring at the rocking interface and damage-free energy dissipation method using HF2V devices enables this testing regime without the need for any intermediate repair or other changes. In most other experimental test specimens, especially monolithic connections, stiffness and strength degradation prevent such a direct investigation and comparison. If multiple experimental specimens are constructed, then variations in material properties can, and likely will, affect the results, limiting the accuracy of any comparisons drawn. The use of armoured DAD connections and repeatable, damage-free HF2V dissipators allows repeated tests to be performed on the same experimental specimen, eliminating these additional uncertainties. These results in total also add a significant level of confidence for full scale implementation.

6.3. Conclusions

Reversed cyclic load test results for the full-scale experimental post-tensioned concrete connection with internally mounted HF2V devices were presented. The ability to parametrically study joint behaviour is a useful technique that is unique to this type of armoured DAD connection with damage-free energy dissipation. Based on the tests conducted, the following two main conclusions are drawn:

1. The uni-directional quasi-static testing of the subassembly has shown significant energy dissipation is provided by the supplemental damping system. Disconnection of the HF2V devices resulted in overall joint hysteretic performance with negligible inherent damping. This phenomenon can be attributed to the straight tendon profile that leads to very low internal friction and consequently essentially no hysteretic energy absorption.
2. Experimental results have shown that reductions in initial prestress force level of up to 60% can be permitted without loss of overall static re-centring ability. This aspect enables designers to either increase the amount of added damping that is provided to the joint from the HF2V device, or to reduce the initial prestress level to reduce the forces transmitted through the structural elements.

Chapter 7: Damage Avoidance Steel Connections Utilizing HF2V Devices

The results presented in Chapters 4-6 provide proof-of-concept validation of the use of HF2V devices to provide stable and consistent energy dissipation for jointed precast concrete connections. Overall, the results show stable hysteresis with significant energy dissipation in a controlled and damage-free manner, without the need for any maintenance or repair following an earthquake. Although these results are a good validation of the concept, it would be very useful to extend the investigation to the equally or far more common steel connections. In doing so, the breadth of possible applications is vastly extended to both concrete and steel connections, increasing the likelihood of uptake.

Similarly to concrete structures, occupant safety and use of steel frame buildings following major earthquakes is often limited by damage to the structural frame system. Most of this damage is restricted to the plastic hinge zones at beam ends or the panel zone within steel beam-column joints. As evidenced by the extensive damage to steel structures following the 1994 Northridge earthquake, repair costs and downtime can be substantial to owners and users of such structures, creating a significant, long-term social and economic impact.

Existing welded steel moment frames are designed to tolerate substantial yielding and plastic rotation under earthquake loads. This sacrificial design approach can lead to permanent, and often irreparable, damage when interstory drifts exceed the 2% design level. The experimental seismic performance of a 50% full-scale damage avoidance designed structural steel beam-column connection is thus presented. The DAD steel connection design in unique and offers a means of easily converting a typical steel connection to a damage-free highly dissipative connection using HF2V devices.

7.1. Introduction

Presently, steel connections are designed using sacrificial yielding at beam ends (plastic hinge formation) to dissipate dynamic response energy (Standards New Zealand. 1997). Plastic hinges form at the ends of beams, causing permanent damage and the possibility of failure under extreme interstory drifts due to flange buckling or weld fracture. The associated damage can be difficult, time consuming and expensive to repair. It is thus desirable to have damage-free connections, eliminating expensive repairs and enabling businesses to continue without causing further financial loss to the owner or tenants.

Previous research has also investigated the concept of damage-free steel structures. The inclusion of post-tensioned steel tendons provides self-centering ability to the joint (Christopoulos et al. 2002; Pekcan et al. 2000; Ricles et al. 2001), with energy dissipation typically provided by either friction, viscous, or yielding steel devices (Christopoulos et al. 2008; Garlock et al. 2005). The systems that utilise post-tensioned tendons have the advantage of joint self-centering. However, these systems also have the limitation that they are dilating frame systems, which must be accommodated by gap-opening or tearing of the flooring system during earthquake response cycles, as discussed in Garlock et al. (2007).

This chapter presents the results of an experimental investigation on the seismic performance of a new type of DAD structural steel beam-column connection designs that utilize HF2V devices. Instead of conventional welding, a bolted top angle and a HF2V device form the moment connection, giving an overall connection similar to that previously presented schematically in Figure 2.2b. Two different experimental set-ups are investigated in this chapter. The devices are either mounted for maximum efficiency below the bottom flange of the beam adjacent to the column face, or connected to the beam web just above the bottom

flange so they are concealed in a building's floor or roof space. Results are reported and discussed for repeated, reversed cyclic tests up to 4% drift amplitudes, which significantly exceed typical design and damage limits. Thus, damage-free behavior to 4% drift or more would also enable a far wider range of structural steel designs.

To summarize, the purpose of the specific research in this chapter is to investigate the viability of using HF2V devices in a typical rigid structural steel beam-to-column connection designs, as part of implementing DAD principles into structural steel frame systems. This approach has the advantage that plastic hinging and thus damage can be avoided during seismic response, in stark contrast to current structural steel design practice. Present codes generally specify rigid welded connections that are expected to sustain considerable sacrificial damage dissipating energy in earthquakes (Standards New Zealand. 1997). Such damage is likely to be irreparable because beam flanges can become buckled, fatigued or fractured leading to expensive repairs and/or structural loss.

Finally, working from a typical rigid steel connection design means that the research presented here is equally applicable to retrofitting existing steel structures. This point is critical given the high prevalence of existing structures to new structures over a realistic 10-20 year period. This approach is thus potentially valid over a far wider range of structures and systems compared to the all-new DAD connections in Chapters 4-6.

7.2. Concept Development

The loading conditions and the implementation of the HF2V device into a steel beam column joint for the experimental tests imitate that of a typical steel structure. The basis for the experimental setup is provided in Figure 7.1. Based on typical steel building dimensions (Figure 7.1a) an approximate 50% scale physical model (Figure 7.1b) was developed.

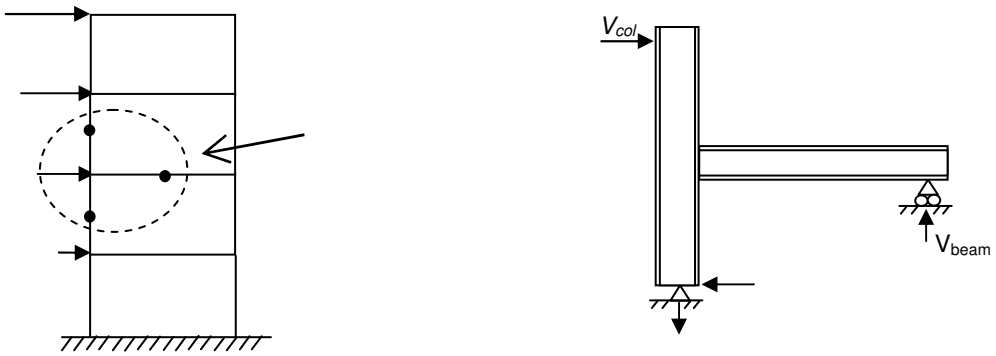

a) Steel moment frame showing location of experimental subassembly

b) Experimental subassembly

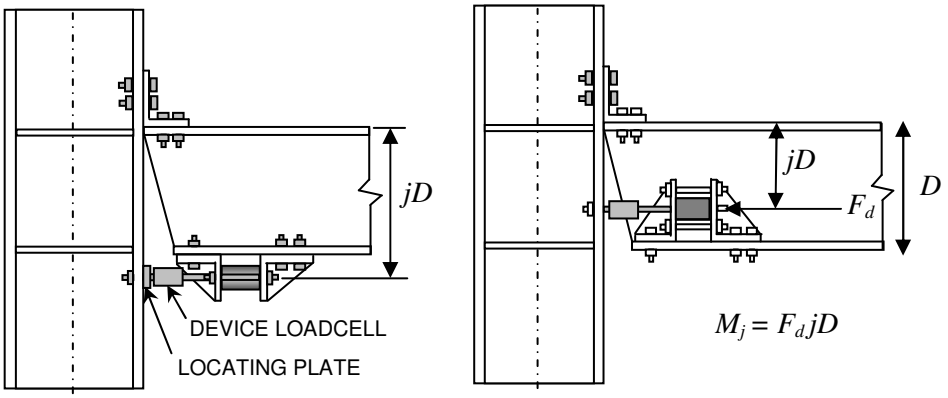

c) HF2V device mounted below beam (j>1)

d) Concealed mounting of the HF2V device above the bottom beam flange (j<1)

Figure 7.1: Steel moment frames fitted with HF2V devices

Within a moment resisting connection as shown in Figure 7.1, the resistance force provided by the device, F_d, leads to a joint moment defined:

$$M_j = F_d jD \tag{7.1}$$

where F_d = damper force during plastic flow; D = overall depth of the steel girder (beam); and j = proportion of the beam depth between the upper (flange) and lower (device) forces, as drawn schematically in Figures 7.1(c) and 7.1(d). These figures show no redundancy for vertical shear transfer at the connection. To provide this, a shear plate could be provided between the column and the beam web. This plate can be slotted in the horizontal direction so that it can carry vertical shear but not prevent joint rotation.

The compact size of the HF2V devices allows them to fit directly beneath (Figure 7.1c) or concealed within the beam at the beam-column connection (Figure 7.1d). The same 120kN capacity devices are used in this experimental study that were used in the investigation presented in Chapter 4. This re-use of existing and well-tested devices is a further indication of the reliability of the devices and their fundamental design. The HF2V devices have been used in numerous tests to large drift levels in the previous experimental investigation, and yet are still performing correctly and can be used in this subsequent experiment. It should be noted that the dampers were slightly modified for the tests using the device below the bottom flange, as this configuration requires a device stroke longer than that designed for in the concrete connection of Chapter 4. The cylinder of the device was thus lengthened for this test alone, allowing increased travel of the damper shaft, via an enhanced device stroke of 32 mm.

When appropriately implemented into a typical steel beam-column joint, lateral frame drift results in hysteretic energy being dissipated though the HF2V device instead of elasto-plastic deformation of the rigid steel beam-column connection. To activate movement in the device the connection needs to be able to rotate. Thus, a bolted connection, rather than a typical moment resisting welded connection is used to permit the required rotation to take place without inducing damage [via yielding] to the structural beam and column elements. A bolted connection should suffice for the purpose of connecting the beam, column and HF2V parts obviating the need to undertake costly on-site welding. Thus, new construction costs might be reduced and retrofit made simpler, as side benefits of this type of steel DAD design.

It should be noted that the rocking behaviour of the concrete connections in Chapters 4-6 has an important distinction from the rocking behaviour for this steel connection. The concrete connections rock about either the top or bottom edge of the beam. Therefore, either positive or negative joint rotations induce the same direction of motion in the damper. In contrast, the

top-flange mount of the steel connection used in this chapter and the seismic gap present between the beam end and the column face result in positive and negative rotations occurring about the same pinned rocking edge. The rocking edge will always be the top flange, and the device will undergo positive and negative displacements from its initial position. Therefore, even if the device was mounted at the same distance from the rocking edge and the connection subjected to the same drift amplitudes, the device will experience twice the stroke compared to a device in the DAD connections of Chapters 4-6. Figure 7.2 presents the schematic response for two reversed sinusoidal cycles of column drift input. The devices in the concrete connections undergo four cycles in one direction from the initial position. The devices for the steel connection undergo two cycles with twice the amplitude, centered on the initial position. Therefore, the devices for use in the steel connection will require a stroke double that which is needed for the concrete connection.

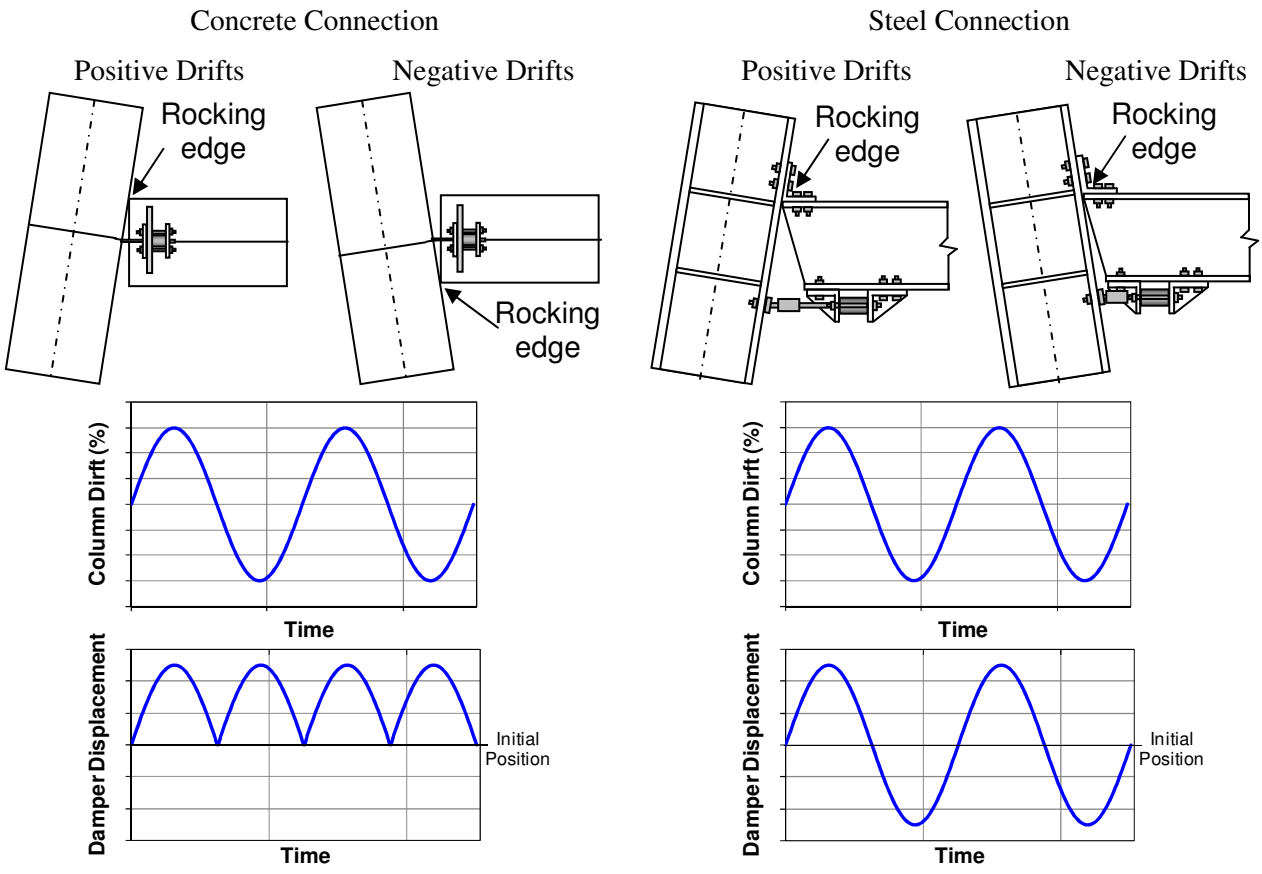

Figure 7.2: Schematic diagram of displacements induced within the damper due to different rocking mechanisms

7.3. Experimental Apparatus and Study

Figure 7.3 presents the experimental setup of the exterior beam-to-column structural steel connection tested in this research. An angle was bolted to the top flange of the 360UB44.7 beam, which in turn was bolted to the 310UC158 column with M20 bolts, as detailed in Figure 7.3(b). Grade 300 hot rolled structural steel was specified for both the beam and column members.

Quasi-static loading was used to test the beam-column joint specimen with the HF2V devices (Figure 7.3a), up to a maximum peak drift of 4%. The theoretical capacity of the lateral load applied to the column to dissipate energy is 28 kN for a single device mounted below the bottom beam flange (Figure 7.3b), and 38 kN for the case where two devices are mounted above the bottom flange (Figure 7.3c). These predictions are based on a simple moment equilibrium based on the quasi-static design force of the HF2V devices and the corresponding lever arms that relate the device force to column base-shear. The devices are intended to provide all energy dissipation, while the top angle essentially acts as a pinned hinge.

An important design feature is the provision of a 30mm movement gap between the column face and bottom beam flange, as shown in Figure 7.3. The beam was cut back at an angle of approximately 5-degrees to prevent the bottom flange from damaging the column under joint-closing up to 4% drift, permitting free-hinged motion in the absence of any resistive devices or elements. Lateral load and displacement of the column was provided by a 100kN capacity hydraulic actuator with a 500mm stroke. The actuator was attached to the top of the column 2.0m above the hinge connection at the base of the column that was in turn connected to the laboratory strong-floor. An end-plate was welded to the base of the column to attach the column to the base hinge.

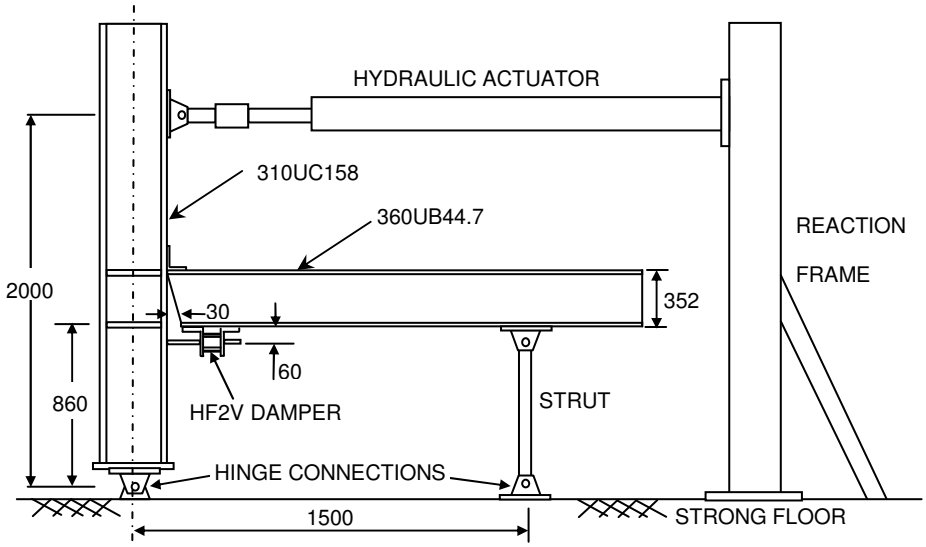

(a) Specimen setup for lateral load tests on strong-floor

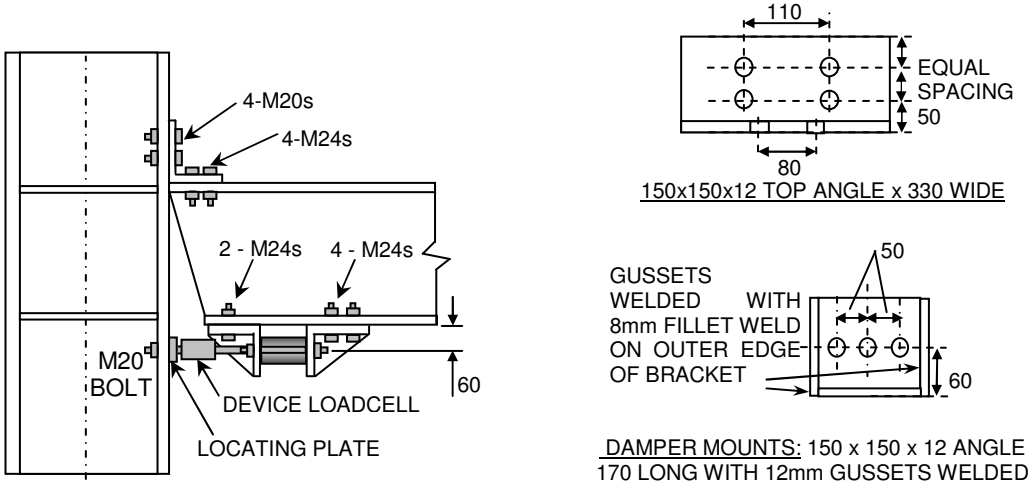

(b) Details of HF2V device mounted below bottom flange of beam (jD=412)

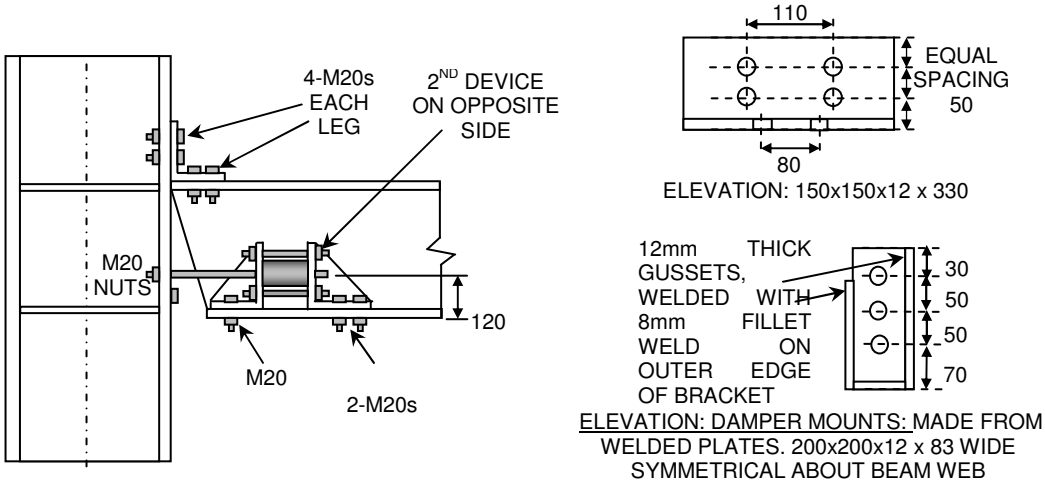

(c) Details of concealed mounting of HF2V fitted on both sides of web (jD=232)

Figure 7.3: Specimen details for experimental study (Dimensions in mm)

Column top displacement was measured with an external string (rotary) potentiometer. Load cells connected to the damper shafts measured the forces in the HF2V devices. A potentiometer was screwed into the end of the shaft to measure the displacement of the shaft in the cylinder. Four potentiometers were placed across the beam-end to column-face region to measure connection rotation and also check for any torsion or out-of-plane effects, as shown in Figure 7.4.

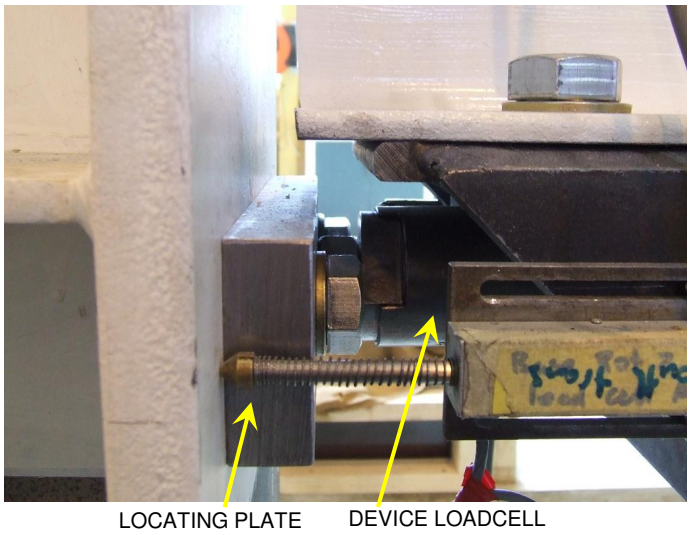

a) Detail of beneath-flange mounted HF2V device

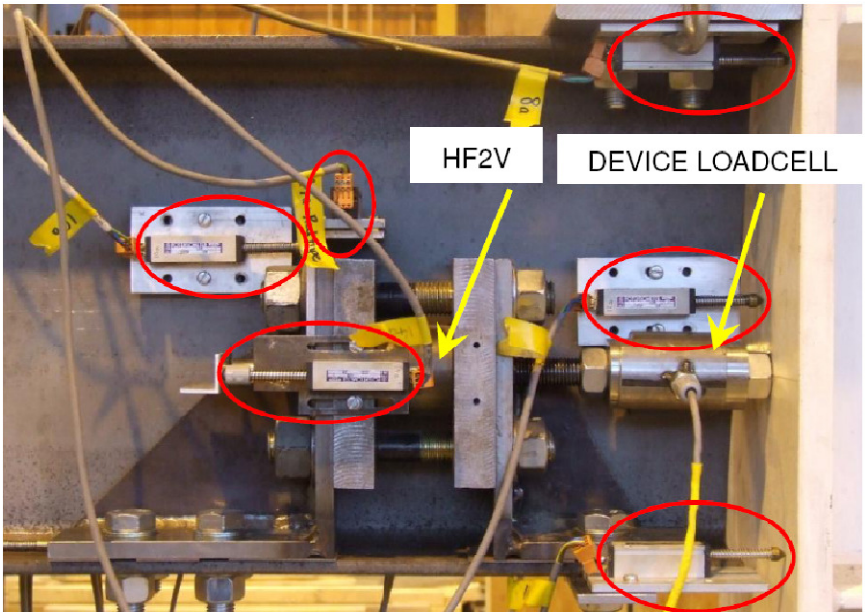

b) Concealed HF2V devices. Shown in circles are linear potentiometers

Figure 7.4: Photographs of the experimental specimens showing the HF2V devices in the joint zone.

Additional linear potentiometers were placed to capture potential losses of stiffness and undesired movement in the subassembly, particularly due to device bracket compliance. Particular attention was given to measuring bracket compliance as it was identified as being a key contributor to the overall response in the experiments undertaken in Chapters 4-6. Figure 7.4 shows the instrumentation used for both configurations. Linear potentiometers measured horizontal and vertical displacement in the HF2V devices mounts, the top angle, and base of the beam flange relative to column face.

7.3.1. HF2V Device Location

Placing the device beneath the bottom flange ($j > 1$ as shown in Figures 7.1c and 7.3b) provides the greatest lever arm between the device and top connection. This arrangement is preferred if the connection cost is to be minimized, as the damper force required for a given resisting moment is minimised. However, in a regular office building or many similar structures, unless this device can be made an architectural feature, such a placement beneath the beam may affect the wall and ceiling placement or simple aesthetics. Placing the device between the beam flanges ($j < 1$ as shown in Figures 7.1d and 7.3c) avoids this issue.

For both arrangements, an important requirement for device performance is a non-slip condition between the damper and the beam flange. Any slip present will reduce the displacements into the HF2V energy dissipation devices and therefore the force provided to the overall joint, reducing the overall dissipation and reducing the efficiency of the dampers. Locating the damper below the bottom flange enables an increased number of bolts to be used by allowing it to be bolted through the flange on either side of the web for one device, rather than bolting to a single side for a device located above the bottom flange. When the

damper was mounted below the beam flange, a total of six Grade 8.8 M24 bolts were used and proof loaded to ensure a non-slip condition under expected serviceability loads (Gorenc et al. 2005), as shown in Figure 7.3(b). In contrast to this case, only half the number of bolts per damper were able to be used for the case when the two dampers were mounted above the flange, as shown in Figure 7.3(c).

Additionally, when two dampers are located above the bottom flange and thus inside the beam and connection, they can be located by bolting directly through the column flange. However, centrally locating one damper below the bottom flange at the beam and column centreline complicates the connection of the damper shaft to the column. The damper shaft coincides with the column web and therefore cannot be bolted directly through the column flange. Therefore, a locating plate was constructed that was drilled and tapped at its midpoint to allow attachment of the device loadcell. This plate was then bolted through the column flange by two M20 bolts, each located at 50 mm from the column centreline, allowing for clearance of the bolt head from the column web and root radius, as shown in Figure 7.4(a).

The damper configuration and mounting detail enabled a non-slip condition using an entirely bolted connection. This outcome is an important economic consideration, as it eliminates the need for any on-site welding, which is a specialized trade that also requires additional skilled inspection. Although the top angle provides a shear connection, this damper configuration also enables a shear connection to be made to the beam web if extra reinforcement is required. This shear connection can be slotted in the horizontal direction, enabling effective shear transfer without preventing joint rotation. Overall, a fully bolted connection is readily designed with many possible variations, creating an economic and potentially feasible construction outcome as well.

7.4. Experimental Results and Discussion

Quasi-static lateral loading was applied to the steel beam-to-column subassemblage at drift amplitudes of 0.25, 0.5, 1, 2, and 3% and four cycles at 4%. Thus, two fully reversed cycles were undertaken at each drift amplitude to demonstrate the ability of the joint to undergo repeated large drifts without the stiffness or strength degradation that is common in all structural reinforced concrete and welded steel connections at similar or smaller drifts. Figure 7.5 presents the resulting experimental lateral load versus drift performance for all cycles.

It should be immediately noted in Figure 7.5 that the results are so consistent over repeated cycles that for large sections of the hysteresis loop it is not immediately apparent that multiple cycles have been performed. In particular, the lines from successive cycles are almost indistinguishable. More importantly, subsequent smaller drift cycles in the second cycle of testing while story drift inputs were decreased shared the same level of dissipation and consistency, which would never occur with sacrificial fuse approaches to this type of DAD connection as seen in Solberg et al. (2008a), Li et al. (2008) and Bradley et al. (2008).

Based on the mechanics of the connections, Figures 7.5(a) and 7.5(b) plot the theoretical lateral strength capacities of 28kN and 36kN, for the cases of one damper below the flange and two dampers above the flange, respectively. Note that because of the mild velocity dependence seen even in relatively slow (0.1 mm/sec or less) quasi-static tests, the observed strength tends to exceed this limit at high drifts when the cyclic testing rate correspondingly increased. This effect is evident in Figures 7.5(c) and 7.5(d), where the measured in-joint damper force is plotted against the “in service” device movement. This slight increase in force for larger drifts is evident and due to a test procedure that moved the column to each drift in a fixed time period for all drift sizes, due to how the load actuator was controlled.

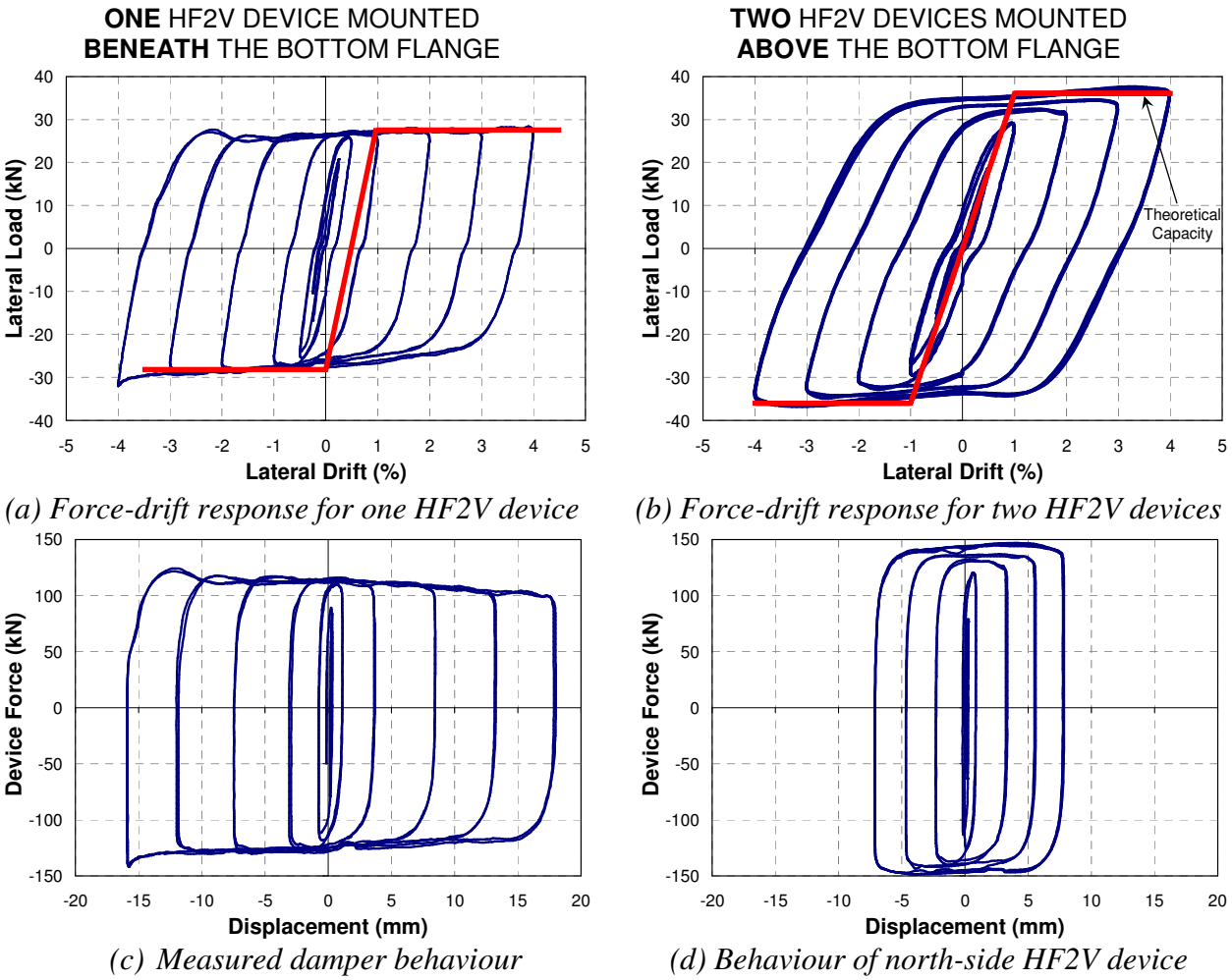

(a) Force-drift response for one HF2V device

(b) Force-drift response for two HF2V devices

(c) Measured damper behaviour

(d) Behaviour of north-side HF2V device

Figure 7.5: Results for the two main experiments - (a,c) and (b,d) are shown for fully reversed loading cycles of 0.25, 0.5, 1.0, 2.0, 3.0 and 4.0% drift. The theoretical capacity is also shown in panel (a) and (b).

7.4.1. Discussion – One Damper Below The Bottom Beam Flange

The results shown in Figure 7.5(a) indicate that the response exhibits some bilinear characteristics. As the overall hysteresis is directly related to the damper performance, it was expected that the in-service hysteretic response of the damper was bilinear, as illustrated in Figure 7.5(c). The reason for this behaviour is not fully clear, although it may be attributable to the inherent bending stresses applied to the shaft as the bottom of the beam moves in an arc about the top flange edge. Such action may induce additional friction and binding where the shaft contacts the endcaps. This phenomenon could be eliminated in future work by the use of

a clevis design at each location point of the damper, eliminating any bending stresses and ensure that any force in the device is purely axial.

When comparing the overall hysteresis of a bottom mounted device to two devices mounted above the bottom flange it is evident that the single configuration has greater initial stiffness, but lower peak force, as shown in Figure 7.5(a) and 7.5(b). These observations can be easily explained by the distance, j, of the dampers from the pivoting top-flange edge. The single damper is mounted below the bottom flange, such that $j = 1.17$, giving a distance from the top flange connection of $jD = 412$ mm, resulting in decreased overall resisting moment being applied to the joint.

Moreover, the theoretical prediction of the yield force for the subassembly is 28kN, which is very close to the average yield force for the device and structural assembly observed in the experimental results, clearly showing the accuracy of the prediction. This accuracy in predicting behavior is a very important aspect for assessing overall structural performance through capacity design methods.

The alternative configuration has two dampers located at $j = 0.66$, giving a distance from the top flange of $jD = 232$ mm below the top flange edge. By considering both the force imparted into the subassembly and the corresponding lever arm provided by the damper eccentricity, jD, then it is evident that the overall joint moment is reduced in that case. Thus, the use of one damper increases the lever arm, but the lever arm is less than doubled so that the overall joint moment is reduced compared to the case using devices within the beam itself.

7.4.2. Discussion – Two Dampers Above The Bottom Beam Flange

An important consideration is that the hysteresis loops shown Figure 7.5(a) and 7.5(b) represent an entirely bolted connection for the single device and a bolted-welded connection for the two devices above the bottom flange. Added local welding was used to prevent slip due to insufficient number of bolts used in the initial design. Initially, the damper mounts were welded to the beam flange and web to provide a non-slip connection between the dampers and the beam. While this additional welding provided improved behaviour, further testing indicated that slip between the top beam flange and angle connection was present. Therefore, the angle connection was subsequently welded to the top beam flange to eliminate slip, and provide improved overall connection behaviour. This outcome is significant, as better overall hysteretic behaviour can be obtained. However, more economical connection detailing could still be obtained provided sufficient allowance is given to enable a fully bolted non-slip condition to be designed for the bolted interfaces.

A larger peak force is easily achieved by incorporating a damper with higher yield force, with experimentally proven devices having been constructed with yield forces up to and exceeding 350kN, as detailed in Chapter 2. Therefore, selection of an upper-bound of device force is dependent upon the strength of the structural system itself, and its ability to maintain a non-slip condition rather than the ability to build large enough devices. Furthermore, the use of larger device forces and larger diameter shafts would see the initial stiffness of the subassembly also increase significantly, providing a stiffer joint while still maintaining a damage-free inelastic response.

For two devices mounted above the bottom flange, the experimental set-up has an experimental yield drift of approximately 1% past which the input into the devices causes them to begin to move. This result is higher than the expected 0.5% elastic drift expected based on column, beam, strut and HF2V device shaft elastic deformation. This increase in the required elastic motion is likely due to the additional flexibility of the damper (angle) mounts and the in-series load cells connected to the HF2V devices.

Instrumentation measured negligible movement vertically or horizontally in the top angle, confirming the rigid, hinged nature assumed. Figure 7.5(b) shows that the stiffness at low force levels in quadrants 2 and 4 is somewhat less than in quadrants 1 and 3. This difference is attributed to the rocking-like flexibility introduced into the system by the HF2V device mounting brackets. This conclusion is supported by the plot in Figure 7.5(d) where the device itself exhibits an almost entirely rigid, perfectly plastic performance. Hence, the difference from the device to the total assembly must be due to elastic compliance in the device connections.

For the case of two dampers mounted above the flange at 0.5% drift amplitude there was little movement (approximately ±2mm) in the device. This small motion resulted in negligible energy dissipation, as seen in Figure 7.5b. As the lateral load increased the bulge began to move more significantly and far more energy was dissipated. Virtually all energy dissipated can be attributed to the device, as there was no yielding or other dissipation from the principal structural elements in the experimental setup.

It should be noted that there was a slightly larger displacement in the device when the beam-column gap opened, compared to when it was closing. Noticeable elongation was observed in

the bolts connecting the damper shaft to the column face when the joint was fully open. This elongation is a contributing factor to this difference, as well as the change in mechanism of the top angle bracket. More specifically, when the gap opens the angle closes, putting it into compression. This motion provides more resistance than when in tension, as plastic hinges can form below the bolt rows and base of the angle (Mander et al. 1994).

The physical gap of 30mm between the column face and bottom beam flange provided adequate space for rotational movement without damaging either element. This approach is realistic as a flush connection would cause undue damage to either element and prevent the device from moving and dissipating energy. The overall design approach is thus one of a hinge connection with a separate HF2V energy dissipation device.

7.4.3. Performance Sensitivity to No-Slip Construction Requirements

This section discusses the rigidity of the connection attachments and their effect on overall performance. The effect of increasing connection rigidity stiffness is presented in Figure 7.6. The initial tests for both configurations used a purely bolted connection. However, once testing commenced on for the case for two dampers located above the bottom flange of the beam, slippage was evident. Due to loss of dissipation from the device mounts slipping, greater restraint was provided to the device mounts. This issue was overcome by progressively welding up the attachment fixtures to inhibit slippage.

From a construction standpoint, the bolted connection is the preferred connection type, as it leads to increased construction speeds and eliminates another specialized on-site trade of welding. Bolted-only connections thus reduce costs and minimize the time for the required inspections and approvals.

Figure 7.6 shows three levels of rigidity for the connection fixtures in the two dampers above the flange case at 3% drift cycles for clarity. The innermost loops in Figure 7.6 show results for the fully bolted connection as designed here. The large amount of measured slip is attributed to the movement of the device mounts and the top angle. The overall hysteresis loops are pinched, and minimal energy is dissipated as the bracket mounts slide. Sliding stopped when the bolts reached the end of their oversized holes at a drift of ~0.5%. Note that all bolt holes were oversized 2mm, as is customary practice (Standards New Zealand. 1997). After this slippage, the stiffness increases in Figure 7.6 as any remaining slip occurs mostly from the top angle. The amount of energy dissipated at this stage was computed to be 1.61kJ.

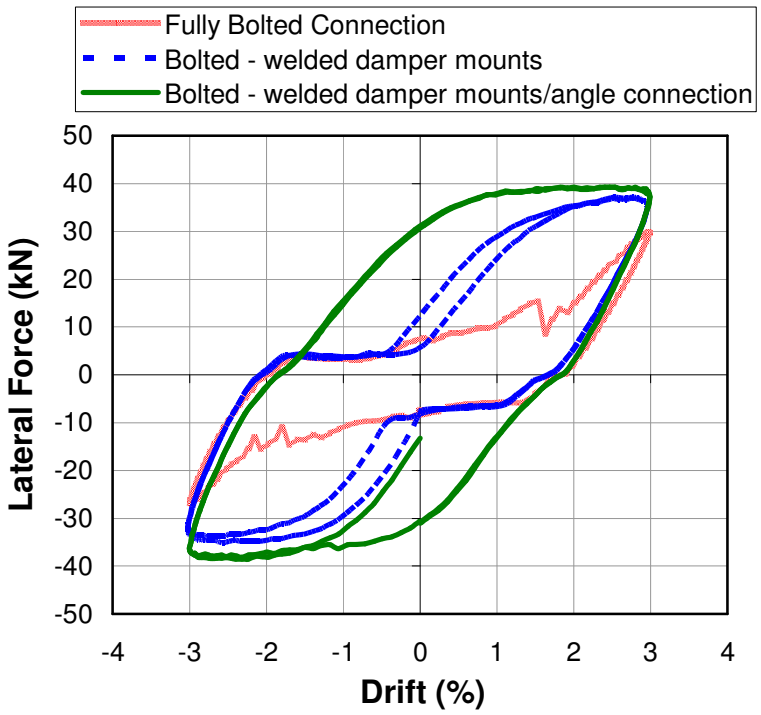

Figure 7.6: Effect of bolted versus no-slip (welded) damper mounts onto bottom beam flange

After the damper mounts were tack welded to the beam (flange and web) this unintended movement was partially prevented and the hysteretic behaviour was improved, as shown by the intermediate dashed (blue) line in Figure 7.6. The energy dissipated was approximately doubled, increasing to 3.36kJ. However, some slip still occurred at low forces following a

change in direction of the applied force seen in the device. This behaviour was mitigated by welding a length of the end of the angle to the top beam flange to provide the required shear strength. The result produced a no-slip rigid angle-to-beam connection capable of dissipating substantially more energy within the HF2V dampers. The energy dissipated for the same 3% peak drift level was then 4.98kJ, which is in excess of three times greater than the energy (1.61kJ) initially dissipated with a fully bolted connection. Note that the outermost loop in Figure 7.6 which includes additional welding, corresponds to results presented in Figure 7.5b.

The non-slip condition is clearly very important for an efficient, energy dissipating connection. The case of two dampers mounted above the bottom beam flange required welding to achieve this non-slip condition. However, this was simply a flaw with this specific design. The concept of achieving a fully-bolted non-slip condition without welding is still feasible (as shown by the case with one damper below the bottom beam flange). The observation of slip within the system was therefore a design flaw, and not a concept flaw.

Pekcan et al, (1999) introduced the concept of an energy absorption efficiency factor, η, defined as the ratio of the area contained within a hysteresis loop, to an elasto-plastic response with the same initial stiffness and strength. Thus, for the 3% drift amplitude shown in Figure 7.6 the energy absorbed by one elasto-perfectly plastic loop is 5.76kJ. Based on this criteria, energy absorption efficiency factors of 30%, 58% and 86% are found for the fully bolted, partially welded and full-welded bracket conditions, respectively. The enclosed area within the hysteresis loop for the fully welded connection and the equivalent elasto-plastic hysteresis loop is presented in Figure 7.7. If all connections through-out a frame structure were similar, then for the 3% drift amplitude this translates into respective equivalent viscous damping factors of 13%, 24% and 36% (Pekcan et al. 1999). Note that all of these equivalent damping factors are: a) higher than or similar to typical steel structures and b) damage-free.

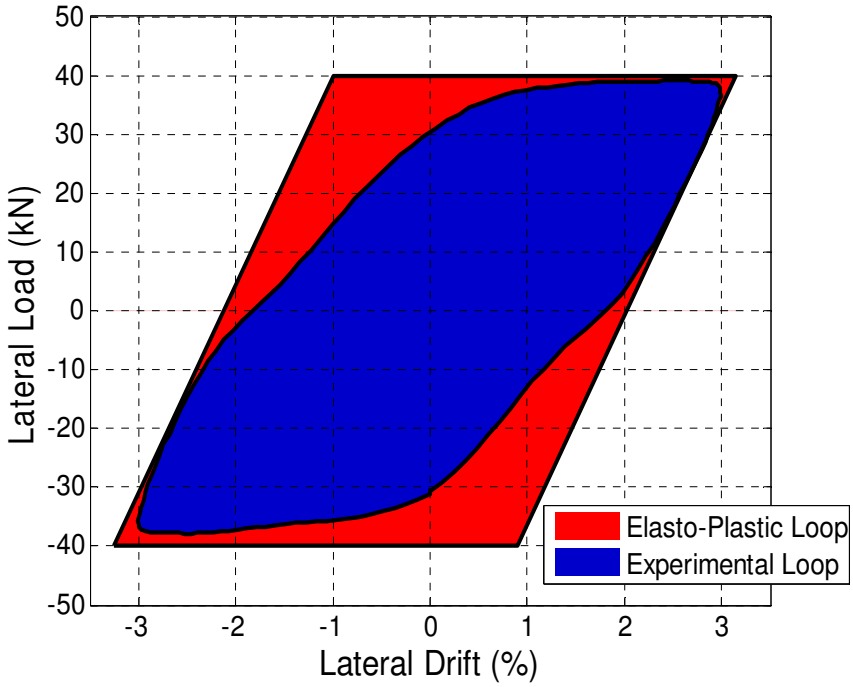

Figure 7.7: Energy absorption indicated by enclosed hysteretic area at 3% drift for the bolted connection with welded damper mounts and angle connection and compared to the equivalent elasto-plastic loop.

According to previous work done by Pekcan et al. (1999) and Shama et al. (2002), the energy efficiency factor, η, for steel structures is 60% (frames) and 75% (steel piles bent in good condition), respectively. Therefore, the fully welded rigid system exceeds a typical steel frame by a factor of 1.33 while the less-optimal partly welded solution (η = 58%) matched the typical sacrificial design (η = 60%). It is thus evident that the use of well detailed HF2V devices incorporated directly into steel beam-to-column joint connections can provide superior energy dissipation than what is available using conventional welding techniques.

These energy efficiency factors are a very simplified indication of how these connections could be incorporated into a performance-based design methodology. The previous research in Chapter 3 looked at the addition of the HF2V devices on a single degree-of-freedom system, looking at the response spectra for suites of ground motion records. From this

spectral investigation average acceleration reduction factors were determined, which can be used in capacity design methods. A more extensive, multi degree-of-freedom analysis will provide more extensive investigation of the influence of this design approach.

The use of two devices mounted above the flange revealed that for this specific design, the achievement of a fully bolted connection is not really feasible. Slip prevention criteria require twice the number of bolts used in the top angle. Providing the extra bolts is not viable due to the size of prefabricated steel angle available. However, a custom design bracket, prefabricated off-site in relatively large numbers required for a large structure would eliminate this issue and enable a purely bolted design.

A top angle bracket bolted into the column and beam flanges was used for the experimental protocol. In practice it would be desirable to have a bottom angle as well to seat the beam during erection (to act as a corbel) before fastening the top angle connection. This bottom angle would exist as a partial non-connected seat, and could form part of the damper mount for the bottom mounted case. This angle may be considered for both construction purposes and as a fail-safe catcher seat in the unlikely event the top angle fails due to low cycle fatigue. The top angle bracket is the only form of damage on the beam-column joint, and is easily replaced by keeping the connection fully bolted, if need be. In seismic resistant structures the sacrificial bracket may be replaced if fatigued, which can be more easily done if an additional angle at the bottom flange of the beam exists to support the floor weight.

7.5. Summary

From the research presented in this chapter the following conclusions are drawn.

1. The sacrificial damage that is expected to occur in conventional welded steel moment frame connections and hinge zones can be avoided by strategically reconfiguring the joint zone to include HF2V devices as the principal energy dissipating elements.
2. At 50% of full-scale, a set of proof-of-concept experiments were undertaken to validate the proposed concept of adding dampers to a top flange-hung bolted connection. This design formed a near-rigid connection dissipating considerable energy at lateral drifts up to 4 percent. Throughout the experiments there was no damage to the main structural beam and columns elements. Repeatable energy dissipation on each cycle was observed with no strength deterioration, regardless of the magnitude of prior cycles. Compared to conventional steel frame connections a far greater dissipative efficiency of 86% (versus 60%) was achieved without sacrificial damage.
3. The research investigated two locations for mounting the dampers: one damper below the bottom flange ($j > 1$); and two concealed dampers mounted above the bottom beam flange ($j < 1$). In both cases it is essential to mount the dampers to ensure a no-slip condition of the mounting fixtures. The more efficient design occurs when $j > 1$, as this minimizes damper force and hence cost, as well as maximizing overall connection (and hence frame) stiffness.

For architectural considerations it may be desirable to conceal the dampers above the beam flange. For cases when $j < 1$, this may mean some welding of brackets to the beam is necessary to improve overall connection rigidity or that better bolted connection designs are detailed, which was not in the scope of this specific study.

Chapter 8: Analytical Model Of Jointed Precast Concrete Connection

The chapter details the analytical modelling and experimental validation of a full-scale beam-column subassembly with internally mounted HF2V devices. The test article is the same experimental subassembly presented in Chapter 5. An explicit, continuously smooth compound equation of modified Menegotto-Pinto form is used to model the entire response cycle. Control point parameters of the backbone curve are calculated from rational mechanics creating a purely applied mechanics model for this type of system. Good agreement between the experiment and model would provide a useful design tool for sizing and detailing these types of connections given overall design demand loads and performance criteria. Hence, this chapter seeks to create a first design model for these HF2V systems based entirely on rational mechanics.

8.1. Introduction

Structural response for a jointed precast system is a combination of elastic member deflection and rigid body rotation. This study develops an analytical model based almost entirely on rational mechanics to predict the experimental subassembly response presented in Chapters 5 and 6. Initially, the control point parameters for the backbone curve are calculated from rational mechanics. The analysis is then extended to a simple explicit formulation of a compound Menegotto-Pinto form that predicts the entire loading and unloading curve. The model is calibrated to the dimensions of the experimental subassembly and validated against the experimental results presented in Chapters 5 and 6. The tri-linear formulation of the equation accounts for yielding of the prestressing tendons during a response cycle, but does not account for the associated loss of prestress on subsequent cycles. The model also does not

include the effects of friction. Therefore, it is expected that the model will provide accurate results for the experimental displacement profiles, provided no tendon yield or notable friction is present, both of which are also very specific to a given specific connection design.

8.2. Modelling Connection Behaviour

Overall joint hysteresis for this type of un-bonded prestressed damage-protected connection is a combination of elastic member deflection and rigid body rotation. Initially, the presence of the unbonded prestress will delay gap opening. The lateral column deflection will thus be a function of elastic deformation of structural elements only. This elastic deformation regime continues until the applied moment exceeds the moment preventing gap opening. This resisting moment is provided by the clamping effect of the prestress in the beam to the column together with the supplemental damping system. The column base-shear required for gap opening is therefore a function of the level of prestress provided by the beam tendons, and the resistive force provided by the HF2V dampers.

Upon gap opening, the prestressing tendons elongate elastically along with deformation of the supplemental damping system. Further lateral deflection is then a combination of further elastic deformation of the sub-assembly, and rigid body rotation associated with joint opening. The column base-shear associated with this deflection can be calculated using beam bending theory and rigid body kinematics. The post gap-opening stiffness remains until the tendon elongation associated with the rigid body component reaches tendon yield. At this point, further column deflection occurs with no further increase in column base-shear.

8.2.1. Modelling the Backbone (Monotonic) Loading Behaviour

This section presents the derivation of the model parameters for the backbone loading behaviour of the connection. This section presents a detailed summary of the derivation, and additional information is provided in Appendix A, where more detailed representation of the deformation regimes and associated equations is provided.

The combination of pre gap-opening elastic member deformation, post gap-opening deformation resulting in elastic tendon elongation, and post gap-opening deformation with inelastic tendon elongation creates a tri-linear elastic-plastic response. This overall tri-linear loading path can be easily calculated based on elastic member deflection and rigid body rotation. Figure 8.1 presents a schematic diagram of the loading behaviour of a jointed, precast concrete connection both with and without a supplemental damping system.

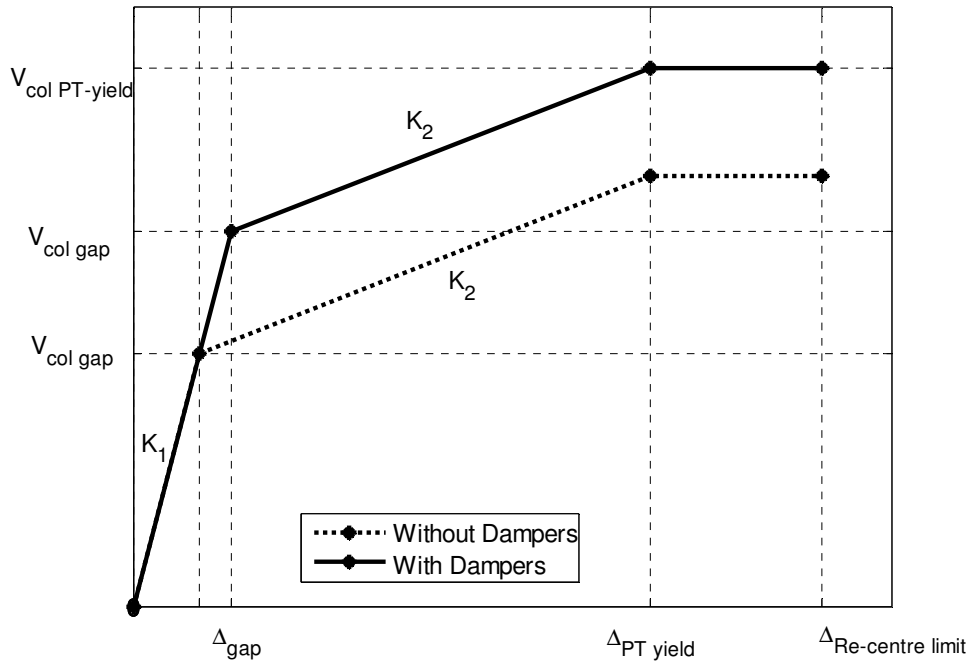

Figure 8.1: Schematic representation of the simplified loading model where K_1 is the initial elastic, pre gap-opening, stiffness, K_2 is the stiffness during elastic and rigid body deflection with elastic tendon elongation, and $K_3 = 0$ occurs when inelastic tendons elongation occurs

The tri-linear behaviour is shown in Figure 8.1. Initial elastic deformation of the subassembly (K_1) is followed by gap opening, where further elastic deformation (K_2) is a combination of elastic member deflection and rigid body rotation. Finally the unbonded post-tensioned tendons yield ($K_3 \cong 0$).

In Figure 8.1, $V_{col\ gap}$ is defined as the column base shear at gap opening, and differs based on whether supplemental energy dissipating devices are present. Thus, Δ_{gap} is the elastic displacement of the subassembly at gap opening and also varies based on the presence of dampers, as it is a function of the applied base shear, $V_{col\ gap}$. Further along the curve, Δ_{PT_yield} is the displacement of the subassembly at the onset of plastic deformation of the post-tensioned tendons, which occurs at a base-shear of $V_{col\ PT\text{-}yield}$.

Finally $\Delta_{Re\text{-}centre\ limit}$ is the maximum subassembly displacement beyond which further tendon yielding leads to inability of the joint to statically recentre on unloading. This re-centre limit displacement is, in fact, also dependent on the presence of dampers, as they will oppose joint closing and this resistance to closing must therefore also be overcome by the post-tensioned and elongated tendon restoring force. However, for the straight tendon profiles used in this test article (see Figure 5.1), the recentring limit is not a practical limit unless the post-tensioning force is substantially reduced, as discussed in Chapter 6 and presented in Figure 6.1.

It has been established in all of the experimental investigations that any significant damper connection flexibility affects results. In this modelling it will result in an additional linear component following gap opening. If perfectly rigid connecting elements were used then the behaviour would follow that shown in Figure 8.1. However, with the addition of elasticity in

the connection elements, this behaviour must be modified to include additional flexibility following gap-opening. This result is shown in Figure 8.2.

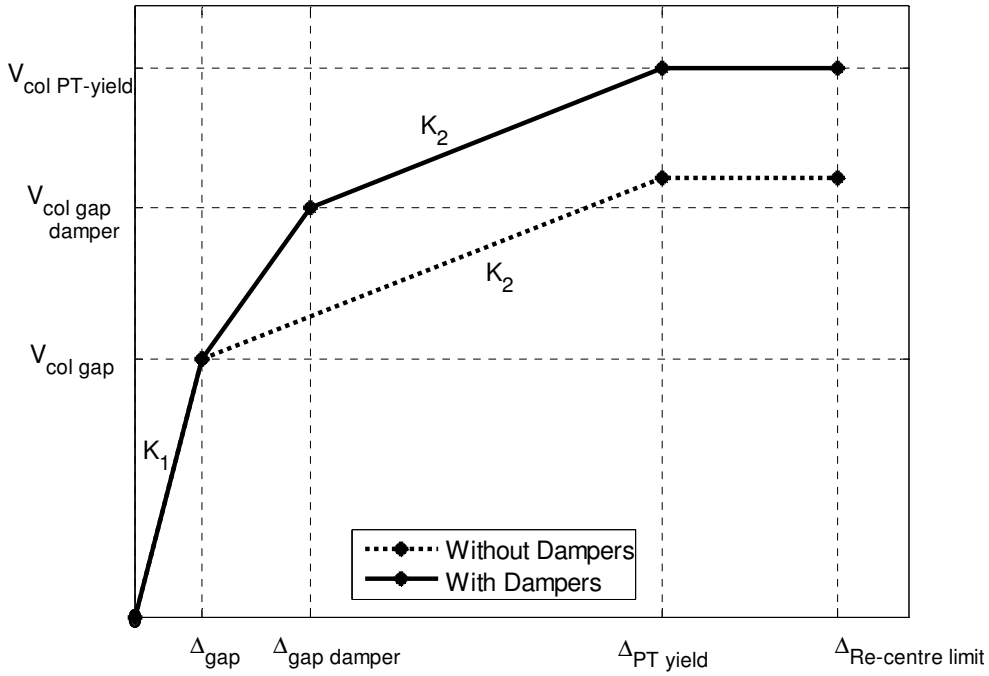

Figure 8.2: Simplified loading model including damper connection flexibility

This added flexibility adds two new variables. First, $V_{col\ gap\ damper}$ is the base-shear after gap-opening when the dampers fully engage. Second, $\Delta_{gap\ damper}$ is the corresponding subassembly displacement at which the dampers fully engage. All of the points shown in Figures 8.1 and 8.2 can be easily calculated from fundamental statics and kinematics, using the subassembly measurements in Figure 8.3.

In Figure 8.3, L_{col} is the length of the column from mid-storey to mid-storey (2.9m), L_b is the length of the beam, which is also the bay width from column face to column face (7.3m). Similarly, L is the bay width from column centreline to column centreline (8m). The width of the column is h_c (0.7m) and D is the beam depth (0.56m).

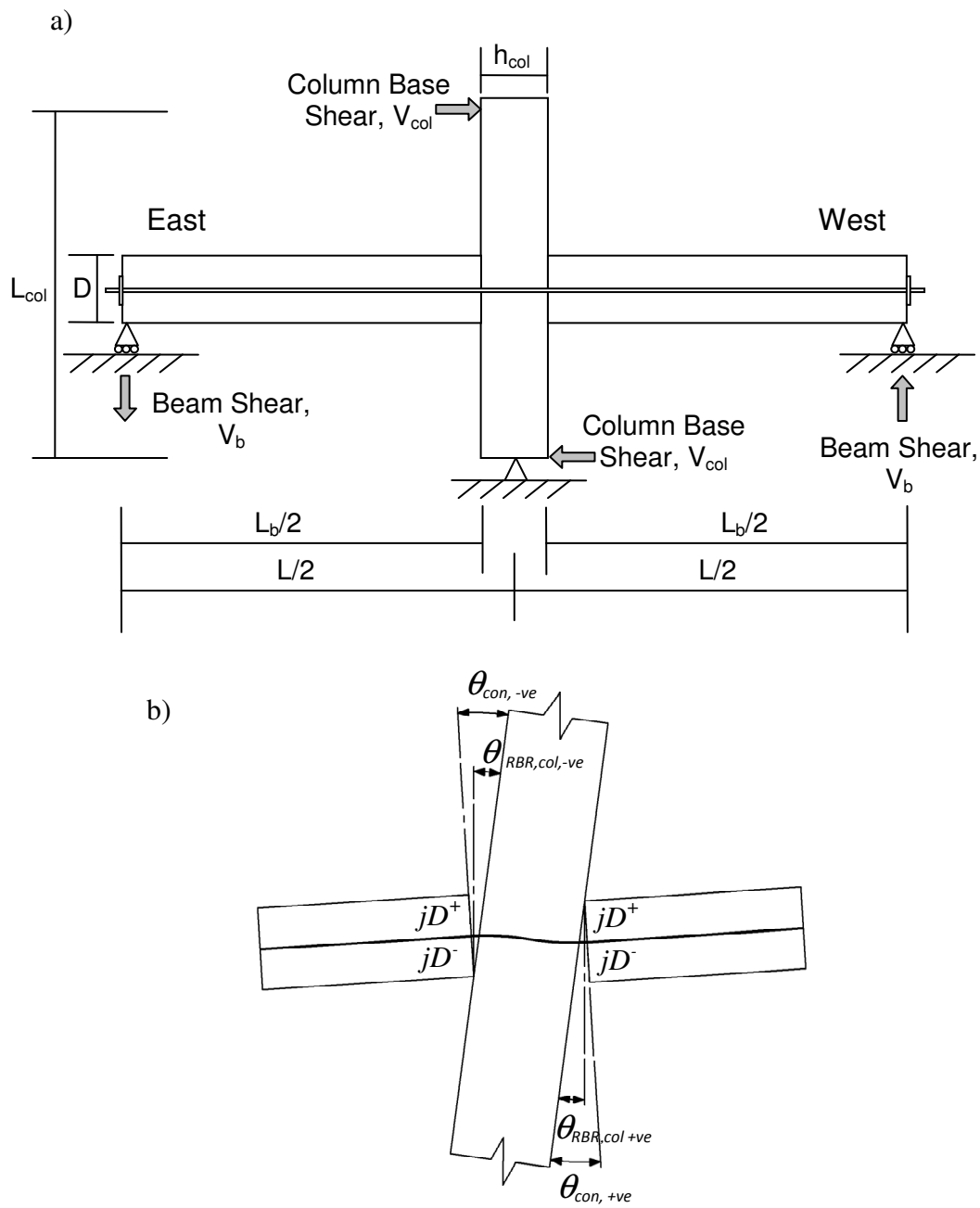

Figure 8.3: a) Schematic diagram showing subassembly parameters, and b) connection rotation convention

The eccentricity from the rocking edge of the post-tensioning tendons and HF2V device, $(jD)^{\pm}_{PT}$ and $(jD)^{\pm}_{dampers}$ respectively, are shown in Figure 8.3b. The notation '±' refers to the eccentricity from the rocking edge for both positive and negative joint rotation. For the East-West seismic direction the tendons and dampers are located at the beam mid-height. Hence, both $(jD)^{\pm}_{PT}$ and $(jD)^{\pm}_{dampers}$ are 280 mm for both positive and negative joint rotations. For the

North-South (gravity beam) direction, the tendons are located at a 30mm vertical offset, resulting in eccentricities of $(jD)^{+}_{PT} = 310$ and $(jD)^{-}_{PT} = 250$ mm. The damper in the North-South gravity beam (not shown in Figure 8.3) is similarly offset from the horizontal centreline by 50mm, giving eccentricities of $(jD)^{+}_{dampers} = 330$ and $(jD)^{-}_{dampers} = 230$ mm.

In Figure 8.3b, θ_{con} is the connection rotation between the beam end and column face. For a theoretical column with no width, the vertical rotation of the column at the centreline will be equal to the connection rotation. For a realistic column width this value will change by a ratio of the beam length (column face to column face, L_b) to bay width (column centreline to centreline, L). Therefore, to get the rigid-body column rotation, θ_{RBR_column}, the connection rotation, $\theta_{connection}$ must be modified by:

$$\theta_{RBR\_column} = \theta_{connection} \frac{L_b}{L} \tag{8-1}$$

where θ_{RBR_column} is the rigid body rotation of the column, relative to a fixed vertical axis. More detail in the derivation of the relationship of Equation (8-1) is presented in Appendix A.

By considering moment equilibrium of the beam about the rocking edge, the relationship between beam shear, V_b, and total connection moment, $M_{conncetion}$, is defined:

$$M_{connection} = V_b \left(\frac{L_b}{2} \right) \tag{8-2}$$

where L_b is previously defined, and shown in Figure 8.3.

By considering overall equilibrium of the subassembly, the relationship between column shear, V_{col}, and beam shear, V_b, is defined:

$$V_b = V_{col}\left(\frac{L_{col}}{L}\right) \tag{8-3}$$

where L_{col} and L are shown in Figure 8.3.

Combining Equations (8-2) and (8-3) and re-arranging yields an expression for the column shear, V_{col}, as a function of connection moment.

$$V_{col} = \frac{2M_{connection}}{L_b}\frac{L}{L_{col}} \tag{8-4}$$

The column base-shear at gap-opening, $V_{col\ gap}$ can thus be calculated from the total connection moment, $M_{connection}$, which is the sum of the applied moment at each rocking interface from post-tensioning ($M_{PT} = F_{PT\_initial}(jD)_{PT}$) and the moment at each rocking interface from the HF2V dampers ($M_{dampers} = F_{dampers}(jD)_{dampers}$) to yield:

$$V_{col\,gap} = \frac{2\left(M_{PT} + M_{dampers}\right)}{L_b}\frac{L}{L_{col}} = \frac{2(F_{PT\_initial}\left(jD\right)_{PT} + F_{damper}\left(jD\right)_{damper})}{L_b}\frac{L}{L_{col}} \tag{8-5}$$

where $F_{PT\_initial}$ is the total initial or design force provided by the post-tensioned tendons; F_{damper} is the nominal damper design force; and the other terms are previously defined in Figure 8.3.

From moment-area methods, the deflection of the column at the loading point due to elastic flexure of the beam and column is defined:

$$\Delta_{gap} = \frac{V_{col,gap}}{12}\left[\frac{(L_{col}-D)^3}{EI^*_{col}} + \frac{{L_{col}}^2 {L_b}^2}{LEI^*_b}\right] \tag{8-6}$$

where EI^*_{col} is the effective column stiffness, and EI^*_b is the effective beam stiffness. These effective stiffness values for the beam and column can be approximated using moment area methods as 26% of the gross stiffness for uni-directional testing and 14% for bi-directional testing (Li et al. 2008). More detail on the derivation of Equation (8-6) and the influence of both the beam and column contributions is presented in Appendix A.

The column base-shear at the point of damper engagement will be higher than at gap opening, as the dampers are now fully engaged and the post-tensioned tendon force has increased due to the increased strain caused by initial gap opening. To predict the displacement required for the dampers to engage, an initial stiffness, K_{damper}, of 200 kN/mm is estimated from the quasi-static experimental device test, as shown in Figure 5.4c. Therefore, the additional strain induced in the tendons at the point of damper engagement, $\Delta\varepsilon_{PT}$, is given by:

$$\Delta\varepsilon_{PT} = \eta \frac{F_{damper\_ref}}{K_{damper}} \frac{1}{L_t} \tag{8-7}$$

where η is the number of rocking interfaces spanned by the tendon; F_{damper_ref} is a nominal reference damper force; and L_t is defined as the total unbonded length of the post-tensioned tendon. Equation (8-5) can thus be modified to include force resulting from this additional strain:

$$V_{col,gap\_damper} = \frac{2(F_{PT}(jD)_{PT} + F_{damper}(jD)_{damper})}{L_{col}} \frac{L}{L_b}$$
$$= \frac{2((\varepsilon_{PT\_iniital} + \Delta\varepsilon_{PT})E_{PT}A_{PT}(jD)_{PT} + F_{damper}(jD)_{damper})}{L_{col}} \frac{L}{L_b} \quad (8\text{-}8)$$

where V_{col,gap_damper} is the column base-shear at full damper engagement as defined in Figure 8.2; F_{PT} is the tendon force at damper engagement; $\varepsilon_{PT\_initial}$ is the initial strain in the tendons from post-tensioning alone before gap opening; $\Delta\varepsilon_{PT}$ is the additional strain induced in the tendon from initial gap-opening, as defined in Equation (8-7); and E_{PT} and A_{PT} are the elastic modulus and total cross-sectional area of the tendons respectively. All the other terms are defined previously.

The displacement at damper engagement, $\Delta_{gap\ damper}$, will be thus a function of both elastic member deflection and rigid body rotation due to joint opening, defined:

$$\Delta_{gap\,damper} = \Delta_{elastic,damper} + \Delta_{rigid-body,damper} \quad (8\text{-}9a)$$

$$\Delta_{gap\,damper} = \frac{V_{col,gap\_damper}}{12}\left[\frac{(L_{col} - D)^3}{EI^*_{col}} + \frac{L_{col}{}^2 L_b{}^2}{LEI^*_b}\right] + L_{col}\frac{F_{damper\_ref}}{K_{damper}(jD)_{damper}}\frac{L_b}{L} \quad (8\text{-}9b)$$

where the first component, $\Delta_{elastic,damper}$, is the elastic deflection of the subassembly at the point of full damper engagement, and is defined the same as defined in Equation (8-6), but uses V_{col,gap_damper} defined in Equation (8-8) in place of $V_{col,gap}$ as defined in Equation (8-5). The second term, $\Delta_{rigid\text{-}body,damper}$, represents the column displacement from rigid body rotation at the point of full damper engagement.

The base-shear and displacement at tendon yield can be similarly calculated, but occurs at the point that plastic strain is induced in the tendons. The base-shear force, V_{col,PT_yield}, is given:

$$V_{col,PT\_yield} = \frac{2(\varepsilon_{PT\_yield} E_{PT} A_{PT} e_{PT} + F_{damper}(jD)_{damper})}{L_{col}} \frac{L}{L_b} \tag{8-10}$$

where ε_{PT_yield} is the yield strain of the tendon, and F_{damper} is used because it is fully engaged and moving.

Finally, the column displacement at tendon yield, Δ_{PT_yield}, can be defined:

$$\Delta_{PT\_yield} = \Delta_{elastic,PT\_yield} + \Delta_{rigid-body,PT\_yield} \tag{8-11a}$$

$$\Delta_{PT\_yield} = \frac{V_{col,PT\_yield}}{12}\left[\frac{(L_{col} - D)^3}{EI^*_{col}} + \frac{{L_{col}}^2 {L_b}^3}{L^2 EI^*_b}\right] + L_{col}\frac{(\varepsilon_{PT\_yield} - \varepsilon_{initial})L_t}{\eta(jD)_{damper}}\frac{L_b}{L} \tag{8-11b}$$

where ε_{PT_yield} is the total tendon strain at the onset of plastic deformation, and the first term on the right hand side of Equation (8-11a), $\Delta_{elastic,PT\_yield}$, is the elastic deformation of the subassembly at the column shear that corresponds to the onset of tendon yield, V_{col,PT_yield}, as defined in Equation (8-10). The second term on the right hand side of Equation (8-11a), $\Delta_{rigid\text{-}body,PT\_yield}$, is the displacement at the top of the column from rigid-body deflection at the onset of tendon yield. Note that the elastic component, $\Delta_{elastic,PT\_yield}$, is simply Equation (8-6) with V_{col,PT_yield} used in place of $V_{col,gap}$.

Note that Appendix A provides additional information on the derivation of model parameters, and in particular, the deformation regimes and geometric relationships that lead to the derivation of Equations (8-1) and (8-6). This section essentially provides a detailed summary, and the Appendix provides additional information for interested readers.

Overall, the model given by Equations (8-5)-(8-11) provides an easy and reasonably accurate prediction of the loading portion of the overall joint hysteresis. Figure 8.4 presents the uni-directional test results and the model prediction from Equations (8-5)-(8-11) both with and without the addition of supplemental HF2V damping systems. It should be noted that if the damper force is set to zero, then the result of Equations (8-8) and (8-9) become equal to that of Equations (8-5) and (8-6) respectively. Overall, Figure 8.4 shows that the hysteresis curve backbone is well captured by this initial model.

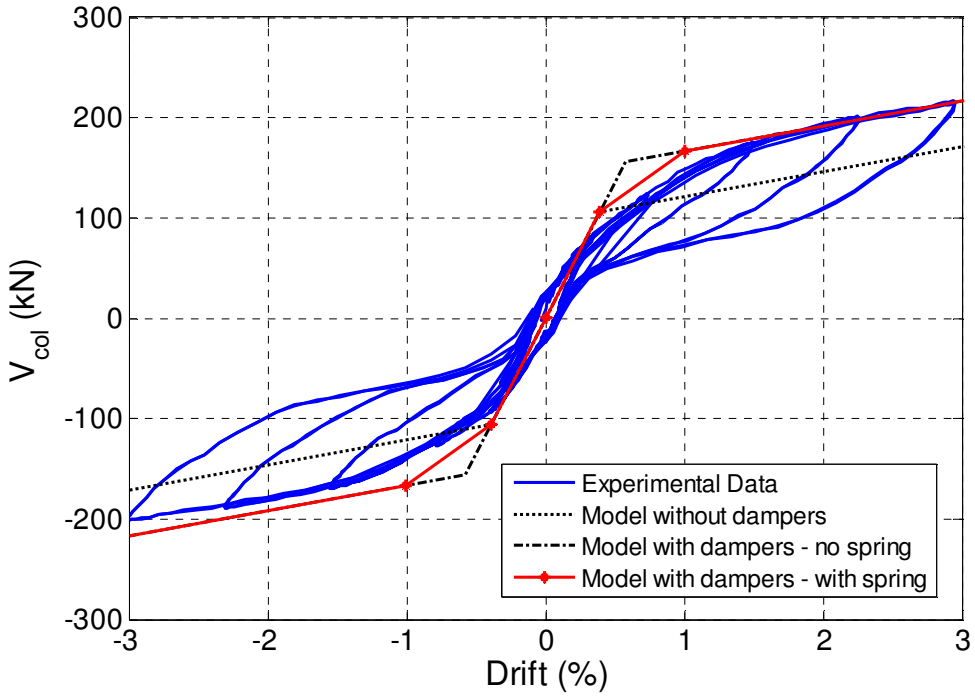

Figure 8.4: Experimental results showing the simple model loading prediction

It can be seen that the spring that represents the additional damper coupling flexibility is an important modification, as there is still an over-prediction at this point of the loading, as clearly seen around 0.5-1% drift in Figure 8.4. Without this addition, there would be a much larger error in the model. It can be seen that the model without additional damping provides a good approximation that is the approximate average of the loading and unloading portions of the hysteresis loop. This latter observation is a good indication that the model will accurately predict the behaviour of the joint without dampers. However, Figure 8.4 also clearly shows that a more advanced model is needed to accurately predict the behaviour under both loading and unloading. Especially, if one desires to capture the true hysteresis loop, rather than approximate its outer envelope, as in Figure 8.4.

8.2.2. Compound Menegotto-Pinto Model

A more advanced model can be derived from this initial framework that accurately predicts both the loading and unloading by applying Equations (8-5)-(8-11) to a compound Menegotto-Pinto model (Menegotto and Pinto 1973). This model will also incorporate a more advanced damper model, rather than just using a simple design force, F_{damper}. As such, the Menegotto-Pinto model takes the previously defined model *without* supplemental damping and applies the damping separately to capture the full hysteresis loop through loading and unloading. Hence, Equations (8-7)-(8-9) become redundant using this model, and the remaining equations are used to define the revised model's stiffness values.

It has been shown in previous chapters that the HF2V dampers can be modelled as non-linear velocity dependent viscous dampers. The stiffness of the rods connecting the dampers to the column is modelled as a spring in series with the damper. Therefore, the damper force

linearly increases after joint opening as the connection rotates, until the point at which the yield force of the dampers is reached, whereupon it is strictly a function of velocity and the device constant, C_α per Equation (2-3) ($F_{damper} = C_\alpha(\dot{x})^\alpha$).

As before, the combination of pre gap-opening elastic member deformation, post gap-opening deformation resulting in elastic tendon elongation, and post gap-opening deformation with inelastic tendon elongation creates an overall tri-linear hysteretic response. However, the smooth non-linear experimental behaviour can be more accurately modelled using a compound version of the Menegotto-Pinto (1973) hysteresis rule (Li 2006), and with the addition of a rate-dependence damper model (Rodgers et al. 2007a) defined:

$$F = \frac{(K_1 - K_2)\theta}{\left(1 + \left|\frac{K_1\theta}{F_p + |F_D|\,\mathrm{sgn}(\dot{x})}\right|^\beta\right)^{\frac{1}{\beta}}} + \frac{K_2\theta}{\left(1 + \left|\frac{K_2\theta}{F_y + |F_D|\,\mathrm{sgn}(\dot{x}) - (F_p + |F_D|\,\mathrm{sgn}(\dot{x})(1 - K_2/K_1))}\right|^\gamma\right)^{\frac{1}{\gamma}}} \qquad (8\text{-}12)$$

where K_1 = stiffness of the sub-assembly during initial pre-gap-opening elastic deformation and can be easily calculated from the result of Equations (8-5) and (8-6), noting that Equation (8-6) gives column displacement and must be divided by column length, L_{col}, to give drift. Similarly, K_2 = stiffness of the sub-assembly during post gap-opening deflection before tendon yield using Equations (8-5), (8-6), (8-10) and (8-11) and is shown schematically in Figures 8.1 and 8.2. Again, the transformation from displacement to drift should be noted. Next, θ = the drift angle of the column, and $\dot{x}$ = the velocity of the damper shaft, corresponding to the velocity of the joint opening at beam centreline, where when $\dot{x} > 0$, sgn($\dot{x}$) = 1, and when $\dot{x} < 0$, sgn($\dot{x}$) = -1. The term F_p = column base-shear required to overcome the resistance to joint opening from prestress alone, equal to $V_{col,gap}$ in

Equation (8-5) when F_{damper} = 0. Similarly, F_y = column base-shear required to open gap to prestress tendon yield, equal to V_{col,PT_yield} in Equation (8-10) when F_{damper} = 0. Finally, β = exponent governing the degree of curvature that joins the tangents between the first and second linear sections of the hysteresis loops, and γ = exponent governing the degree of curvature between the second and third linear sections of the hysteresis loop, where large exponents give sharper corners closer to the tri-linear behaviour of Figure 8.1. The last term is F_D = column base shear required to overcome the lateral resistance of the subassembly due to the damper force, F_{damper}.

Damper connection flexibility is incorporated by using a spring in series with the damper, where the damper force is the minimum of the spring force, or device model force, defined (Pekcan et al. 1999):

$$F_{damper} = \mathrm{sgn}(\dot{x}) * \min\begin{cases} abs(K_{damper}(jD)_{damper}\theta_{connection}) \\ abs(C_{\alpha}|\dot{x}|^{\alpha}) \end{cases} \qquad (8\text{-}13)$$

where K_{damper} = the effective spring stiffness of the damper shaft and connecting elements, $(jD)_{damper}$ = the eccentricity of the dampers from the rocking edge, $\theta_{connection}$ = the connection rotation due to only the rigid body rotation component of drift, C_{α} = damper constant determined by testing at a reference velocity before installation into the joint, $\dot{x}$ = the velocity of the damper shaft, α = velocity coefficient (constant) = 0.12, and sgn($\dot{x}$) is defined previously.

When considering the influence of the lead extrusion damper on the subassembly, the following relationship can be used to calculate the base-shear required to overcome the damper force:

$$F_D = F_{damper} \frac{D}{L_{col}} \frac{L}{L_b} \tag{8-14}$$

where F_{damper} is defined in Equation (8-13), and F_D is thus the base shear force that this value, F_{damper}, equates to via kinematics and moment balancing.

8.3. Results and Discussion

The test specimen underwent quasi-static uni-directional displacement tests in the East-West direction using fully reversed sine wave profiles up to 4% inter-story drift. Once overall testing and characterisation of the specimen with the supplemental damping system was complete, the joint was opened and the connecting rods to the dampers cut. The specimen then underwent repeated testing to characterise the overall hysteresis without the supplemental damping system. These experiments were run to explicitly delineate the individual contributions of the dampers and tendons, as detailed in Chapter 6.

The post-tensioning system initially provided a total force to the joint of 500kN. The initial force in the post-tensioning system was also reduced to 400kN, 300kN, and down to 200kN in Chapter 6, to investigate the contribution of elastic member deflection to the overall hysteresis. This procedure also provides a means of experimentally investigating the factor of safety on the ability of the connection to statically re-centre. By reducing the level of post-tensioning force for a set level of added damping, the factor of safety on re-centering is reduced.

The experimental and Menegotto-Pinto results for the joint with and without supplemental HF2V damping at 1, 2, 3, and 4% drift with total post-tensioning forces of 500, 400, and 300kN are presented in Figures 8.5 a-c respectively. The left column shows the experimental test data and Menegotto-Pinto model prediction for the system with the supplemental damping system. The right column shows the experimental and model results for the subassembly without the supplemental damping system in Figures 8.5d-f. Overall, the analytical response from the Menegotto-Pinto model shows very good agreement with the experimental results, although the base-shear at gap opening appears to be slightly over-predicted for the negative direction with the addition of supplemental damping.

The predicted response from the rate-dependent Menegotto-Pinto equation in Figure 8.5 show very close agreement to the experimental results across different levels of post-tensioning, both with and without the supplemental damping system. The modified Menegotto-Pinto model can also accurately predict the entire response cycle, and not just the loading portion given by the simplified model presented earlier and shown in Figures 8.1 and 8.2. The ability to model the joint at any level of prestress force and damper size is an extremely valuable tool for future design analyses. A second trend that is clearly evident across both the modelled and experimental results presented in Figure 8.5 is the minimal reduction in connection force levels due to the reduction in total prestress force of up to 200kN from its original 500kN level.

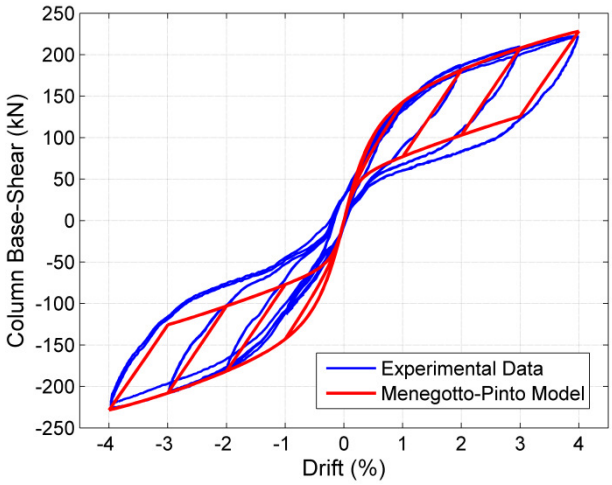

a) 500 kN total prestress, with dampers

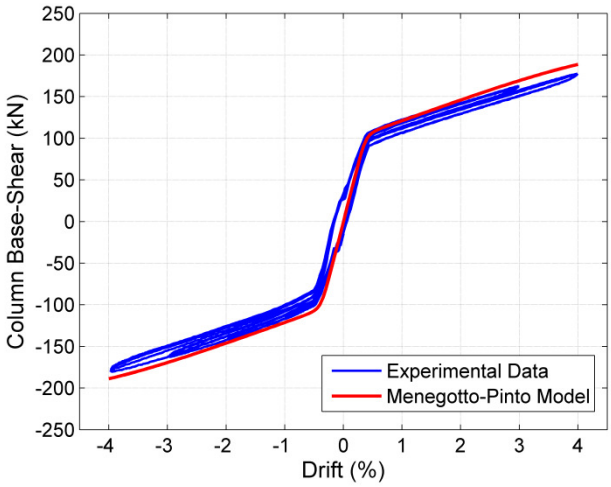

d) 500 kN total prestress, without dampers

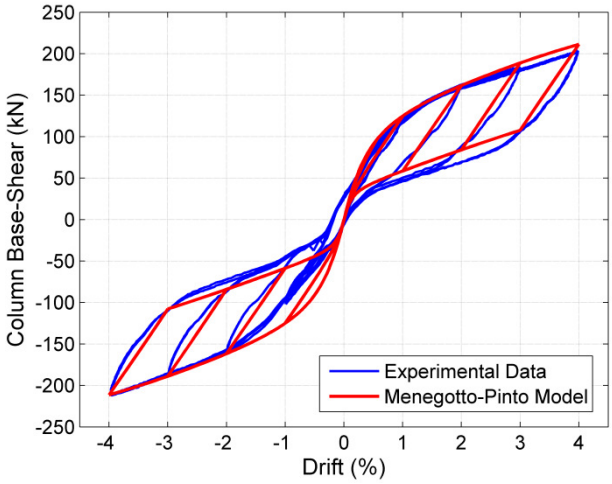

b) 400 kN total prestress, with dampers

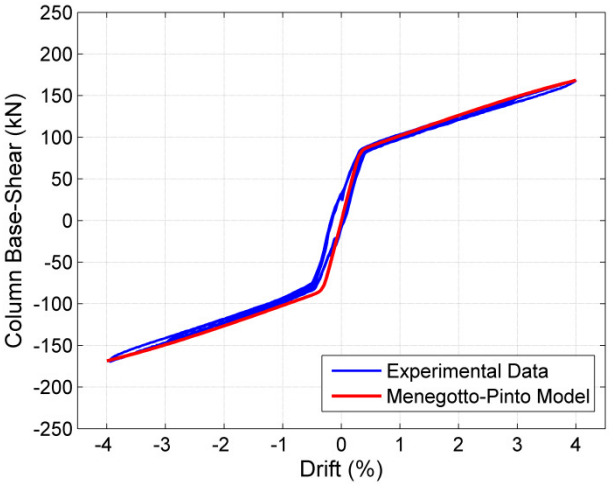

e) 400 kN total prestress, without dampers

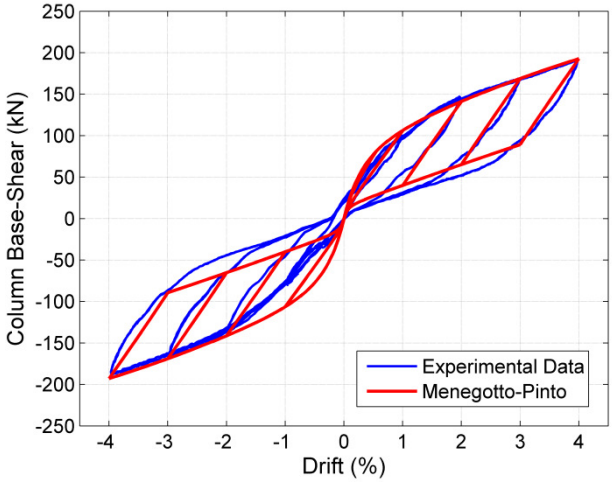

c) 300 kN total prestress, with dampers

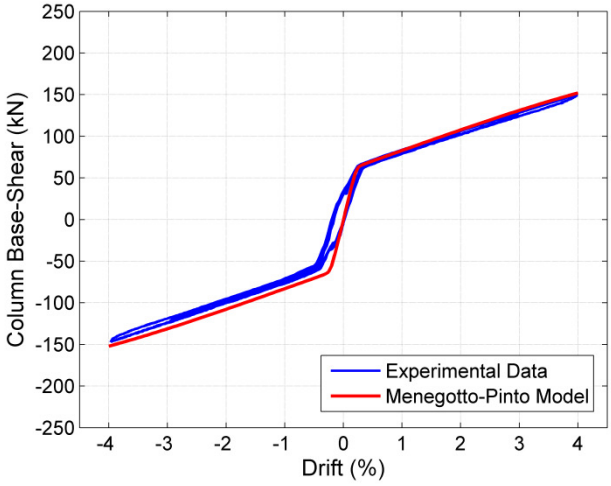

f) 300 kN total prestress, without dampers

Figure 8.5: Experimental and predicted response for the prototype specimen

It can be seen in Figure 8.5 that the overall joint hysteresis without the supplemental damping system exhibits extremely limited hysteretic energy dissipation, as expected (Li 2006; Priestley et al. 1999; Solberg 2007). The previous research into connections using bent tendon profiles in Chapter 4 showed much larger inherent hysteretic energy due to the friction of the tendons within the ducts. The straight tendon profile of the prototype specimen tested in this study results in much lower friction, and thus much lower inherent damping is provided by hysteretic energy absorption. Therefore, joints of this type are particularly suitable for supplemental damping systems to provide a means of absorbing response energy.

Finally, it should be noted that the model in this chapter is for the structural connection only, and does not include the influence of a floor slab. This influence is important for the overall structural system, but is outside the scope of this work.

8.4. Summary

Uni-directional quasi-static testing of the subassembly has shown significant, consistent and repeatable energy dissipation is provided by the supplemental damping system. A simplified backbone model is presented that can provide a good approximation to the loading portion of the joint hysteresis with minimal computation. A more advanced analytical model of joint hysteresis using a tri-linear Menegotto-Pinto model shows very good agreement to experimental results across different post-tensioning force levels, both with and without added damping. Column base-shear at gap opening is slightly over-predicted for the system with negative drift angles and added damping, but this result does not significantly impact the prediction. The ability to accurately predict the entire hysteretic response of the connection at any drift level is an important outcome for design purposes. The simple, yet accurate models developed will thus enable ready design in combination with existing spectral analysis results, and any specific set of seismic demand loads or deflections.

Chapter 9: Modelling Of HF2V Devices With Coupling Flexibility And Damage Avoidance Steel Connections

In the previous chapters, high force-to-volume (HF2V) lead based dampers have been developed that can provide large resistive forces and maintain compact outer dimensions. These devices have been implemented into several large-scale experiments, using both jointed-precast concrete and steel beam-to-column rigid connections. During these experimental investigations it has become apparent that the influence of connecting elements has a large effect on the connection rigidity and energy dissipation capacity. Specifically, any flexibility and take-up of the connecting elements reduces the displacements induced in the damper, thereby reducing the ability of the damper to efficiently dissipate energy. Therefore, for optimal behavior it is important to minimise the damper connection flexibility.

Despite efforts to reduce the flexibility, the connecting elements will always influence the damper behavior. Moreover, practical limitations on shaft and connection sizes dictate that a measure of connection flexibility will always exist and have some effect on overall behavior. Therefore, it is of importance to develop a model that incorporates both the fundamental damper mechanics, while also incorporating the effects of connecting element flexibility.

9.1. Introduction

Previous research in this area has looked at overall flexibility components of steel connections and how they relate to subassembly deformation and fatigue considerations (Mander et al. 1994). Other research has investigated experimental testing and modeling the response of post-tensioned steel connections (Garlock et al. 2007; Pekcan et al. 2000), but has

not investigated the use of non-linear viscous dampers within the connections of a steel moment frame.

There has also been previous research that has investigated the response of viscoelastic damping for seismic mitigation in structural applications, and for industrial applications of vibration isolation (Hwang and Ku 1997; Makris and Constantinou 1991; Shen and Soong 1995). This prior research typically utilizes fractional derivatives and frequency domain analysis to model the damper properties and define the overall response. These techniques provide good agreement with experimental results, and are typically applied for damper elements that exhibit viscoelastic properties.

Makris and Constantinou (1991) investigated spring-viscous damper systems, and their application for both seismic and vibration isolation. Hwang and Ku (1997) use system identification methods and fractional derivatives to model high-damping rubber bearings for seismic isolation of bridge decks. Hwang and Ku (1997) also discusses the historical lack of time-history analysis techniques for high-damping rubber bearings, due to their complex characteristics, and the traditional use of equivalent linear models. Fractional derivatives have also been used to analyse free damped vibrations of suspension bridges (Rossikhin and Shitikova 1998), and to model the effects of temperature on the energy dissipation of viscoelastic dampers (Aprile et al. 1997).

Although similar in basic concept to several of these applications, the HF2V damper system presented in this thesis is a system of a non-linear viscous damper with a stiff elastic spring element in series for the shaft and connecting rod mechanics. The analysis presented in this chapter utilizes time domain analysis to provide the model solution, and thus represents a different approach to the previous work. In addition, the previous research noted utilizes

fractional derivatives in the analysis, where this research uses a standard first derivative raised to a fractional power. As such, the time domain approach was selected to easily incorporate the non-linear effects of the damper element into the analysis.

This chapter describes the non-linear viscous damper and flexibility model, and also explains the incorporation of this model into a broader structural sense. In particular, the damper model presented is incorporated into the DAD steel beam-column moment frame connection of Chapter 7. This overall model can be used to determine the overall connection behavior from damper, connection and member properties, using an entirely rational mechanics based approach.

9.2. Transient Model of Damper Behaviour

Consider a non-linear HF2V damper connected in series with a linear axial spring to give a system of the Maxwell type, which is schematically presented in Figure 9.1. The displacement across the spring is defined as x, the displacement across the damper is y, and the total displacement across the system is defined as z. The system is formulated such that z is a known input displacement as a function of time, and the values of x, y, and the overall system force, F_D, are calculated.

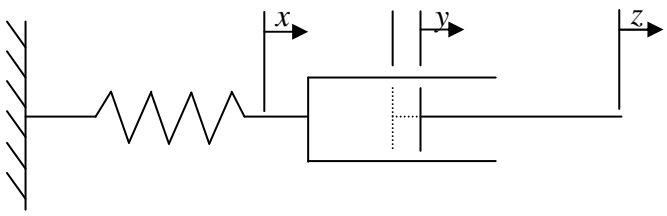

Figure 9.1: Schematic diagram of the damper-spring system

Due to the series connected nature of the system, the displacements and velocities (using dot notation) will sum, therefore:

$$x + y = z \tag{9-1a}$$

$$\dot{x} + \dot{y} = \dot{z} \tag{9-1b}$$

The applied force, F_D, must also equal the spring force (Kx) and the damper force. Using the Pekcan et al (1999) model for non-linear viscous dampers:

$$F_D = \frac{x}{f_D} = C_\alpha (\dot{y})^\alpha \tag{9-2}$$

in which f_D = the axial flexibility of the spring component of the damper assembly ($f_D = 1/K_D$), where K_D is the spring stiffness of the damper assembly; C_α = a damper constant; α = the velocity exponent; and $\dot{y}$ = the velocity across the damper. Note that due to the series nature of the system, the same force, F_D, is present within both the spring and damper elements at any point in time.

By re-arranging and differentiating (using dot notation) Equation (9-2), the following relationship can be obtained:

$$\dot{x} = f_D \dot{F}_D \tag{9-3}$$

where $\dot{F}_D = dF/dt$; and $\dot{x} = dx/dt$.

If Equation (9-3) is substituted into a re-arranged Equation (9-1b), the relationship is defined:

$$\dot{y} = \dot{z} - f_D \dot{F}_D \tag{9-4}$$

Substituting Equation (9-4) into Equation (9-2) yields:

$$F_D = C_\alpha \left(\dot{z} - f_D \dot{F}_D \right)^\alpha \tag{9-5}$$

Equation (9-5) can be re-written as:

$$\left(\frac{F_D}{C_\alpha} \right)^{1/\alpha} = \dot{z} - f_D \dot{F}_D \tag{9-6}$$

Defining first-order finite differences for $\dot{z}$ and $\dot{F}_D$ yields:

$$\left(\frac{F_{D,i+1}}{C_\alpha} \right)^{1/\alpha} = \frac{\left(z_{i+1} - z_i \right)}{\Delta t} - f_D \frac{\left(F_{D,i+1} - F_{D,i} \right)}{\Delta t} \tag{9-7}$$

This can be re-written as:

$$\Delta t \left(\frac{F_{D,i+1}}{C_\alpha} \right)^{1/\alpha} + f_D F_{D,i+1} = z_{i+1} - z_i + f_D F_{D,i} \tag{9-8}$$

It is evident that Equation (9-8) is actually a polynomial with variable $F_{D,i+1}$ to a power dependent on the value of $(1/\alpha)$. Note that the right hand side of the Equation (9-8) consist of the known input displacement into the system and the result from the previous time step, and are therefore all known values. One solution technique is to evaluate the roots of the equation using a standard root finding algorithm. Some of the roots will be complex, and can be disregarded as they have no physical application to the system. The appropriate root can be selected from the remaining roots by adding simple heuristics to determine which value (positive or negative) makes physical sense, and also by checking for roots in the vicinity of the solution from the previous time steps.

Alternatively, if Equation (9-8) is rearranged to get the system equations in terms of $F_{D,i+1}$ then the solution can be iteratively solved. Therefore, taking a common factor in Equation (9-8) yields:

$$\left(\frac{F_{D,i+1}}{C_\alpha}\right)^{1/\alpha}\left(\Delta t + f_D C_\alpha{}^{1/\alpha} F_{D,i+1}{}^{1-1/\alpha}\right) = z_{i+1} - z_i + f_D F_{D,i} \tag{9-9}$$

$$\left(\frac{F_{D,i+1}}{C_\alpha}\right)^{1/\alpha} = \frac{z_{i+1} - z_i + f_D F_{D,i}}{\Delta t + f_D C_\alpha{}^{1/\alpha} F_{D,i+1}{}^{1-1/\alpha}} \tag{9-10}$$

$$F_{D,i+1} = C_\alpha\left(\frac{z_{i+1} - z_i + f_D F_{D,i}}{\Delta t + f_D C_\alpha{}^{1/\alpha} F_{D,i+1}{}^{1-1/\alpha}}\right)^{\alpha} \tag{9-11}$$

Equation (9-11) will give erroneous results with complex terms in the current format, as both the last term in the denominator and the overall bracketed expression take a fractional exponent of a number that may take a negative value. By applying a signum function to the input argument (which is ultimately just the next approximation of $\dot{y}$) then the equation becomes:

$$F_{D,i+1} = C_\alpha\left|\frac{z_{i+1} - z_i + f_D F_{D,i}}{\Delta t + f_D C_\alpha{}^{1/\alpha}\left|F_{D,i+1}\right|^{1-1/\alpha}}\right|^{\alpha} * sign\left(\frac{z_{i+1} - z_i + f_D F_{D,i}}{\Delta t + f_D C_\alpha{}^{1/\alpha}\left|F_{D,i+1}\right|^{1-1/\alpha}}\right) \tag{9-12}$$

The bracketed expression in Equation (9-12) is simply the latest prediction of the damper shaft velocity, $\dot{y}$. Therefore, Equation (9-12) can actually be expressed in two equations, defined:

$$\dot{y}_{i+1} = \frac{z_{i+1} - z_i + f_D F_{D,i}}{\Delta t + f_D C_\alpha{}^{(1/\alpha)}\left|F_{D,i+1}\right|^{1-1/\alpha}} \tag{9-13}$$

$$F_{D,i+1} = C_\alpha\left|\dot{y}_{i+1}\right|^{\alpha}\operatorname{sgn}\left(\dot{y}_{i+1}\right) \tag{9-14}$$

The coupling of Equations (9-13) and (9-14) requires that these equations must be solved in a predictor-corrector or iterative sense. In addition to this, the initial time steps must be treated differently, as there is no ability to draw on data from previous time steps. In this situation, a solution can be easily obtained by considering the physics of the system. Initially, the spring must stretch from zero force to induce any force into the system and start the damper moving. Therefore, for the first time step, the force can be easily defined as:

$$F_{D,1} = \frac{z_1}{f_D} \tag{9-15}$$

And for all subsequent steps the following has been found to be a suitable predictor:

$$F_{D,i+1} = F_{D,i} + \frac{\Delta t}{f_D}\left(2\dot{x}_i - \dot{x}_{i-1}\right) \tag{9-16}$$

From this solution the value of the system force on each successive time step can be obtained. This result is then used to give the value of the spring displacement, x, as well as the damper displacement, y, and their derivatives.

This predictor-corrector approach provides an accurate solution to the system equations (without iteration) as long as the time step is kept relatively very small, as it is only conditionally stable. Although the solution method presented in Equations (9-13) to (9-16) provides accurate results and is relatively easy to implement, accuracy can be improved if they are solved iteratively. Providing the time step used is appropriately small, convergence is rapid. For larger time steps, iteration will be necessary, or any appropriate root finding numerical method may be used.

Figure 9.2 presents the response of the predictor-corrector model in Equations (9-13) to (9-16) to a 0.01Hz sinusoidal displacement input. Figure 9.2a shows the response with a 0.02s time step, and Figure 9.2b shows the response with a 0.125s time step. Figure 9.2b shows the onset of instability in the numerical solution due to the increased time step. The instability is observed to be self-damping with notable oscillation converging back onto the correct solution.

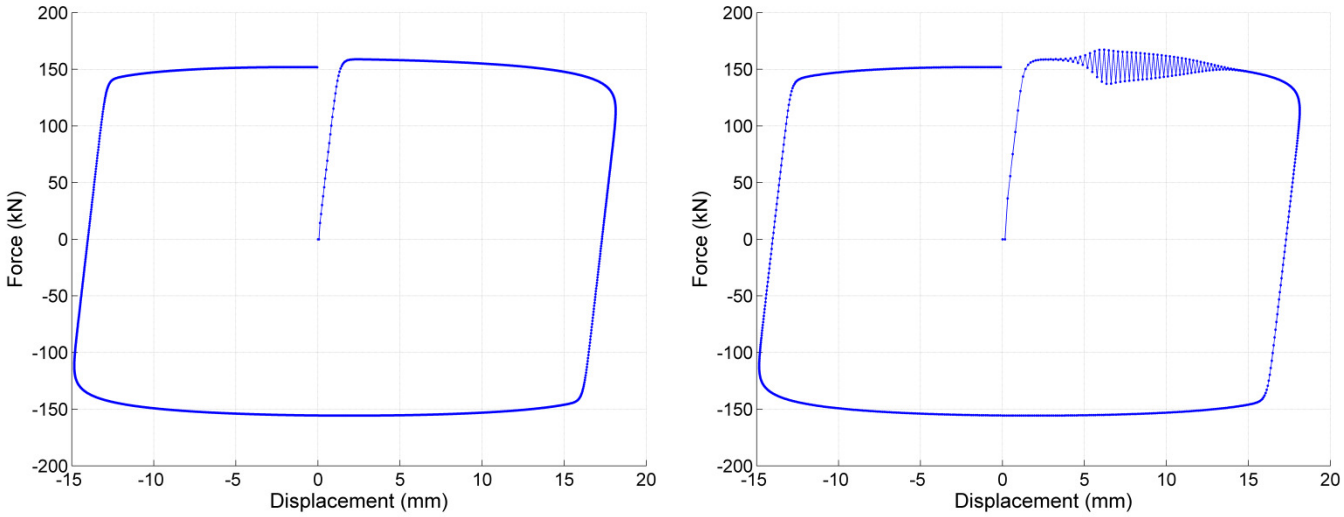

a) Stable model solution with Δt = 0.02s *b) Unstable model solution with Δt = 0.125s*

Figure 9.2: Onset of instability for the damper model

9.2.1. Damper Model Validation

Experimental results of a velocity-dependent HF2V device are now used to validate the force-displacement analytical model. The HF2V device was tested at a range of different velocities in a DARTEC™ universal testing machine to characterize the damper constant, C_α, and the velocity exponent, α. Figure 9.3 presents the experimental set-up for the HF2V device characterization tests used here. Two independent sets of measurements were recorded. The internal machine load-cell and LVDT displacement transducer were recorded, as well as the measurements of a load-cell connected in series with the device and a potentiometer across the stressed part of the device shaft.

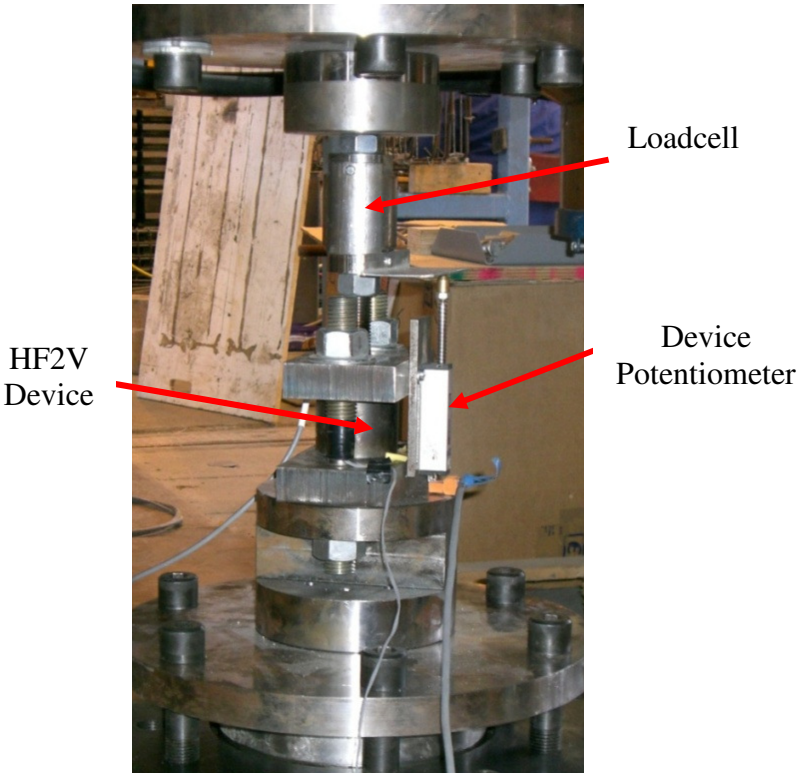

Figure 9.3: Experimental set-up for HF2V device characterization

The force readings should show only minor differences, but the displacement measurements are somewhat different. The reason for this difference is that the HF2V device potentiometer measured actual device motion as well as elastic deformation of the stressed length of the shaft. The internal LVDT of the DARTEC testing machine measurements included the device displacement, shaft deformation, and the deformation of all the device mounts, locating bolts and the main actuator. Thus the internal LVDT recorded all connection flexibilities and a larger motion.

The experimental data was used to characterize the velocity exponent, by taking the force at peak velocity for a range of sine-wave input motions at different periods and thus, for a given amplitude, different velocities. Using this data, a trend-line is fitted to characterize the damper constant, C_α, as well as the velocity exponent α. The velocity exponent has been investigated briefly in Chapter 2 and shows the device velocity exponent was in the range of

α = 0.11 to 0.12. This result is within the same range previously found in the characterisation on much larger lead extrusion damping devices (Cousins and Porritt 1993).

Figures 9.4a-b present the results of experimental tests at two different input sine-wave frequencies of 0.01 and 0.0025 Hz along with the analytical modelling of the HF2V device response. When applying the model in Equations (9.1) to (9.16), the following parameters were used, α = 0.12 based on the results of the prior velocity dependence study in Chapter 2, and C_α = 170, and f_D = 3.3 x 10^{-3} mm/kN based on an empirical fit to the damper constant and spring flexibility respectively. From Figures 9.4a-b it is evident that overall good agreement exists between the experimental behavior and the analytical model prediction. The model results using the predictor-corrector model presented in Figure 9.4b are validated against the exact solution using a MATLAB^{TM} root finding algorithm and selection of the appropriate, real-valued, root. The exact solution from this method is presented overlaid on the 0.01Hz results in Figure 9.4b. It is evident that both methods give the same solution, validating the use of the predictor-corrector formulation.

Figure 9.4 also presents the overall results of the experimental study into the velocity exponent. The least-squares fit to the data points gives a velocity exponent, α, equal to 0.1085, which is marginally lower than the value found in the more limited velocity study in Chapter 2, but is still close to the values expected based on this and previous research (Cousins and Porritt 1993).

It should be noted that this specific velocity dependence study was more advanced than the previous study by utilizing displacement controlled sine-wave profiles, rather than the simple linear quasi-static tests used in Chapter 2. The velocity range in this study, and presented in

Figure 9.4, also has an equipment-based restriction in maximum test velocity to only 1 mm/s, due to limitations in the experimental equipment and set-up. The testing machines available at the University of Canterbury either have a very large force capacity and low velocity capability, or a high velocity capability and low force capacity, which limited the test velocity applied to these high force devices in this research. In future tests, it is advisable that either an alternative testing machine is found, perhaps at an external engineering company, or a very low force capacity device is designed specifically for higher velocity testing.

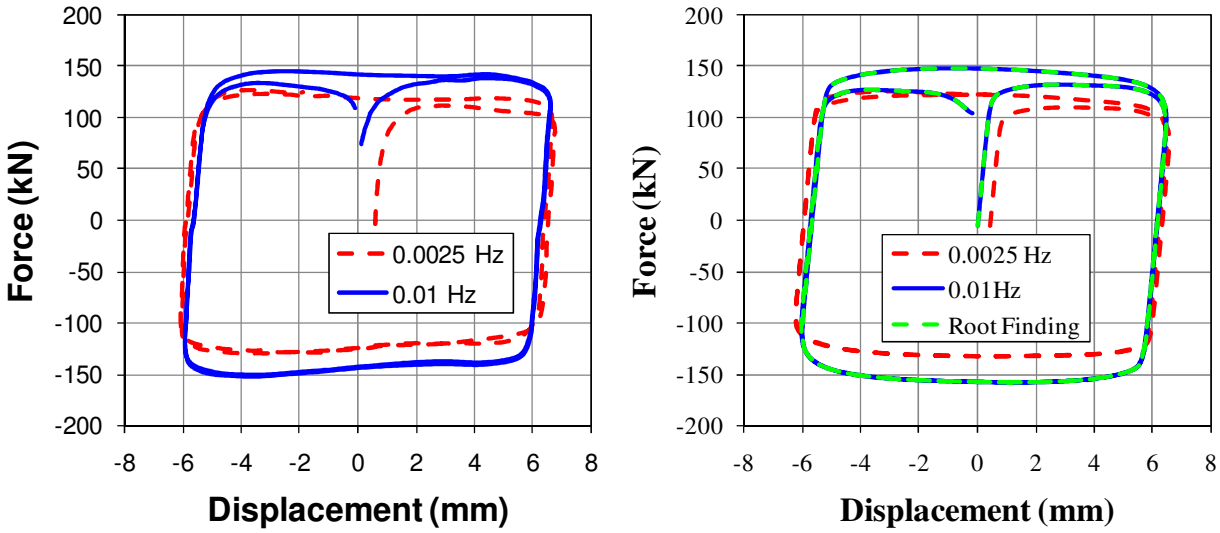

a) Experimental Results *b) Model Results*

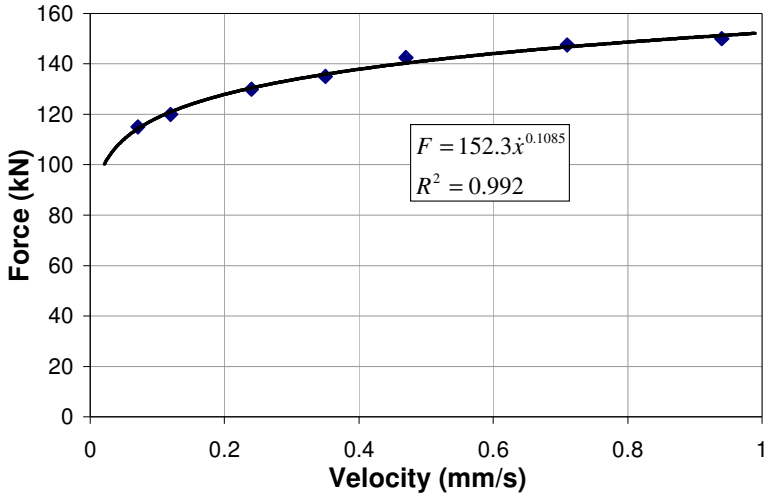

c) Empirical velocity dependent power law

Figure 9.4: Comparison of modelled and experimental results for sample velocity tests and the overall velocity exponent investigation.

The MTS-810 machine in the Mechanical Engineering department has a maximum test velocity of approximately 300-400 mm/sec. This velocity would provide a more defendable upper limit, as it represents an upper bound on the velocity that any of these devices is likely to experience in the structural applications presented within this thesis. Based on a realistic eccentricity of 300mm, and an assumed sinusoidal structural response of 2Hz at drift amplitudes of 3%, the device response amplitude would be 9 mm. This drift value and frequency equates to a maximum velocity of approximately 115 mm/sec if implemented as a sinusoidal input, which is well below the velocity of 300-400 mm/sec.

However, the maximum force capacity of this specific MTS machine is 100 kN. A device that could be tested at the maximum machine velocity of 300-400 mm/sec would have to have a device force under these conditions of less than 100kN. Using the velocity relationship, as defined in Equation (9-2), this 100kN limit equates to a quasi-static force capacity of approximately 35kN. Although it was a desired outcome of this work, budget constraints did not allow a device of this size to be constructed.

However, it should be noted that although this research has not extended to these high velocity tests, previous research into the larger devices has. In the work of Robinson and Greenback (1976) and Cousins and Porritt (1993), testing of similar devices is undertaken at velocities up to approximately 5m/s without any notable change in device behavior. Originally, these works reported a different response regime at higher velocities (Robinson and Greenbank 1976). However, that phenomenon was later attributed to the difference between the bulged-shaft and constricted tube type of devices. Therefore, although the work of this thesis has not been able to undertake high velocity testing of the devices, the behavior under these circumstances can be predicted with a reasonable level of confidence and the results presented fit the context and values derived in the other work very well.

9.3. Rotational Formulation for Moment Frame Conncetions

9.3.1. Structural Flexibility

Chapter 7 investigated the use of HF2V devices in a steel beam-to-column moment frame connection, as shown schematically in Figure 9.5a. The top-hung steel flange (beam) connection can be modeled as a rotational version of the linear (translational) damper model presented above. The presence of the beam and column in effect provide additional sources of flexibility. Thus, in extending the behavioural model to capture the rotational effects, the structural elements must first be considered without the displacement/rotation contributions from the damper displacement, y. If the damper is locked, such that $y = 0$, then the flexibility contributions of the structural elements can be determined. Figure 9.5b has the potentiometers on the damper which record these displacements labelled. The total displacement between the damper mount and the column face is the system displacement, z, and the potentiometer acting on the unstressed end of the shaft measures the actual damper displacement, y. The effective spring displacement, x, was not directly measured, but this measurement can be obtained from the measurements of z and y, and using Equation (9-1a).

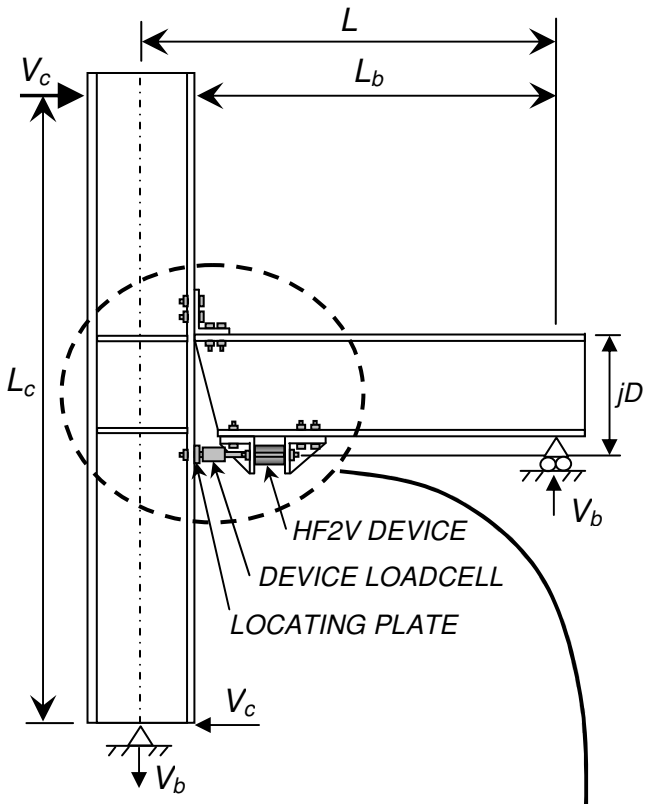

a) Experimental subassemblage

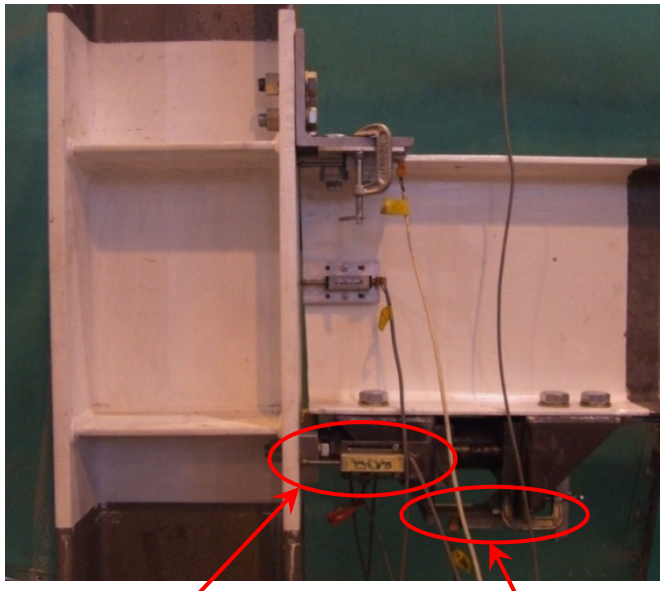

b) Photograph of joint with damper

Figure 9.5: Steel beam-to-column connection with HF2V device

The total displacement at the top of the column shown in Figure 9.5a becomes a combination of displacement contributions from the column, the beam, and the connection rotation due to damper connection flexibility and angle flexibility. This relationship can be written:

$$\Delta_T = \Delta_C + \Delta_b + \Delta_x \tag{9-17a}$$

$$\theta_T = \theta_C + \theta_b + \theta_x \tag{9-17b}$$

where Δ_T = the total displacement due to all flexibility effects; Δ_C = the displacement contribution from column flexibility; Δ_b = the contribution from beam flexibility; and Δ_x = the contribution due to the connection rotation as a result of damper connection and top angle flexibility, and shear deformation of the column panel zone. The symbols in Equation (9-17b) are the rotational contributions, where θ_T = the total rotation due to all flexibility effects; θ_C = the rotation of the column due to column flexure; θ_b = the rotation due to beam flexure; and θ_x = the rotation due to connection and damper connecting element flexibility.

Each of these individual contributions can be individually defined based on well-known structural mechanics. The drift angle due to column deflection is:

$$\theta_C = \frac{V_C L_C^2}{12EI_C} \tag{9-18}$$

Where V_c = the column base-shear; L_c = defined as the column height, as shown in Figure 9.5a; and EI_c = the column rigidity.

Similarly, the beam rotation, θ_b, due to the beam shear, V_b, is defined:

$$\theta_b = \frac{V_b L_b^2}{3EI_b} \tag{9-19}$$

where L_b = the clear beam length, as shown in Figure 9.5a; and EI_b = the beam rigidity.

From moment equilibrium of the subassembly, the beam shear can be defined:

$$V_b = V_C \frac{L_C}{L} \tag{9-20}$$

where L = the distance from the column centerline to the beam strut location, as shown in Figure 9.5a.

Equation (9-20) can then be substituted into Equation (9-19) to define the beam rotation in terms column shear:

$$\theta_b = V_C \frac{L_b^2}{3EI_b} \frac{L_c}{L} \tag{9-21}$$

During elastic deformation the beam rotation will be equal to the column rotation, so no further transformation is required.

The rotation of the column due to the overall joint flexibility components, f_D, can be determined based on simple geometric transformations. For a given damper force, F_D, the

displacement across the connecting elements, x, is given by Equation (9-2) ($x = f_D F_D$). From this displacement, x, the column rotation can be defined as:

$$\theta_x = \frac{f_D F_D}{jD} \tag{9-22}$$

where f_D = the flexibility associated with the damper connections, shear deformation of the panel zone, and deflection of the top angle; jD = the internal lever arm between the top angle/flange-hung connection and the line of the re-action of the damper, as shown schematically in Figure 9.5a. Moment equilibrium of the beam requires:

$$F_D = \frac{V_b L_b}{jD} \tag{9-23}$$

This result can be combined with Equation (9-20) to give column shear as a function of the damper resistance:

$$V_C = F_D \frac{jD}{L_b} \frac{L}{L_C} \tag{9-24}$$

Substituting Equation (9-24) into Equation (9-22) gives the column rotation as a function of column base-shear, V_c:

$$\theta_x = V_C \frac{f_D L_b L_c}{(jD)^2 L} \tag{9-25}$$

All of these components can now be summed to obtain the overall elastic structural drift, θ_S, as a function of column base-shear:

$$\theta_S = V_c f_\theta \tag{9-26}$$

where f_θ = the total rotational elastic flexibility, defined by dividing Equation (9-17b) by the column shear force, V_C, to get rotation flexibility:

$$f_\theta = f_{\theta c} + f_{\theta b} + f_{\theta x} \tag{9-27}$$

where the results of Equations (9-18), (9-21), and (9-25) are divided by the column base-shear to obtain the flexibility and substituted into Equation (9-27) to give:

$$f_\theta = \frac{L_C^2}{12EI_c} + \frac{L_C L_b^2}{3LEI_b} + \frac{f_D L_b L_C}{(jD)^2 L} \tag{9-28}$$

9.3.2. Connection Flexibility

In Equation (9-28) the connection flexibility, f_D, encompasses components from the damper and its connection elements. This expression can be expanded as follows:

$$f_D = f_{tr} + f_{dr} + f_{aa} + f_{af} + f_s \tag{9-29}$$

in which f_{tr} = the axial flexibility associated with the damper tie-rods/connecting rods and load-cell; f_{dr} = the axial flexibility associated with the retaining bolts across the damper,

which stretch during damper action; f_{aa} = the axial flexibility of the bottom leg of the angle connection; f_{af} = the flexibility associated with flexure/bending of the angle bracket during loading; and f_s = the flexibility associated with the column shear across the column panel zone. These components of flexibility are defined as follows.

The tie-rod flexibility is defined:

$$f_{tr} = \frac{L_{tr}}{EA_{tr}} \tag{9-30}$$

where L_{tr} = the stressed length of the damper shaft and axial elements connecting the damper to the column face; and A_{tr} = the total cross-sectional area of the tie-rods/damper shaft.

The damper rods/retaining bolts that hold the damper end-caps together elongate during tensile loading of the damper, with flexibility defined:

$$f_{dr} = \frac{L_{dr}}{EA_{dr}} \tag{9-31}$$

where L_{dr} = the stressed length of the damper retaining bolts; and A_{dr} = the total cross-sectional area of the damper-rods/retaining bolts.

The axial flexibility of the bottom leg of the angle connection is defined:

$$f_{aa} = \frac{L_{aa}}{EA_{aa}} \tag{9-32}$$

where L_{aa} = the effective stressed length of the bottom leg of the angle connection; and A_{aa} = the cross-sectional area of the bottom leg of the angle.

The flexibility associated with the flexural deformation/bending of the top angle is defined:

$$f_{af} = \frac{L_{af}^{\ 3}}{C\,EI_{af}} \qquad (9\text{-}33)$$

in which L_{af} = the effective length of the top leg of the angle that is undergoing bending; I_{af} = the second moment of area of the top leg of the angle about the axis of bending; and C = a constant dependent on the assumption used for the boundary conditions, where C = 3 for fixed-free boundary conditions and C = 12 for fixed-fixed boundary conditions based on elementary beam bending theory.

The flexibility from shear deformation is defined:

$$f_S = \frac{jD}{G\,t_w\,D_{col}} \qquad (9\text{-}34)$$

where jD = as previously defined in Figure 9.5a, the distance between the damper line of action and the top flange connection; G = the shear modulus of the column material; t_w = the thickness of the column web; and D_{col} = the total depth of the column.

Damper shaft motion, y, results in small angle rigid body rotation component that must also be considered in addition to the elastic components. The rotation of the column due to damper motion can be determined from:

$$\theta_y = \frac{y}{jD} \tag{9-35}$$

where θ_y = the drift angle due to damper displacement y, and in derivative form is defined:

$$\dot{\theta}_y = \frac{\dot{y}}{jD} \tag{9-36}$$

Thus, from Equations (9-2) and (9-24), the column base-shear can now be defined as a function of damper properties:

$$V_C = F_D\left(\frac{jD\,L}{L_b L_C}\right) = \left(\frac{jD\,L}{L_b L_C}\right) C_\alpha \left|\dot{y}\right|^\alpha \operatorname{sgn}(\dot{y}) \tag{9-37}$$

Or in terms of rotational velocity using Equation (9-36):

$$V_c = C_\theta \left|\dot{\theta}_y\right|^\alpha \operatorname{sgn}\left(\dot{\theta}_y\right) \tag{9-38}$$

where:

$$C_\theta = \frac{jD\,L}{L_b L_C} C_\alpha \left(jD\right)^\alpha \tag{9-39}$$

9.3.3. Numerical Implementation

The model terms for the moment-rotation structural system are analogous to the force-deformation (translational) damper system model that was previously presented and validated in Section 9.2. The flexibility terms, as expressed in Equations (9-26) and (9-28) are analogous to the spring flexibility, f_D, in the simple translational model. Likewise, the rotation component from damper motion, $\dot{\theta}_y$, defined in Equation (9-36) is analogous to the damper term, y, in the damper model. Therefore, the numerical predictor-corrector solution can be modified to utilize these common facets, and thus be re-formulated to define a relationship between joint rotation and column base-shear.

From Equation (9-16) it follows that the predictor step is:

$$V_{c,i+1} = V_{c,i} + \frac{\Delta t}{f_\theta}\left(2\dot{\theta}_{S,i} - \dot{\theta}_{S,i-1}\right) \tag{9-40}$$

During the initial few time-steps, a different approximation must be used, as the backward difference values may not be available for application. Therefore, during these initial few steps, the base-shear can be obtained by considering that initial deformation will be essentially governed by the elastic regime only, thus:

$$V_{C,i} = \frac{\theta_{z,i}}{f_\theta} \tag{9-41}$$

where θ_z = the total known input rotation to the system; and f_θ = the total elastic flexibility as defined previously in Equation (9-27).

The corrector step takes a very similar form to that previously presented for the simplified damper model presented in Equations (9-13) and (9-14), and is defined:

$$\dot{\theta}_{y,i} = \frac{\theta_{z,i+1} - \theta_{z,i} + \theta_{S,i}}{\Delta t + f_\theta C_\theta^{1/\alpha} \left| V_{C,i} \right|^{1-1/\alpha}} \tag{9-42}$$

This new value of $\dot{\theta}_{y,i}$ can then be used as a corrector step, to re-calculate the system force, $V_{c,i}$, using:

$$V_{c,i} = C_\theta \left| \dot{\theta}_{y,i} \right|^\alpha \operatorname{sgn}\left(\dot{\theta}_{y,i} \right) \tag{9-43}$$

As before, this system of equations can be iterated to converge onto a solution within each time-step. Alternatively, this predictor-corrector approach can be used without iteration, with the limitation that it is only conditionally stable and must utilize a sufficiently fine time-step.

9.3.4. Joint Opening-Closing: Modelling Stiffness Switching

When a top flange-hung beam-to-column moment connection of the type described in Chapter 7 and shown in Figure 9.5 opens and closes, different stiffnesses are observed. When the connection is undergoing a loading portion of the response, and the sign of the velocity is the same sign as the force, the vertical leg of the top angle is being subjected to single bending, thus a value of $C = 3$ is applicable in Equation (9-33). Conversely, when the connection is being unloaded and the sign of the velocity is different to the sign of the force, the vertical leg of the top angle is being subjected to double bending, thus a value of $C = 12$ is applicable in Equation (9-33). Based on the above arguments and supported by experimental

observations, under one completely reversed cycle of loading the stiffness/flexibility of the connection will switch when these criteria are met. A switching function has been devised to model this phenomenon:

$$f_\theta = \left(\frac{f_{\theta 1} + f_{\theta 2}}{2}\right) + A\left(\frac{f_{\theta 1} - f_{\theta 2}}{2}\right)\tanh\left[50\left|\theta_{Z,i} - \theta_{reset}\right| - \pi\right] \tag{9-44}$$

where $f_{\theta 1}$ = the overall flexibility when C = 3; and $f_{\theta 2}$ = the overall flexibility when C = 12. In Equation (9-44) a constant of 50 was found to provide a suitable rate of change of the stiffness, and the argument A is calculated at each time step, and is defined:

$$A = \text{sgn}\left((\theta_{Z,i} - \theta_{Z,i-1})(V_{C,i-1})\right) \tag{9-45}$$

where the argument A can be monitored for a change, and when the change is detected, the current value of θ_Z is defined as the reset drift, θ_{reset}. The reset displacement is then used to define the change in flexibility in Equation (9-44).

9.3.5. Beam-Column Joint Model Validation

A steel beam-column connection with top-hung angle connection was used as the experimental specimen, as described in Chapter 7 and shown in Figure 9.5. The 2D specimen utilized a cut back beam end to allow positive and negative (gap-opening and closing) joint rotations. Basic specimen dimensions, as defined in Figure 9.5, were L_c = 2 m, L = 1.5 m, using member sections 360UB44.7 and 310UC15 for the beam and column respectively. The HF2V device utilized was the same as that previously characterized and shown in Figures 9.3 and 9.4.

The connection between the beam and column was fitted with four potentiometers to measure connection rotation and any torsion present. A photograph of the experimental setup is presented in Figure 9.5b which shows the location of the three potentiometers on the south side of the setup. The top potentiometer measured angle displacement/pull-off from the column face, while the remaining potentiometers at the approximate beam mid-height, and at the damper line of action measured the connection rotation.

Ideally, the top potentiometer would be measuring at the top angle-beam flange interface. However, physical constraints restricted the position of the potentiometer stylus to be 25mm below this interface. If the beam end acts with only rigid rotation and shear deformation, the potentiometer reading can be expected to be linear with eccentricity from the centre of rotation. By checking the potentiometers for this linearity, the translation of the angle bracket at the angle/flange interface can be calculated, and can be used to validate the assumptions used to predict the angle flexibility contributions.

Figure 9.6a presents the experimentally observed connection behavior under reversed cyclic loading for drift amplitudes of 0.25, 0.5, 1, 2, 3, and 4%. Figure 9.6b shows the modeled results using Equations (9-40) to (9-45). Although good agreement between the observed and modeled results is evident, several points should be noted and are discussed in the next section.

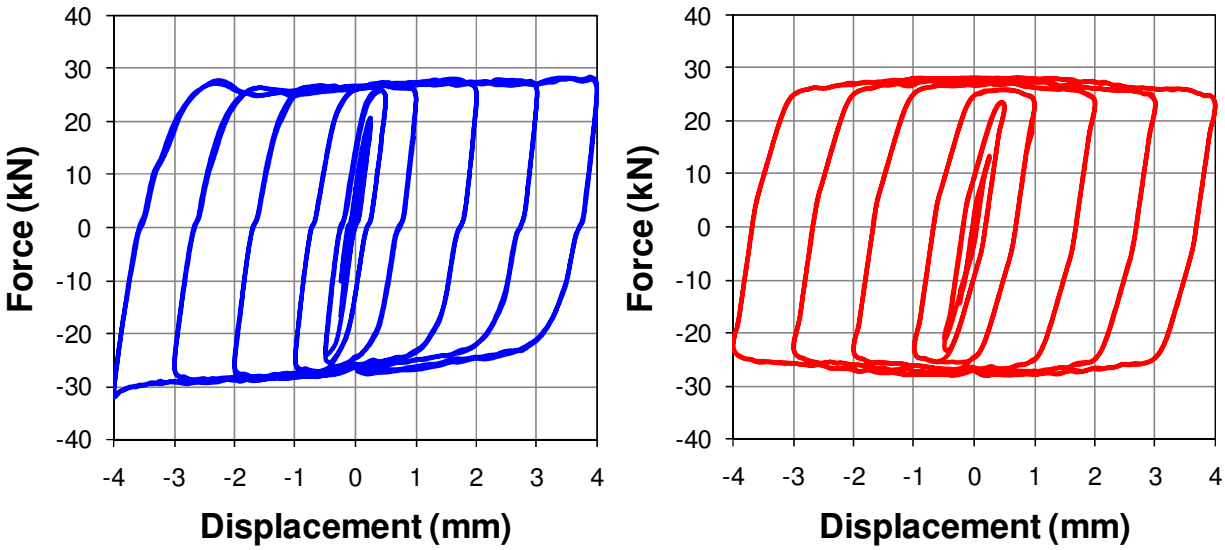

a) Experimental Results *b) Model Results*

Figure 9.6: Comparative results for the overall subassembly performance

9.4. Discussion: The Influence of Flexibility on Performance

9.4.1. Damper System Flexibility

It is evident that the analytical model and experimental results show good agreement. To thoroughly validate the analytical model, each flexibility component can be individually examined based on local potentiometer data. By delineating these effects the model assumptions can be individually validated, providing a thorough validation of the analytical model, and greater insight into key design aspects of such a connection. This result enables the experimentally validated assumptions and fundamental rational mechanics to be used for any such connection to accurately predict the overall response.

The displacements recorded by the two potentiometers located at the damper line of action are very similar, and indicate that no significant out-of-plane motion or torsion is present. The rigid body connection rotation can be determined from the joint potentiometers, which can determine the input value z into the damper-spring system, and the elastic deflections that can be used to experimentally determine an overall elastic subassembly stiffness.

The measured damper force is plotted against the measured damper system displacement, z, (from the potentiometer shown in Figure 9.5b) to present the overall damper/connection system response in Figure 9.7a. Also plotted in Figure 9.7a is the measured damper force against the damper displacement, y, measured by a potentiometer on the unstressed portion of the damper shaft (shown in Figure 9.5b). The difference in these two plots is the result of connection flexibility. It is evident in Figure 9.7a that the connection components have added significant flexibility to the system.

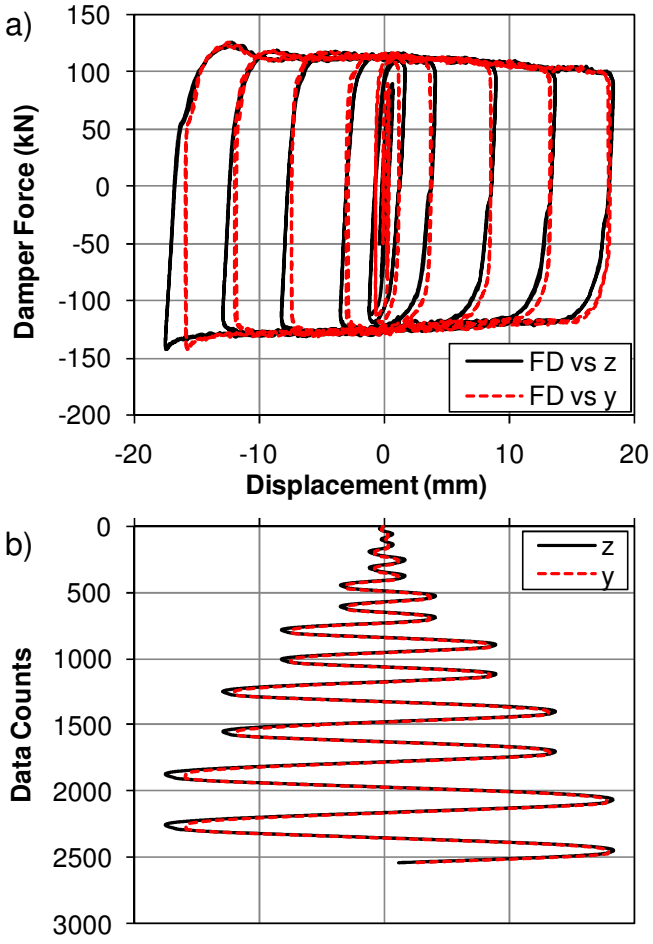

Figure 9.7: a) The damper force F_D plotted against the damper displacement y, and joint displacement at damper location, z, and b) the damper and joint displacements corresponding to those in a).

Figure 9.7b shows the displacement values of y and z plotted against data counts, which correspond to the displacements in Figure 9.7a. They are quite similar at small drifts, but at larger drifts they show increased disparity. These peaks correspond to where device velocity $\dot{y} = 0$, and the direction switches. These observations imply that the regions where connection flexibility has the biggest influence is on direction changes at large drifts, where the reaction mechanisms change and take-up/slack in the system will have the biggest effect.

9.4.2. Connection Flexibility

The difference between the plots in Figure 9.7b represents the flexibility components and is the effective spring displacement, x, as defined in Equation (9-1a) and plotted in Figure 9.8a. This result can be used to derive an experimental value of the spring flexibility f_D. The measured value of x is compared to a calculated value of x based on the measured damper force F_D and Equation (9-2) ($x = f_D F_D$). The value of f_D is modified to minimize the least-squares error between the measured and calculated values of x. The resulting plot of the measured and calculated values of spring/connection displacement, x, is presented in Figure 9.8a.

It is evident that a single (uniform) value of f_D may not accurately represent the experimental data. The most obvious cause of this issue is the different reaction mechanism in the top-hung angle connection. The angle will be in axial tension in the bottom leg and bending in the top leg during gap closing, but will act with axial compression and a form of direct bearing onto the column face during gap opening. These mechanisms have different associated flexibilities that must be reflected in the analytical model. These differences in flexibility were incorporated into the analytical model by the addition of the stiffness switching presented in Section 9.3.4.

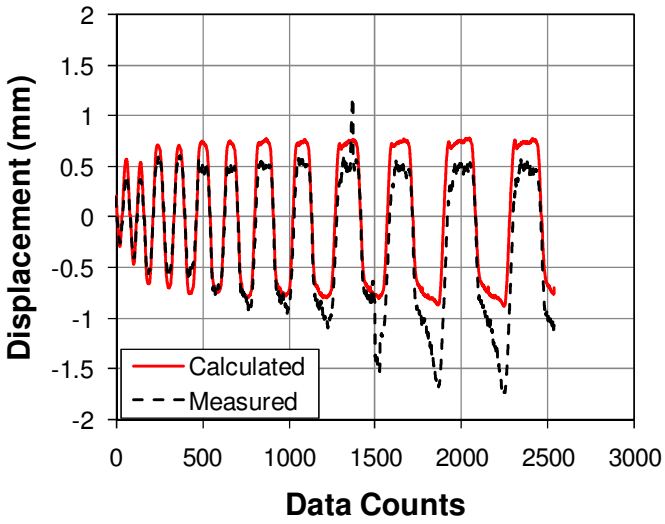

a) elastic spring/connection displacement, x (= z - y)

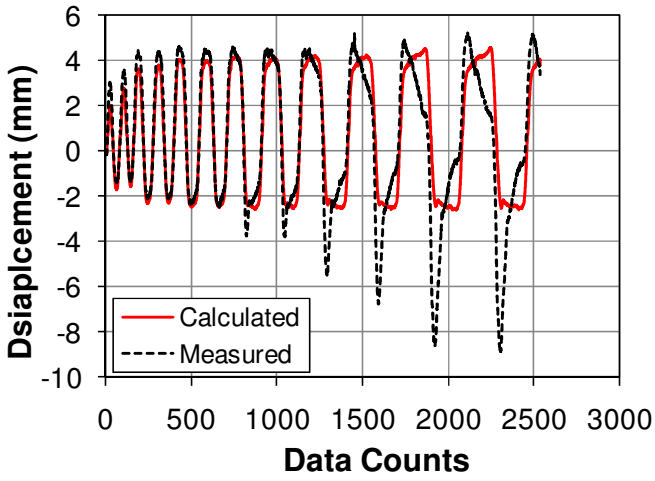

b) elastic structural displacement component

Figure 9.8: Experimentally measured and calculated elastic displacement values

Another important aspect evident in Figure 9.8a is that the measured and calculated values of spring displacement, x, follow a very similar trend for small amplitude motions. It is only for large amplitude motions that significant deviations are seen. These deviations are due to prying effects, where the vertical leg of the top angle lifts off the column face under large drifts, and possible low level yielding of the connection elements at the hinged connection.

The analytical value of the connection flexibility parameter, f_D, can be calculated based on the experimental dimensions. Table 9.1 presents the individual contributions and the overall

flexibility values for the experimental set-up, as used in the model presented in Figure 9.6b. From these values of flexibility, the overall structural flexibility parameter, f_θ can be determined using Equation (9-28). Since the rigid body connection angle can be obtained from the joint potentiometers, the rigid body component of column displacement can be subtracted to get the elastic component. This elastic component is a function of elastic member deformations and elastic deformation of the experimental setup, such as the axial compression/tension in the beam support strut, and connection to the strong floor.

Table 9.1: Damper/Connection Flexibility Components

Flexibility Component	**Calculated Value (x 10^{-6} mm/kN)**	**Equation**
Angle-flexure: $f_{af} = \frac{L_{af}^{\ 3}}{C\,EI_{af}}$	15.7 (3.9)*	(9-33)
Angle-axial: $f_{aa} = \frac{L_{aa}}{EA_{aa}}$	0.1	(9-32)
Shear: $f_S = \frac{jD}{G\,t_w\,D_{col}}$	1.0	(9-34)
Damper-rods: $f_{dr} = \frac{L_{dr}}{EA_{dr}}$	0.5	(9-31)
Tie-rod: $f_{tr} = \frac{L_{tr}}{EA_{tr}}$	3.2	(9-30)
Total Flexibility: f_D	20.4 (8.6)*	(9-29)
*for C = 3 and (C = 12) where applicable		

From the elastic displacement component, a total experimental elastic member flexibility can be calculated. The displacement is defined as $d = f_\theta V_{col}$ and the value of f_θ is adjusted to minimize the least-squares error to the calculated value, the result of which is presented in Figure 9.8b. As before, a single uniform stiffness value does not provide good agreement with the experimental data due to the different deformation regimes during different loading directions, or at points when the load or direction switch.

It is evident in Figure 9.6 that the variable stiffness is important to capture the different reaction mechanisms that are present in the experimental results. Overall, the model and experimental results show good agreement. However, as previously discussed in Chapter 7, the experimental results show a slight bi-linear behavior that is attributed to additional friction/binding of the shaft due to the lateral loading. This lateral load is due to joint motion, which is an arc about the rocking edge, whereas the shaft can only move in a linear path. Therefore, some bending may well be induced within the shaft, resulting in a variable friction force which contributes to the column base-shear. The use of clevis attachments that allow rotation at the shaft connection in future tests will maintain only axial force in the damper, eliminate the bi-linear component, and show an improved agreement between the model and experimental results.

Another key aspect evident in Figure 9.6 is the large influence that the angle reaction regime and associated flexibility has on the overall elastic stiffness of the subassembly. It is advantageous to have a high initial stiffness and low yield drift, for a given yield force. Therefore, to stiffen the connection the angle connection is a primary consideration, and in future connections the top-hung angle may be modified to incorporate a split-tee connection (WT-shape). The angle used in the experiment was equivalent to a L6 x 6 x ½ and could be easily replaced by a WT shaped connection, such as the WT6x39.5. The flange could then be bolted to the column face above and below the top beam flange, and the web would be used for connection to the beam flange. Using such a split-tee connection would reduce the flexibility to approximately 10% of that defined for the top-hung angle under fixed-pinned conditions. This would reduce the overall flexibility by approximately 70% for that case, and by at least 25% for the fixed-fixed angle assumption. This connection detailing should result

in a higher initial elastic stiffness (reduced flexibility), lower yield drift, and a more rigid structure. It is advantageous to have this higher initial stiffness to reduce structural drifts.

9.5. Summary

Based on the investigation described in this chapter, the following conclusions are drawn:

1. A simple damper model was developed that accounts for connection flexibility and velocity-dependence of the damper. The damper model was calibrated to experimental data, and shows good agreement with the overall behavior, as well as the velocity-dependence. The iterative predictor-corrector solution was also validated with the exact solution from a standard root-finding algorithm, showing an almost perfect match.

2. The damper model was then extended to a base-shear to drift relationship, by accounting for structural member flexibility and geometric transformations. The model, based entirely on rational mechanics, provides a good analytical representation of lateral load-rotation behavior, without empirically determined constants.

3. It is important to recognise the slight asymmetry that exists in the steel connection behavior due to different reaction mechanisms of the top angle connection. To accommodate this phenomenon a continuous numerical switch function was developed. Implementation shows good agreement with the experimental results.

Assessment of the flexibility components for all structural elements provides insight into both model prediction and design improvements for future connections. Individual consideration of the member flexibility effects indicates that the top angle may contribute a large amount to the total flexibility.

Chapter 10: Advanced Model Of Jointed Precast Concrete Connections

In Chapter 8 a relatively simple model is presented for jointed precast concrete connections with unbounded, post-tensioned prestress and HF2V devices. Although this model is relatively easy to implement and provides good agreement with the experimental results of Chapters 5 and 6, some limitations exist. In particular, the model did not incorporate friction, did not include prestress reduction on subsequent cycles if any tendon yield occurred, and did not provide any means to easily incorporate asymmetry from non-centrally located prestressing tendons. This chapter presents a more detailed model that incorporates these additional effects and provides a more robust model that can be used on a broader range of prestressed DAD connection designs.

Particular attention is given in this chapter to developing a robust model that can also accommodate small reversals within the displacement loading regime, as would be seen in a typical seismic event. The model is also extended to incorporate the effects of the HF2V devices, and the associated flexibility from the elements that connect the devices to the structure. Although the model is applied to the use of HF2V energy dissipation devices, it is general, and can accommodate any non-linear rate-dependent damper, or structural dissipator.

10.1. Introduction

The model of Chapter 8 will provide accurate results for jointed precast connections that utilise straight tendon profiles and have low inherent friction if no tendon yield is observed. However, if any notable friction is present and/or if any tendon yield occurs, the model of Chapter 8 no longer provides accurate results. This chapter extends Chapter 8 to incorporate these aspects, and the results are validated against the experimental results of Chapter 4.

10.2. Modelling Connection Behaviour

As detailed in Chapter 8, overall joint hysteresis for this type of un-bonded post-tensioned prestressed armoured (damage-protected) concrete connections is a combination of elastic member deflection and rigid body rotation. The presence of the unbonded post-tensioned prestress initially delays gap opening. Lateral column deflections in this regime are thus a function of the elastic deformation of structural elements only, until the applied moment at the connection leads to gap opening. This resisting moment is provided by the clamping effect of the prestress within the beam at the column interface. The column shear required for gap opening is therefore a function of the level of prestress provided by the beam tendons.

The column shear and flexural displacements associated with gap-opening deflection can be calculated using beam bending theory and rigid body kinematics. The post gap-opening stiffness remains until the tendon elongation associated with the rigid body component reaches tendon yield. At this point, further column deflection occurs with no further increase in column shear. Any inelastic (plastic) tendon elongation will reduce the initial post-tensioning force on unloading and any subsequent cycles.

10.2.1. Modelling the Initial Elastic Loading Behaviour

Under initial elastic loading both the beam and column deflect without gap-opening at the connection and contribute to the total subassembly displacement. Figure 10.1 present a schematic diagram of the subassembly showing the associated nomenclature. Note that the definitions are slightly different to those defined in Chapter 8.

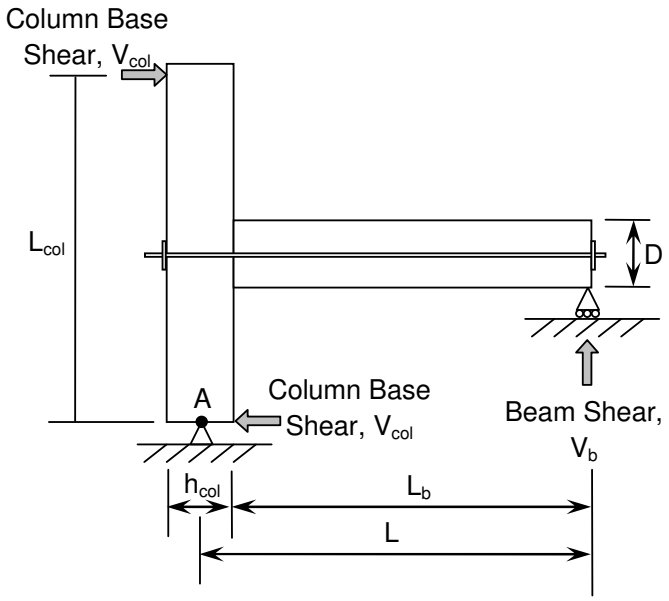

Figure 10.1: Beam-column subassembly dimensions

During the initial elastic deformation regime the column elastically deflects in double-bending, as shown in Figure 10.2. The lateral deflection at the top of the column due to column deflection is defined as $\Delta_{col,C}$ and can be divided by the column height, L_{col}, to obtain the associated column rotation (or drift), $\theta_{col,C}$, if desired. The deflection, $\Delta_{col,C}$, as a function of the applied column shear force, V_{col}, can be calculated from beam bending theory:

$$\Delta_{col,C} = V_{col}\left[\frac{(L_{col}-D)^3}{12EI^*_{col}}\right] \tag{10-1}$$

where EI^*_{col} is the effective column stiffness, $(L_{col}-D)$ is the effective column length, and all other terms are defined in Figure 10.1.

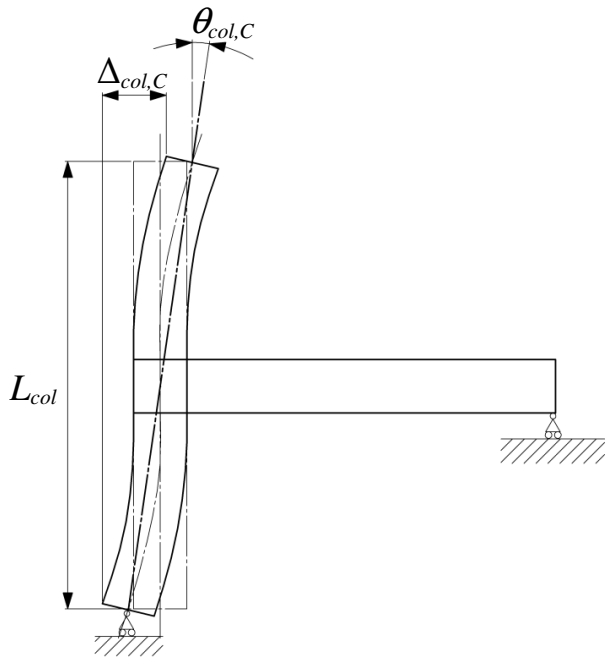

Figure 10.2: Schematic Diagram of elastic column deflection

In addition, the beam will elastically deflect under lateral loading, inducing a rigid column displacement, $\Delta_{col,B}$, and rotation, $\theta_{col,B}$, as shown in Figure 10.3, where $\Delta_{col,B} = \theta_{col,B} L_{col}$. The column rotation resulting from beam deflection is equal to the chord angle of the beam, as shown in Figure 10.3.

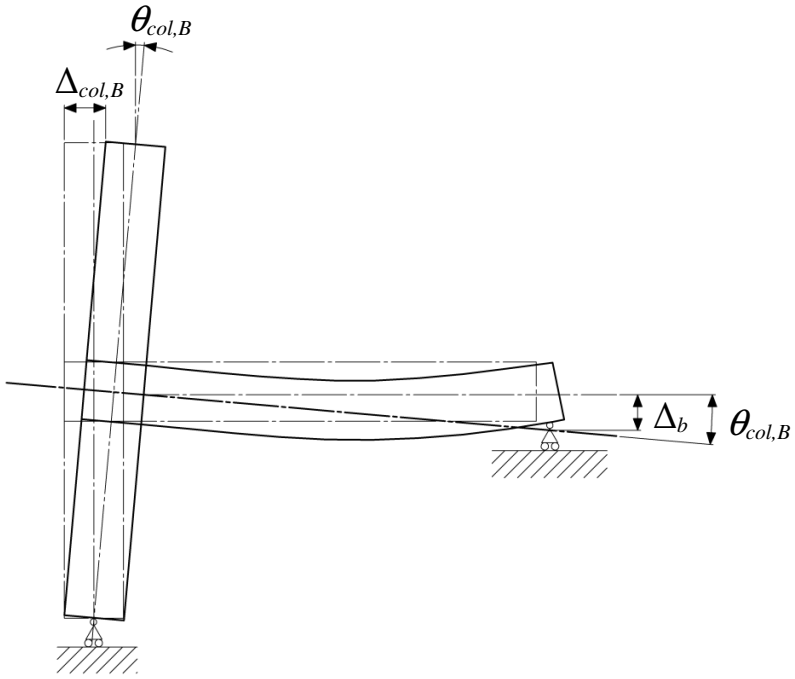

Figure 10.3: Schematic diagram of column rotation from beam deflection, where Δ_b is the effective vertical deflection of the beam ($\Delta_b = \theta_{col,B} L_b$)

The effective vertical deflection/centre-line displacement at the tip of the beam, Δ_b is also shown in Figure 10.3. Note that due to the pinned connection, no actual displacement exists at the beam end, and Δ_b is the effective displacement of the beam end from the position it would be had the beam remained rigid. Thus, Δ_b is given from elementary beam bending theory as a function of beam shear, V_b:

$$\Delta_b = \frac{V_b L_b^3}{3EI_b^*} \tag{10-2}$$

where EI_b^* is the effective beam stiffness. The effective stiffness values for the beam, EI_b^*, and column, EI_{col}^*, have been approximated using moment area methods as 26% of the gross stiffness for uni-directional testing and 14% for bi-directional testing (Li et al. 2008).

Equation (10-2) can be divided by the beam length, L_b, to obtain the beam chord angle, which is also equal to the column rotation, $\theta_{col,B}$, as shown in Figure 10.3, and defined:

$$\theta_{col,B} = \frac{V_b L_b^2}{3EI_b^*} \tag{10-3}$$

By considering overall moment equilibrium of the subassembly about the pivot at the base of the column, labelled A in Figure 10.1, the relationship between column shear, V_{col}, and beam shear, V_b is defined:

$$\sum M_A = 0 = V_{col} L_{col} - V_b L \tag{10-4a}$$

$$V_b = V_{col} \frac{L_{col}}{L} \tag{10-4b}$$

So that the deflection at the top of the column resulting from beam deflection can be expressed as a function of column shear using Equations (10-3) and (10-4b):

$$\Delta_{col,B} = \theta_{col,B} L_{col} = V_{col} \frac{L_{col}^2 L_b^2}{3LEI_b^*} \tag{10-5}$$

The components of deflection at the top of the column that result from column and beam deflections will sum to give a total displacement, Δ_{col}, defined:

$$\Delta_{col} = \Delta_{col,C} + \Delta_{col,B} \tag{10-6a}$$

$$\Delta_{col} = V_{col} \left[\frac{(L_{col} - D)^3}{12EI_{col}^*} + \frac{L_{col}^2 L_b^2}{3LEI_b^*} \right] \tag{10-6b}$$

10.2.2. Inclusion of Rigid-Body Loading Behaviour

Following the elastic deformation regime, the subassembly will undergo rigid-body rotation after gap-opening, as shown in Figure 10.4. This rigid body regime requires additions to the model for the post gap-opening regime and associated mechanics.

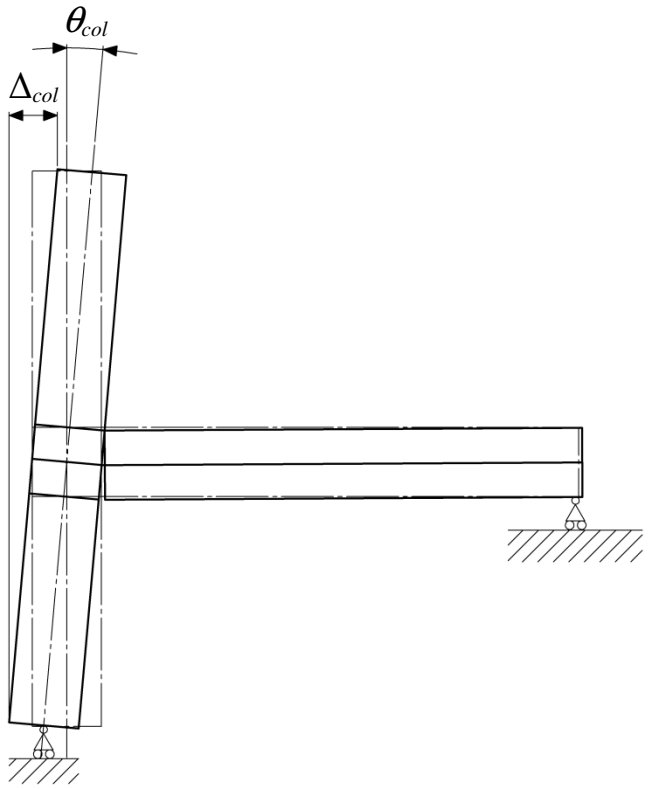

Figure 10.4: Schematic diagram of column rotation from rigid body motion due to gap-opening at the beam-column interface

Figure 10.5 presents the bi-linear elasto-plastic backbone curve for monotonic (pushover) behavior of the subassembly. It includes the pre-gap-opening elastic deflection, and post-gap-opening behavior. This plot does not include the effects of friction, or any contributions from supplemental damping.

The combination of pre gap-opening elastic beam deformation, post gap-opening deformation resulting in elastic tendon elongation, and post gap-opening deformation with inelastic (plastic) tendon elongation creates an overall tri-linear response. This overall tri-linear loading path can be calculated based on elastic member deflection and rigid body rotation. Note that Figure 10.5 is similar to Figure 8.1, but now the backbone curve is defined in terms of the connection moment, rather than column shear.

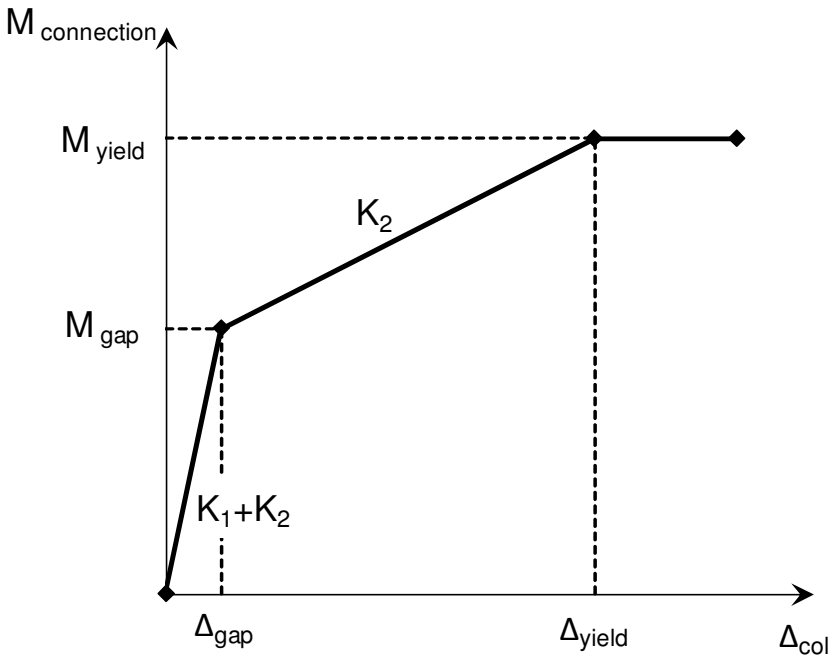

Figure 10.5: Bilinear-elastic-plastic monotonic backbone curve of a jointed precast system, where the connection moment is defined $M = V_{col}L_{col}$.

Initial elastic deformation of the subassembly prior to gap-opening has stiffness (K_1+K_2). Further elastic beam deflection and rigid body rotation after gap-opening gives stiffness K_2. Finally, the unbonded post-tensioned tendons yield.

In Figure 10.5, M_{gap} is defined as the connection moment at gap opening. Here Δ_{gap} is the displacement at the top of the column from elastic deformation of the subassembly at gap opening. Further, Δ_{yield} is the displacement of the subassembly from beam deflection at the onset of plastic deformation of the post-tensioned tendons, which occurs at a connection moment of M_{yield}. All of the points shown in Figure 10.5 can be easily calculated from statics and kinematics, using the subassembly measurements in Figure 10.1.

The moment produced at the beam-column interface (rocking connection) at gap-opening, M_{gap}, under positive and negative rotations is respectively defined:

$$M_{gap} = F_{PT\_initial}\left(j_{PT}^{\pm}\right)D \tag{10-7}$$

where $F_{PT\_initial}$ is the total initial tensioning force in the tendons, j_{PT} is the fractional lever-arm of the tendon, the + and – indices refer to rocking about the bottom and top corners of the beam end, respectively, and D is the beam depth. Note that j^{+} and j^{-} are proportional scalars of the beam depth with $j^{+} + j^{-} = 1$, as shown in Figure 10.6.

In Figure 10.6, θ_{con} is the connection rotation between the beam end and column face. For a theoretical column with no width, the vertical rotation of the column at the centreline is equal to the connection rotation. For a realistic column width, this value will change by a ratio of half the beam length, L_b (half the column face to column face length) to half the bay width, L (column centreline to centreline). Therefore, using kinematics to obtain the rigid-body column rotation, θ_{RBR_column}, the connection rotation, $\theta_{connection}$ must be modified by the relation:

$$\theta_{RBR\_column} = \theta_{connection}\,\frac{L_b}{L} \tag{10-8}$$

where θ_{RBR_column} is the rigid body rotation of the column.

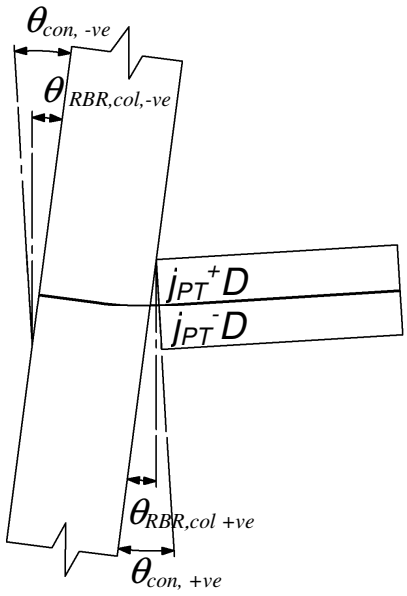

Figure 10.6: Rigid body subassembly deflections showing sign convention and fractional lever-arms j_{PT}^{+} and j_{PT}^{-}, where a centrally located tendon yields $j_{PT}^{+} = j_{PT}^{-} = 0.5$ and equal moments due to prestress for motion in both directions

The displacement at the top of the column due to beam deflection at gap-opening, Δ_{gap}, is defined from the value of connection moment at gap-opening M_{gap} in Equation (10-7). Equation (10-6b) can be re-written at gap opening using $V_{col,gap} = M_{gap}/L_{col}$:

$$\Delta_{gap} = \frac{M_{gap}}{L_{col}}\left[\frac{(L_{col}-D)^3}{12EI_{col}^{*}} + \frac{L_{col}^2 L_b^2}{3LEI_b^{*}}\right] \qquad (10\text{-}9)$$

Moreover, the initial elastic stiffness of the subassembly, (K_1+K_2), as presented in Figure 10.5, can be calculated using Equations (10-7) and (10-9) and is defined:

$$K_1 + K_2 = \frac{M_{gap}}{\Delta_{gap}} \qquad (10\text{-}10a)$$

$$K_1 + K_2 = \frac{M_{gap}}{\frac{M_{gap}}{L_{col}}\left[\frac{(L_{col}-D)^3}{12EI^*_{col}} + \frac{L^2_{col}L^2_b}{3LEI^*_b}\right]} \tag{10-10b}$$

$$K_1 + K_2 = \frac{L_{col}}{\left[\frac{(L_{col}-D)^3}{12EI^*_{col}} + \frac{L^2_{col}L^2_b}{3LEI^*_b}\right]} \tag{10-10c}$$

The connection moment and displacement at tendon yield can be similarly calculated, but occur at the point that plastic strain is induced in the tendons. The connection moment, M_{yield} is given:

$$M_{yield} = \sigma_{yield} A_{PT}\left(j^{\pm}_{PT}\right)D = F_{PT\_yield}\left(j^{\pm}_{PT}\right)D \tag{10-11}$$

where σ_{yield} is the yield stress of the tendons, A_{PT} is the total cross-sectional area of the tendons, and F_{PT_yield} is the total force in the tendons at yield.

Finally, the displacement at the top of the column from elastic and rigid body beam deflection at tendon yield, Δ_{yield}, can be defined:

$$\Delta_{yield} = \Delta_{elastic,yield} + \Delta_{RBR,yield} \tag{10-12a}$$

$$\Delta_{yield} = \frac{M_{yield}}{L_{col}}\left[\frac{(L_{col}-D)^3}{12EI^*_{col}} + \frac{L^2_{col}L^2_b}{3LEI^*_b}\right] + L_{col}\theta_{con,RBR,yield}\frac{L_b}{L} \tag{10-12b}$$

$$\Delta_{yield} = \frac{M_{yield}}{L_{col}}\left[\frac{(L_{col}-D)^3}{12EI^*_{col}} + \frac{L^2_{col}L^2_b}{3LEI^*_b}\right] + L_{col}\frac{(\varepsilon_{yield}-\varepsilon_{initial})L_t}{\eta\left(j^{\pm}_{PT}\right)D}\frac{L_b}{L} \tag{10-12c}$$

where $\Delta_{elastic,yield}$ is the displacement at the top of the column due to elastic subassembly deflection at the onset of tendon yield, $\Delta_{RBR,yield}$ is the displacement at the top of the column resulting from rigid body rotation of the subassembly at the onset of tendon yield, $\theta_{con,RBR,yield}$ is the rigid body connection rotation at the onset of tendon yield, ε_{yield} is the total tendon strain at the onset of plastic deformation, $\varepsilon_{initial}$ is the initial strain in the tendons from post-tensioning alone before gap opening, and η is the number of rocking interfaces spanned by the tendons. In particular, $\eta = 1$ for a subassembly such as that in Figure 10.1, and $\eta = 2$ for the connection of Chapters 5 and 6 where the straight tendon spanned two beam-column interfaces where gap-opening occurs.

Finally, the value of the post gap-opening stiffness, K_2 can easily be calculated from the geometry in Figure 10.5. The stiffness is defined:

$$K_2 = \frac{M_{yield} - M_{gap}}{\Delta_{yield} - \Delta_{gap}} \tag{10-13}$$

If Equations (10-7), (10-9), (10-11), and (10-12c) are substituted into Equation (10-13) and re-arranged then K_2 can be expressed:

$$K_2 = \frac{\left(j_{PT}^{\pm}\right)D\left(F_{PT,yield} - F_{PT,initial}\right)}{\Delta_{RBR,yield} + \left(\Delta_{elastic,yield} - \Delta_{gap}\right)} \tag{10-14a}$$

$$K_2 = \frac{\left(j_{PT}^{\pm}\right)D\left(F_{PT,yield} - F_{PT,initial}\right)}{L_{col}\dfrac{(\varepsilon_{yield} - \varepsilon_{initial})L_t}{\eta\left(j_{PT}^{\pm}\right)D}\dfrac{L_b}{L} + \dfrac{\left(j_{PT}^{\pm}\right)D\left(F_{PT,yield} - F_{PT,initial}\right)}{L_{col}}\left[\dfrac{(L_{col} - D)^3}{12EI_{col}^*} + \dfrac{L_{col}^2 L_b^2}{3LEI_b^*}\right]} \tag{10-14b}$$

Note that the terms in the denominator can be segregated into the rigid body deflection component, $\Delta_{RBR,yield}$, and post gap-opening elastic deflection component $\left(\Delta_{elastic,yield} - \Delta_{gap}\right)$, as seen in Equation (10-14a). If the elastic stiffness is much higher than the post gap-opening stiffness, then the rigid body component will have the major influence of the denominator.

10.2.3. Accounting for Reduced Sections of Tendons

The experimental specimen presented in Chapter 4 had reduced section regions on the post-tensioning thread-bars, where the bars were machined to 75% of the nominal tendon cross-sectional area. These machined down sections localised any inelastic tendon elongation. The tendon sections with this reduced area were coupled to the main tendons and are utilised to enable easy replacement if large tendon yield occurs. These reduced section regions reduce the tendon force, and thus the connection moment at tendon yield. Thus, the value of A_{PT} in Equation (10-11) must represent the cross-sectional area of the machined down section.

Moreover, the reduced section regions will have a higher strain than the rest of the tendon, and as such will induce tendon yield at a reduced total tendon elongation. This factor must be incorporated into the model for accuracy. Figure 10.7 presents a schematic diagram of a tendon under axial tension with a reduced cross-sectional area region.

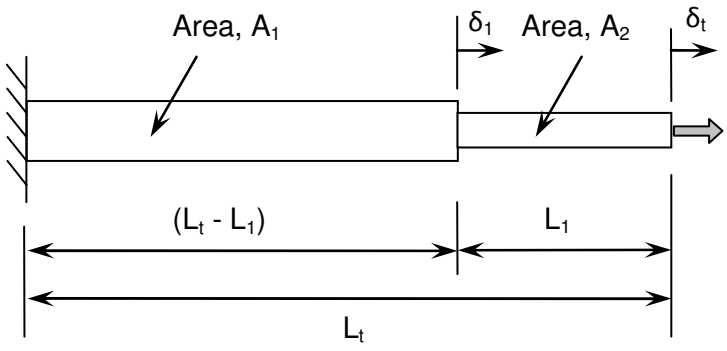

Figure 10.7: Schematic diagram of post-tensioning tendon with reduced section region.

At the onset of yielding in the reduced section region of the tendon, the force, F_{PT_yield}, is defined:

$$F_{PT\_yield} = \sigma_{yield} A_2 = \varepsilon_{yield} E A_2 \tag{10-15}$$

where A_2 is the reduced cross-sectional area of the tendon.

The displacement across the larger section of the tendon, shown as δ_1 in Figure 10.7, due to the applied tendon yield force, F_{PT_yield}, is defined from elementary mechanics and Equation (10-15):

$$\delta_1 = \frac{F_{PT\_yield}(L_t - L_1)}{A_1 E} = \frac{\varepsilon_{yield} A_2 (L_t - L_1)}{A_1} \tag{10-16}$$

where $(L_t - L_1)$ is the length of the larger section of the bar, as shown in Figure 10.7.

Tendon yield occurs when the yield strain is reached in the reduced section region of the bar. Thus, the displacement across this reduced region section of the bar, $(\delta_t - \delta_1)$, at tendon yield is defined simply by multiplying the yield strain by the length of the reduced section of the bar, L_1:

$$(\delta_t - \delta_1) = \varepsilon_{yield} L_1 \tag{10-17}$$

Equations (10-16) and (10-17) can be combined to give the total displacement in the tendon at yield, δ_t:

$$\delta_t = \varepsilon_{yield} L_1 + \frac{\varepsilon_{yield} A_2 (L_t - L_1)}{A_1} \tag{10-18a}$$

$$\delta_t = \varepsilon_{yield} \left[L_1 + \frac{A_2 (L_t - L_1)}{A_1} \right] \tag{10-18b}$$

From Equation (10-18b) an effective tendon length can be defined that encompasses the increase in strain induced from the reduced section region, and the corresponding reduction in total tendon elongation at the onset of yield. The effective tendon length, L_{t_eff}, is defined:

$$L_{t\_eff} = \left[L_1 + \frac{A_2 (L_t - L_1)}{A_1} \right] \tag{10-19}$$

Note that if $A_1 = A_2$, then Equation (10-19) simplifies to $L_{t\_eff} = L_t$. If a reduced section region is machined into the prestressing tendons to localise yielding, then the effective tendon length, L_{t_eff} must be used in place of the gross tendon length, L_t, to predict the yield displacement of the subassembly, Δ_{yield}, in Equation (10-12c), and the stiffness, K_2 in Equation (10-14b). Moreover, the value of the initial strain in the tendon, $\varepsilon_{PT\_initial}$, as used in Equation (10-12c) and (10-14b) must represent the strain in the reduced section of the tendon and is defined:

$$\varepsilon_{PT\_initial} = \frac{F_{PT\_initial}}{A_2 E} \tag{10-20}$$

10.2.4. Incorporation of Prestress Friction Effects

If the connection utilizes a straight unbounded tendon profile and the duct is of a notably larger diameter than the tendon, it is unlikely any significant friction will exist. However, if a draped or bent tendon profile is utilized, as is commonly done for beams carrying gravity loads and for the seismic beams within this study, then frictional effects will affect cyclic loading performance.

Using the formula for prestress loss effects presented in Li et al. (2008), the prestress force F_{PT2} at the joint face with respect to the applied jacking force F_{PT1} is (Li et al. 2008):

$$F_{PT2} = F_{PT1} e^{(-\mu_f \alpha_{PS})} \tag{10-21}$$

where μ_f = angular coefficient of friction; and α_{ps} = the angle change of the tendon (in radians). It should be noted that this equation is an approximation of the force differential that exists within the tendon due to friction between the tendon and the duct it is located in.

Providing the product ($\mu_f \alpha_{PS}$) is small so that higher order terms in the expanded exponential expression can be neglected, the prestress losses due to frictional effects are defined:

$$\delta F = F_{PT1} - F_{PT2} = \mu_f \alpha_{PS} F_{PT1} \tag{10-22}$$

Figure 10.8 presents the effect of friction on the monotonic pushover behaviour. The gap-opening resistance increases. Under cyclic loading, the stiffness changes due to frictional effects. By considering the mechanics of the connection, it is evident that the presence of friction within the tendon-duct system will affect the force in the prestressing tendon across the beam-column interface. A force differential will be present within the tendon where it contacts the duct. Upon reversal the tendon will elastically relax before a force differential of

an opposite sign exists. The elastic relaxation within the tendon during the changing of direction results in a stiffness, K_{fr}, as shown in Figure 10.8, rather than a vertical discontinuity of force, as predicted by models that utilise a signum function on the velocity to define to friction force (Li et al. 2008).

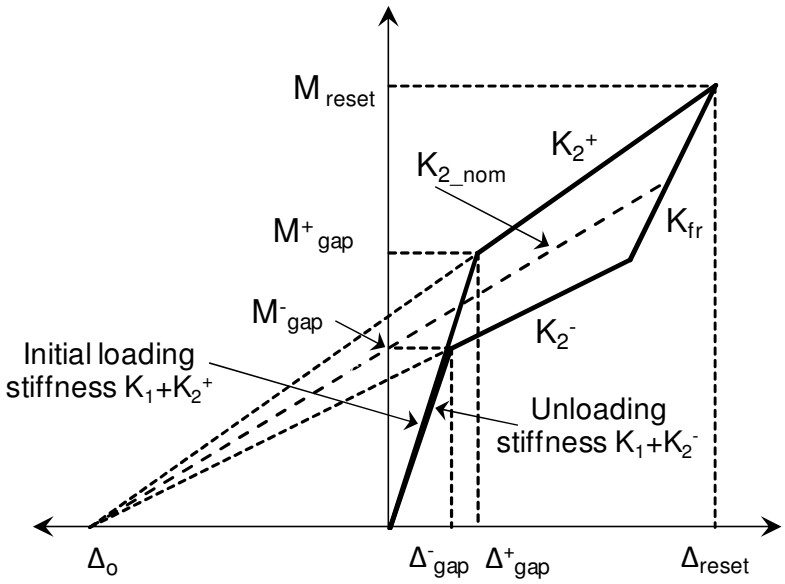

Figure 10.8: Schematic representation of the loading regime with the addition of friction. The dashed line labelled K_{2_nom} represents the post-gap opening stiffness without friction.

The elastic components are now defined as (K_1 + K_2^+) for loading, and (K_1 + K_2^-) for unloading, with the post-gap opening stiffness defined:

$$K_2^+ = K_{2\_nom}\left(1+\mu_f \alpha_{PS}\right) \tag{10-23a}$$

$$K_2^- = K_{2\_nom}\left(1-\mu_f \alpha_{PS}\right) \tag{10-23b}$$

where K_{2_nom} is the nominal post-gap opening stiffness, K_2, without any friction modification, as defined in Equation (10-14), and shown in Figure 10.8. The intersection of the different K_2 lines on the horizontal axis, Δ_o, is the effective origin for the post-gap opening regime. If no initial post-tensioning was present, then the initial elastic loading branch would not exist, and Δ_o would move to the axes origin, such that $\Delta_o = 0$.

10.2.5. Loading Stiffness Definition

In Chapter 8, an explicit compound Menegotto-Pinto formulation is utilised. However, in this chapter, to computationally model this piece-wise behavior in a smooth continuous sense, differential versions of the Menegotto-Pinto (1973) and Ramberg-Osgood (1943) equations are used. To capture all of the different regimes in the response of Figure 10.8, it is necessary to develop different stiffnesses for the loading and unloading behaviour. The overall loading stiffness, $K^{+}(\Delta)$, has three different regions, as shown in Figure 10.9, where the stiffness plot of Figure 10.9b uses the same horizontal axis as Figure 10.9a for clarity.

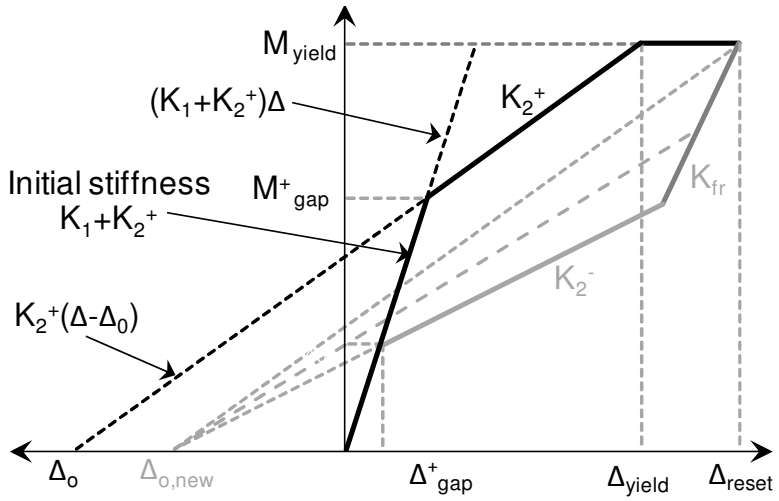

a) loading portion of connection response

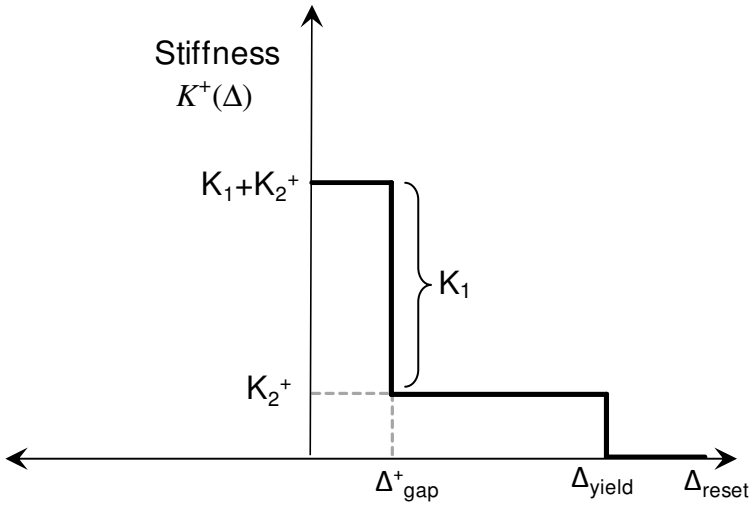

b) stiffness associated with the loading portion of connection response

Figure 10.9: Schematic diagram of the loading portion of the connection response

From Figure 10.9 it is evident that the K_1 component of stiffness should be active when the value of the $(K_1 + K_2^+)\Delta$ line yields a moment smaller than the value from the $K_2^+(\Delta - \Delta_o)$ line, as shown in Figure 10.9a. This condition corresponds to when $\Delta < \Delta_{gap}^+$. Moreover, the K_2^+ component should be active when the input is less than Δ_{yield}, which corresponds to the connection moment, M_{yield}. Therefore, the loading stiffness as a function of input displacement, $K^+(\Delta)$ can be defined:

$$K^+(\Delta) = K_1^{*+}(\Delta) + K_2^{*+}(\Delta) \tag{10-24}$$

where $K_1^{*+}(\Delta)$ is defined using a differential version of the Menegotto-Pinto equation:

$$K_1^{*+}(\Delta) = \frac{K_1}{\left\{1 + \left|\frac{(K_1 + K_2^+)(\Delta)}{K_2^+(\Delta - \Delta_o)}\right|^{R_P}\right\}^{(1/R_P+1)}} \tag{10-25}$$

where the denominator term goes to 1.0 when $(K_1 + K_2^+)(\Delta) < K_2^+(\Delta - \Delta_o)$ which corresponds to when $\Delta < \Delta_{gap}^+$. The denominator goes to infinity, and K_1^{*+} goes to 0, when $(K_1 + K_2^+)(\Delta) > K_2^+(\Delta - \Delta_o)$, corresponding to when $\Delta > \Delta_{gap}^+$. The rate of change of the denominator at the transition, when the relative magnitudes of the $(K_1 + K_2^+)(\Delta)$ and $K_2^+(\Delta - \Delta_o)$ terms are similar (when $\Delta \approx \Delta_{gap}^+$) is defined by the value of R_p. For large values ($R_p >> 1.0$), the transition is very sharp, approximating the change seen in Figure 10.9b. For lower values ($R_p \approx$ 2-5), the transition is more gradual. The slower transition in stiffness induces a more rounded transition in the overall model response.

The stiffness component $K_2^{*+}(\Delta)$ should be active when the connection moment is less than that which corresponds to tendon yield and is defined:

$$K_2^{*+}(\Delta) = \frac{K_2^+}{1 + (R_Y - 1)\left|\frac{M_{i-1}}{M_{yield}}\right|^{(R_y - 1)}} \tag{10-26}$$

where the denominator term goes to infinity (and hence the overall term K_2^{*+} goes to 0) when the value of the connection moment from the previous step, M_{i-1}, approaches the value of the connection moment at tendon yield, M_{yield}. The value of the exponent, R_y, defines the rate of change of the gradient transition as the yield point is approached, using a Ramberg-Osgood type of formulation.

Figure 10.10 shows the response of Equation (10-24), using Equations (10-25) and (10-26), plotted against the input Δ. The different components (K_1^{*+} and K_2^{*+}) of stiffness are shown, as well as the total stiffness K^+, which is simply the sum of these two components, as defined in Equation (10-24). The values of $R_p = 20$ and $R_y = 200$ are used in Figure 10.10.

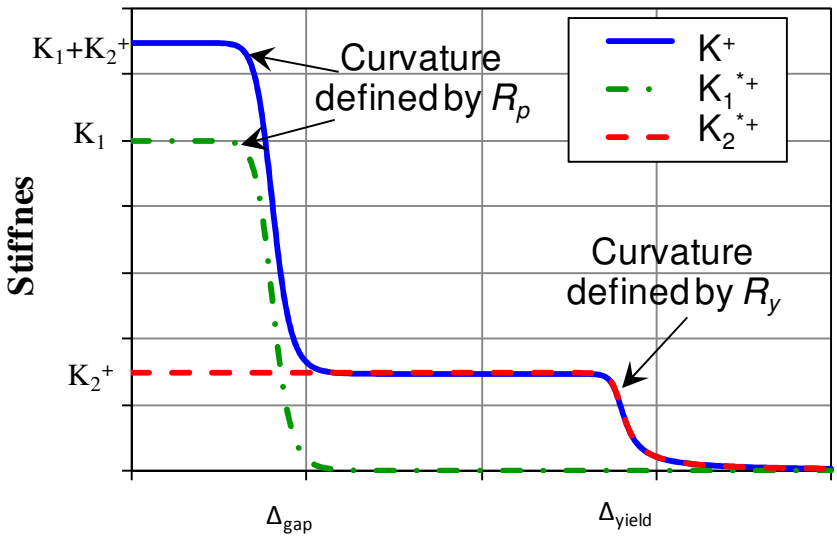

Figure 10.10: Loading stiffness as predicted by Equations (10-24) to (10-26), showing individual contributions and overall stiffness. Note that as R_p and R_y increase the corners become sharper and more like the schematic of Figure 10.9b.

Although the loading stiffness definition presented in Equations (10-24) to (10-26) and Figures 10.9 and 10.10 provide an accurate description of the stiffness for complete loading cycles, one major complication needs to be considered. If a small reversal was to occur during loading at a displacement above the gap-opening point (therefore located on the K_2^+ line) then the stiffness on reloading will be defined as K_2^+ when the initial reloading should be equal to (K_1+ K_2^+). This phenomenon is presented graphically in Figure 10.11, where the loading portion of the blue line indicates the model response using the stiffness values defined in Equations (10-24) to (10-26), and the dashed red line indicates the desired response. Upon initial reloading after the small reversal (starting at point (Δ_{reset},M_{reset})), the higher initial stiffness should be present until the response converges back onto the $K_2^+(\Delta-\Delta_o)$ line, as defined by the dashed red line in Figure 10.11.

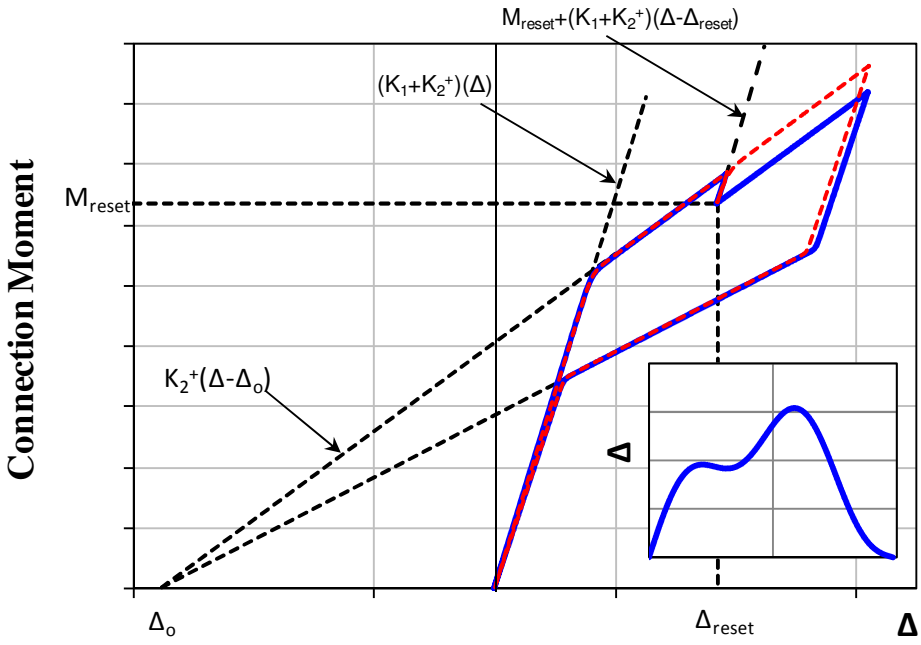

Figure 10.11: Response as predicted by Equations (10-24) to (10-26) noting the response to a small reversal in the loading (blue line). The desired response to this input is shown as the dashed red line. Inset is the input displacement profile.

Equations (10-24) to (10-26) will currently predict the stiffness on initial reloading as K_2^+. At this point, the value of $(K_1 + K_2^+)(\Delta)$ will be much larger than the value of $K_2^+(\Delta - \Delta_o)$. Thus, the term $K_1^{*+}(\Delta)$, as defined in Equation (10-25), will be forced to be close to zero, yielding the incorrect (reloading) blue line in Figure 10.11.

The higher stiffness required on initial reloading can be incorporated into the model by redefining Equation (10-25) to incorporate the small reversal. To achieve this outcome, the value of the model response parameters at the point at which re-loading begins must be recorded or stored. Therefore, two parameters, M_{reset} and Δ_{reset}, must be recorded any time the input displacement or input velocity changes sign (ie: at any change in direction or at any time the response passes through the origin).

Using these values, the presence of the K_1 term can be determined by defining a line originating at the reset point with a stiffness $(K_1 + K_2^+)$, and comparing the magnitude to the $K_2^+(\Delta - \Delta_o)$ line. The line originating at the reset point is shown in Figure 10.11, and is defined as $M_{reset} + (K_1 + K_2^+)(\Delta - \Delta_{reset})$. From this equation, the term in the denominator of Equation (10-25) which determines the transition can be modified to give an updated definition of $K_1^{*+}(\Delta)$, which will include the effects of small reversals.

$$K_1^{*+}(\Delta) = \frac{K_1}{\left\{1 + \left| \frac{M_{reset} + (K_1 + K_2^+)(\Delta - \Delta_{reset})}{K_2^+(\Delta - \Delta_o)} \right|^{R_P}\right\}^{(1/R_P+1)}} \qquad (10\text{-}27)$$

where M_{reset} = the connection moment at the beginning of re-loading, and Δ_{reset} = the input displacement at the beginning of re-loading. Note that for a cycle that begins at the origin (0,0) and has no small reversal in the input, then M_{reset} = 0, and Δ_{reset} = 0, and as such Equation (10-27) will take the same form as previously defined in Equation (10-25).

10.2.6. Unloading Stiffness Definition

To capture the different regimes in the unloading response of the model (presented in Figure 10.8), it is necessary to develop a stiffness definition for the unloading behaviour similar to that used for loading. Similar to the loading path, the overall unloading stiffness, $K^-(\Delta)$, has three different regions, as shown in Figure 10.12, where the stiffness plot of Figure 10.12b uses the same horizontal axis as Figure 10.12a, and the appropriate stiffness values are projected down onto the lower figure for clarity.

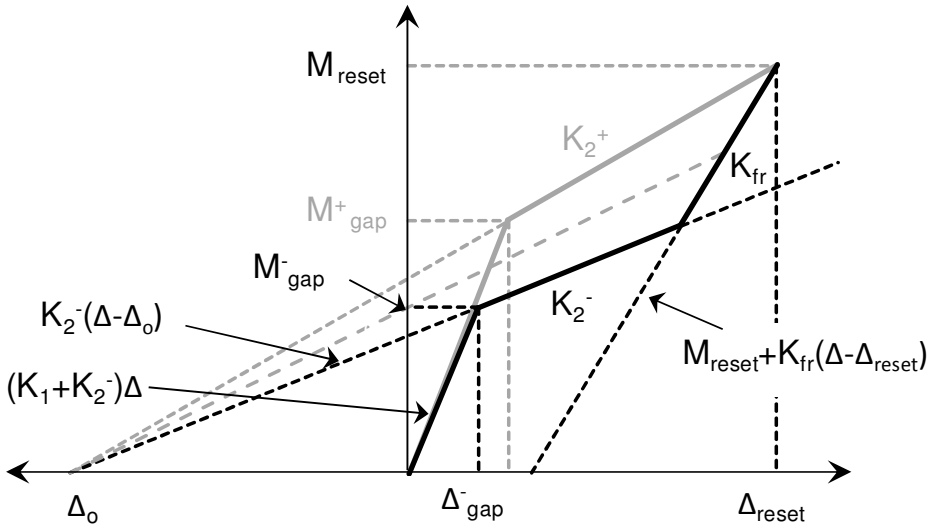

a) unloading portion of connection response

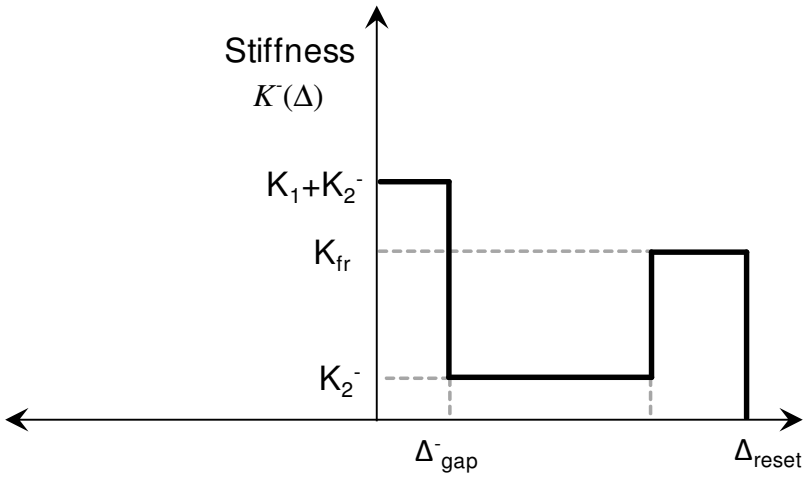

b) stiffness associated with the unloading portion of connection response

Figure 10.12: Schematic diagram of the unloading portion of the connection response. The overall stiffness defined in b) is $K^{-}(\Delta)$, and is a function of Δ.

As before, M_{reset} and Δ_{reset} are respectively defined as the connection moment and displacement at the last reset, which correspond to where the unloading branch of the response originates in Figure 10.12a. The required stiffness as a function of the input displacement, $K^{-}(\Delta)$, is presented in Figure 10.12b. A line that determines the friction slope, K_{fr}, is defined relative to the reset point, using a similar approach to that utilised for initial re-loading in Figure 10.11 and Equation (10-27).

From Figure 10.12 it is evident that the total unloading stiffness should be equal to the tendon relaxation stiffness, K_{fr}, when the value of the $M_{reset} + K_{fr}(\Delta - \Delta_{reset})$ line has a magnitude greater than the value of the $K_2^-(\Delta - \Delta_o)$ line, as shown in Figure 10.12a. Moreover, the unloading stiffness should be equal to K_2^- when the magnitude of the $K_2^-(\Delta - \Delta_o)$ line is greater than the $M_{reset} + K_{fr}(\Delta - \Delta_{reset})$ line, but less than the $(K_1 + K_2^-)\Delta$ line. Finally, the total unloading stiffness should be equal to $(K_1 + K_2^-)$ when the magnitude of the $(K_1 + K_2^-)\Delta$ line is less than the $K_2^-(\Delta - \Delta_o)$ line, which corresponds to when $\Delta < \Delta_{gap}$.

From these observations, the unloading stiffness, K^-, is defined:

$$K^-(\Delta) = K_1^{*-}(\Delta) + K_{fr} + K_2^{*-}(\Delta) \tag{10-28}$$

where the K_{fr} term is always present, and is not dependent on any response parameters. $K_1^{*-}(\Delta)$ is defined:

$$K_1^{*-}(\Delta) = \frac{K_1}{\left\{1 + \left|\frac{(K_1 + K_2^-)\Delta}{K_2^-(\Delta - \Delta_o)}\right|^{R_P}\right\}^{(1/R_P+1)}} \tag{10-29a}$$

where the denominator term approaches 1.0, and the $K_1^{*-}(\Delta)$ term goes to K_1 when $(K_1 + K_2^-)\Delta < K_2^-(\Delta - \Delta_o)$ (ie: when $\Delta < \Delta_{gap}$), and the denominator goes to infinity, and the $K_1^{*-}(\Delta)$ goes to zero, when $(K_1 + K_2^-)\Delta > K_2^-(\Delta - \Delta_o)$ (ie: when $\Delta > \Delta_{gap}$). Moreover, by expanding the brackets, it is evident that both sides of this inequality contain the $K_2^-\Delta$ term,

and it can be simplified to $K_1\Delta > -K_2^-\Delta_o$. Therefore, Equation (10-29a) can be written more simply as:

$$K_1^{*-}(\Delta) = \frac{K_1}{\left\{1+\left|\frac{K_1\Delta}{-K_2^-\Delta_o}\right|^{R_P}\right\}^{(1/R_P+1)}} \tag{10-29b}$$

The $K_2^{*-}(\Delta)$ term is defined:

$$K_2^{*-}(\Delta) = \frac{\left(K_2^- - K_{fr}\right)}{\left\{1+\left|\frac{M_{reset}+K_{fr}(\Delta-\Delta_{reset})}{K_2^-(\Delta-\Delta_o)}\right|^{R_{fr}}\right\}^{(1/R_{fr}+1)}} \tag{10-30}$$

where the denominator term goes to 1.0 and $K_2^{*-}(\Delta)$ approaches the value $\left(K_2^- - K_{fr}\right)$when $M_{reset}+K_{fr}(\Delta-\Delta_{reset}) < K_2^-(\Delta-\Delta_o)$, and the denominator goes to infinity, and $K_2^{*-}(\Delta)$ approaches zero when $M_{reset}+K_{fr}(\Delta-\Delta_{reset}) > K_2^-(\Delta-\Delta_o)$. The transition point when the two terms are equal coincides with the intersection of the $M_{reset}+K_{fr}(\Delta-\Delta_{reset})$ and $K_2^-(\Delta-\Delta_o)$ lines is shown in Figure 10.12a. It should be noted that the rate of change of the stiffness is determined by the value of R_{fr}, where large values give sharp transition and lower values give a more gradual transition. The total unloading stiffness $K^-(\Delta)$ and the individual contributions, $K_1^{*-}(\Delta)$, $K_2^{*-}(\Delta)$, and K_{fr}, using Equations (10-28) to (10-30) are presented in Figure 10.13.

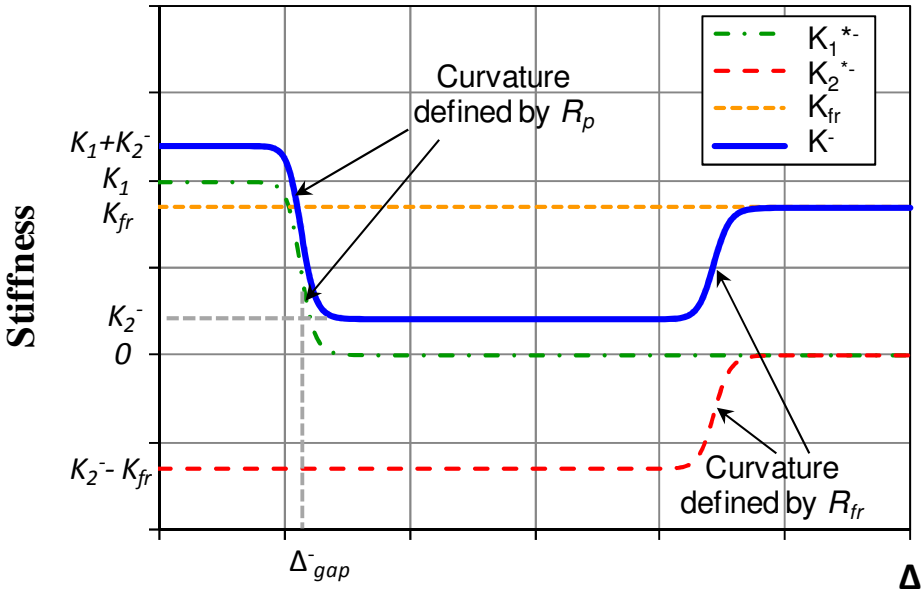

Figure 10.13: Unloading stiffness as predicted by Equations (10-28) to (10-30), showing individual contributions and overall stiffness. Note that as R_p and R_y increase the corners become sharper and more like the schematic of Figure 10-12b.

Although the unloading stiffness described in Equations (10-28) to (10-30) provides a description of the three regions in Figures 10.12b and 10.13, one final complication must still be considered. The transition from K_{fr} to K_2^- is based on the relative magnitudes of the $M_{reset} + K_{fr}(\Delta - \Delta_{reset})$ and $K_2^-(\Delta - \Delta_o)$ lines. Although this approach provides an accurate description for some combinations of stiffness values, Figure 10.14a presents a schematic diagram of when this formulation can provide inaccurate results. Figure 10.12a only shows the $M_{reset} + K_{fr}(\Delta - \Delta_{reset})$ line until it intersects the horizontal axis. Importantly, if the line is continued backward into negative values, then it may end up having a negative value with a larger magnitude than the $K_2^-(\Delta - \Delta_o)$ line, erroneously altering the $K_2^{*-}(\Delta)$ term. Figure 10.14b presents the model behaviour when this erroneous feature occurs. Note that the point at which this error occurs, and whether it is observed at all depends on the relative magnitudes of the K_{fr} and K_2^- stiffness components.

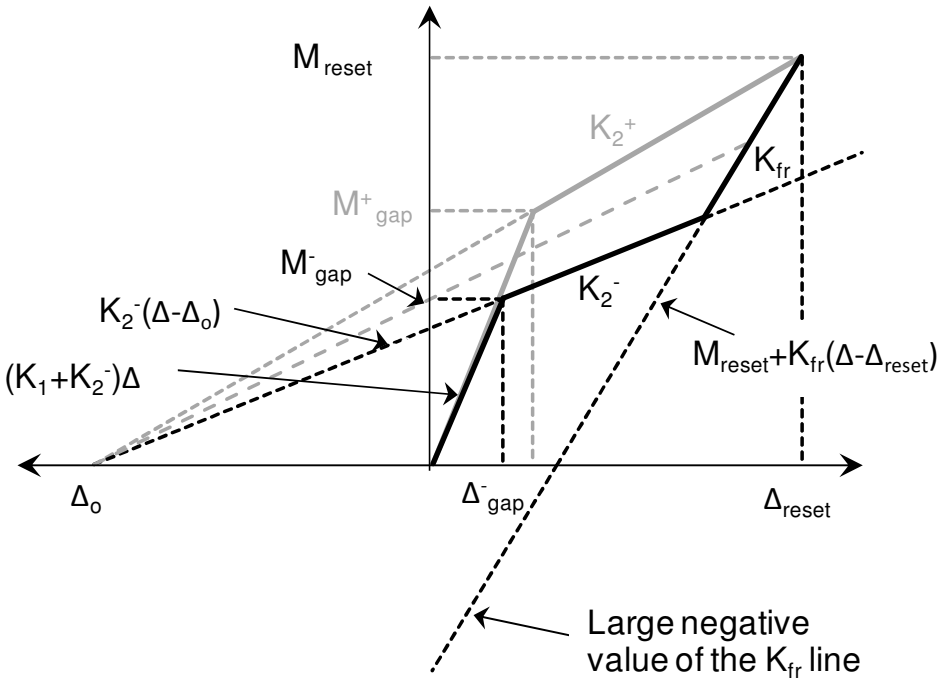

a) Schematic diagram showing the large negative values possible for the $M_{reset} + K_{fr}(\Delta - \Delta_{reset})$ *line*

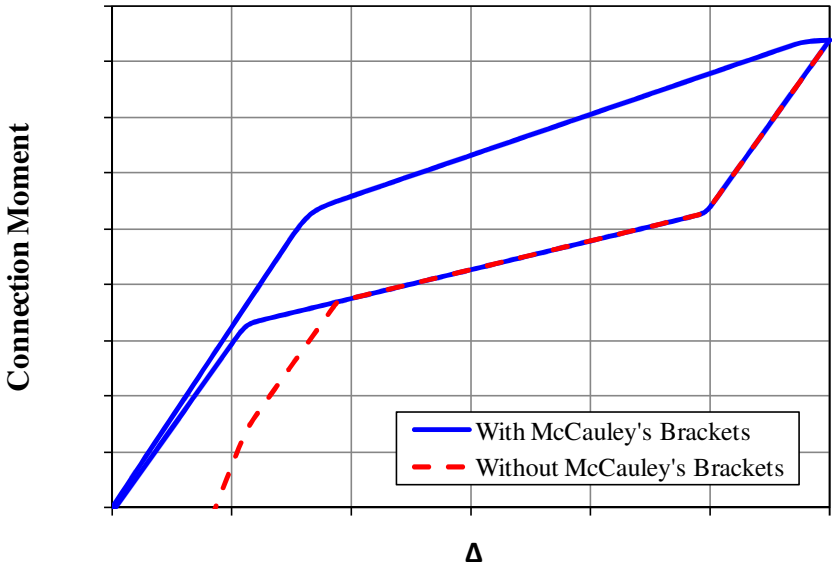

b) Response of the overall model with and without the McCauley's brackets.

Figure 10.14: Model behaviour showing the need for McCauley's brackets. Negative magnitudes of the K_{fr} line can be larger than the positive value of the K_2^- line, erroneously forcing the (K_2^- - K_{fr}) component to become active.

By adding McCauley's brackets to the term that represents this line in the denominator of Equation (10-30), the effect of any large negative values can be eliminated, providing a response that will provide correct results regardless of the relative stiffness magnitudes. Using this approach, the $K_2^{*-}(\Delta)$ term is now defined:

$$K_2^{*-}(\Delta) = \frac{\left(K_2^- - K_{fr}\right)}{\left\{1 + \left|\frac{\left\langle M_{reset} + K_{fr}(\Delta - \Delta_{reset})\right\rangle}{K_2^-(\Delta - \Delta_o)}\right|^{R_{fr}}\right\}^{(1/R_{fr}+1)}} \tag{10-31}$$

where the McCauley's brackets term, indicated by $\langle\ \rangle$ is defined as $\langle A \rangle = A$ if $A > 0$, and $\langle A \rangle = 0$ if $A \le 0$ for any value of input A. Thus, they are similar to the well-known Heaviside function.

10.2.7. Calculating Δ_o

The equations describing the stiffness can be considered a beam-column-tendon model relating positive displacements to the connection moment. Although negative values will be present at the interface due to reversed loading, a positive value is maintained, and the sign of the lever-arm term for the tendons, $(jD)_{PT}^{\pm}$, is utilized to correct for the associated directional dependence.

The initial value of the connection moment at gap opening, M_{gap} can be calculated based on the observed initial prestressing force, and using Equation (10-7). From this calculated value the origin of the K_2^+ and K_2^- lines, Δ_o can be calculated from the geometry as:

$$\Delta_o = \frac{-K_1}{K_{2\_nom}\left(K_1 + K_{2\_nom}\right)} M_{gap} \tag{10-32}$$

where K_{2_nom} = the nominal post gap-opening stiffness without modification for friction, as labelled in Figure 10.8.

10.2.8. Predictor Formulation for Δ

Finally, the equations for the stiffness terms presented all utilise the value of the input displacement, Δ. If the connection is to be modelled by itself, then Δ will likely be a known input value. However, if the connection model is part of a broader structural system, then it is likely that the value of Δ at the current time step is not known.

By implementing a first order finite difference on the values at the previous time steps, a linear extrapolation can be used to predict the value:

$$\Delta_i = \Delta_{i-1} + \left(\frac{\Delta_{i-1} - \Delta_{i-2}}{h}\right) h \tag{10-33a}$$

$$\Delta_i = 2\Delta_{i-1} - \Delta_{i-2} \tag{10-33b}$$

where h = the step size. The approximate value of Δ_i in Equation (10-33b) can then be used in the calculation of the stiffness value using Equations (10-24) to (10-31). Note that Equation (10-33) uses only a first order finite difference, and as such, the error is on the same order of magnitude as the step size ($O(h)$). If greater accuracy is required then a higher-order finite difference can be used.

If the model was put into an overall structural model, Δ may be calculated and thus be a known input vector on each time step. Therefore, the use of the predictor may not be necessary, depending on the way in which the model is implemented. Therefore, the use of either no predictor, the predictor presented in Equation (10-33b) or a higher-order predictor can be chosen for the specific application.

10.2.9. Yielding Effects and Prestress Force Reduction

Although the model currently accounts for yielding within a response cycle due to the tri-linear behaviour, the model must also account for the prestress force reduction on unloading and on subsequent cycles. Any inelastic tendon elongation will result in a decrease in prestress force and therefore alter the behaviour on unloading and any subsequent cycles. This reduction represents a shift in the location of the origin of the K_2^+ and K_2^- lines, Δ_o. Figure 10.15 shows the effect of yielding on the location of Δ_o, which changes by the amount of inelastic tendon elongation, and relocates to $\Delta_{o,new}$.

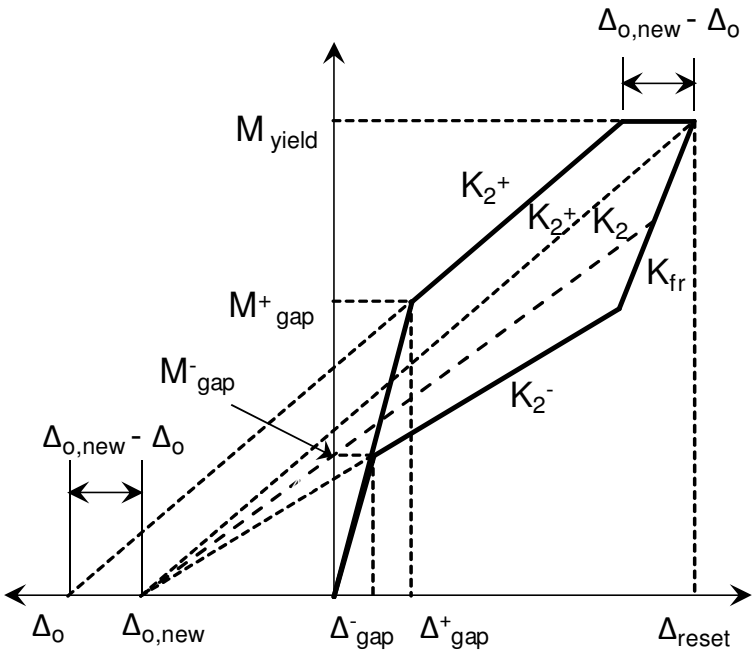

Figure 10.15: Schematic representation of the different loading regimes

The modification to the value of Δ_o can be easily calculated based on the new K_2^+ line that originates at $\Delta_{o,new}$ and intersects the reset point. It should also be noted that this K_2^+ line is the re-loading path for subsequent cycles. The value of $\Delta_{o,new}$ is defined:

$$\Delta_{o,new} = \Delta_{reset} - \frac{M_{reset}}{K_2^+} \tag{10-34}$$

Note that in Figure 10.15, $M_{reset} = M_{yield}$. However, due to the curvature that may exist near the yield point from the gradual transition in the model, M_{reset} must be used in Equation (10-34). Equation (10-34) must only be implemented on a reset (when the loading direction changes – ie: the sign of the velocity changes) and only when tendon yield has also occurred (when $\Delta_{reset} > (\Delta_o + M_{yield} / K_2^+)$).

10.2.10. Modifications for 100% Loss of Prestress (Modelling Slack)

If extremely large plastic strain is induced within the prestressing tendons, then it is possible that the reduction in prestress will lead to a total elimination of prestress to the point that there is slack in the system, as depicted by the unloading branch shown in Figure 10.16. In this situation, there will be induced displacement without any resisting force, giving an initial zero stiffness. Although this scenario is well outside the intended design limitations of this type of connection, it may be present in simulations and the computational model should be sufficiently robust to incorporate this phenomenon.

It should be noted that care should be taken to consider the impact of this scenario. If large amounts of slack are present, then the connection may move sufficiently that the beams lose contact with the shear keys and shear slip occurs. If this slippage happens, then the

connection would behave in a manner that is no longer predicted by the model. Therefore, if the value of Δ_o becomes positive, careful consideration should be given to the model response to ensure that the results remain realistic.

If tendon yield has occurred such that the value of Δ_o is positive ($\Delta_{o,new} > 0$), then there is slack present. By noting that the tendon displacement is always positive, a gradient multiplier can be introduced that sets the gradient to zero and prevents any force within the tendon before the slack is taken up. Figure 10.16 schematically presents the hysteretic response of the connection under these conditions, noting that the gradient should be equal to zero for all displacements less than $\Delta_{o,new}$.

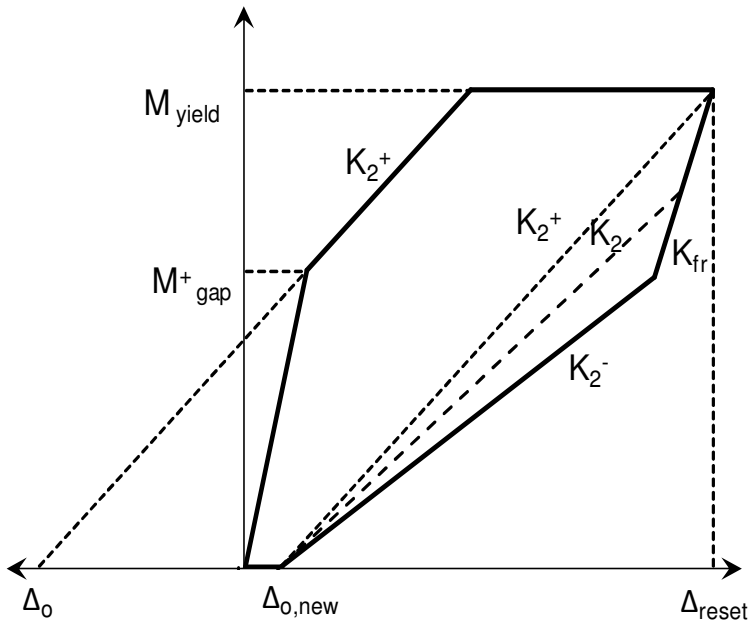

Figure 10.16: Schematic model response accounting for complete loss of prestress and slack in the system

To implement the zero gradient under these conditions a hyperbolic tangent function is utilized to approximate a gradient multiplier. The gradient multiplier is a continuous function and is a multiplier to the tangent stiffness defined in Equations (10-24) to (10-31). The multiplier used at every time step, is defined:

$$K_{mult} = 0.5\left(1 + \tanh\left(C\left(\left(2\Delta_{i-1} - \Delta_{i-2}\right) - \Delta_o\right)\right)\right) \tag{10-35}$$

where C = a constant that defines how fast the rate of change of the stiffness occurs. Note that, as before, a predictor (as defined in Equation (10-33)) is incorporated into the equation so that the current value of the connection displacement is not required. Note that Equation (10-35) has a value between 0 and 1.0, and if a very large value of C was used, then $K_{mult} = 0$ if $\Delta < \Delta_o$, and $K_{mult} = 1.0$ if $\Delta > \Delta_o$. For smaller values of C the transition between these values is more gradual.

10.2.11. Additional Modifications for Small Cyclic Reversals

An important consideration to note is that the stiffness defined in Equations (10-24) to (10-31) are tangent stiffnesses for use in an approximate dynamic, time-incremental formulation. As such, the influence of small reversals within the response are of particular importance. The modification to induce a higher initial stiffness on initial re-loading is defined in Equation (10-27), and produces the desired response, as shown in Figure 10.11. However, when a small reset occurs, the curvature of the transition between the elastic loading $K_1 + K_2^+$, and the K_2^+ line will need to be much sharper than the overall gap-opening transition. Therefore, a modifier to the value of the transition exponent, R_p, can be defined:

$$R_p = R_{p,nom}\left(1 + Ae^{\left(-B\left|(2\Delta_{i-1}-\Delta_{i-2})-\Delta_{reset}\right|\right)}\right) \qquad (10\text{-}36)$$

where R_p is the value of the curvature exponent used in Equations (10-25), (10-27), and (10-29), $R_{p,nom}$ is the nominal value of the curvature exponent, A is a constant that defines the increase in magnitude of R_p that is desired for a small reset, and B is a constant that defines how fast the value of R_p reduces near a reset point.

An identical approach is used to define higher values for the other curvature exponents, R_y and R_{fr} near reset points. The hysteretic response using this approach for a loading profile containing small reversals is presented in Figure 10.17. Note that the curvature near the reset is much sharper than the curvature at the gap-opening transition point, a result of the increase in R_p from Equation (10-36).

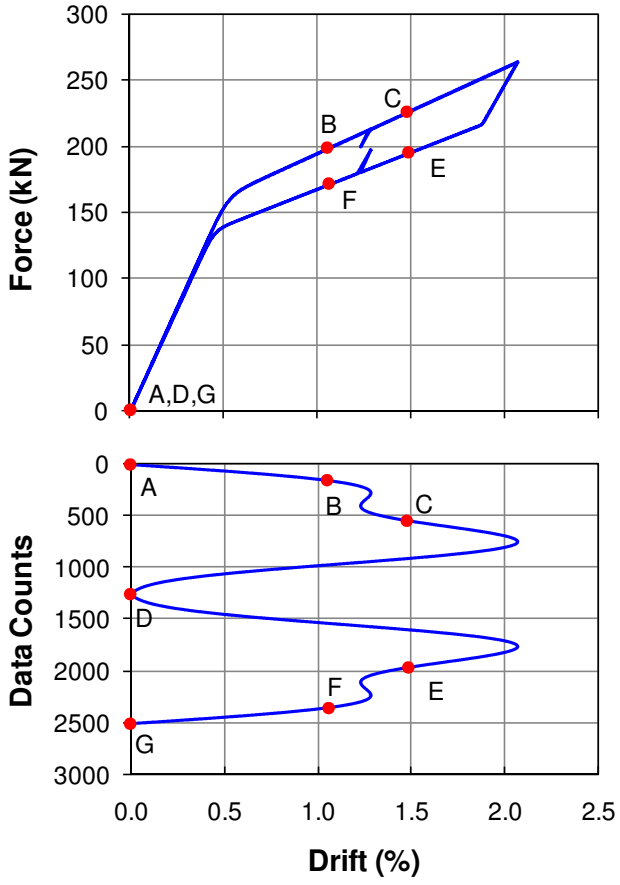

Figure 10.17: Response cycles showing the effects of small reversals in the displacement input loading

10.3. Overall Connection Modelling

The approach presented has been formulated as a subassembly model where the connection moment and displacement are always positive. The subassembly model can be considered to be formulated to give the connection moment for a normalized value of lever-arm, *jD*, where the fractional lever-arm, $j = 1.0$. The beam model will always yield positive moments, but the inclusion of the directionally dependent multiplier j corrects for the sign, providing the overall connection behaviour for both positive and negative connection displacements.

The connection moment at the gap opening point is linearly proportional to the magnitude of j. However, the post-gap opening stiffness can be shown to be approximately proportional to the square of the magnitude of the fractional lever-arm, j. This quadratic relationship is explained by considering the underlying kinematics. Compared to a nominal value of fractional lever-arm, j, halving the magnitude will induce only half of the displacement in the tendon, and therefore result in only the half the increase in tendon force. Furthermore, this increase in force will only contribute half of the moment to the connection, due to the smaller lever arm, providing in combination the quadratic relationship.

Figure 10.18 presents the schematic model response for two different values of j. By considering the geometry of the model response, it is evident from Figure 10.18 that the location of the origin of the K_2 lines, defined as Δ_o, is therefore also dependent on the value of the fractional lever-arm, j. The K_2 line must intersect the $(K_1 + K_2^+)$ at a location linearly proportional to the value of j but with a slope approximately quadratically proportional to magnitude of j. Therefore, the location of Δ_o will be approximately inversely proportional to magnitude of j.

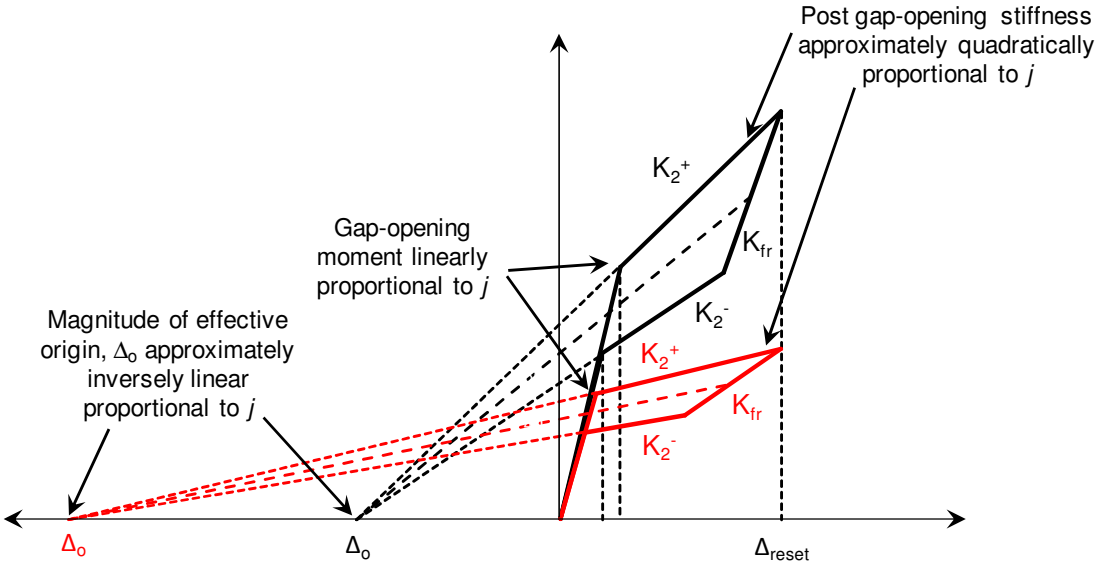

Figure 10.18: Schematic representation of the dependence of the effective origin, Δ_o on the fractional lever-arm, j.

Under full cyclic loading the model must incorporate connection behaviour for both positive and negative rotations in the presence of prestressing tendons that are not centrally located ($j^+ \neq j^-$) with respect to the beam centreline. Under these conditions, the model parameters, M_{gap}, M_{yield}, K_2 and Δ_o are all directionally dependent, as they are all a function of the fractional lever-arm, j, as defined in Equations (10-7), (10-11), (10-14), and (10-34), respectively. To accommodate this directional dependence, the values need to be switched based on the direction of loading, and the associated value of either j_{PT}^+ or j_{PT}^-, shown in Figure 10.6. However, all other model equations hold given this switching to account for the directional response behaviour.

This switching can be readily implemented a number of ways, including: 1) using conditional statements, or 2) incorporating a switching function using Heaviside functions, sigmoid functions, or hyperbolic tangents. The implementation is straightforward computationally and only requires that the values be assigned at any change in the sign of the input displacement. Note that the directional dependence of the effective origin, Δ_o, can be incorporated into the model using Equations (10-7) and (10-32).

10.3.1. Model Implementation without Supplemental Damping

The overall tangent stiffness is defined as K_t, and incorporates the model developed within the previous sections of this chapter, accounting for elastic beam and column flexibility and the contributions from the rigid body rotations and tendon behaviour, defined in Equations (10-24) to (10-31). Note that this model includes the modifications presented to account for friction, yielding, prestress reduction or loss, and overall connection behaviour and directional dependence. The tangent stiffness can therefore be used in a time-incremental formulation to relate input column displacement, Δ, to connection moment and thus, column shear.

10.3.2. Model Implementation with Supplemental Damping

The structural system can be extended to include the modelling of a rate-dependent high force-to-volume (HF2V) energy dissipation device. The model of the device that provides the supplemental damping is a non-linear viscous damper that acts on only the rigid body component of the subassembly deflection. This approach is utilised as the energy dissipating elements are usually connected across this beam-column interface and are not affected by elastic deformations. The energy dissipation devices will have associated connection stiffness that must be incorporated into the model. The basic damper system is presented schematically in Figure 10.19, and is the same system presented in Figure 9.1. The displacement components x, y, and z are defined as the displacement across the spring, the displacement across the damper, and the total displacement across the system, respectively.

The system is formulated such that z is a known input displacement as a function of time, or can be approximated using a predictor approach such as that defined in Equation (10-33), and the values of x, y, and the overall system force, F_D, are calculated. The predictor-corrector approach to solving the system, as derived and validated in Chapter 9, is utilised again here. The predictor-corrector equations are presented again here for reference, but are identical to those utilised in Chapter 9.

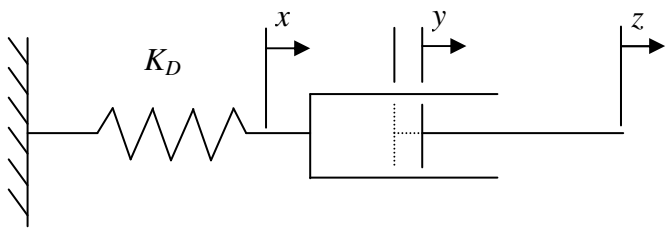

Figure 10.19: Schematic diagrams of the damper-spring system model

The predictor-corrector equations derived in Chapter 9 for the HF2V device are defined:

$$\dot{y}_i = \frac{z_i - z_{i-1} + f_D F_{D,i-1}}{\Delta t + f_D C_\alpha^{(1/\alpha)} \left| F_{D,i} \right|^{1-1/\alpha}} \tag{10-37}$$

$$F_{D,i} = C_\alpha \left| \dot{y}_i \right|^\alpha \operatorname{sgn}\left(\dot{y}_i \right) \tag{10-38}$$

where the coupling of Equations (10-37) and (10-38) requires that these equations be solved in a predictor-corrector sense, or by using root-finding or other iterative methods, as detailed in Section 9.2. For the initial time step the first predictor of force is defined:

$$F_{D,1} = \frac{z_1}{f_D} \tag{10-39}$$

For all subsequent time steps, the following has been found to be a suitable predictor:

$$F_{D,i} = F_{i-1} + \frac{\Delta t}{f_D}\left(2\dot{x}_{i-1} - \dot{x}_{i-2}\right) \tag{10-40}$$

From this solution, the value of the system force on each successive time step can be obtained. This result is then used to give the value of the spring displacement, *x*, as well as the damper displacement, *y*, and their derivatives.

The overall system places the HF2V devices in parallel to the subassembly model, but with one important distinction. As previously discussed, the total damper displacement, *z*, relates only to the rigid body component of the total deflection. Therefore, the elastic subassembly displacement is subtracted from the total displacement. The total column shear is defined as V_C. The relationship between the total linear damper system displacement, *z*, and the total column displacement, Δ, is defined:

$$\Delta = L_{col}\frac{z}{\left(j_D^{\pm} D\right)}\frac{L_b}{L} + \frac{M_i}{\left(K_1 + K_2^{+}\right)} \tag{10-41}$$

where $j_D^{\pm}$ is the fractional lever-arm of the damper system from the rocking edge, similar to $j_{PT}^{\pm}$ in Figure 10.6. The final term in Equation (10-41) represents the elastic column deflection component.

Using the equations presented for the damper and the overall system, an overall matrix formulation can be obtained. For clarity, the 6 equations are presented in the order in which they appear in the matrix below to indicate the derivation of the matrix system. Note that this

system is formulated in an absolute sense, but the first equation is formulated in an incremental sense, due to the use of a tangent stiffness, K_t, defined in the model, by subtracting the previous values in the right hand side vector.

The stiffness defined by the model presented in this chapter gives a tangent stiffness, K_t, which relates input displacement, Δ, to connection moment, M:

$$K_t\left(\Delta_i - \Delta_{i-1}\right) = \left(M_i - M_{i-1}\right) \tag{10-42a}$$

$$M_i = K_t\left(\Delta_i - \Delta_{i-1}\right) + M_{i-1} \tag{10-42b}$$

The connection moment can be divided by the column height, L_{col}, to get the equivalent column shear, and added to the damper contribution (noting the geometric transformation for the damper force F_D to column shear contribution) to get V_c:

$$-\frac{M_i}{L_{col}} + V_{C,i} - \frac{\left(j_D^{\pm}\right)DL}{L_{col}L_b}F_{D,i} = 0 \tag{10-43}$$

The damper system force, F_D, and spring displacement, x, can be related with the spring stiffness, K_D:

$$K_D x_i - F_{D,i} = 0 \tag{10-44}$$

The damper system displacements can be equated such that:

$$x_i + y_i - z_i = 0 \tag{10-45}$$

Equation (10-41) can now be re-arranged to:

$$\frac{1}{\left(K_1 + K_2^+\right)} M_i + L_{col} \frac{L_b}{\left(j_D^{\pm}\right) DL} z_i = \Delta_i \tag{10-46}$$

Finally, the last equation in the matrix is defined by the predictor-corrector formulation. The overall matrix formulation is thus defined:

$$\begin{bmatrix} 1 & 0 & 0 & 0 & 0 & 0 \\ -1/L_{col} & 1 & 0 & 0 & 0 & -(j_D^{\pm})DL/(L_{col}L_b) \\ 0 & 0 & 1 & 0 & 0 & -1/K_D \\ 0 & 0 & 1 & 1 & -1 & 0 \\ 1/(K_1+K_2) & 0 & 0 & 0 & L_{col}L_b/((j_D^{\pm})DL) & 0 \\ 0 & 0 & 0 & 0 & 0 & 1 \end{bmatrix} \begin{Bmatrix} M_i \\ V_{C,i} \\ x_i \\ y_i \\ z_i \\ F_{D,i} \end{Bmatrix} = \begin{Bmatrix} K_t(\Delta_i - \Delta_{i-1}) + M_{i-1} \\ 0 \\ 0 \\ 0 \\ \Delta_i \\ F_{D,i} \end{Bmatrix} \tag{10-47}$$

where $F_{D,i}$ (the last element of the right hand side vector) is given by the right hand side of either Equation (10-38) or (10-40). Which of these two equations governs will depend on whether the current step is using the predictor or corrector equation for the damper force, $F_{D,i}$. Again the results of this analysis can be used with the geometric transformations to obtain the input displacements to the subassembly model.

10.4. Experimental Validation

The corner joint configuration presented in Chapter 4 (and shown Figures 4.11 and 4.12) that utilized a bent tendon profile and HF2V devices for supplemental energy dissipation was chosen for the experimental validation. This configuration was chosen as it presents very complex overall hysteretic response that captures almost all of the considerations presented in the model development. The experimental specimen had basic dimensions, as defined

schematically in Figure 10.1, of L_{col} = 2.9m, h_{col} = 0.7m, L = 4m, L_b = 3.65m, and D = 0.56m. The supplemental damping is provided by two externally mounted HF2V devices, with one located on each vertical face of the seismic beam. Each of the HF2V devices had a design force of 120 kN, providing a total damper contribution of 240 kN, as detailed in Chapter 4. Note that for the experimental set-up and positive joint rotations, j_{PT}^{+} = 0.66, and D = 560mm so that $(jD)_{PT}^{+}$ = 370 mm, and for negative joint rotations, j_{PT}^{-} = 0.34 so that $(jD)_{PT}^{-}$ = 190mm. The HF2V devices were both located at the beam vertical centreline, such that the magnitude of the lever-arm is equal for both positive and negative joint rotations, thus $j_D^{+} = j_D^{-} = 0.5$, giving $(jD)_D^{+} = (jD)_D^{-} = 280$mm.

10.5. Results and Discussion

As described previously in Chapter 4, the test specimen underwent quasi-static uni-directional displacement tests in the seismic direction using fully reversed sine wave profiles up to 4% inter-story drift. The specimen was tested both with and without the supplemental damping system to characterize the overall hysteresis under both criteria to delineate the individual contributions.

The experimental data for the exterior connection was utilized as it is the most difficult case to model due to the asymmetry in gap opening force, friction, and yield displacement. An interior connection of this type, with two beams present was also tested in Chapter 4, but is not used for comparison. The interior connection was symmetrical, and although the tendons were non-centrally located, the overall joint exhibited symmetrical hysteretic behavior. The reason for this observation is that the two connections are undergoing opposite rotations, and the asymmetry from the non-central location of the tendons is balanced by the opposing

connection. Therefore, the exterior connection is the most stringent test of the model, and once validated can be extended to also model the interior joint if desired. The model is developed such that the connection can be described as a beam element model, and can be added to the column spring to obtain a result for any configuration. Figure 10.20 presents the experimental and model results for the subassembly with the prestress alone, and where the experimental specimen also had the supplemental damping system.

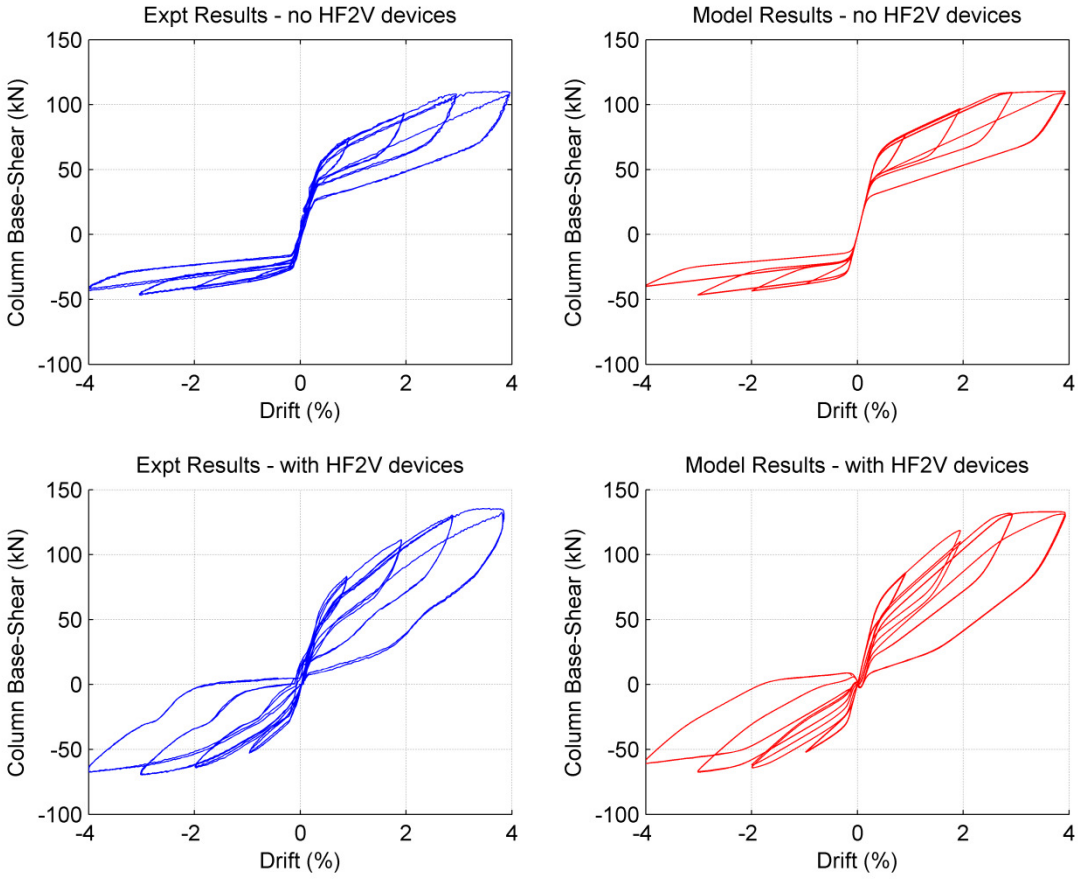

Figure 10.20: Experimental (left) and model results (right), both with (bottom) and without the HF2V devices (top).

Overall, very good agreement is evident between the computational model and the experimental test results. The subassembly without the HF2V dampers shows very good agreement, and captures the tendon yield, friction, and loss of prestress following large response cycles that caused tendon yield. The subassembly with the HF2V devices also

shows good agreement. One minor discrepancy, not attributed to the computational modeling precision, is the presence of inflection points at lateral loads of -30kN and +60kN. This discrepancy is attributed to slack in some of the threaded (nut-bolt) connections of the experimental test apparatus.

10.6. Summary

A simplified model is presented that can provide a good approximation to the loading portion of the joint hysteresis with minimal computation. A more advanced analytical model of joint hysteresis using a compound, time-incremental Menegotto-Pinto and Ramberg-Osgood model shows very good agreement to experimental results across different post-tensioning force levels, both with and without added damping. The ability to accurately predict the entire hysteretic response of the connection at any drift level is an important outcome for analysis purposes.

Overall, this model is more complex and harder to implement than the simpler explicit forms in previous research. However, this model provides a much more robust description. If any significant friction or tendon yield is likely to occur then the simpler explicit models will no longer provide accurate results. The presence of friction, yielding and prestress reduction or elimination are all modelled accurately, providing good overall agreement. This model is not intended for initial design, but rather as an analysis tool once a preliminary design is produce. This model could be incorporated into a commercial or open source analysis program as a reliable means of modelling a jointed precast concrete connection. Finally, as with the model presented in Chapter 8, this model does not consider the influence of floor slab effects, and this aspect is something that could be added to simulate the overall structural system.

Chapter 11: Conclusions

This thesis explores the design development and experimental testing of high force-to-volume damping devices and their structural implementation and associated modelling. Overall, the HF2V devices provide repeatable, consistent energy dissipation on repeated cycles, without any stiffness or strength degradation, and without any requirements for repair or replacement following an earthquake. This outcome is unique to these devices, and these characteristics are not available with the alternatives typically used within this field, such as yielding steel fuse-bars or proprietary viscous dampers. The structural implementations showed significant promise and highlighted several key design recommendations to optimise their use. Finally, analytical modelling of the device and connection response provides the tools to incorporate these device into design practices and creates a bridge to the profession.

The initial concept of high force-to-volume (HF2V) dissipation devices based on the much larger devices previously used led to the construction and testing of initial prototype devices. These prototype devices indicated several key design issues. Specifically, careful consideration must be used in design, and prestress must be applied to the devices to avoid trailing voids, and achieve optimal device behaviour. If these issues are appropriately addressed, then the devices will exhibit predictable, repeatable, behaviour that is consistent for any number of response cycles. These devices therefore provide a unique opportunity to provide large energy dissipation in a very compact package that can easily be incorporated into a structural connection. At $100-300 each the devices cost several orders of magnitude less than proprietary viscous dampers and are much smaller physically, but provide equivalent or greater force capacity, making them an economically and technologically feasible option.

Analytical modelling of the response spectra of a structure utilising these devices has shown that significant response reductions can be achieved with realistically sized devices. The development of empirical design equations to relate the damper size to the likely response reduction provides an important analysis tool and creates an important bridge to the profession to increase the likelihood of uptake.

The devices were implemented into three structural systems, with numerous configurations tested for each structural system to provide alternate methodologies and delineate the contributions to response. The structural implementation tests indicated several key design aspects. In any connection in which these devices are to be used, the influence of flexibility in the elements that connect the devices to the structural system will have a significant impact on the overall system response. This issue can be reasonably managed by careful design where the load path must be considered, and the length and number of connecting elements minimised. This approach will minimise the elastic strain energy in the connecting elements, and provide the largest input displacements into the HF2V devices, therefore providing the most optimal energy dissipation.

The effects of unbounded, post-tensioned prestress on response was identified through a parametric study on the experimental specimen of Chapter 5 and 6, indicating that significant prestress loss (up to 60% or more) can be tolerated within any loss of static re-centering ability of the connection. This observation indicates a robustness of the connection design. The connection will continue to behave safely even if large amounts of tendon yield occur. Alternatively, if tendon yield is not expected to occur at design drift level of 2-2.5%, then a designer has the option of either increasing the damping forces, or reducing the total initial post-tensioning to the connection, and therefore reducing the forces transmitted through the connection while maintaining safe operating behaviour of the connection.

The extension of the devices for use in steel connections vastly increases possible applications, both for new buildings, and for retrofit. This is an important addition, as a large amount of the existing built environment has significant design life remaining, and the ability to retrofit a structure and increase the earthquake resistance is often going to be an economical option. Key design issues observed in the steel connection of Chapter 7 is the large influence of flexibility of the top-hung angle connection, and the need to design damper connections for no-slip conditions. Care must be taken to ensure a non-slip condition between the damper mounts and beam flange to eliminate slip and ensure the dampers work effectively. The use of a split-tee bracket in place of the angle connection is recommended in future tests to reduce unwanted flexibility and provide a more rigid connection.

The development of analytical models to predict the response of connections with these HF2V devices is an important final step of this research. The influence of connecting element flexibility is a recurring theme in the experimental tests. Although this effect can be minised be careful design, it will always be present and have a measurable impact on results. A damper model is developed that incorporates the effects of this flexibility, and provides good agreement with the experimental results. The damper model is then extended to a rotational, column shear to drift formulation which includes member flexibility and geometric transformations and provides an accurate model of the damage-free steel connection. This model is simple, based entirely on rational mechanics, and requires no reset points to be recorded, but rather utilises only the results of the immediately prior time steps. As such the model is easy to implement and provides good agreement with the experimental results.

For the jointed precast concrete connections several models are presented of varying complexity. A simple model is presented that is based almost entirely on rational mechanics, is easy to implement and provides accurate results for the connection of Chapters 5 and 6.

This model does not incorporate the effects of friction, does not fully model the effects of tendon yield, and does not easily model the asymmetry that can result from non-centrally located prestressing tendons or damping devices. A more advanced model was presented in Chapter 10 that incorporates these additional features, but is more intensive to implement. While the simpler model is intended as a basic tool for initial structural design, the later model is intended as an analysis tool for further evaluation once an initial design is completed. The choice of the model to use can be based upon a tradeoff between computational expense and the accuracy needed.

Overall, this thesis has developed high force-to-volume damping devices from an initial concept, through prototype development, to structural implementation and associated modelling. The key issues have been identified and significant progress has been made towards this design approach receiving uptake by the profession.

In summary, the unique contributions from this research and thesis to the earthquake engineering field include:

- The HF2V damping devices developed provide the unique ability to impart significant energy dissipation into a structural connection from a very compact, economically feasible device. Although numerous different design approaches exist for these types of low damage and damage-free connections, the ability to provide a reliable energy dissipation mechanism has become the key design aspect. The alternate methods of dissipating energy generally focus on sacrificial yielding elements, which simply move the damage mechanism to a different component, and provide a non-optimal solution.

- The HF2V devices developed are very economical, and are sufficiently small to fit into almost any realistic structural application. By undertaking a range of structural experiments, implementation issues and design consideration are identified, and provide greater confidence in optimal outcome
- The development of analytical models for the damper, and for both steel and concrete connections using these devices creates the ability for these devices to be incorporated into the design and analysis of future connections. This creates an important bridge to the profession and increases the likelihood of uptake.
- The use of response spectra and development of simple relationships that relate device performance to known design guidelines provides a means by which these devices can be incorporated into overall performance based design methods.

Chapter 12: Future Work

The research within this thesis has provided significant insight into the design and implementation of the high force-to-volume energy dissipation devices. Several areas of further interest have been identified as a result of this work. The areas of particular interest for future work are detailed within this chapter.

12.1. Floor Slab Considerations

The precast jointed concrete connections of Chapters 4-6 have shown significant promise. However, the experimental subassembly does not include floor slabs, and has several associated limitations. In particular, the connection designs presented within these chapters are referred to as “tearing” or “gapping” solutions. As the subassembly deflects and the gap between the beam and column opens, the effective length of the beams increase due to the rigid-body displacement regime. This effect may result in damage to a floor slab, and the dilation of the columns will have an additional effect on the post-tensioning of adjacent floors in a multi-story building. Studying these effects is outside the scope of this thesis, and research at the University of Canterbury and elsewhere is examining these effects. While these effects are important, this thesis is focussed primarily on the means of energy dissipation. The devices developed within this study are equally amenable the other design approaches that do not have these displacement incompatibilities, referred to as “non-tearing” or “non-gapping” solutions. These type of connections typically utilise a hinging mechanism such as that utilised in the steel connection of Chapter 7, where positive and negative rotations rock about the same point. As previously mentioned, the devices developed within this thesis are a general solution, and can be applied to any type of connection. Therefore, this aspect has not been a focus of the work within this thesis.

12.2. Device Velocity Dependence

The limited velocity dependence studies presented within this thesis have provided limited insight into the velocity characteristics of the HF2V damping devices. The results have been at very limited velocities of approximately 1-3 mm/sec and indicated that the devices exhibit closely similar behaviour to the previous, much larger devices used in previous research (Cousins and Porritt 1993). This previous research has investigated the velocity dependence at much higher velocities and shown an increase in resistive forces at the higher velocities, but no change in overall device characteristics. Higher velocity testing and repeated cycling would provide greater confidence in the velocity dependence of the smaller devices in this thesis, and in particular the effects of heating under high frequency loading.

The heat produced within the devices will soften the lead and reduce the resistive force produced. The work of Cousins and Porritt (1993) has indicated that repeated sinusoidal loading with a peak velocity of approximately 31 mm/sec shows a decrease in force that plateaus at an approximate 40% reduction. This reduction will likely be different for the smaller devices presented within this research as the smaller device size results in a smaller thermal mass of the device, and therefore more rapid heating of the working material. The larger devices will act as a bigger heat sink and the increased surface area will provide greater convective heat dissipation to the surrounding air. Although the devices are unlikely to exhibit any major heating during the limited number of response cycles from an earthquake, characterising of the velocity dependence and heating effects will provide greater insight into the devices developed.

The testing of the structural connections at more realistic earthquake speeds would also be an important addition to this research. While the structural implementation tests presented within this thesis have shown promise, they have only been conducted at quasi-static velocities. Higher speed testing of both the devices alone, and the connections using the devices would give increased confidence in the system. In particular, the use of realistic earthquake protocols, with small reversals and large irregularity, performed at realistic velocities, would be an important addition to this research.

These velocity effects are of particular importance for the steel joint, compared to the concrete connections, as the damper force contributes a much larger proportion of the overall system response. While the concrete connections have significant contributions from the prestressing system, the steel joint is dependent almost entirely on the resistive force provided by the HF2V devices. The damper mounts and the overall connection must be designed for the peak device forces, so it is important that this force level is identified. While the standard reaction frames and control systems within Civil Engineering at the University of Canterbury cannot provide these velocities, it may be possible to conduct these tests using the shake table or a high-speed actuator.

12.3. Overall System Modelling

The extension of the modelling work of Chapters 8-10 to a large-scale multi-degree of freedom structure is a key next step in the analysis. Specifically, this would involve developing the individual connection models into finite element codes, and then extending them to large structures. This procedure has already been performed with the results of Chapter 7, where an ABAQUS model of the connection results was developed which included the device velocity dependence. This connection model was then extended to model the SAC LA3 structure subjected to the SAC suites of earthquakes. The model developed and resulting analysis of the SAC structure are presented in journal articles which, at the time of writing this thesis, are currently in review. The results of the SAC3 analysis is presented in condensed form in the conference paper of Rodgers et al (2009a).

Other initial analyses have also been performed, looking at the steel connection of Chapter 7, and the overall system response. In particular, the ability for the overall system to re-centre was of primary interest. Several key aspects were considered, such as relying on the gravity frame to help provide an overall recentering stiffness, and the addition of steel straps to the structure to help provide recentering stiffness. This modelling work is being developed in parallel to this thesis, and is ongoing.

12.4. Financial Loss Modelling

The key advantage of these types of connections and in particular, this type of energy dissipation, is the damage-free behaviour of the subassembly, and the associated reduction in economic cost from an earthquake. There has been significant research in recent years into the development of financial loss models. These models provide a estimate of the likely reduction in cost from damage that will result from earthquakes of different magnitude and likelihood of occurrence, and convert the outcomes into an expected annualised cost. The results of such an analysis can be used to present a tradeoff between initial design costs to the expected cost due to damage from earthquakes.

To use the financial loss models, a large number of response simulations are required that determine the structural response from a range of different earthquake inputs. The process is similar to that done in Chapter 2 of this thesis, but utilises large, multi degree-of-freedom models to simulate the response of a multi-story building to these earthquake inputs. Models have been developed in related research for use in ABAQUS that capture the hysteretic response of the steel connection in Chapter 7. Response simulations for the multi-story building have been performed for suites of earthquake inputs. These response simulations could be extended to financial loss modelling in future research.

To perform such an analysis for a jointed precast concrete connection, the model developed within Chapter 10 should be incorporated into a finite element code such as ABAQUS, or an open source program such as OpenSEES (Open Source Earthquake Engineering Software). If the model was written into a standard package, then large numbers of response simulations could be performed and the financial loss models can be developed from the results.

12.5. Effective Member Stiffness Investigation

The almost entirely rational mechanics model developed in Chapter 8, has one major source of uncertainty that makes modelling the connection from specimen parameters difficult. The effective section stiffness (EI^*_{col} and EI^*_b) are approximated from the gross section properties using the approach defined in Li et al (2008). Although this approach has some rationale behind the values of 26% and 14% of gross section properties for uni-directional and bi-directional loading, the multiplying factors remain somewhat empirical. A more detailed analysis looking at the specific boundary conditions and including the effect of the axial load induced from the post-tensioned prestress may provide insight into this phenomenon.

The calculation of elastic bending deflections assumes a rigid cantilever connection to the column face. In reality, the boundary conditions are better modelled by point loads at the top and bottom of the beam. When the beam shear is such that gap-opening is approached, then the reaction at the support comes entirely from a point load at the rocking edge, and the boundary conditions do not match the assume rigid connection. Moreover, the shear is not distributed evenly across the restrained end, but is instead concentrated in the regions near the shear keys. This localised increase in shear force is likely to result in increased localised shear deformations and is therefore likely to alter the effective stiffness of the beam.

It should be noted that this issue is not specific to this research, and the multipliers relating gross section properties to effective section properties are commonly used in structural engineering. Therefore, this piece of research is also identified within this research as useful future work, and if a rational basis can be determined to define this relationship, then it would be a useful addition to this research area.

12.6. Implementation in the Field

The final and most important step for this research is uptake by the profession. There has been interest expressed from several consultant engineers at different stages of the work. However, at the time or writing, no definite plans have been formed to implement these devices in a structure. The work within this thesis has provided all the basic tools needed for these devices to be incorporated into a design. Ongoing work will hopefully see this most important final step undertaken, and ideally lead to eventual uptake for both new building designs and retrofit applications.

Appendix A: Model Parameter Derivation

Chapter 8 presents a detailed summary of the model derivation for a jointed precast concrete connection with unbounded post-tensioned tendons. It is, however, noted that the derivation of several of the key equations in the chapter could provide a useful addition. This appendix provides more detail about the different deformation regimes, and their contribution to the overall model response. More specifically, this appendix provides additional detail about the transformation from rigid-body connection rotation to rigid-body column rotation as presented in Equation (8-1), and the derivation of the Equation (8-6).

A.1. Elastic Deformation Regime

The column base-shear at gap-opening is easily defined from simple statics. However, the derivation of the corresponding deflection is not as elementary. First, the overall elastic deformation regime must be considered. If only the deflection of the beams is considered, then the induced curvature within the beams will result in a rotation of the column at the beam-column interface. The displacement at the top of the column due to only the column rotation from beam bending is defined $\Delta_{elastic,beam}$ and shown in Figure A.1.

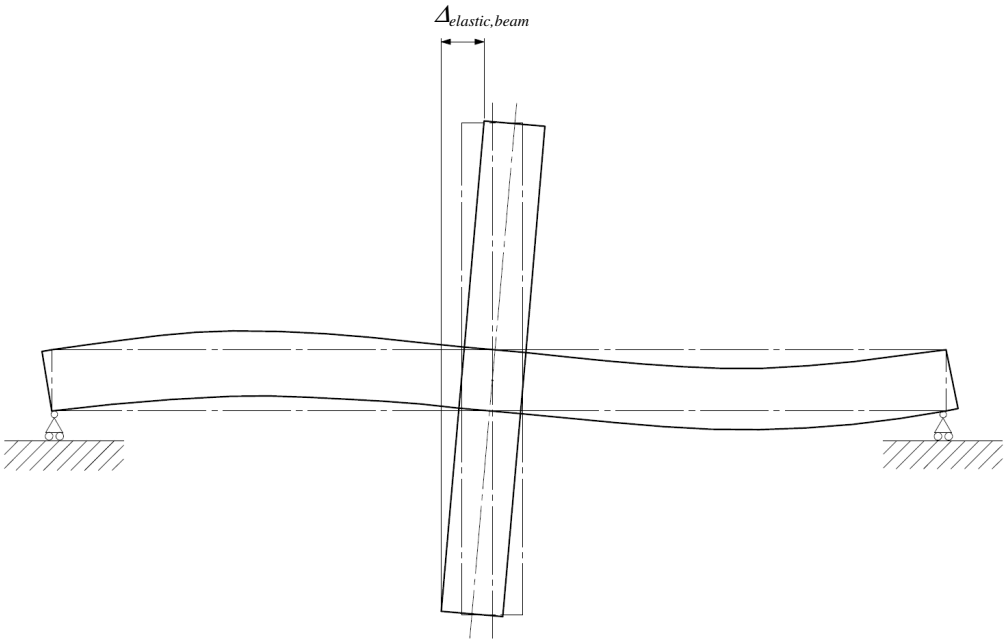

Figure A.1: Schematic diagram of the column displacement from beam deflection alone.

In addition to the displacement due to beam deflection, the column will also elastically deflect essentially behaving as two fixed cantilevers connected by a rigid block at the connection region. The deflection resulting from this column deflection is defined $\Delta_{elastic,column}$ and shown in Figure A.2.

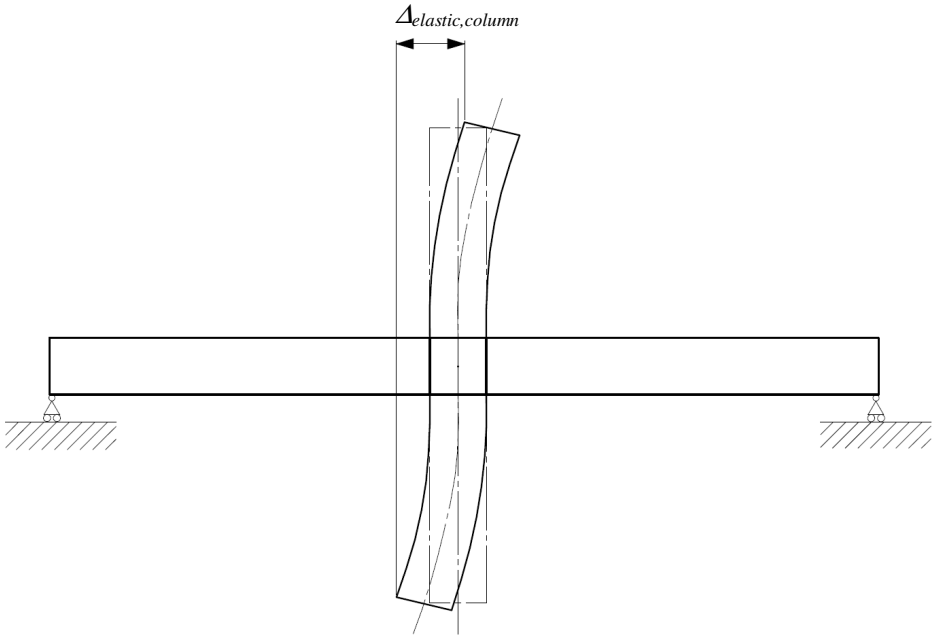

Figure A.2: Schematic diagram of the column displacement from column deflection alone.

Overall, the elastic deflection is the addition of these two components, and is defined $\Delta_{elastic}$ and shown in Figure A.3.

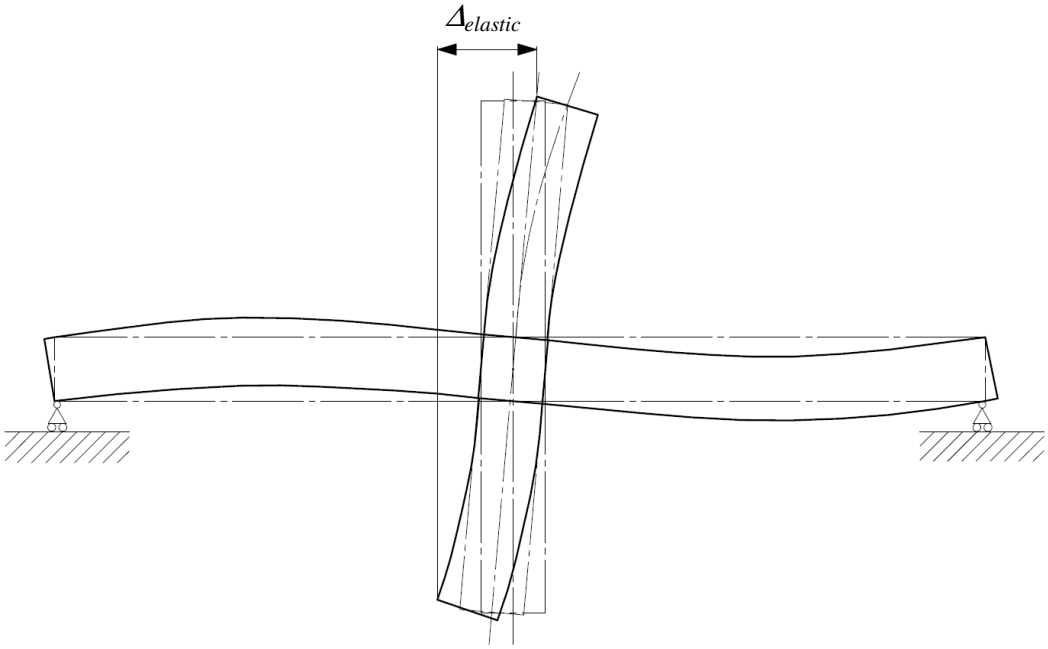

Figure A.3: Schematic diagram of the column displacement from beam and column deflection.

For a given applied base-shear, Equation (A-3) can be used to define the value of the total elastic deflection, $\Delta_{elastic}$. However, the derivation of Equation (A-3) involves several individual equations, and begins with the beam rotation component presented in Figure A.1.

The deflection resulting from this column deflection is defined $\Delta_{elastic,column}$ and shown in Figure A.2. The deflected shape can be represented by two cantilever beams where each takes the form shown in Figure A.4.

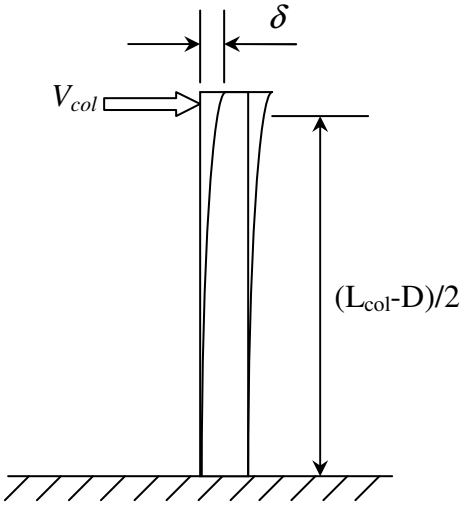

Figure A.4: Deflection of half column cantilever.

where L_{col} is the column length, D is the beam depth, and V_{col} is the column base-shear. By double integrating the moment equation and evaluating the boundary conditions we obtain the general equation for the deflection of a cantilever with a concentrated end load of:

$$\delta = \frac{Fl^3}{3EI} \tag{A-1}$$

where δ is the deflection at the tip, F is the applied load (applied at the tip), l the length of the cantilever, and EI the column stiffness. Substituting in the specific values for the length, $l = (L_{col}\text{-}D)/2$, base-shear, $F = V_{col}$, and effective column stiffness, $EI = EI^*_{col}$, we obtain:

$$\begin{aligned} \delta &= \frac{V_{col}}{3EI^*_{col}}\left[\frac{(L_{col}-D)}{2}\right]^3 \\ &= \frac{V_{col}}{24EI^*_{col}}(L_{col}-D)^3 \end{aligned} \tag{A-2}$$

However, as this equation represents only one half of the column, and from symmetry, the total deflection of the column due to column flexure will be equal to twice this value:

$$\Delta_{elastic,column} = 2\delta$$
$$= \frac{V_{col}}{12EI^{*}_{col}}(L_{col} - D)^3 \qquad \text{(A-3)}$$

The additional column deflection due to beam rotation is simply the column length multiplied by the rotation at the beam-column interface. A diagram of the deflected beam shape is presented in Figure A.5.

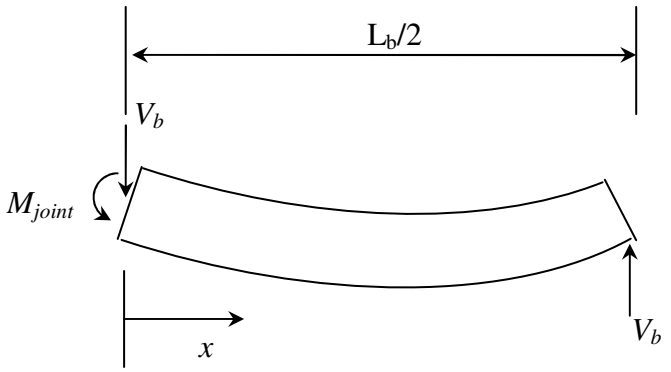

Figure A.5: Deflection of the beam

From statics we can integrate the internal moment in the beam is given:

$$M = V_b\left(\frac{L_b}{2} - x\right) \qquad \text{(A-4)}$$

where V_b is the beam shear, and L_b is the beam length. Substituting Equation (A-4) into the moment-curvature equation and integrating yields:

$$y = -\frac{V_b}{6EI^*_{beam}}\left(\frac{L_b}{2} - x\right)^3 + Ax + B \qquad \text{(A-5)}$$

where A and B are integration constants, and EI_b is the effective beam stiffness. By defining the boundary conditions of y(0) = 0 and y(L_b/2) = 0, the constants are defined:

$$\begin{aligned} B &= \frac{V_b}{6EI^*_{beam}}\left(\frac{L_b}{2}\right)^3 \\ A &= -\frac{V_b}{6EI^*_{beam}}\left(\frac{L_b}{2}\right)^2 \end{aligned} \qquad \text{(A-6)}$$

The rotation of the column at the beam-column interface is simply the first derivative of Equation (A-5) evaluated at y = 0, yielding:

$$\begin{aligned} \left.\frac{dy}{dx}\right|_{y=0} &= \frac{V_b}{2EI^*_{beam}}\left(\frac{L_b}{2}\right)^2 - \frac{V_b}{6EI^*_{beam}}\left(\frac{L_b}{2}\right)^2 \\ &= \frac{V_b L_b^2}{12EI^*_{beam}} \end{aligned} \qquad \text{(A-7)}$$

from overall subassembly equilibrium, it can also be seen that the beam shear is related to the column base-shear:

$$V_b = V_{col}\frac{L_{col}}{L} \qquad \text{(A-8)}$$

which, when substituted into Equation (A-7) yields:

$$\theta_{con} = \left.\frac{dy}{dx}\right|_{y=0} = \frac{V_{col} L_{col} L_b^2}{12 L EI^*_{beam}} \tag{A-9}$$

where θ_{con} is the connection rotation due to beam flexure. During the elastic deformation regime the connection rotation and the column rotation are equal, assuming that the region of the column at the joint region behaves as a rigid block. Therefore, the result of Equation (A-9) can be multiplied by the column length to get the total elastic column deflection due to beam bending:

$$\Delta_{elastic,beam} = \theta_{col} L_{col} = \frac{V_{col} L_{col}^2 L_b^2}{12 L EI^*_{beam}} \tag{A-10}$$

Therefore, the overall elastic deflection of the subassembly, $\Delta_{elastic}$, is given:

$$\begin{aligned} \Delta_{elastic} &= \Delta_{elastic,column} + \Delta_{elastic,beam} \\ &= \frac{V_{col}}{12 EI^*_{col}} (L_{col} - D)^3 + \frac{V_{col} L_{col}^2 L_b^2}{12 L EI^*_{beam}} \\ &= \frac{V_{col}}{12} \left[\frac{(L_{col} - D)^3}{EI^*_{col}} + \frac{L_{col}^2 L_b^2}{L EI^*_{beam}} \right] \end{aligned} \tag{A-11}$$

which is the result presented in Equation (8-6) when the base-shear is equal to V_{col_gap}.

A.2. Rigid-Body Deformation Regime

In addition to the elastic deflection present in Equations (A-1) to (A-11) there will also be a rigid body rotation of the structural members following gap opening. The rigid body regime is presented schematically in Figure A.6.

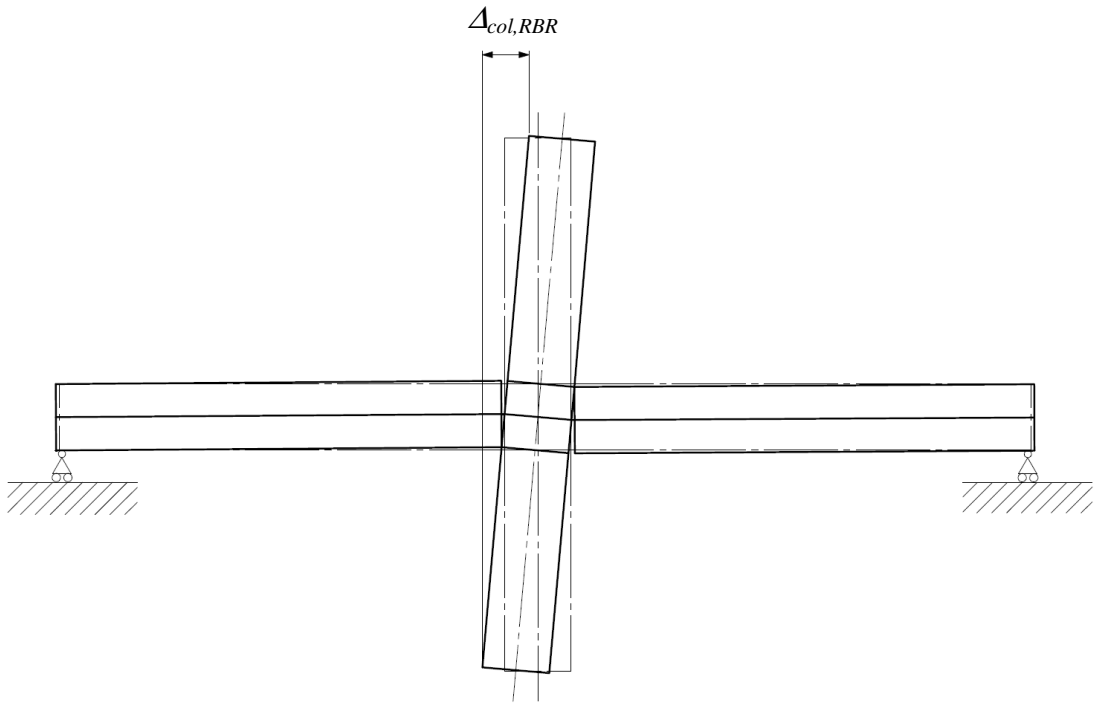

Figure A.6: Schematic diagram of the column displacement from rigid body rotation

Following gap opening, the total deflection of the joint is a combination of the elastic member deflection previously defined, and the rigid body rotation shown in Figure A.6. The relationship between the applied base-shear and the rigid body deflection can be easily defined from simple kinematics. However, the effect on column width to the relationship between connection rotation, θ_{con}, and column rotation, θ_{col}, must also be defined. Figure A.7 presents the deflected shape of the subassembly and shows this relationship.

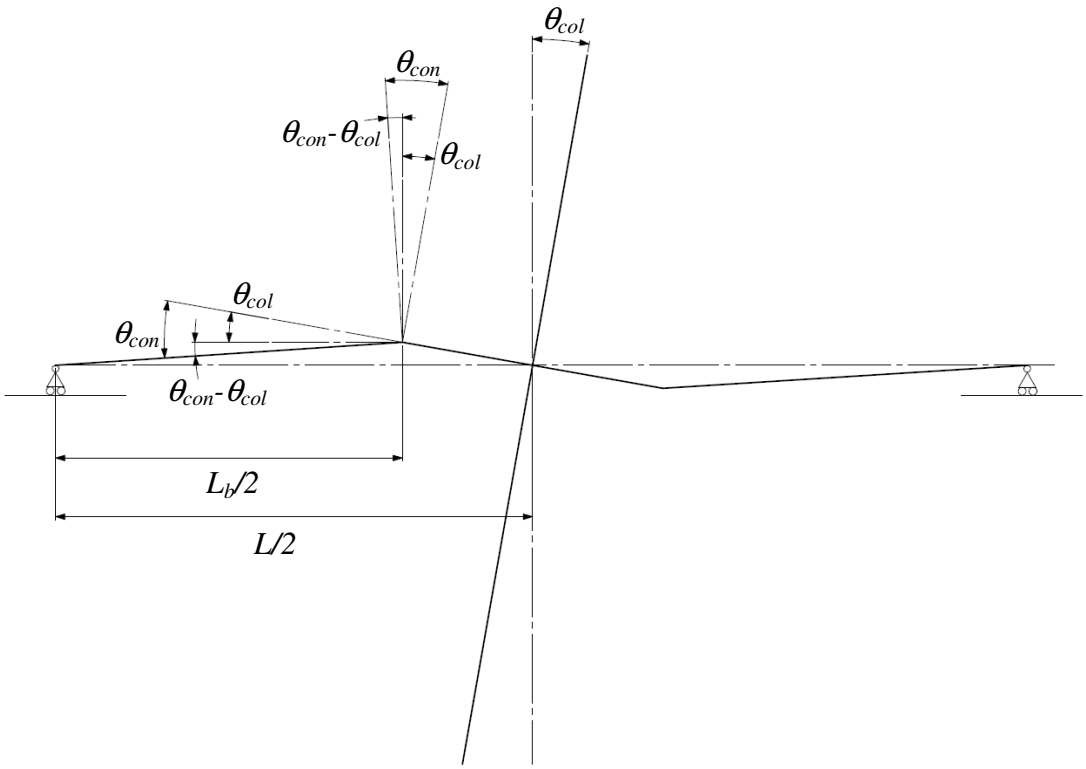

Figure A.7: Diagram showing the relationship between rotation of the column θ_{col} and connection θ_{con}

Simple trigonometric relationships thus yield:

$$\theta_{col} = \theta_{con} \frac{L_b}{L} \qquad \text{(A-12)}$$

which is the same as that presented in Equation (8-1).

Equation (8-7) is obtained from simple kinematics, where the increased strain is calculated from the required damper displacement, number of connections spanned and total length of the tendon. Equation (8-8) is obtained from simple statics and is essentially the same as Equation (8-5), but with the increase in post-tensioning force due to the increased strain calculated in Equation (8-7). Moreover, Equation (8-8) is a modified version of

Equation (8-5) with different applied base shear and includes an added component due to rigid body rotation. The rigid body component is defined as:

$$\Delta_{gap,damper,RBR} = L_{col}\theta_{col} = L_{col}\theta_{con}\frac{L_b}{L} \qquad \text{(A-13)}$$

where the connection rotation, θ_{con}, is defined from simple trigonometry, assuming small displacements, whereby the damper displacement at full engagement is determined from Hooke's Law, and then divided by the eccentricity to obtain a required connection rotation and yields the last component of Equation (8-9).

Equation (8-10) is merely an extension of Equation (8-5) where the post-tensioned tendon force is now equal to its yield force. Equation (8-11) is merely a modification of Equation (8-9) where the applied base-shear is now as defined in Equation (8-10) and the rigid body component corresponds to the required increase in tendon strain to induce plastic deformation.

References

Ajrab, J. J., Pekcan, G., and Mander, J. B. (2004). "Rocking wall-frame structures with supplemental tendon systems." *Journal of Structural Engineering*, 130(6), 895-903.

Amaris, A., Pampanin, S., and Palmero, A. (2006). "Uni And Bi-Directional Quasi-Static Tests On Alternative Hybrid Precast Beam Column Joint Subassemblies." *New Zealand Society for Earthquake Engineering Annual Conference (NZSEE06)*, Napier, New Zealand, 8-pages.

Aprile, A., Inaudi, J. A., and Kelly, J. M. (1997). "Evolutionary Model of Viscoelastic Dampers for Structural Applications." *Journal of Engineering Mechanics*, 123(6), 551-560.

ATC-40. (1996). "Seismic Evaluation and Retrofit of Concrete Buildings Volume 1. - *Applied Technology Council Report No. ATC-40*."

Boss, R. B. (1968). *Metallic materials*, Chapman & Hall, London.

Boss, R. B. (1992). *Metallic materials specification handbook*, Chapman & Hall, London : New York.

Bradley, B. A., Dhakal, R. P., Mander, J. B., and Li, L. (2008). "Experimental multi-level seismic performance assessment of 3D RC frame designed for damage avoidance." *Earthquake Engineering & Structural Dynamics*, 37(1), 1-20.

Chase, J. G., Barroso, L. R., and Hunt, S. (2004). "A Semi-Active Acceleration-Based Control for Seismically Excited Civil Structures Including Control Input Impulses." *Journal of Structural Engineering & Mechanics (SE+M)*, 18(3), 287-301.

Cheok, G. S., and Lew, H. S. (1991). "Performance of precast concrete beam-to-column connections subject to cyclic loading." *PCI Journal*, 36(3), 56-67.

Chopra, A. K. (1995). *Dynamics of structures : theory and applications to earthquake engineering*, Prentice Hall, Englewood Cliffs, N.J.

Christopoulos, C., Filiatrault, A., Uang, C.-M., and Folz, B. (2002). "Posttensioned Energy Dissipating Connections for Moment-Resisting Steel Frames." *Journal of Structural Engineering*, 128(9), 1111-1120.

Christopoulos, C., Tremblay, R., Kim, H. J., and Lacerte, M. (2008). "Self-Centering Energy Dissipative Bracing System for the Seismic Resistance of Structures: Development and Validation." *Journal of Structural Engineering*, 134(1), 96-107.

Clifton, G. C. (2005). "Semi-rigid joints for moment-resisting steel framed seismic-resisting systems," *PhD Thesis*, The University of Auckland, Auckland, New Zealand.

Comerio, M. C. (2006). "Estimating downtime in loss modeling." *Earthquake Spectra*, 22(2), 349-365.

Cousins, W. J., and Porritt, T. E. (1993). "Improvements to lead-extrusion damper technology." *Bulletin of the New Zealand National Society for Earthquake Engineering*, 26(3), 342-348.

Dhakal, R. P., and Maekawa, K. (2002). "Path-dependent cyclic stress-strain relationship of reinforcing bar including buckling." *Engineering Structures*, 24(11), 1383-1396.

Garlock, M. M., Ricles, J. M., and Sause, R. (2005). "Experimental studies of full-scale posttensioned steel connections." *Journal of Structural Engineering*, 131(3), 438-448.

Garlock, M. M., Sause, R., and Ricles, J. M. (2007). "Behavior and design of posttensioned steel frame systems." *Journal of Structural Engineering*, 133(3), 389-399.

Gorenc, B. E., Syam, A., and Tinyou, R. (2005). *Steel Designers Handbook*, UNSW Press, Sydney.

Holden, T., Restrepo, J., and Mander, J. B. (2003). "Seismic performance of precast reinforced and prestressed concrete walls." *Journal of Structural Engineering*, 129(3), 286-296.

Horwich, G. (2000). "Economic lessons of the Kobe earthquake." *Economic Development and Cultural Change*, 48(3), 521-542.

Hwang, J. S., and Ku, S. W. (1997). "Analytical Modeling of High Damping Rubber Bearings." *Journal of Structural Engineering*, 123(8), 1029-1036.

Li, L. (2006). "Further Experiments on Damage Avoidance design of Beam-to-column joints," *Master of Engineering Thesis*, University of Canterbury, Christchurch, New Zealand.

Li, L., Mander, J. B., and Dhakal, R. P. (2008). "Bi-Directional Cyclic Loading Experiment on a 3-D Beam-Column Joint Designed for Damage Avoidance." *ASCE Journal of Structural Engineering*, 134(11), 1733-1742.

Limpert, E., Stahel, W. A., and Abbt, M. (2001). "Log-normal distributions across the sciences: Keys and clues." *Bioscience*, 51(5), 341-352.

Lin, Y.-Y., and Chang, K.-C. (2004). "Effects of site classes on damping reduction factors." *Journal of Structural Engineering*, 130(11), 1667-1675.

MacRae, G. A., MacKinven, H., Clifton, G. C., Pampanin, S., Walpole, W., and Butterworth, J. (2007). "Tests of sliding hinge joints for steel moment frames." Wairakei, New zealand, 109-114.

Makris, N., and Constantinou, M. C. (1991). "Fractional-Derivative Maxwell Model for Viscous Dampers." *Journal of Structural Engineering*, 117(9), 2708-2724.

Mander, J. B. (2004). "Beyond ductility: The quest goes on." *Bulletin of the New Zealand Society for Earthquake Engineering*, 37(1), 35-44.

Mander, J. B., Chen, S. S., and Pekcan, G. (1994). "Low-cycle fatigue behavior of semi-rigid top-and-seat angle connections." *Engineering Journal*, 31(3), 111-122.

Mander, J. B., and Cheng, C.-T. (1997). "Seismic Resistance Of Bridge Piers Based On Damage Avoidance Design." Technical Report NCEER-97-0014, U.S. National Center for Earthquake Engineering Research (NCEER), Department of Civil and Environmental Engineering, State University of New York at Buffalo, Buffalo, USA

Marriott, D. J., Pampanin, S., Bull, D., and Palmero, A. (2009). "A Probabilistic Seismic Loss Assessment of Advanced Post-Tensioned Precast Bridge Systems." *New Zealand Society for Earthquake Engineering Annual Conference (NZSEE09)*, Christchurch, New Zealand, 10-pages.

Menegotto, M., and Pinto, P. (1973). ""Method of analysis for cyclically loaded reinforced concrete plane frames including changes in geometry and non-elastic behavior of elements under combined normal force and bending."." *IABSE Symposium on the Resistance and Ultimate Deformability of Structures Acted on by Well-defined Repeated Loads,*, Lisbon.

Pearson, C. E., and Parkins, R. N. (1960). *The Extrusion of Metals*, London: Chapman & Hall Ltd,.

Pekcan, G., Mander, J. B., and Chen, S. S. (1999). "Fundamental considerations for the design of non-linear viscous dampers." *Earthquake Engineering and Structural Dynamics*, 28(11), 1405-1425.

Pekcan, G., Mander, J. B., and Chen, S. S. (2000). "Experiments on steel MRF building with supplemental tendon system." *Journal of Structural Engineering*, 126(4), 437-444.

Pereira, A. S. (2006). "The Opportunity of a Disaster: The Econominc Impact of the 1755 Lisbon Earthqauke." *Centre for Historical Economics and Related Research at York (CHERRY) - CHERRY Discussion Paper Series*, 03/06.

Priestley, M. J. N., Sritharan, S., Conley, J. R., and Pampanin, S. (1999). "Preliminary results and conclusions from the PRESSS five-story precast concrete test building." *PCI Journal*, 44(6), 42-67.

Priestley, M. J. N., and Tao, J. (1993). "Seismic Response of Precast Prestressed Concrete Frames with Partially Debonded Tendons." *PCI Journal*, 38((1)), 58-69.

Ramberg, W., and Osgood, W. R. (1943). "Description of Stress-strain Curves by Three Parameters." *National Advisory Committee on Aeronautics, Technical Note 902*.

Ricles, J. M., Sause, R., Garlock, M. M., and Zhao, C. (2001). "Posttensioned seismic-resistant connections for steel frames." *Journal of Structural Engineering*, 127(2), 113-121.

Robinson, W. H., and Greenbank, L. R. (1975). "Properties Of An Extrusion Energy Absorber." *Bulletin of the New Zealand Society for Earthquake Engineering*, 8(3), 187-191.

Robinson, W. H., and Greenbank, L. R. (1976). "Extrusion Energy Absorber Suitable For The Protection Of Structures During An Earthquake." *Earthquake Engineering & Structural Dynamics*, 4(3), 251-259.

Rodgers, G. W., Chase, J. G., Macrae, G. A., Bacht, T., Desombre, J., and Dhakal, R. P. (2009a). "Analytical Investigation of the Effects of HF2V Damping Devices on the Seismic Performance of the SAC LA3 Building." *13th Asia Pacific Vibration Conference*, Chirstchurch, New Zealand.

Rodgers, G. W., Chase, J. G., Mander, J. B., Dhakal, R. P., and Solberg, K. M. (2007a). "DAD Post-Tensioned Concrete Connections with Lead Dampers: Analytical Models and Experimental Validation." *8th Pacific Conference on Earthquake Engineering*, Singapore, 9 pages.

Rodgers, G. W., Chase, J. G., Mander, J. B., Leach, N. C., and Denmead, C. S. (2007b). "Experimental development, tradeoff analysis and design implementation of high force-to-volume damping technology." *Bulletin of the New Zealand Society for Earthquake Engineering*, 40(2), 35-48.

Rodgers, G. W., Mander, J. B., Chase, J. G., Dhakal, R. P., Leach, N. C., and Denmead, C. S. (2008a). "Spectral analysis and design approach for high force-to-volume extrusion damper-based structural energy dissipation." *Earthquake Engineering & Structural Dynamics*, 37(2), 207-223.

Rodgers, G. W., Solberg, K. M., Mander, J. B., Chase, J. G., Bradley, B. A., and Dhakal, R. P. (2009b). "High Force-to-Volume Seismic Dissipators Embedded in a Jointed Precast Concrete Frame." *Journal of Structural Engineering*, In Reivew.

Rodgers, G. W., Solberg, K. M., Mander, J. B., Chase, J. G., Bradley, B. A., Dhakal, R. P., and Li, L. (2008b). "Performance Of A Damage-Protected Beam-Column Subassembly Utilizing External HF2V Energy Dissipation Devices." *Earthquake Engineering & Structural Dynamics*, 37(13), 1549-1564.

Rossikhin, Y. A., and Shitikova, M. V. (1998). "Application of Fractional Calculus for Analysis of Nonlinear Damped Vibrations of Suspension Bridges." *Journal of Engineering Mechanics*, 124(9), 1029-1036.

Shama, A. A., Mander, J. B., and Chen, S. S. (2002). "Seismic investigation of steel pile bents: II. Retrofit and vulnerability analysis." *Earthquake Spectra*, 18(1), 143-160.

Shen, K. L., and Soong, T. T. (1995). "Modeling of Viscoelastic Dampers for Structural Applications." *Journal of Engineering Mechanics*, 121(6), 694-701.

Shigley, J. E., Mischke, C. R., and Budynas, R. G. (2004). *Mechanical Engineering Design*, McGraw-Hill, New York, NY.

Skinner, R. I., Robinson, W. H., and McVerry, G. H. (1993). *An introduction to seismic isolation*, Wiley, Chichester ; New York.

Solberg, K. M. (2007). "Experimental and financial investigations into the further development of damage avoidance design," *Master of Engineering Thesis*, University of Canterbury, Christchurch, New Zealand.

Solberg, K. M., Dhakal, R. P., Bradley, B. A., Mander, J. B., and Li, L. (2008a). "Seismic performance of damage-protected beam-column joints." *ACI Structural Journal*, 105(2), 205-214.

Solberg, K. M., Dhakal, R. P., Mander, J. B., and Bradley, B. A. (2008b). "Computational and rapid expected annual loss estimation methodologies for structures." *Earthquake Engineering & Structural Dynamics*, 37(1), 81-101.

Solberg, K. M., Mashiko, N., Mander, J. B., and Dhakal, R. P. (2009). "Performance of a damage protected highway bridge pier subjected to bi-directional earthquake attack." *ASCE Journal of Structural Engineering*, (In Press).

Somerville, P., Smith, N., Punyamurthula, S., and Sun, J. (1997). "Development of Ground Motion Time Histories For Phase II Of The FEMA/SAC Steel Project, SAC Background Document Report SAC/BD-97/04."

Standards New Zealand - Technical Committee Bd-006-04. "NZS1170.5 Supp 1:2004:Structural Design Actions - Part 5: Earthquake Actions - New Zealand - Commentary." Standards New Zealand, Wellington, New Zealand, 2004.

Standards New Zealand. (1997). *Steel Structures Standard - NZS 3404: Part 1: 1997*, Standards New Zealand, Wellington [N.Z.].

Stanton, J., Stone, W. C., and Cheok, G. S. (1997). "Hybrid reinforced precast frame for seismic regions." *PCI Journal*, 42(2), 20-32.

Ugural, A. C. (1991). *Mechanics of Materials*, McGraw-Hill, New York.

United States Geological Survey (USGS). (1999a). "Major Quake Likely to Strike Between 2000 and 2030." Understanding Earthquake Hazards in the San Francisco Bay Region - USGS Fact Sheet-152-99.

United States Geological Survey (USGS). (1999b). "Progress Towards a Safer Future Since the 1989 Loma Prieta Earthquake." Understanding Earthquake Hazards in the San Francisco Bay Region - USGS Fact Sheet-151-99.

United States Geological Survey (USGS). (2008). "Forecasting Califronia's Earthquakes - What Can We Expect in the Next 30 Years?", USGS Fact Sheet 2008-3027.